2014

The effect of surface patterning and unidirectional roughness on corrosion of metals

Alisina Toloei
University of Windsor

The effect of surface patterning and unidirectional roughness on corrosion of metals

By

Alisina Toloei

A Dissertation
Submitted to the Faculty of Graduate Studies
through Mechanical, Automotive and Materials Engineering
in Partial Fulfillment of the Requirements for
the Degree of Doctor of Philosophy
at the University of Windsor

Windsor, Ontario, Canada

2014

The effect of surface patterning and unidirectional roughness on corrosion of metals

By

Alisina Toloei

APPROVED BY:

J. R. Kish, External Examiner
McMaster University

R. Aroca
Department of Chemistry and Biochemistry

R. Bowers
Department of Mechanical, Automotive and Materials Engineering

D. Green
Department of Mechanical, Automotive and Materials Engineering

V. Stoilov, Co-Advisor
Department of Mechanical, Automotive and Materials Engineering

D.O. Northwood, Co-Advisor
Department of Mechanical, Automotive and Materials Engineering

May 7, 2014

DECLARATION OF CO-AUTHORSHIP AND PREVIOUS PUBLICATION

I hereby declare that this thesis does not incorporate material that is result of joint research.

In all cases, the key ideas, primary contributions, experimental designs, data analysis and interpretation, were performed by the author, Dr. D. O. Northwood and Dr. V. Stoilov as advisors.

I certify that, with the above qualification, this thesis, and the research to which it refers, is the product of my own work.

I certify that the above material describes work completed during my registration as a graduate student at the University of Windsor.

I declare that, to the best of my knowledge, my thesis does not infringe upon anyone's copyright nor violate any proprietary rights and that any ideas, techniques, quotations, or any other material from the work of other people included in my thesis, published or otherwise, are fully acknowledged in accordance with the standard referencing practices.

I declare that this is a true copy of my thesis, including any final revisions, as approved by my thesis committee and the Graduate Studies office, and that this thesis has not been submitted for a higher degree to any other University or Institution.

ABSTRACT

In this study two different surface modification methods, namely surface patterning and unidirectional roughness, were applied to nickel and mild steel specimens to investigate the effect of surface roughness on the corrosion resistance. The goal is to decrease the contact area between the corrosive electrolyte and the substrate by creating different surface morphologies using different methods including surface patterns by laser ablation and unidirectional surface roughness through using SiC papers with different grits (G60- to G1200) on nickel and mild steel with different passivation behaviours.

Electrochemical impedance spectroscopy measurements (EIS), potentiodynamic polarization and different surface characterization methods were performed to investigate the protection performance of the metals. In the first phase, patterns of holes with specific diameters (D) and inter-hole spacings (L) were created by laser ablation on nickel and corrosion tests were carried out in a 0.5 M H_2SO_4 solution. The corrosion potential, E_{Corr}, and current density (I_{Corr}) were determined and compared for different ratios of (D/L). Energy dispersive spectroscopy (EDS) was performed on the surface of the samples to investigate the chemical composition, specifically the oxygen content of different regions of the patterned area before and after corrosion testing. By creating such patterns we are able to produce a surface with heterogeneous wetting properties, to decrease the contact area between the liquid and the substrate. It has been shown that for a few specific patterns the corrosion resistance can be increased by orders of magnitude.

In the next phase, the effect of unidirectional surface roughness on the corrosion of nickel and mild steel was investigated using EIS and potentiodynamic polarization techniques. Scanning electron micrographs were also taken and roughnesses were measured before and after corrosion testing with a profilometer. EDS also measured oxygen concentration. By decreasing the roughness, the corrosion resistance of nickel and mild steel increased and decreased respectively. The patterned sample showed the best corrosion resistance as a result of the heterogeneous wetting phenomenon that happened on the surface. Surface patterning also can achieve a much larger improvement in corrosion resistance compared to unidirectional roughness.

DEDICATION

I would like to dedicate this dissertation to my grandpas (RIP), my parents, Nina and Sanam for their unconditional love, support and encouragement.

ACKNOWLEDGEMENTS

I would like to thank God for giving me the strength and endurance to accomplish this work.

I would like to thank my doctoral advisors, Dr. D. O. Northwood and Dr. V. Stoilov, for their dedication and continuous support and help.

I would like to extend my thanks to my committee members, Dr. D. Green, Dr. R. Bowers, Dr. R. Aroca and Dr. J. R. Kish for their time and effort during my PhD study with special thanks to them for reviewing this dissertation, and their continuous support and advice.

I would like to thank Ms. Sanam Atashin for helping me with roughness measurement tests, Dr. D. Shoesmith (Western University), and Dr. J. Wang (Chemistry, University of Windsor), for their help with my experimental work and giving me the opportunity to use their laboratory facilities.

TABLE OF CONTENTS

DECLARATION OF CO-AUTHORSHIP AND PREVIOUS PUBLICATION iii

ABSTRACT iv

DEDICATION vi

ACKNOWLEDGEMENTS vii

LIST OF TABLES xii

LIST OF FIGURES xiv

LIST OF ABBREVIATIONS xiv

NOMENCLATURE xxiv

Chapter 1 Introduction 1

1.1 Dissertation Outline 4

Chapter 2 Literature Review 6

2.1 Corrosion 6

2.1.1 Combating Corrosion and Prevention Methods 7

2.1.2 Corrosion of Metallic Materials and Their Behaviour (Active-Passive) 8

2.1.3 Corrosion of nickel and mild steel in dilute sulfuric acid: 10

2.1.4 Important Parameters Affecting Corrosion 25

2.2 Surface Patterning and Surface Roughness 25

2.2.1 Effect of surface roughness on corrosion properties 31

2.2.2 Different methods for generating patterned surfaces 44

2.2.3 Applications of textured surfaces 49

2.3 Wetting 51

2.4 Hydrophobicity 56

2.5 Water repellant properties and corrosion 61

Chapter 3 Experimental Procedures 66

3.1 Sample preparation of nickel and mild steel 66

3.1.1 Laser ablation method 67

3.1.2 Unidirectional roughness 69

3.2 Corrosion Testing 71

3.2.1 Open circuit potential (OCP) and potentiodynamic polarization technique 71

3.2.2 Electrochemical Impedance Spectroscopy (EIS) 72

3.3 Scanning Electron Microscopy (SEM) and Energy Dispersive Spectroscopy (EDS) 73

3.4 XRD 73

3.5 Roughness Measurements 74

Chapter 4 Surface Patterning of Nickel 75

4.1 Corrosion Testing Results 75

4.1.1 Potentiodynamic Polarization Technique 75

4.2 SEM Images 80

4.2.1 Before corrosion: 80

4.2.2 After corrosion: 85

4.3 Roughness Measurement Results 91

4.3.1 Before corrosion 91

4.3.2 After corrosion: 95

4.4 EDS Results 101

Chapter 5 Unidirectional Roughness on Nickel 107

5.1 Corrosion Testing Results 107

5.1.1 Potentiodynamic Polarization Technique Results 107
5.1.2 EIS Results 114
5.2 SEM Images 122
5.2.1 Before corrosion: 122
5.2.2 After corrosion: 125
5.3 Roughness Measurement Results 128
5.4 Roughness profiles before and after corrosion 132
5.5 EDS Results 149
5.5.1 Before corrosion 149
5.5.2 After corrosion: 150
5.6 Roughness parameters before and after corrosion 152
5.7 Relationship between corrosion rate and different roughness parameters 155
Chapter 6 Unidirectional Roughness on Mild Steel 162
6.1 Corrosion Testing Results 162
6.1.1 Potentiodynamic Polarization Technique 162
6.1.2 EIS Results 168
6.2 SEM Images 177
6.2.1 Before Corrosion: 177
6.2.2 After Corrosion: 179
6.3 Roughness Measurement Results 183
6.4 Roughness profiles before and after corrosion 188
6.5 EDS Results 204
6.5.1 Before Corrosion: 205

6.5.2 After Corrosion 206

6.6 XRD 208

6.7 Roughness parameters before and after corrosion 209

6.8 Relationship between corrosion rate and different roughness parameters 212

Chapter 7 General Discussion and Conclusions 222

7.1 Discussion on surface patterning through laser ablation 222

7.2 Discussion for nickel surface with unidirectional roughness 225

7.3 Discussion for mild steel surface with unidirectional roughness 229

7.4 Conclusions 234

7.4.1 Surface Patterning 234

7.4.2 Unidirectional Roughness 234

7.5 Recommendations for Future Research 236

Appendices 237

Publications 273

REFERENCES 275

VITA AUCTORIS 289

LIST OF TABLES

Table 2-1 Relationship between surface roughness and corrosion for different metals. 43

Table 2-2 A summary on different methods for generating patterned surfaces and their characteristics. 48

Table 3-1. Hole sizes and distances between holes of the textures created on nickel 68

Table 3-2. Sample coding system 69

Table 4-1 Corrosion parameters for patterned nickel samples with different (D) and (L) values. 77

Table 4-2. Oxygen concentration (wt. %) before and after corrosion testing 102

Table 5-1: Corrosion parameters obtained from dynamic polarization measurements for nickel. 110

Table 5-2: Equivalent circuit elements for nickel with various surface roughnesses. 119

Table 5-3 R_a values before and after corrosion testing of nickel 128

Table 5-4 R_q values before and after corrosion testing of nickel 129

Table 5-5 R_z values before and after corrosion testing of nickel 130

Table 5-6 R_t values before and after corrosion testing of nickel 130

Table 5-7: Oxygen contents on the surface of the nickel samples before and after corrosion testing. 152

Table 6-1 Different corrosion parameters obtained from potentiodynamic polarization technique 164

Table 6-2 EIS data for mild steel samples with different roughnesses 176

Table 6-3 R_a values for mild steel before and after corrosion testing 184

Table 6-4 R_q values for mild steel before and after corrosion testing 185

Table 6-5 R_z values for mild steel before and after corrosion testing..... 186

Table 6-6 R_t values for mild steel before and after corrosion testing 187

Table 6-7 Oxygen and sulphur contents on the surface of mild steel samples before and after corrosion testing. 205

LIST OF FIGURES

Figure 2-1 Different anodic behaviours of metals 9

Figure 2-2 Pourbaix diagram for iron (SCE) 11

Figure 2-3 Pourbaix diagram for nickel (SCE) 13

Figure 2-4 Experimental impedance spectra and the equivalent circuit for mild steel in dilute H_2SO_4 15

Figure 2-5 Experimental impedance spectra and the equivalent circuit for mild steel in dilute H_2SO_4 16

Figure 2-6 Experimental impedance spectra and the equivalent circuit for mild steel in dilute H_2SO_4 17

Figure 2-7 Experimental impedance spectra and the equivalent circuit for mild steel in dilute H_2SO_4 18

Figure 2-8 Experimental impedance spectra and the equivalent circuit for mild steel in dilute H_2SO_4 18

Figure 2-9 Experimental impedance spectra and the equivalent circuit for nickel in dilute H_2SO_4 19

Figure 2-10 Experimental impedance spectra and the equivalent circuit for nickel in dilute H_2SO_4 20

Figure 2-11 Experimental impedance spectra and the equivalent circuit for nickel in dilute H_2SO_4 21

Figure 2-12 Experimental impedance spectra and the equivalent circuit for nickel in dilute H_2SO_4 22

Figure 2-13 Experimental impedance spectra and the equivalent circuit for nickel in dilute H_2SO_4 23

Figure 2-14 Grooved pattern of the shark skin surface 29

Figure 2-15 (a) Microstructure of the hairs in gecko's foot. (b) SEM micrograph of micro-fabricated polyimide dry adhesive 30

Figure 2-16 Laser Ablation System 48

Figure 2-17 Wetting regimes of a rough surface: (a) homogeneous wetting, (b) heterogeneous wetting 52

Figure 2-18 Contact angle on a smooth surface 53

Figure 2-19 Composite surface 54

Figure 2-20 The hierarchical structure of a water strider's leg with numerous oriented microsetae. (b) Each seta has a nanoscale grooved surface texture ... 57

Figure 2-21 Plant leaves with water-repellent surfaces 57

Figure 2-22 Microscale protuberances on the surface of a lotus leaf. (b) Each protuberance is covered with a nanoscale needle-like structure 58

Figure 2-23 (a) An almost ballshaped water droplet on a non-wettable plant leaf.(b) Low- and (c) high-magnification scanning electron microscope images of the surface structures on the lotus leaf [148]. 60

Figure 2-24 A typical 2-D microtexture: (a) noncomposite; (b) composite 64

Figure. 3-1. Schematic of the proposed surface texture model; D is the hole diameter and L is the inter-hole spacing. The grey area is the laser ablated region. 67

Figure 3-2. Flowchart of experimental procedures. 70

Figure 4-1 Potentiodynamic polarization curves for patterned samples (SCE)... 76

Figure 4-2 Current density of the patterned samples of nickel versus (1/D). 79

Figure 4-3 SEM micrographs of the patterned samples a) reference, b) D2L4, c) D2L8 and d) D3.5L3.5 before corrosion. 81

Figure 4-3 (Cont) SEM micrographs of the patterned samples e) D3.5L7, f) D3.5L14, g) D30L30 and h) D30L60 before corrosion. 82

Figure 4-3 (Cont) SEM micrographs of the patterned samples i) D5L5, j) D5L10, k) D5L20 and l) D10L10 before corrosion. 83

Figure 4-3 (Cont) SEM micrographs of the patterned samples m) D10L20, n) D10L30, o) D20L20, p) D20L30 and q) D20L40 before corrosion. 84

Figure 4-4 SEM micrographs of the patterned samples a) reference, b) D2L4, c) D2L8 and d) D3.5L3.5 after corrosion. 86

Figure 4-4 (Cont) SEM micrographs of the patterned samples e) D3.5L7, f) D3.5L14, g) D30L30 and h) D30L60 after corrosion. 87

Figure 4-4 (Cont) SEM micrographs of the patterned samples i) D5L5, j) D5L10, k) D5L20 and l) D10L10 after corrosion. 88

Figure 4-4 (Cont) SEM micrographs of the patterned samples m) D10L20, n) D10L30, o) D20L20, p) D20L30 and q) D20L40 after corrosion. 90

Figure 4-5 Sample D2L4 3D roughness before corrosion 91

Figure 4-6 Sample D2L8 3D roughness before corrosion 92

Figure 4-7 Sample D3.5L3.5 3D roughness before corrosion 93

Figure 4-8 Sample D3.5L7 3D roughness before corrosion 93

Figure 4-9 Sample D3.5L14 3D roughness before corrosion 94

Figure 4-10 Sample D30L30 3D roughness before corrosion 94

Figure 4-11 Sample D30L60 3D roughness before corrosion 95

Figure 4-12 Sample D2L4 3D roughness after corrosion 96

Figure 4-13 Sample D2L8 3D roughness after corrosion 97

Figure 4-14 Sample D3.5L3.5 3D roughness after corrosion 98

Figure 4-15 Sample D3.5L7 3D roughness after corrosion 98

Figure 4-16 Sample D3.5L14 3D roughness after corrosion 99

Figure 4-17 Sample D30L30 3D roughness after corrosion 100

Figure 4-18 Sample D30L60 3D roughness after corrosion 100

Figure 4-19 EDS analysis of sample D30L60 before the corrosion test inside the hole..... 103

Figure 4-20 EDS analysis of sample D30L60 before the corrosion test outside the hole..... 104

Figure 4-21 EDS analysis of sample D30L60 after the corrosion test inside the hole..... 104

Figure 4-22 EDS analysis of sample D30L60 after the corrosion test outside the hole..... 105

Figure 5-1: Typical polarization curves for nickel in 0.5M H_2SO_4..... 108

Figure 5-2: Polarization curves for samples G60, G400, G1200 and D10L20.. 109

Figure 5-3 Dependence of i_{corr} on surface finish of nickel..... 111

Figure 5-4 Dependence of CR on surface finish of nickel..... 112

Figure 5-5 E_{corr} vs surface finish on nickel (including patterned samples) 113

Figure 5-6 Dependence of R_p on surface finish of nickel..... 113

Figure 5-7: Equivalent circuit model 114

Figure 5-8: Nyquist diagrams for nickel with different roughnesses..... 116

Figure 5-9: (a) Bode magnitude and (b) Bode phase plots for fitted and experimental results for sample G60 of nickel. 118

Figure 5-10: Change in n with surface roughness of nickel..... 120

Figure 5-11: Change in CPE with surface roughness of nickel..... 121

Figure 5-12 SEM micrographs of nickel samples with unidirectional roughnesses a)G1200, b)G800, c)G600, d)G400, e)G320, f)G240, g)G180 and h)G120 before corrosion..... 123

Figure 5-12 (cont) SEM micrograph of nickel sample with unidirectional roughness i)G60 before corrosion 124

Figure 5-13 SEM micrographs of nickel samples with unidirectional roughness a)G1200, b)G800, c)G600, d)G400, e)G320, f)G240, g)G180 and h)G120 after corrosion..... 126

Figure 5-13 (Cont) SEM micrograph of nickel sample with unidirectional roughness i)G60 after corrosion 127

Figure 5-14 Sample G120 2D roughness before corrosion 133

Figure 5-15 Sample G120 2D roughness after corrosion 133

Figure 5-16 Sample G120 3D roughness before corrosion 134

Figure 5-17 Sample G120 3D roughness after corrosion 135

Figure 5-18 Sample G1200 2D roughness before corrosion 137

Figure 5-19 Sample G1200 2D roughness after corrosion 137

Figure 5-20 Sample G1200 3D roughness before corrosion 138

Figure 5-21 Sample G1200 3D roughness after corrosion 138

Figure 5-22 X-profile and Y-profile of sample G120 before corrosion..... 140

Figure 5-23 X-profile and Y-profile of sample G120 after corrosion..... 140

Figure 5-24 X-profile and Y-profile of sample G1200 before corrosion..... 142

Figure 5-25 X-profile and Y-profile of sample G1200 after corrosion..... 142

Figure 5-26 Histogram curve of sample G120 before corrosion 145

Figure 5-27 Histogram curve of sample G120 after corrosion 145

Figure 5-28 Histogram curve of sample G1200 before corrosion 148

Figure 5-29 Histogram curve of sample G1200 after corrosion 148

Figure 5-30 EDS analysis of sample G600 of nickel before corrosion..... 149

Figure 5-31 EDS analysis of sample G600 of nickel after corrosion..... 150

Figure 5-32 R_a values for nickel before and after corrosion testing. 153

Figure 5-33 R_q values for nickel before and after corrosion testing. 153

Figure 5-34 R_t values for nickel before and after corrosion testing. 154

Figure 5-35 R_z values for nickel before and after corrosion testing. 154

Figure 5-36 Dependence of corrosion rate on (R_a) for nickel..... 156

Figure 5-37 Dependence of corrosion rate on (R_q) for nickel..... 157

Figure 5-38 Dependence of corrosion rate on (R_z) for nickel..... 157

Figure 5-39 Dependence of corrosion rate on (R_t) for nickel 158

Figure 5-40: The effect of average roughness on R_p and R_{ct} for nickel..... 159

Figure 6-1 Polarization curves for samples G60, G400 and G1200 (SCE)..... 163

Figure 6-2 Dependence of i_{corr} on surface finish of mild steel 165

Figure 6-3 Dependence of E_{corr} on surface finish of mild steel 166

Figure 6-4 Dependence of corrosion rate on surface finish of mild steel 167

Figure 6-5 Dependence of R_p on surface finish of mild steel 168

Figure 6-6 Equivalent circuit model for mild steel 170

Figure 6-7 Nyquist curve-fitted impedance results for sample G600 171

Figure 6-8 (a)Bode (b)Bode phase curve-fitted impedance results for sample G600..... 172

Figure 6-9 Nyquist plots of mild steel samples with different roughnesses..... 174

Figure 6-10 (a)Bode and (b)Bode-Phase plots for mild steel with different roughnesses 175

Figure 6-11 SEM micrographs of mild steel samples a) G1200, b) G800, c) G600, d) G400, e) G320, f) G240, g) G180 and h) G120 before corrosion 178

Figure 6-11 (Cont) SEM micrograph of mild steel sample i) G60 before corrosion 179

Figure 6-12 SEM micrographs of mild steel samples a) G1200, b) G800, c) G600, d) G400, e) G320, f) G240, g) G180 and h) G120 after corrosion 181

Figure 6-12 (Cont) SEM micrograph of mild steel sample i) G60 after corrosion 182
Figure 6-13 Sample G60 2D roughness before corrosion 190
Figure 6-14 Sample G60 2D roughness after corrosion 190
Figure 6-15 Sample G60 3D roughness before corrosion 191
Figure 6-16 Sample G60 3D roughness after corrosion 191
Figure 6-17 Sample G800 2D roughness before corrosion 193
Figure 6-18 Sample G800 2D roughness after corrosion 193
Figure 6-19 Sample G800 3D roughness before corrosion 194
Figure 6-20 Sample G800 3D roughness after corrosion 194
Figure 6-21 X-profile and Y-profile of sample G60 before corrosion..... 196
Figure 6-22 X-profile and Y-profile of sample G60 after corrosion..... 196
Figure 6-23 X-profile and Y-profile of sample G800 before corrosion..... 198
Figure 6-24 X-profile and Y-profile of sample G800 after corrosion..... 198
Figure 6-25 Histogram curve of sample G60 before corrosion 201
Figure 6-26 Histogram curve of sample G60 after corrosion 201
Figure 6-27 Histogram curve of sample G800 before corrosion 203
Figure 6-28 Histogram curve of sample G800 after corrosion 203
Figure 6-29 EDS analysis of sample G320 before corrosion testing 206
Figure 6-30 EDS analysis of sample G320 after corrosion testing 207
Figure 6-31 XRD analysis of samples G1200 and G60 after corrosion 208
Figure 6-32 R_a values for mild steel before and after corrosion testing. 210
Figure 6-33 R_q values for mild steel before and after corrosion testing. 210
Figure 6-34 R_z values for mild steel before and after corrosion testing. 211

Figure 6-35 R_t values for mild steel before and after corrosion testing. 211

Figure 6-36 Dependence of corrosion rate of mild steel on R_a 213

Figure 6-37 Dependence of corrosion rate of mild steel on R_q 214

Figure 6-38 Dependence of corrosion rate of mild steel on R_t 214

Figure 6-39 Dependence of corrosion rate of mild steel on R_z 215

Figure 6-40 The effect of surface roughness of mild steel on R_p and R_{ct} 216

Figure 7-1 Schematics of the patterned surface on nickel a) complete protection before corrosion b) heterogeneous interface c) non-heterogeneous interface. 225

Figure 7-2 Schematics of the unidirectional nickel surface a) before corrosion, b)rough surface after corrosion and c)smooth surface after corrosion. 228

Figure 7-3 Schematic of the unidirectional mild steel surface a) before corrosion, b) smooth surface after corrosion and c) rough surface after corrosion. 233

Figure A-1 2D images for nickel samples a)G60, b)G180, c)G240, d)G320, e)G400, f)G600 and g)G800 before corrosion 238

Figure A-2 3D surface textures for nickel samples a)G60, b)G180, c)G240, d)G320, e)G400, f)G600 and g)G800 before corrosion 239

Figure A-3 2D images for nickel samples a)G60, b)G180, c)G240, d)G320, e)G400, f)G600 and g)G800 after corrosion 241

Figure A-4 3D surface textures for nickel samples a)G60, b)G180, c)G240, d)G320, e)G400, f)G600 and g)G800 after corrosion 242

Figure A-5 X and Y profiles for nickel samples a)G60, b)G180, c)G240, d)G320, e)G400, f)G600 and g)G800 before corrosion 244

Figure A-6 X and Y profiles for nickel samples a)G60, b)G180, c)G240, d)G320, e)G400, f)G600 and g)G800 after corrosion 246

Figure A-7 Histograms for nickel samples a)G60, b)G180, c)G240, d)G320, e)G400, f)G600 and g)G800 before corrosion 248

Figure A-8 Histograms for nickel samples a)G60, b)G180, c)G240, d)G320, e)G400, f)G600 and g)G800 after corrosion 250

Figure B-1 EDS analysis for nickel samples before corrosion 252

Figure B-2 EDS analysis for nickel samples after corrosion 254

Figure C-1 2D images for mild steel samples a)G120, b)G180, c)G240, d)G320, e)G400, f)G600 and g)G1200 before corrosion 256

Figure C-2 3D images for mild steel samples a)G120, b)G180, c)G240, d)G320, e)G400, f)G600 and g)G1200 before corrosion 257

Figure C-3 2D images for mild steel samples a)G120, b)G180, c)G240, d)G320, e)G400, f)G600 and g)G1200 after corrosion 259

Figure C-4 3D images for mild steel samples a)G120, b)G180, c)G240, d)G320, e)G400, f)G600 and g)G1200 after corrosion 260

Figure C-5 X and Y profiles for mild steel samples a)G120, b)G180, c)G240, d)G320, e)G400, f)G600 and g)G1200 before corrosion 262

Figure C-6 X and Y profiles for mild steel samples a)G120, b)G180, c)G240, d)G320, e)G400, f)G600 and g)G1200 after corrosion 264

Figure C-7 Histograms for mild steel samples a)G120, b)G180, c)G240, d)G320, e)G400, f)G600 and g)G1200 before corrosion 266

Figure C-8 Histograms for mild steel samples a)G120, b)G180, c)G240, d)G320, e)G400, f)G600 and g)G1200 after corrosion 268

Figure D-1 EDS analysis for mild steel samples before corrosion 270

Figure D-2 EDS analysis for mild steel samples after corrosion 272

LIST OF ABBREVIATIONS

AJM	Abrasive Jet Machining
CPE	Constant Phase Element
CR	Corrosion Rate
CV	Cyclic Voltametry
DLC	Diamond Like Coating
EDS	Energy Dispersive Spectroscopy
EIS	Electrochemical Impedance Spectroscopy
LBM	Laser Beam Machining
LST	Laser Surface Texturing
MEMS	Micro-Electrical Mechanical Systems
OCP	Open Circuit Potential
PR	Polarization Resistance
RIE	Reactive Ion Etching
RMS	Root Mean Squares
SEM	Scanning Electron Microscopy
VMT	Vibro-Mechanical Texturing
WYKO	Profilometer brand name

NOMENCLATURE

A	Contact area
A_r	Real area of contact
D	Diameter of the holes
L	Linear distance between the centers of any two adjacent holes(Inter-hole spacing)
r	Surface roughness factor
R_s	Solution resistance
i_{corr}	Corrosion current density
E_{corr}	Corrosion potential
j^2	Imaginary number
n	Constant phase element exponent
R_{ct}	Charge transfer resistance
P_i	Corrosion rate
EW	Alloy equivalent weight
z	Impedance
R_z	Average of the ten greatest peak-to-valley separations on the sample
R_t	Peak-to-valley difference calculated over the entire measured array
R_q	Root-mean-squared roughness calculated over the entire measured array
R_a	Average roughness

θ_w	Apparent contact angle
θ_{FLAT}	Contact angle of the flat surface
ω	Angular frequency
ρ	Alloy density
β_a	Anodic Tafel constants
β_c	Cathodic Tafel constants

Chapter 1 INTRODUCTION

The definition of corrosion in the context of Corrosion Science is the reaction of a solid with its environment and the definition of corrosion in the context of Corrosion Engineering is the reaction of an engineering constructional metal (material) with its environment with a consequent deterioration in properties of the metal (material). There are four important requirements for corrosion to occur including an anode, a cathode, connection or contact and an electrolyte. All methods for preventing corrosion, such as coatings, inhibitors, materials selection and cathodic protection, affect one or more of these requirements and decrease corrosion [1].

There are different methods for decreasing the corrosion including surface modification which will be discussed in the literature review section. If we can modify the surface in a manner that decreases the contact area of the electrolyte with the substrate, we will be able to decrease the effect of one of those four parameters and decrease the corrosion. The effect of surface modification on various metals is different. In some cases, the metal has the ability to form a protective passive layer such as nickel and stainless steel but in some other cases, including mild steel, the metal doesn't have such ability. Thus, the reaction mechanism and the effect of surface modification on corrosion rate in both cases are expected to be different from each other. Based on the literature, different roughnesses including bio inspired patterns, micro surface texturing have proven to be an effective means of enhancing corrosion resistance or

tribological performance. Most of the studies investigated the effects of surface texturing on friction and wear and the majority of them showed the potential benefits of adding micro surface texturing to the substrate [2-6]. In the present study, the corrosion of the surface is addressed, and the effect of surface textures including surface patterns and unidirectional surface roughnesses on protection of the metal surface is evaluated.

In this study, the improvement of corrosion resistance through surface texturing is investigated. The goal of this work was to fabricate functional surfaces that simultaneously combined water repellency with high corrosion resistance. Two different surface texturing techniques were used, namely, (i) holes with different diameters and inter-hole spacings created through laser ablation method and (ii) unidirectional roughness made by grinding with different grit size SiC papers. To accomplish the objective of improving corrosion resistance, a thorough analysis of the mechanisms involved in both techniques is made. Nickel as a metal with the ability to form a passive layer, and mild steel with no ability to form a passive layer, have been selected to investigate the simultaneous effect of surface roughness and passive layer in both cases.

In most of the previous studies, surfaces with water repellant properties were achieved using a roughness on a surface along with a chemical to decrease surface energy. But in this research the novelty is to create these surfaces or improve their corrosion resistance without using any other material and only by surface modification.

In the first part of this research, which will be about surface patterning on nickel, for the first time the effect of surface modification on non-wetting properties of nickel was investigated. To the best of knowledge, similar work has been performed on other metals such as stainless steel, Cu, Al and Zn [7-12]. But no work has been done on surface patterning and surfaces with unidirectional roughnesses on the nickel. The aim of this work was to create special surface patterns and unidirectional roughnesses on a pure nickel surface and study the corrosion behaviour of the surfaces and compare the results with mild steel, which is a metal with no ability to form a passive layer (in contrast with nickel). In fact, in this research the novelty was first to select pure nickel; second to create a water repellant surface using laser ablation method on pure nickel sheet without using any materials to decrease the surface energy; and finally to compare the dependence of corrosion resistance with the increase or decrease of roughness on surfaces with unidirectional roughnesses on two different metals with various characteristics.

First, the textures are created on both nickel and mild steel. Patterned textures are created on nickel and unidirectional roughnesses on both metals. Scanning electron microscopy (SEM), Energy dispersive spectroscopy (EDS) and roughness measurement are performed before any corrosion testing. Then corrosion testing methods including potentiodynamic polarization technique and electrochemical impedance spectroscopy (EIS) are performed. SEM, EDS and profilometry are carried out again after corrosion testing to evaluate the effect of creating different surface textures. Surface appearance and composition are

analysed and different surface roughness parameters including average roughness, root mean square roughness and other roughness parameters are discussed and compared before and after corrosion for patterned and unidirectional roughnesses for both nickel and mild steel. Finally, by comparing all the corrosion results and other experiments before and after corrosion, the most corrosion resistant sample is introduced.

1.1 Dissertation Outline

Chapter 2 introduces the problem of corrosion, prevention methods, and parameters affecting corrosion including surface roughness. The effect of surface texturing on corrosion is explained. The concepts of surface roughness, wetting and hydrophobicity are discussed. Different methods of creating textured surfaces including laser technique and the applications of such surfaces are introduced. Finally it describes the objectives and the approaches followed to accomplish the objectives.

Chapter 3 the experimental procedure is explained including different corrosion measurement techniques, surface analysis methods and various roughness parameters.

Chapter 4 contains the results and discussion on the surface patterns fabricated by the laser ablation technique on nickel and the effect of different textures on the corrosion rate of nickel.

Chapter 5 contains the results and discussion shows the effects of unidirectional roughnesses, which are fabricated by SiC papers, on corrosion of nickel.

Chapter 6 contains the results and discussion on the effects of unidirectional roughnesses, which are fabricated by SiC papers, on the corrosion of mild steel.

Chapter 7 highlights the conclusions arising from the current study.

Chapter 2 LITERATURE REVIEW

2.1 Corrosion

A general definition of corrosion is the degradation of a material's properties over time due to environmental effects [13]. Corrosion of metals in aqueous environments is almost always electrochemical in nature. The electrochemical reactions occur uniformly or non-uniformly on the surface of the metal. It occurs when two or more electrochemical reactions take place on a metal surface. As a result, some of the elements of the metal or alloy change from a metallic state into a non-metallic state. The products of corrosion may be dissolved species or solid corrosion products; in either case, the energy of the system is lowered as the metal converts to a lower-energy form. Rusting of steel is the best known example of conversion of a metal (iron) into a non-metallic corrosion product (rust) [14].

Over the years, corrosion scientists and engineers have recognized that corrosion manifests itself in forms that have certain similarities and therefore can be categorized into specific groups. However, many of these forms are not unique but involve mechanisms that have overlapping characteristics that may influence or control initiation or propagation of a specific type of corrosion. The most familiar and often used categorization of corrosion is probably the eight forms presented by Fontana and Greene [15], namely uniform attack, crevice

corrosion, pitting, intergranular corrosion, selective leaching, erosion corrosion, stress corrosion, and hydrogen damage. This classification of corrosion was based on visual characteristics of the morphology of attack. Fontana and Greene's introductory remarks in their chapter on forms of corrosion indicate that this classification is arbitrary and that many of the forms are interrelated, making exact distinction impossible [15].

2.1.1 Combating Corrosion and Prevention Methods

Materials selection, environmental control, barrier coatings, electrochemical techniques, inhibitors, electrical isolation, chemical surface modification and physical surface modification are some of the commonly used corrosion control methods [14, 16].

In this thesis, physical surface modification methods are applied and corrosion properties are investigated. The advantages of a physical surface modification approach to promoting corrosion resistance include:

1. Alteration of the surface without sacrifice of bulk properties
2. Conservation of scarce, critical, or expensive alloying elements
3. Production of novel surface alloys with superior properties such as wear and corrosion resistant surfaces (unattainable by conventional metallurgical techniques)
4. Avoidance of coating adhesion problems [14]

2.1.2 **Corrosion of Metallic Materials and Their Behaviour (Active-Passive)**

In this research the corrosion resistance of mild steel and nickel as two metals with different corrosion behaviours is studied.

Carbon, or mild, steels are by their nature of limited alloy content, usually less than 2% by weight for the total of all additions. Carbon steel, the most widely used engineering material, accounts for over 64 million tons, or approximately 88%, of the annual steel production in the United States. Despite its relatively limited corrosion resistance, carbon steel is used in large tonnages in marine applications, nuclear power and fossil fuel power plants, transportation, chemical processing, petroleum production and refining, pipelines, mining, construction, and metal-processing equipment. Uniform corrosion, atmospheric corrosion, erosion corrosion, galvanic corrosion and aqueous corrosion are the most important types of corrosion for carbon steel [14].

Nickel and its alloys, like stainless steels, offer a wide range of corrosion resistance. However, nickel-base alloys, in general, can be used in more severe environments than the stainless steels. The types of corrosion of greatest importance in the nickel-base alloy system are uniform corrosion, pitting and crevice corrosion, intergranular corrosion, and galvanic corrosion [14].

One of the most important differences between nickel and mild steel is their corrosion behaviour. Generally, two types of behaviour are exhibited by metals in solution:

- Type I, in which the corrosion or anodic current increases monotonically with potential (Figure 2-1).
- Type II, in which the anodic current initially increases with potential (active behaviour), then decreases to a small constant value (passive behaviour), and finally increases again. (transpassive) (Figure 2-1)

These two types of behaviour are not intrinsic properties of an alloy, such as the modulus of elasticity, but are the result of the interaction of the alloy with a given environment [14].

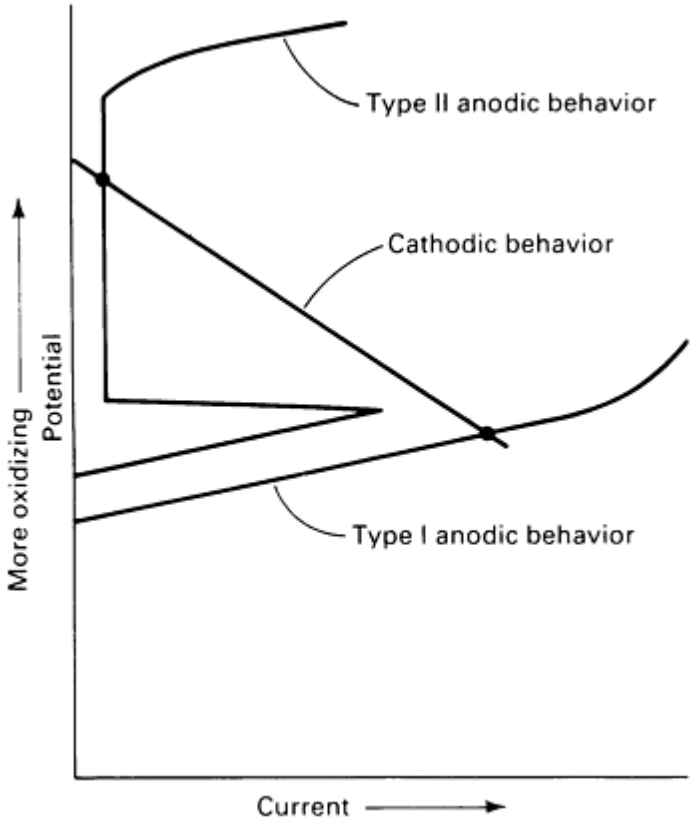

Figure 2-1 Different anodic behaviours of metals [14].

2.1.3 **Corrosion of nickel and mild steel in dilute sulfuric acid:**

H_2SO_4 is generally an oxidizing acid at dilute concentrations (below 20%) and also at high concentrations (above 70%). Oxidizing acids are generally referred to as those where the cathodic reaction involves the reduction of the acid anion rather than hydrogen evolution [17].

(a) Mild steel in dilute H_2SO_4:

Mild steel is an important material due to its excellent mechanical properties [18]. Iron and its alloys could corrode on exposure to acids, particularly sulphuric acid, which results in a significant waste of both resources and money [19]. Despite its limited corrosion resistance, carbon steel is used in many industries including the chemical and allied industries to handle acidic, alkaline and salt solutions, the petroleum industries as pipelines, storage tanks, and reaction vessels and in chemical batteries [20]. But, its susceptibility to corrosion in an acid medium is the major obstacle limiting its larger scale application [21]. Iron electro-dissolution in an acidic solution depends primarily on the adsorbed intermediate $FeOH_{ads}$ according to the mechanisms shown in equations 2-1 to 2-4 [22].

$$Fe + H_2O \leftrightarrow Fe.H_2O_{ads} \quad (2\text{-}1)$$

$$FeH_2O_{ads} \leftrightarrow FeOH_{ads} + H^+ + e^- \quad (2\text{-}2)$$

$$FeOH_{ads} \rightarrow FeOH^+ + e^- \quad (2\text{-}3)$$

$$FeOH^+ + H^+ \leftrightarrow Fe^{2+} + 2e^- \quad (2\text{-}4)$$

Figure 2-2 shows the Pourbaix diagram for iron with various compounds that can be formed at different pH and potentials (vs SCE). Acidic pH values and potentials from -0.5 to 2V (vs SCE), as used in this research, will bring the metal in the corrosion region and resulted in the formation of the ferrous ion (Fe^{2+}).

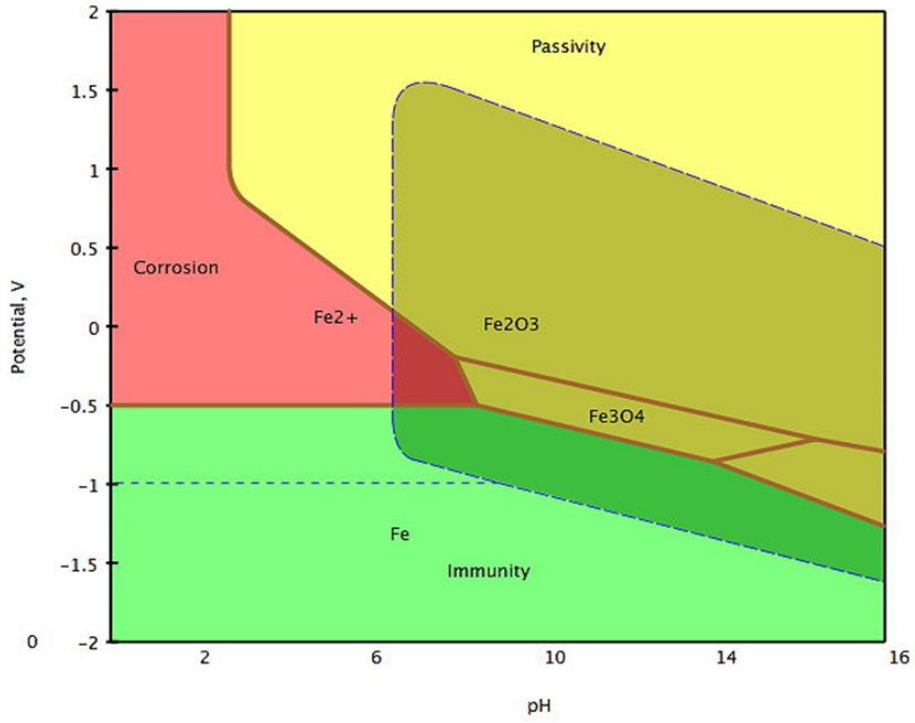

Figure 2-2 Pourbaix diagram for iron (vs SCE) [14]

(b) Nickel and its alloys in dilute H_2SO_4:

The corrosion of nickel in different electrolytes has been the subject of numerous studies due to the high technological importance of Ni and Ni-base alloys [23]. With respect to the corrosion mechanisms in acids, in particular H_2SO_4, researchers have shown that the initial step in the corrosion of nickel in

sulphuric acid is the formation of an unstable adsorbed intermediate, NiOH, as shown in equation (2-5) [24, 25]

$$Ni+H_2O \rightarrow NiOH+H^+ + e^- \quad (2\text{-}5)$$

NiOH can then react in two different ways. If, oxidation of NiOH leads to Ni^{2+}, there is no passivation of the metal, but rather active corrosion of Ni according to equation (2-6):

$$NiOH + H^+ \rightarrow Ni^{2+} + e^- + H_2O \quad (2\text{-}6)$$

However, if oxidation of the intermediate leads to NiO formation, there can be passivation of the Ni as shown in equation (2-7):

$$NiOH \rightarrow NiO + H^+ + e^- \quad (2\text{-}7)$$

The surface NiO film constitutes only the first step in passivation. By polarization of the electrode towards more positive potential values, higher oxides of Ni can be formed. The presence of NiO_x imparts stable passivity to the metal. Gilli et al. [24] consider that the formation of a passive film on nickel surface to be the main reason for the good corrosion resistance of nickel.

Figure 2-3 shows the Pourbaix diagram for nickel with various compounds that can be formed at different pH values and potentials. For 0.5 M H_2SO_4 (used in this research) with pH of 0.3 and the potential range used, the formation of Ni^{2+} is indicated.

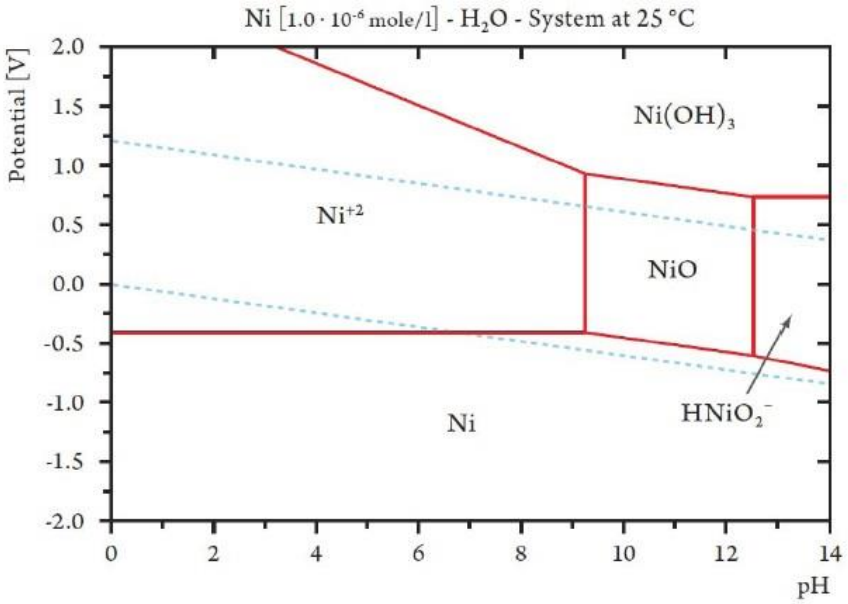

Figure 2-3 Pourbaix diagram for nickel (vs SCE) [14, 26]

Nickel has good resistance to corrosion in normal atmosphere, natural fresh water, and deaerated nonoxidizing acids [27]. Nickel is a transitional metal and is able to passivate in many environments including H_2SO_4 solution. The anodic polarization curve of nickel has an S-shape which will result in a decrease in corrosion of nickel in passive region at anodic potentials. The passive layer formed prevents the dissolution of nickel by forming a physical barrier between the metal and solution [25].

Two different mechanisms have been suggested for the formation of passive layer on nickel. First, dissolution-precipitation mechanism [28] and second, direct oxidation of the nickel [25]. Armstrong and Henderson [29] however, investigated the corrosion of nickel in 0.5 M sulfuric acid and considered the second mechanism, as a direct electrochemical reaction between

water and acid, is the cause of oxide formation. Depending on the pH and potential of the solution the oxide layers have been identified to range from NiO to Ni_2O_3. Sato and Okamoto [30] suggested that at the onset of passivity the transformation of NiO to Ni_3O_4 happens and polarization to higher potentials leads to formation of Ni_2O_3. It is also said that in the case of nickel in 1N H_2SO_4 solution, the passive layer is composed of NiO [31]. This passive layer can be destroyed in presence of certain anions including chloride and lead to a localized form of corrosion. The presence of hydrogen has also been found to increase corrosion on nickel [31]. This implies that for the same concentration of corrosive ions, an acid solution, like dilute sulfuric acid, is more aggressive than an alkaline solution. In another study by Cid et al, [32] found that nickel in sulfuric acid solution shows an intergranular corrosion, although the passive layer is not entirely destroyed. So, one can observe selective dissolution of grain boundaries, in spite of a more or less protective layer.

(c) EIS as a corrosion mechanism evaluation tool:

EIS is one of the methods to study the corrosion behaviour of metals in different solutions. EIS has been used extensively to study the corrosion of mild steel and nickel in sulfuric acid, and a number of different equivalent circuits have been proposed for the analysis of the EIS results.

The results of impedance measurements for corrosion of mild steel in 0.5 M H_2SO_4 solution were reported by Li et al. [33] in de-aerated condition. Their Nyquist plot included a semicircle with a tail at the end of the plot and their

equivalent circuit had an inductor and a resistance of the inductor with a series combination of resistances and inductor in parallel with resistances and a capacitance. The presence of an inductor in the circuit is attributed to the increase in the surface coverage of intermediate species formed during the metal dissolution. Figure 2-4 shows the designed model that resulted in a good fit between the experimental results and the simulations.

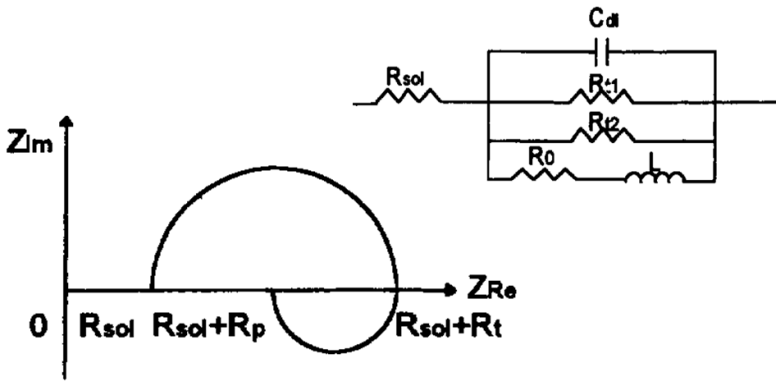

Figure 2-4 Experimental impedance spectra and the equivalent circuit for mild steel in dilute H_2SO_4 [33]

Corrosion and hydrogen evolution rate of mild steel alloy have been investigated by Fekry and Mohamed [34] using various electrochemical techniques. Mild steel was polarized vs. saturated calomel electrode (SCE) in naturally aerated 0.1 M H_2SO_4 solution. The impedance measurements agreed well the polarization results. The experimental results were compared with the simulated results calculated from an equivalent circuit, Figure 2-5. The appropriate equivalent model consists of two series circuits, $R_1Z_wC_1$ and R_2C_2 in series with R_s. C_1 is related to the inner layer capacitance and the faradaic

reaction therein and C_2 pertains to the outer layer, while R_1 and R_2 are the respective resistances of the inner and outer layers constituting the surface film, respectively. A Warburg impedance (Z_w) can be related to ion diffusion process indicating that the corrosion mechanism is controlled not only by a charge-transfer process but also by a diffusion process.

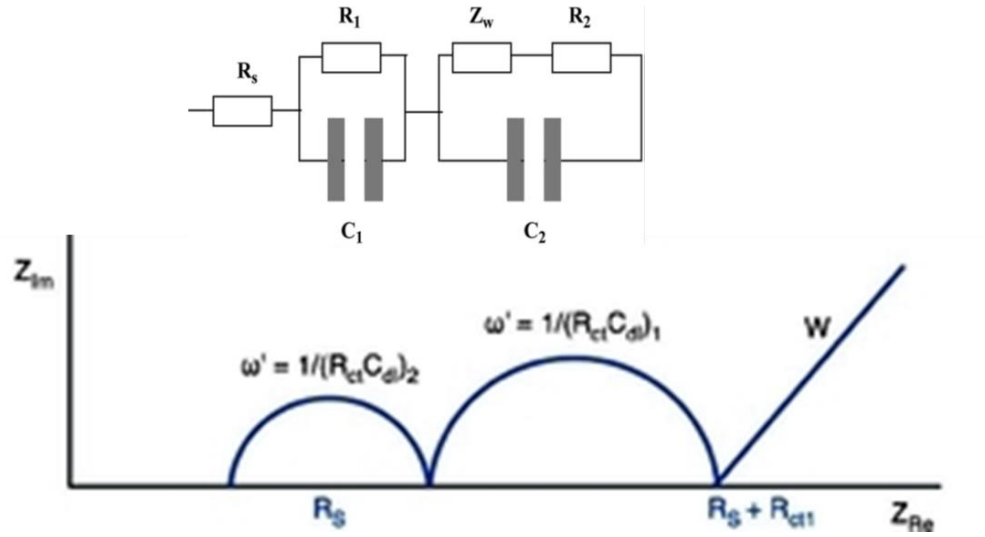

Figure 2-5 Experimental impedance spectra and the equivalent circuit for mild steel in dilute H_2SO_4 [34]

Equivalent circuit used to fit experimental EIS data recorded for mild steel electrode in 0.5 M H_2SO_4 solutions in the absence and presence of various concentrations of the three thiazole derivatives at 25°C with inductive loop was introduced in the study of Khaled and Amin [35]. In this circuit, the solution resistance, R_s, the charge-transfer resistance, R_{ct}, the constant phase element, CPE, and the inductive arrangement, R_L and L. The presence of the inductive R_L-L loop in EIS is attributed to the relaxation process obtained by adsorption species like H_{ads+} on the electrode surface, Figure 2-6.

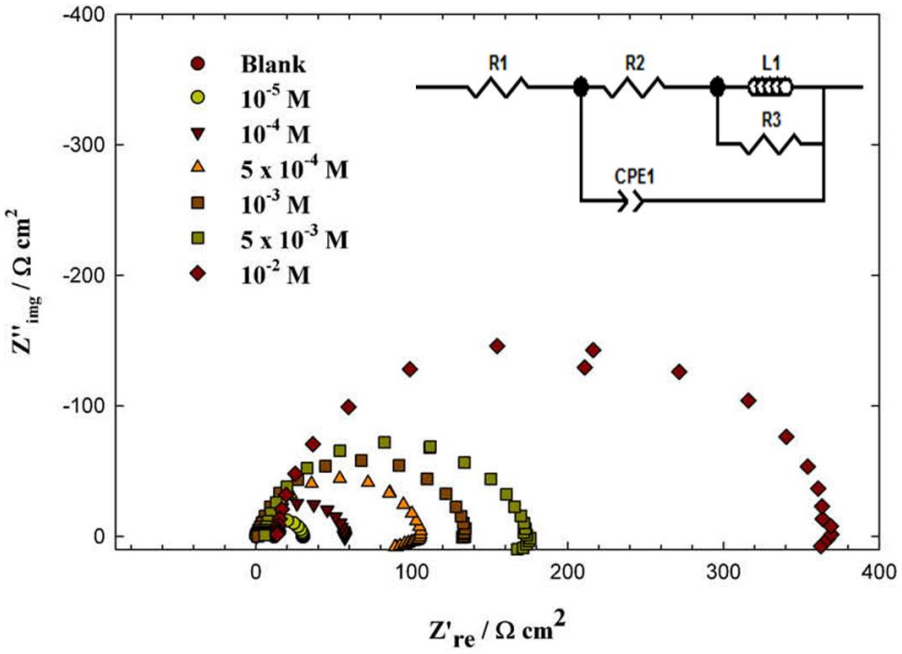

Figure 2-6 Experimental impedance spectra and the equivalent circuit for mild steel in dilute H_2SO_4 [35]

Singh et al. [36] also investigated corrosion of mild steel in 0.5 M H_2SO_4 solution. They compared the corrosion resistance of mild steel for a pure acidic solution and also a solution containing some inhibitors. Their designed circuit for their simulations is presented in Figure 2-7. In this model there is a constant phase element (double layer capacitance) which is in parallel to the charge transfer resistance and is in series to the parallel of inductive elements.

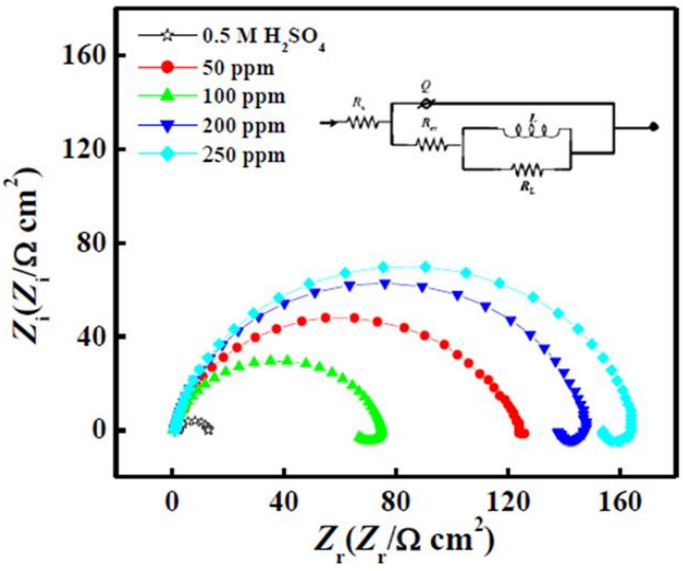

Figure 2-7 Experimental impedance spectra and the equivalent circuit for mild steel in dilute H_2SO_4 [36]

Noor [37], however, suggested a simple circuit for fitting the results of impedance test for mild steel in 1M H_2SO_4 solution for both in the presence and absence of inhibitors. (Figure 2-8)

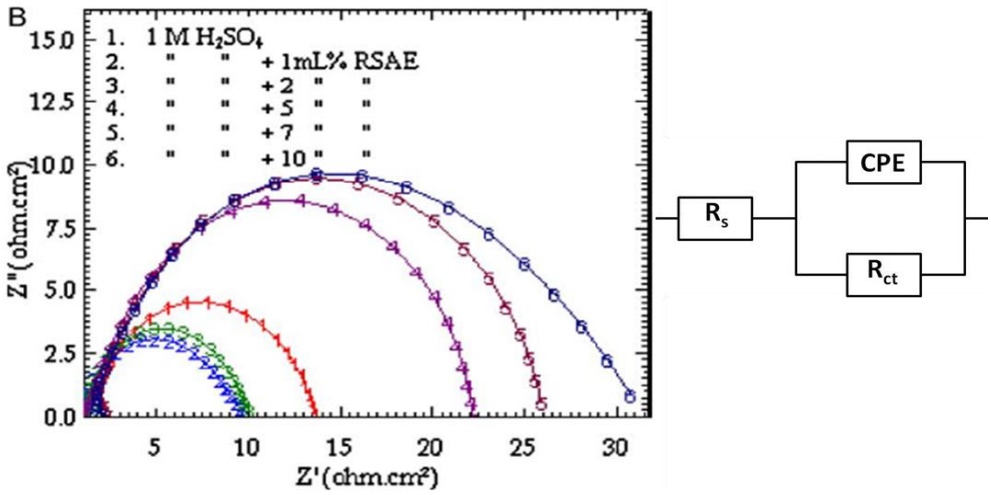

Figure 2-8 Experimental impedance spectra and the equivalent circuit for mild steel in dilute H_2SO_4 [37]

Different equivalent circuits have also been proposed for nickel to simulate the EIS experimental results. Turner et al [38], did the EIS analysis by a complex method of Sluyters and only one semicircle was observed for the dissolution of nickel in 0.5 M H_2SO_4 indicating a single stage reaction over the range of potentials studied. Their circuit only consisted of a solution resistance in series with a capacitor and a resistor in parallel. (Figure 2-9) The same model was used for nickel by Darowicki et al. [39].

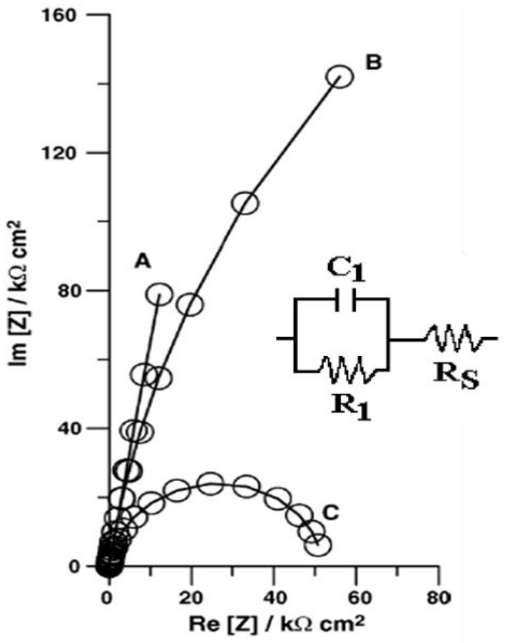

Figure 2-9 Experimental impedance spectra and the equivalent circuit for nickel in dilute H_2SO_4 [38]

Gregori et al. [40] studied anodic dissolution of nickel in solutions including H_2SO_4 through EIS. The experimental impedance spectra were fitted to the equivalent circuit, Figure 2-10, where, R_1C_1 (resistance and capacitance) are

related to Ni(I) and R_2C_2 related to Ni(II) species, R is the charge transfer resistance and CPE is the constant phase element.

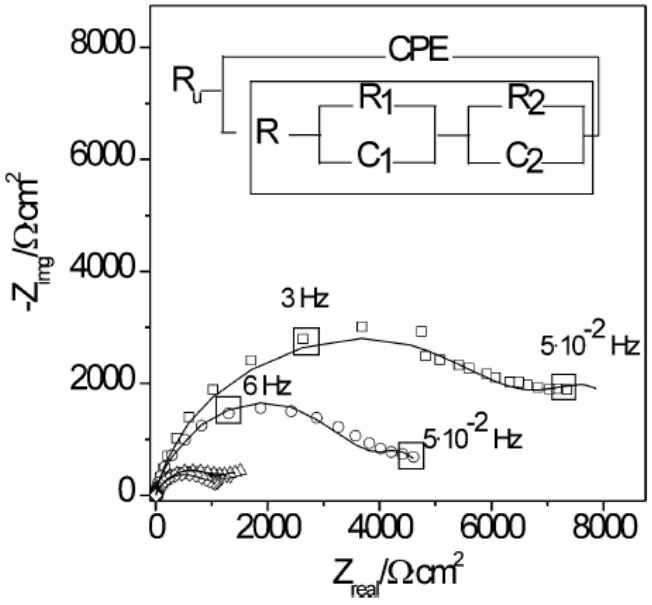

Figure 2-10 Experimental impedance spectra and the equivalent circuit for nickel in dilute H_2SO_4 [40]

Goncalves et al. [41] performed their experiments for pure nickel in 0.5 M sulfuric acid solution in the presence of 10 mM alcohol and observed good agreement between the results of the EIS test and simulations carried out through designing the equivalent circuits. Their circuit and experimental impedance spectra can be seen in Figure 2-11. As can be seen, the overall impedance is characterized by a parallel combination of capacitance and resistances. This model has been extensively used to describe inhomogeneous systems. In this model R_s is the electrolyte resistance, R_1 and R_2 correspond to external and internal layers on the surface, C_1 is the capacitance and Q the

constant phase element. Bode plots from the experiments showed one time constant and one maximum phase angle.

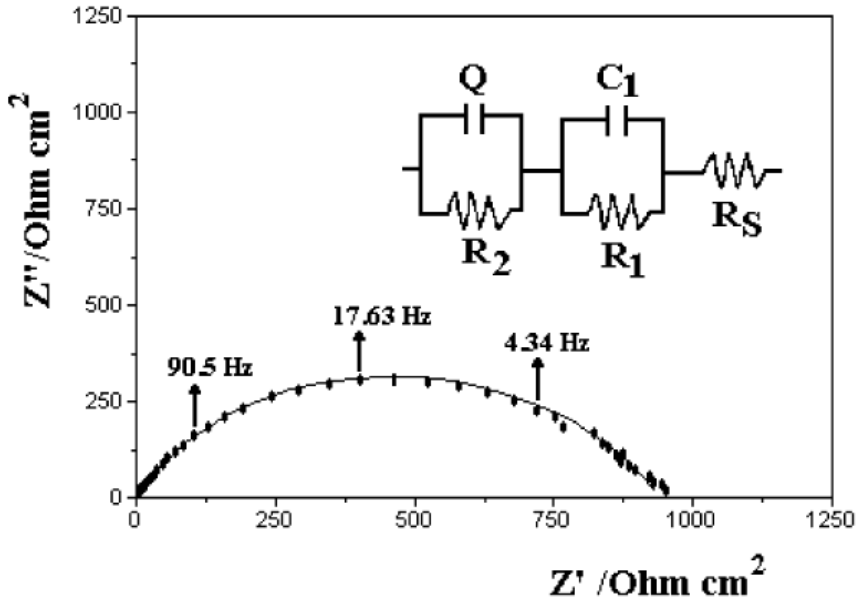

Figure 2-11 Experimental impedance spectra and the equivalent circuit for nickel in dilute H_2SO_4 [41]

Amin et al. [42] also studied corrosion behaviour of nickel in dilute H_2SO_4 (1M) and investigated the effect of adding different inhibitors on the corrosion resistance of nickel. Their designed equivalent circuit for the pure solution without inhibitors is seen in Figure 2-12. Their EIS results were characterized by two capacitive loops. The first loop was small with a diameter of R_1 and the other one with a higher resistance of R_2. So, the overall impedance was characterized by a parallel combination of capacitance and resistance of two charge transfer processes. The total charge transfer resistance is equal to (R_1+R_2). By adding the inhibitors in the system the charge transfer resistance increased and improved corrosion resistance. In this study no change was observed in the

shape of the EIS plots and the same equivalent circuit was used for both H_2SO_4 solutions contained inhibitors and with no inhibitor.

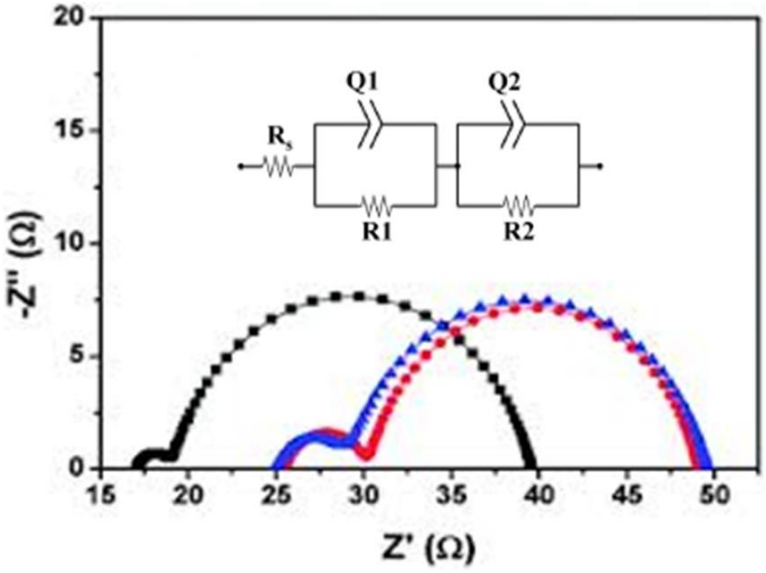

Figure 2-12 Experimental impedance spectra and the equivalent circuit for nickel in dilute H_2SO_4 [42]

In another study by Hamed et al. [43], however, a different model was used for corrosion of nickel in 1M H_2SO_4 in the presence and absence of an inhibitor. Experimental plots showed one time constant which indicates that the corrosion process occurred via one step. The equivalent circuit used to fit the results was as shown in Figure 2-13. R_{ct} is the charge transfer resistance. The same equivalent circuit was suggested by Abd-Al-Nabey [44] for corrosion of nickel in a 0.5 M H_2SO_4 solution.

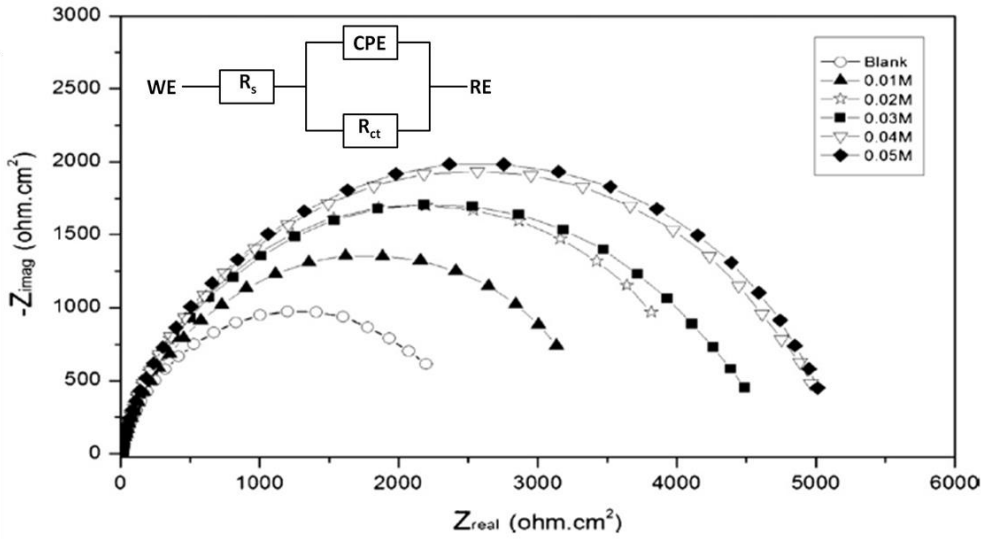

Figure 2-13 Experimental impedance spectra and the equivalent circuit for nickel in dilute H_2SO_4 [43]

In investigation of corrosion resistance with EIS method, different parameters are introduced including solution resistance, charger transfer resistance, constant phase element (CPE) (used instead of a capacitor for more accurate fitting results) and inductance. The charge transfer resistance is a measure of electron transfer across the surface and is inversely proportional to the corrosion rate, and is equal to diameter of the semicircle in a Nyquist plot.

The impedance, Z, of CPE is calculated using equation 2-8:

$$Z_{CPE} = [\, Q\, (j\omega)]^{-n} \qquad (2\text{-}8)$$

Q and n define the CPE. Q is the CPE constant, which is a combination of properties related to the surface and electro-active species, $j^2 = -1$ the imaginary number and ω the angular frequency. There is also n value which is the constant phase element exponent which can be used as a measure of the heterogeneity

or roughness of the surface. Depending on the value of n, CPE can represent resistance (n = 0, Q = 1/R), capacitance (n = 1, Q = C), inductance (n = -1, Q = 1/L) or Warburg impedance (n = 0.5, Q = W) [45, 46]. Aramaki et al [47], said that the increase in (n) value could be attributed to the formation of an oxide layer at the metal surface. In other research by Gregori [40], it was also reported that the different values obtained for the n and CPE exponent can be related to the roughness of the surface. The rougher the samples, the lower the n value and the higher the CPE values. Generally, unchanged n values for different samples suggest the formation of the same protective layer on the surface [40].

2.1.4 Important Parameters Affecting Corrosion

The corrosion rate is said to be strongly affected by the environmental and metallurgical variables [14]. Environmental parameters are acidity, potential, temperature, velocity and solution constituents. Metallurgical parameters are crystal structure, alloying elements, heat treatments, and the surface microstructure. Schweinsberg and Flitt [48] have shown that the purity of the anode and the electrolyte, the metallurgical history of the material and pre-treatment of the working electrode (abrasion technique, pre-polarization, time of immersion in the electrolyte) are amongst the most important parameters governing corrosion current density, and the corrosion rate. In different studies, grain size, material composition, mode of manufacturing, geometry and roughness have been reported to be the most important parameters affecting corrosion potential and current density [14, 49, 50].

One of the approaches available for controlling corrosion is the treatment and modification of the surface of a metal to increase its resistance to corrosion [51, 52]. One of these methods to do a treatment or modify a surface is creating different shapes and sizes of roughnesses on the surface. In Section 2.2 the various types of surface roughness are discussed.

2.2 Surface Patterning and Surface Roughness

Surface roughness and surface texture are the most important parameters affecting properties such as wetting, friction, wear and corrosion. A patterned

surface with a composite heterogeneous solid–liquid–air interface is notable as it has the features of liquid repellency and low surface energy. These two attributes have vast potential in various applications such as anti-sticking, self-cleaning, wettability improvement, anti-fouling, anti-corrosion, friction reduction, and heat transfer enhancement and have been successfully fabricated on various metallic substrates, such as stainless steel, Cu, Al, Zn and Ti [4-6, 53, 54].

For some time it has been considered that roughness plays an important role in wetting ability. The basic study for equilibrium wetting on rough surfaces was established by Wenzel and Cassie [55-57] and is discussed in more detail in Section 2.3. Recently, applying different surface roughnesses and bio-inspired surface structures on the surface of metals have attracted a considerable attention. Most of the studies have focused on improving the wear and friction properties and there have been relatively few studies on corrosion resistance [58, 59].

Surface texturing, was initially used to improve tribological performance [60]. Kovalchenko et al. [61] looked into the effects of laser surface texture on the lubrication regime transition on hardened steel. The effects of the sliding speed, normal pressure, and the lubricant viscosity on the friction were examined. The laser surface texturing had more impact on friction in cases of higher normal loads, higher sliding speed, and higher viscosity.

Another study was carried out by Ryk et al. [62] that showed the negative effect of dimples under boundary lubrication conditions, if the depth of the groove

is not appropriately chosen, or if the lubricant feed rate is not sufficiently high. This study showed that the deeper the dimples, the higher is the coefficient of friction. In addition, at a very low rate of lubricant supply, the friction resulting from the textured surface is higher than that of the flat surface on cast-iron.

Another study by Suh [63] investigated the effect of the width and orientation of undulations with respect to the sliding direction on the friction and wear, under boundary sliding conditions. Pin-on-disk tests were done on steel, with the disks textured by abrasive machining. Grooves which were parallel to the sliding direction showed no improvement in either friction or wear. However, grooves perpendicular to the sliding direction decreased both the wear and friction.

Dumitru et al. [3] investigated the effects of micro dimples on stainless steel disks under mixed lubrication conditions. The micro surface texturing dimples were arranged in arrays of micro-holes. The diameters ranged between 50 to 100 μm and the depths were between 5 to 8 μm. The spacing distance of the holes ranged between 30 to 60 μm. The study showed eight times the improvement of the lifetime of the samples. The lifetime of the sample was defined as the sliding distance at which the coefficient of friction increased rapidly and reached the coefficient of friction of an un-textured surface.

Varenberg et al. [64] investigated the influence that groove depth had on wear and friction of 4140 steel. In the cases where friction was concerned, wider grooves lead to greater friction reduction due to the fact that more wear particles

could be contained in the grooves. Friction also decreased with the groove depth to a point, after which increasing the depth had no effect. They deduced that wear debris fell into the surface depressions. The particles first gathered around the edge of a dimple and then built inward and downward, not necessarily ever reaching the bottom. Once the depth of the groove was below the lowest particle size that the wear particles could reach, there was no benefit to creating a deeper groove.

Thus, surface texturing can be an important parameter which affects the tribological and wear properties of alloys.

The idea of surface texturing or patterning comes from nature. Shark skin [65], for instance, boosts swim speed by cutting the drag force; therefore, the skin suits of Olympic athletes have v-shaped grooves called riblets which mimic the texture of shark skin [66]. Shark skin is a good example of biological surfaces that maintain a low friction with the surrounding environment. The surface texture of shark skin reduces the turbulence of water in the solid/fluid boundary, resulting in a reduction in the friction between the water and the shark's body. Figure 2-14 shows the surface texture of a shark skin [67]. The skin consists of hard, tooth-like scales with spines that point backward. The surface of these small scales is covered with microscale grooves that lie parallel to the longitudinal body axis. This special structure allows water to flow along the shark's body with minimum friction, and it reduces the adhesion of marine species to the skin. Based on the structure of shark skin, industrial applications have been developed to decrease

drag resistance in airplanes and boats. For example, applying a vinyl tape with tiny v-shaped grooves to the surface of airplane and boat hulls can alter the character of the air and water flow inside the boundary layer, resulting in a reduction in the friction [66].

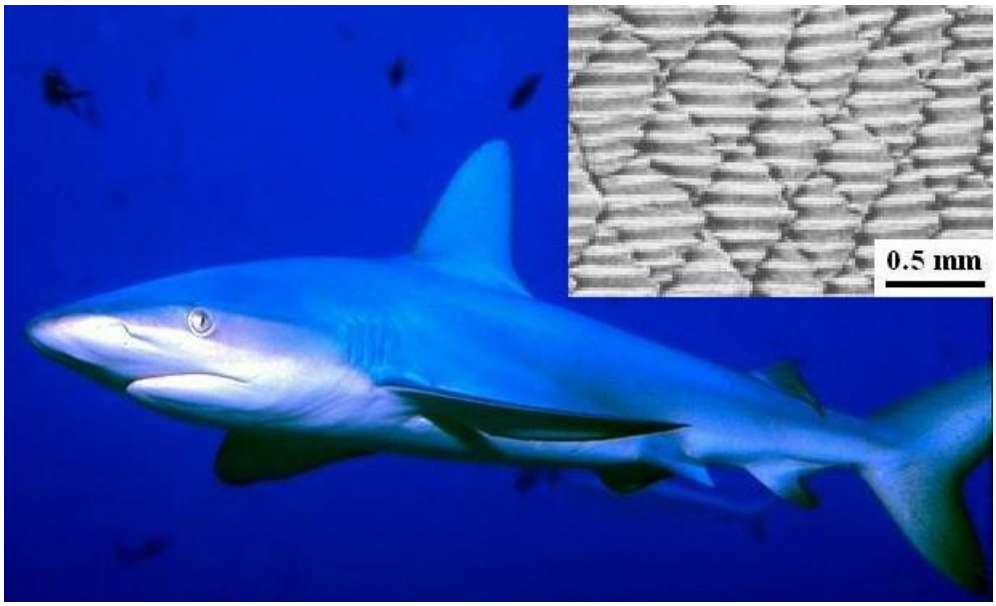

Figure 2-14 Grooved pattern of the shark skin surface [67].

The gecko foot is another example from nature that inspired many adhesive systems [68]. The gripping foot of a gecko is probably the best biological example for utilizing van der Waals forces. Capable of climbing smooth vertical surfaces, the gecko has about 5×10^5 keratinous hairs (setae) on each foot. Each seta has a length of 30-130 μm and features hundreds of pads at its end. The adhesive force of a single gecko foot-hair has been studied and concluded that hundreds of pads at the end of each seta interact on a molecular level with any surface. This creates a strong adhesion as a result of van der

Waals forces. The gecko releases its foot by peeling off the hairs at a critical angle [68]. Based on the gecko's mechanism for increasing friction, scientists developed a micro-fabricated polyimide dry adhesive (Figure 2-15). The surface of this material is covered by submicron, aligned posts that simulate the keratinous hairs on a gecko's foot [2].

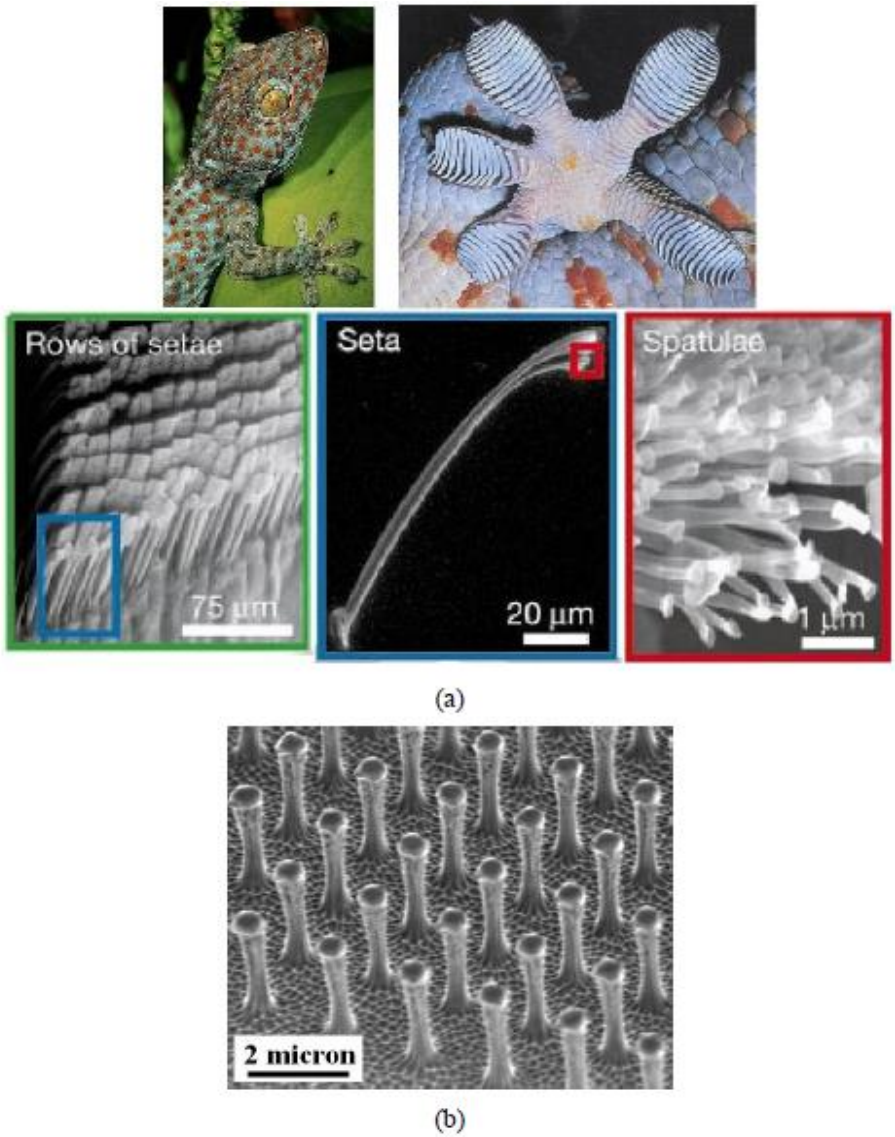

Figure 2-15 (a) Microstructure of the hairs in gecko's foot. (b) SEM micrograph of micro-fabricated polyimide dry adhesive [68].

Many studies have investigated the effect of surface texturing on the performance of a variety of mechanical systems. It was found that surface texturing has great potential for improving the tribological performance in terms of reducing the wear, friction, and lubrication consumption. This includes a discussion of the surface texturing parameters, the different benefits of the textured surfaces based on lubrication regimes, the various methods which are used to fabricate the textured surface, and the applications that widely employ micro-surface texturing.

It is suggested that the dispersive component of the adhesion forces (van der Waals forces) can be significantly reduced with proper surface patterning. Thus, by creating patterned surfaces it is possible to decrease the friction and get advantage of it in some cases like rolling and forming processes. In the opposite side, it is also possible to create surfaces with high friction and strong adhesion [69].

2.2.1 **Effect of surface roughness on corrosion properties**

Among the investigated parameters, surface roughness has a major impact both on general corrosion, and the nucleation of metastable pitting and the pitting potential [70].

Zuo et al. [70] investigated the metastable pitting behaviour of 316 L stainless steel with various surface roughnesses using corrosion measurement analysis and statistical treatments. They showed that as the surface roughness decreased, the nucleation rate of metastable pits decreased. In their research the

aspect ratio of surface groove, w/d, was suggested to indicate the openness of surface groove in which w is the width of the groove at the openness and d the depth of groove. A higher w/d ratio, which indicates a smoother surface, made it more difficult for micro-pits to nucleate. They determined a critical w/d ratio for which metastable pits may nucleate only on those surfaces whose w/d values are less than that critical value. Thus, according to their experiments, as the aspect ratio of w/d increased, the nucleation rate of metastable pits decreased linearly and the pitting potential moved toward the positive direction. Burstein and Pistorius [71] investigated the effect of surface roughness on metastable pitting of 304 stainless steel in a nitrogen-purged solution containing 0.025 M HCl, 0.075 M $HClO_4$, at ambient temperature. Their studies showed that an increase in the roughness lowers the pitting potential in 304L stainless steel. They showed that the smoother surface in stainless steel is less capable of propagating metastable pits than the rougher one, mainly because of the reduction of active sites on the surface and also more open sites of pitting on the smoother surface.

Surface roughness is also known to affect the hydrodynamic and mass-transfer boundary layer, thus influencing the corrosion mechanism and rate [72]. Due to the significant effect of surface roughness on the corrosion resistance, it is possible to meet certain corrosion resistance requirements by specifying a surface finish rather than by upgrading the chosen alloy. Abosrra et al. [73] studied the corrosion behaviour of 316L austenitic stainless steel in saline solutions containing 1 and 3% NaCl. Specimens with different surface roughness were investigated and the anodic polarization measurement technique was

performed. The experimental results revealed that chloride ions have a significant effect on the corrosion behaviour of the 316L stainless steel. As the surface roughness of 316L stainless steel increased, the breakdown potential (E_{break}), the free corrosion potential (E_{corr}) and the width of passivity decreased, hence the corrosion rate increased. Metallographic examination of corroded specimens after electrochemical corrosion tests confirmed that the breakdown of the passive region was due to pitting corrosion [73]. Corrosion resistance was also drastically reduced with increasing NaCl concentration up to 3%.

Sasaki and Burstein [74] studied the role of surface roughness on the breakdown potential of stainless steel in 0.6 M NaCl and it was confirmed that smoother surfaces had a higher breakdown potential. Their potentiodynamic results showed that the width of the passive region is highly dependent on the surface condition. When the surface finish varied from smooth to rough, the passive film terminated at a lower breakdown potential and the passive region became shorter due to the effect of surface topography, which enhanced the presence of more aggressive corrosion media inside such rough surfaces. The pitting potential is said to be more sensitive to surface roughness changes and the relatively large increase in pitting potential by several tenths of a mV from the roughest to smoothest surface, suggested that both the nucleation and propagation of metastable pits depends on the steel surface. This implies that for the metastable pit or pits to grow on a smoother surface is more difficult than on a rougher surface [74]. The reason for the lower pitting potential of rougher surfaces is considered to be related to maintaining less-open pit sites during their

early stages of growth as metastable pits. Less-open metastable pits give rise to more restricted diffusion of metal cations during propagation, allowing the transition from metastable to stable pit growth to be made at lower potentials. Since the pitting potential actually defines a minimum condition under which pits can become stable, the effect is to lower the pitting potential. In another study, Burstein and Vines [75] also claim that the smoother surface is less capable of propagating metastable pits than the rougher one because the sites of pitting on the smoother surface are on average more open.

A deterministic model for the growth of single pits in stainless steel has been combined with a purely stochastic model of pit nucleation by Laycock et al [76]. Monte-Carlo simulations have been used to compare the predictions of this model with potentiodynamic experimental measurements of the pitting potential in 1M NaCl. The quantitative agreement between model and experiment is reasonable for both 304 and 316 stainless steel, and the effects of varying surface roughness, solution chloride concentration and potential sweep rate have been considered. They demonstrated that for any potential high enough to cause some pit initiations, increasing surface roughness will increase the total number of initiation events.

Other studies have also shown that an increase in the surface roughness of stainless steels increases the pitting susceptibility and general corrosion rate in the presence of corrosive ions which is attributed to the passive film breakdown [71, 77]. Similar behaviour to stainless steel has also been observed

in aluminium, titanium-based alloys and copper [78-80]. However, in the case of magnesium a reverse trend has been observed because it has no ability to form a stable protective passive film [49].

Suter et al. [79] studied the onset of pitting in 1 M NaCl solution on high purity and ultra-high purity aluminum by using a micro-electrochemical cell in order to evaluate parameters that induce localized corrosion. The studies showed that on rough surfaces, areas with some defects (weak points) are more activated than on smooth surfaces and locally measured pitting potentials of polished samples which were smoother shifted to more positive values than those measured on ground samples with higher roughnesses.

Walter and Kannan [81] investigated the influence of surface roughness on the passivation and pitting corrosion behaviour of AZ91 magnesium alloy in a chloride-containing environment using electrochemical techniques. Their potentiodynamic polarization and electrochemical impedance spectroscopy tests suggested that the passivation behaviour of the alloy was affected by increasing the surface roughness. Consequently, the corrosion current and the pitting tendency of the alloy also increased with increase in the surface roughness and the scanning electron micrographs of 24 h immersion test samples clearly revealed pitting corrosion in the highest surface roughness alloy, whereas in the lowest surface roughness alloy no evidence of pitting corrosion was observed. Interestingly, when the passivity of the alloy was disturbed by galvanostatically holding the sample at anodic current for 1 h, the alloy underwent high pitting

corrosion irrespective of its surface roughness. Thus the study suggests that the surface roughness plays a critical role in the passivation behaviour of the alloy and hence the pitting tendency.

The influence of surface morphology, represented by roughness, on the corrosion and electronic behaviour, represented by the electron work function (EWF), of copper was investigated by Li and Li [80], using an atomic force microscope and a scanning Kelvin probe. Experimental results in 3.5 wt% NaCl showed that the corrosion rate increased with an increase in surface roughness, whereas its surface EWF decreased. It was theoretically showed that roughness can decrease the average EWF but increase the fluctuation of the local EWF. Such fluctuation could promote the formation of microelectrodes and, therefore, accelerate corrosion. The study demonstrates that the surface morphology can make a considerable contribution to corrosion and thus corrosive wear.

Cabrini et al. [78] performed direct and alternating current electrochemical tests on Ti6Al4V with different surface finishes and also with hydroxyapatite (HA) coatings in a physiological solution contained NaCl, $NaHCO_3$, Na_2HPO_4 and NaH_2PO_4. On the basis of electrochemical corrosion tests conducted in simulated physiological solution on Ti6Al4V with different surface finishes and with HA deposits, it was concluded that, surface treatments such as sand blasting or deposit of rough pure titanium, bring about an increase of corrosion current density compared to smooth Ti6Al4V as a consequence of the increase of the surface exposed to the aggressive environment. .

In the case of mild steel, however, a reverse trend has been reported [73]. Corrosion rate measurements for mild steel showed contradictory results and the conventional trend is that increasing the surface roughness decreases corrosion resistance. They compared their results with stainless steel and the polarization curves indicated that the tendency of the stainless steel was to undergo oxidation and passivation, followed by breakdown, i.e. a typical characteristic. The passivity and hence the breakdown potential was affected by the surface roughness. Specimen with less roughness, i.e. 1μm diamond finish surface, had the highest breakdown potential, followed by 600 and 200 grit surface roughness specimens. The passivity of rougher surfaces of 200 and 600 grit failed at less noble potentials. By increasing the concentration of solution to 3% NaCl, the polarization curves of the investigated specimens showed the conventional trend of the effect of chlorides and surface roughness. As the chloride concentration and the surface roughness increased, the breakdown potential values decreased and the free corrosion potential moved in a more active direction (less stable).

Also, Alvarez et al. [49] in their work on AE44 magnesium alloy in 3.5% NaCl solution have shown a corrosion behaviour that is consistent with that of mild steel, and opposite to the trend reported by Walter and Kannan on AZ91 magnesium alloy [81]. The corrosion rate of polished coupons was notably greater than the corrosion rate of semi-polished (ground with grit 500 of SiC papers) coupons for general corrosion indicating that when the surface roughness was greater, less general corrosion occurred. This trend is also opposite of previous research on stainless steel and aluminum, where the pitting

and corrosion potentials were lower, meaning faster corrosion, for the rough surfaces as compared to the smooth surfaces. In addition, they claim that the polished coupons allowed for greater initial pitting and higher pitting volumes, while the semi-polished coupons allowed for greater pit radii. Thus, it means that there are more pits on the smoother surface at the beginning of contact with the corrosive solution and these pits propagate and cause more pitting on smoother surfaces but on rougher surfaces there are less pits but they are larger. These pits on rough surfaces will stop growing earlier and will cause less degradation of the surface. A passivated surface, whether it is aluminum or stainless steel, has a higher corrosion potential when compared to an unpassivated, or active, surface. Both aluminum and stainless steel quickly passivate, or develop stable oxide films, when exposed to the atmosphere or water. However, unlike stainless steel and aluminum, magnesium does not quickly form a passive film. In fact, on magnesium, the passive film forms in the presence of water ($MgOH_2$), but water also can form galvanic cells between the magnesium grains and other phases in the structure. While a passive film on stainless steel and aluminum would decrease the ability of the chloride ions to react with the metal surface, the formation of $MgCl_2$ on the magnesium would cause the passive magnesium film to break down [49]. The slow forming passive film on magnesium, as compared to the fast forming passive films on stainless steel and aluminum, and the formation of $MgCl_2$ both served to allow pitting to ‘‘easily” occur on the magnesium surface. While a passive film did not form quickly on magnesium, this alone did not explain why the polished magnesium surface experienced higher

pitting rates than the semi-polished magnesium surface. Suter et al. [79] also has mentioned another reason that corrosion occurs on alloys which is the presence of active sites, such as the differentiation between different phases and the magnesium grains. These active sites on stainless steel and aluminum were more available on a rougher surface as compared to a smoother surface, because the protective oxide film did not form on the rougher surfaces.

Despite the significant attention that has been paid to the influence of the surface roughness on the pitting corrosion resistance in stainless steels, very little is known of the influence of the surface roughness on the general corrosion resistance [77]. In addition, to the author’s best knowledge, there have been no studies on the effect of surface roughness on the corrosion behaviour of nickel and its alloys. One of the studies that has investigated the effect of surface roughness on both general and localized corrosion of metals is the work of Shahryari et al [77]. They investigated the effect of surface roughness on stainless steel and realized that a decrease in surface roughness of stainless steel on which a passive film is naturally formed, results in an increase in the alloy's resistance to pitting corrosion. However for the surface on which the passive film is formed using the cyclic potentiodynamic passivation method (CPP), an increase in both general and pitting corrosion resistance was observed. Passivation of 316LVM stainless steel employing cyclic potentiodynamic polarization is extremely effective in improving the material's general and pitting corrosion resistance, and its biocompatibility. All the corrosion measurements were performed in 0.16 M NaCl, which corresponds to a

physiological chloride concentration in a human body. The pitting measurements were performed using cyclic potentiodynamic polarization technique, and the general corrosion measurements were performed using electrochemical impedance spectroscopy (EIS) technique.

Qiao et.al [82] investigated the effects of oxygen, H_2SO_4 concentration and surface roughness on the electrochemical behaviour of high nitrogen bearing stainless steel (HNS) in 0.05 H_2SO_4 + 0.5M NaCl solution. The surface roughness increased the values of the corrosion potentials and passivation current densities with increase in the surface roughness. The surface roughness had no evident effect on the cathodic process but acceleration of the anodic corrosion rate with increased surface roughness could be assumed to be due to the reduction in the average electron work function (EWF) with surface roughness [82].

Sharland [83] suggested that the local concentration of a solution was influenced by the geometry of a surface's peaks and valleys. This, in turn, affected the diffusion of active ions during the corrosion process. It is also suggested that the corrosion resistance is closely related to the distribution of the valleys on the surface. The significant influence of the valleys on corrosion resistance is related to the depth of the valleys which affects the diffusion of active ions during corrosion [74, 79, 83, 84].

Another research by Celik et al. [85] showed the corrosion behaviour of grit-blasted AISI 304L stainless steel substrates coated with Al_2O_3 in 1 N H_2SO_4

solution. The results showed that the corrosion resistance of plasma-sprayed coatings is reduced with increasing surface roughness.

It is said that the pitting potential, which is the minimum potential at which stable pits are observed to propagate, is lower for rougher surfaces than for smoother ones which means that the corrosion occurs earlier for such surfaces. [86] Hong and Nagomu showed that in the case of type 301 stainless steel which is wet ground on silicon carbide papers ranged from 240 grit to 400, 800, 1000 and 1500 grits the higher the number of the silicon carbide paper, the higher the E_{corr} value. This fact suggests that metastable pits or pits starting to grow on the smoother surfaces are more difficult than that on rougher surfaces. [86] Pits initiate at specific sites on the surface and rougher surfaces generally provide sites with a more occluded geometry. It is easier to maintain a concentrated local chemistry at these occluded sites, and so rougher surfaces tend to support a higher frequency of pit initiation [87]. A smoother surface shows a smaller frequency of metastable pitting in comparison with a rougher one. The surface with the smoother finish, however, also shows a far higher frequency of nucleation events. This apparently paradoxical phenomenon is said to be attributed to the repetitive nucleation of pits from individual sites of pitting [74]. Studies show that the potential at which the metastable pit or pits start to grow on the surface depends on surface roughness.

Typically, the general and localized corrosion behaviour of alloys would depend on their passivation properties. Hence, it is important to know the

passivation behaviour of alloys with different kinds of surface finish to correlate the surface roughness to their general corrosion and pitting tendency [49, 81]. For metals with the ability to form a passive layer, a decrease in surface roughness increases the corrosion resistance but for the ones with no passive film a reverse trend has been observed e.g. mild steel [73] and AE44 magnesium alloy [49]. Table 2-1 summarizes the relationship between surface roughness and corrosion resistance for different metals discussed in this chapter.

Table 2-1 Relationship between surface roughness and corrosion for different metals.

Metal	Electrolyte	Ability to form a passive layer	Change of corrosion rate by increasing the roughness	Reference
Aluminium	1M NaCl solution	Yes	Increase	[79]
Stainless steel	Chloride containing solutions	Yes	Increase	[70, 71, 73, 75, 77, 82]
AZ91 Magnesium alloy	0.5 wt% NaCl solution	No	Increase	[81]
Copper	3.5 wt% NaCl solution	Yes	Increase	[80]
Titanium alloys	NaCl+$NaHPO_3$+ Na_2HPO_4	Yes	Increase	[78]
AE44 Magnesium alloy	3.5 wt% NaCl solution	No	Decrease	[49]
Mild steel	1 and 3% NaCl solution	No	Decrease	[73]

2.2.2 **Different methods for generating patterned surfaces**

Different studies have investigated the effect of surface texturing on the performance of various mechanical systems. It is said that surface texturing has great potential for improving the corrosion and tribological performance in terms of reducing the wear and friction. Therefore, some researchers have focused on designing patterned surfaces and then followed by various experimental methods to examine corrosion and tribological properties. By the improvements in micro/nanofabrication techniques, it is possible now to control and tailor micro/nanoscale structures on solid surfaces to achieve a suitable surface topology. These surfaces have been fabricated on various metallic substrates [4-6].

Different methods have been developed to fabricate patterned surfaces, such as plasma etching, laser etching, and chemical etching. One of the most commonly used techniques is the lithographic technique which involves the replication of patterns on photoresist through light irradiation and transfer to the substrate by an etching process. Different types of lithographic techniques such as X-ray lithography [88], near-field scanning optical lithography [89] and E-beam lithography [90] are capable of producing patterns in nanometer scale. Electron beam lithography can provide a resolution of 10 nm but the technique is limited by low throughput and high sample cost. The photolithographic technique is another technique which was used with potassium hydroxide as an anisotropic etchant, to create runners and square depressions of 5μm in depth on silicon wafers [91]. Photolithography has been extensively used for fabrication of

patterned surfaces due to its ease of repetition and capability of large area fabrication. Unfortunately, the minimum feature size is limited by the diffraction limit. Generally, lithographic techniques suffer from either high setup cost or low throughput that concerns the manufacturing industry [6, 54].

Various machining methods have been employed to create micro-texturing on the surface of different materials [63, 92]. One technology was developed named vibro-rolling method to create shallow channels using a hard indenter that vibrates as it translates across the work piece [92]. Chemical etching and abrasive machining were also used to create modulated or undulated patterns that act as traps for oxide wear debris [63].

Reactive ion etching (RIE) has been used to explore the influence of micro-dimples on the silicon carbide surface sliding in water. Large circular dimples and small square depressions can be fabricated using Reactive Ion Etching, where high energy chemical plasma is directed at the part causing surface material removal [93].

Abrasive jet machining (AJM) is another technique in which the surface is bombarded with high-velocity fine abrasive particles that cause a physical removal of material. Excimer laser beam machining (LBM) can also be used to produce different textures. These two fabrication methods result in different profile shapes, circular and angular from AJM and LBM respectively, though the effect of the texture shape is found to be insignificant [94].

The vibro-mechanical texturing (VMT) technique was developed by Greco et al. [95], and this technique is based on the conventional turning operation with a fast tool servo that is used to oscillate the cutting tool. This oscillating motion creates holes when the cutting tool contacts the work piece.

Another method which has been used for a long time in different applications is laser surface texturing (LST) [60]. LST has great potential for enhancing different surface properties including friction, wear and corrosion in a variety of applications. This technique has many advantages over the previously mentioned texturing fabrication methods since it is very fast, environmentally clean, precise, and maskless. In addition, a variety of sizes can be created, and it can be used with most material types.

When a focused laser beam is localized on the surface of a material, the molten material evaporates immediately at a very high rate without causing severe damage to the surface or bulk material. Different types of laser beams are used to create the craters on the surface, and different media can generate the laser beam (photons). Examples of the gaseous media are He-Ne, Ar, Kr, Xe, N_2, and CO_2. Excimer laser beams that include halides in the ultraviolet (UV) range are ArF, KrF, XeCl, and XeF, and they are used frequently to create patterns in the hard coating layer, such as TiN, CrN, and DLC. Another type of laser medium is a metallic vapour, such as Cu, Au, HeCd, HeSe, and HeHg. In addition, the semiconductor media are GaN and GaAs based, and finally the most popular type, which is extensively used in the micro-machining, is the solid state media

Nd:YAG laser [96]. Many of the parameters of laser surface texturing must be optimized in order to get high quality, precise micro-craters. The resolution, for instance, depends on the wavelength of the laser source, whereas the ablation rate is based on energy density, and the depth of the craters is controlled by the number and duration of the pulses [97].

Laser ablation is one of the more promising methods for surface patterning (Figure 2-16). It is fast and allows short processing time, it is clean to the environment and provides excellent control of the shape and size of the microdimples, which allows realization of optimum designs. Laser ablation has also the ability of generating complicated structures without the need of a photomask, and can work in different environments. By controlling the energy density, laser ablation can be applied to process metals, ceramics, polymers and crystalline structures [54, 98, 99]. Laser ablation has been also used to produce non-wetting surfaces and showed an increase of 10-20° in contact angle [100].

Table 2-2 summarizes different methods for fabricating patterned surfaces and their relative advantages and disadvantages.

Table 2-2 A summary of different methods for generating patterned surfaces and their characteristics.

Method	Advantages	Disadvantages	Reference
E-beam lithography	Good resolution	High sample cost and low throughput	[90]
Photolithography	Ease of repetition	Limit feature size	[54]
Reactive ion etching	Can be selective and good resolution	High amount of residue, low rate	[93]
Abrasive jet machining	No chemical change with just physical removal	Inaccurate	[94]
Laser texturing	Fast, clean, precise, maskless, used for metals, polymers and ceramics	Some splashes which can be removed	[98, 99]

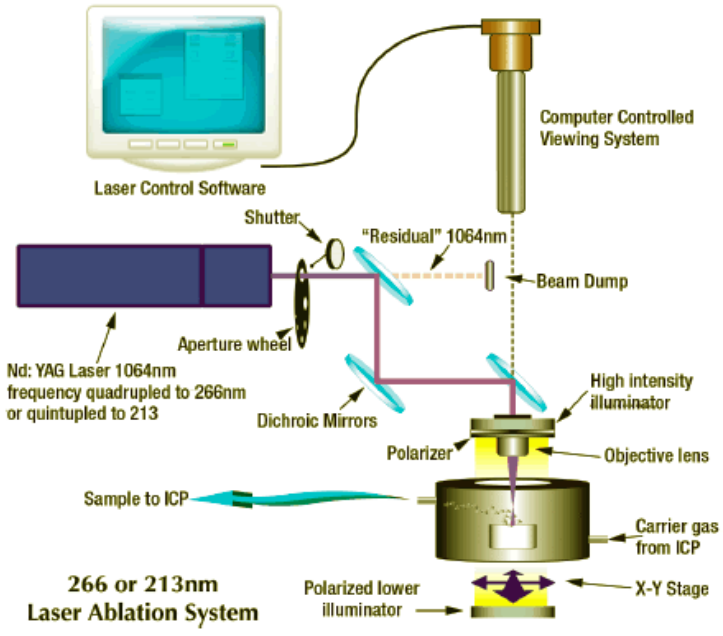

Figure 2-16 Laser Ablation System [100]

2.2.3 **Applications of textured surfaces**

On a textured surface shape, the size, density and depth, or a combination of these parameters, influence the tribological, wear and corrosion resistance [101]. Surface texture may be positive, in that it protrudes out of the surface, or negative, such as holes or sometimes continuous grooves, channels, or undulations which can be distributed evenly or randomly. Positive surface textures are used extensively in micro-electrical mechanical systems (MEMS), and magnetic hard disks to decrease the friction by decreasing the area of contact. Negative texturing, which is the focus of the current study, is mostly employed in automotive components, in machining tools and punches for metal forming processes and non-wetting surfaces. Surface texturing has been used in various applications for different purposes. Mainly, it is used to enhance tribological performance which includes decreased wear and friction. In this section, the applications in which surface texturing is widely used are discussed [101]. Most of these applications are automotive components, tools and punches of metal forming processes. Other applications related to water repellant surfaces, hydrophobic properties and corrosion resistance properties will be discussed in the sections 2.3, 2.4 and 2.5.

The idea of having micro asperities act as hydrodynamic bearings in parallel sliding applications such as rotary shaft face seals is an example of the application of such surfaces. This idea was verified that higher load carrying capacities were achieved when only one of the parallel surfaces of the rotary shaft face seals had micro-asperities in the form of cylinders [102].

Wakuda et al. [94] investigated the influence of textured micro dimples on nitride silicon ceramic plates, which are used as a structural element in automotive engines, in contact with the hardened steel cylinder. Different texture densities, texture shapes, and texture sizes were investigated, but the texture depth was kept constant at 5 μm. Abrasive jet machining and excimer laser beam machining were used to fabricate the micro dimples with circular and angular profiles, respectively. Pin-on-disk tests were performed to measure the coefficient of friction under boundary and mixed lubrication conditions. A reduction of 20% in the coefficient of friction was obtained. The optimal texture parameters were identified as a texture size of 100 μm and a texture density of 5 to 20%. The texture shape was recognized as an insignificant factor. Wang et al. [103] tried to find the optimum texture parameters that improved the load carrying capacity of SiC thrust bearings sliding in water. Micro pits were fabricated using RIE on one of the contact surfaces. The experiments showed that the critical load carrying capacity of the textured surface was doubled when compared to the un-textured surface for the transition between the hydrodynamic to mixed lubrication condition.

As another example, laser surface texturing was used on mechanical face seal rings. The results showed a significant reduction in frictional losses [104]. The effect of the surface texturing on the friction losses by the cylinder liner-piston ring system was estimated at 30% of the total engine friction [55]. Friction was reduced by 30% through laser surface texturing of the cylinder liner [105].

Due to the high surface to volume ratios in MEMS, surface forces play a crucial role in adhesion and high friction between contacting surfaces. In such systems, attention has been paid to surface texturing as an effective means to control both adhesion and friction. A laser surface texturing technique was used by Baumgart et al. [106] to create discrete round dome-like protrusions on the inner diameter of the hard disk to reduce the stiction at the start up. The effects of surface roughness, asymmetry, and peakiness on the adhesion and friction coefficients under low external normal forces were also studied by researchers [107]. It was found experimentally and analytically that as the surface roughness, asymmetry, and peakiness of the contacting surfaces increased, the coefficient of friction and pull off force were reduced by an order of magnitude.

Rivin [108] proved that surface texturing also increased the static contact pressure, so this surface modification approach could effectively increase the stiffness of tool fixtures. In stainless steel sheet forming, the study of Wiklund et al. [109] showed a linear relationship between the surface roughness and the coefficient of friction. Geiger et al. [110, 111] also were the first to consider laser texturing on the forging tool. They found in strip drawing that the texture shape and depth had an impact on the friction.

2.3 Wetting

It has been known for a long time that the wetting properties of solids are enhanced by creating surface roughnesses [112]. The wetting of rough surfaces

has been investigated since the 1930s; [57] however, the topic has received special attention in the past few years because of the development of micro/nanoscale applications [113, 114]. The surface area-to-volume ratio grows with miniaturization and surface forces become dominant, so the ability to measure and control surface properties becomes critical. One of the crucial surface properties for materials in micro/nanoscale applications is non-wetting.

Wetting on rough surfaces may assume either of two regimes: homogeneous wetting, [57] where the liquid completely penetrates into the roughness grooves (Figure 2-17a), or heterogeneous wetting [56], where air (or another fluid) is trapped underneath the liquid, inside the roughness grooves (Figure 2-17b).

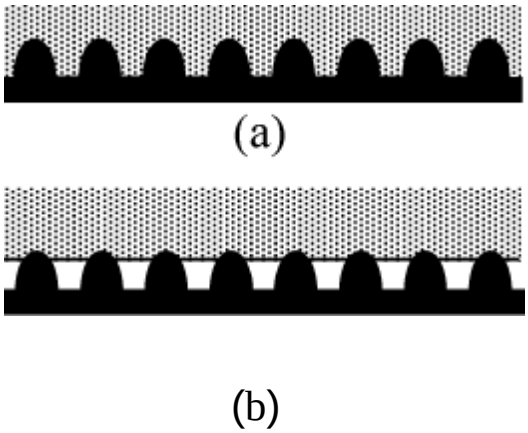

Figure 2-17 Wetting regimes of a rough surface: (a) homogeneous wetting, (b) heterogeneous wetting [115].

Wetting of solid substrates by liquids is a fundamental phenomenon related to many applications, including lubrication, coating, printing, waterproofing, and detergency (cleaning power of detergents) [116, 117].

Understanding and characterizing the wettability of solid surfaces is thus of significant importance. Wettability is often characterized by measuring the contact angle formed between a liquid drop and a solid surface, and surface roughness may be estimated from contact angle measurements (Figure 2-18). The roughness of a surface also has a significant effect on its wettability.

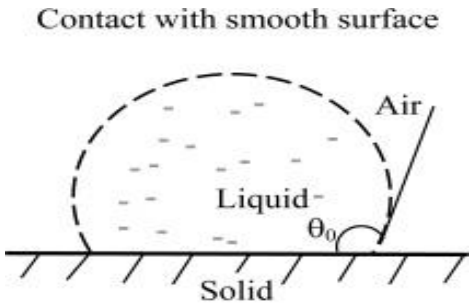

Figure 2-18 Contact angle on a smooth surface [56, 118].

It is believed that in order to be water repellant, a rough surface should be able to maintain a composite interface with air pockets or bubbles trapped in the valleys between the asperities [56, 119-121], as opposed to a homogeneous solid-liquid interface. In many cases both the composite interface and the homogeneous interface may exist for the same surface; however, only the composite interface provides the required water repellant properties.

As roughness increases, air can become trapped underneath the liquid locally, resulting in the formation of a composite surface with a large contact angle (Figure 2-19) [56, 122]. Therefore, increasing the roughness of a surface may also result in a reduction in corrosion by reducing the real area of contact with the electrolyte [123, 124].

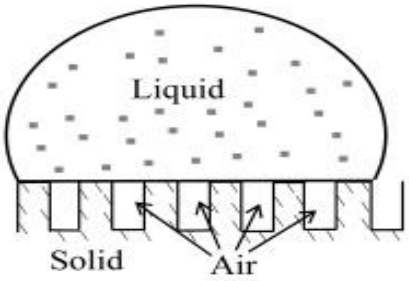

Figure 2-19 Composite surface [56, 118].

When a liquid drop sits on a rough solid surface, it could be in two states: one is the Wenzel's state [55], in which the liquid conformably covers the surface structure; and the other is Cassie's state [125], in which the liquid sits on top of a composite solid/air surface [126-129]. The latter is typically essential for non-wetting properties. The effects of roughness on the wettability are described by these limiting models. In Wenzel wetting, the effect of roughness on the apparent contact angle of a surface is accounted for by the increased area of contact [55], where:

$$\cos \theta_w = r. \cos \theta_{FLAT} \quad (2\text{-}1)$$

In this equation, θ_w is the apparent or measured contact angle in the Wenzel state, θ_{FLAT} is the contact angle of the flat surface of the same material, and r is the ratio of the total area in contact with the liquid to the projected area or the surface roughness factor. Wenzel wetting results is complete wetting of all surface features. Roughness can lead to the incomplete wetting of the surface such that the liquid does not sample the entire surface area. In this case, the drop wets a composite or chemically heterogeneous surface made up of both solid and gaseous components. Such wetting is typically described using the

Cassie equation [125] (Equation (2-2)) for heterogeneous surfaces, or the Cassie-Baxter equation (Equation (2-3)) when the second surface component is in the (vapor-saturated) gaseous state and not the solid state:[56, 130]

$$\cos \theta_w = \Sigma f_i \, \mathrm{Cos} \, \theta_i \qquad (2\text{-}2)$$

$$\cos \theta_{cb} = -1+f(r \cos \theta+1) \qquad (2\text{-}3)$$

The term f is the fraction of the area of the solid in direct contact with the liquid drop that is wet by the liquid. θ_{CB} is the apparent contact angle in the Cassie-Baxter (CB) state, r is the roughness ratio of the wet area and θ is the intrinsic contact angle on a flat surface of the same material. When f = 1, r = r, and the CB equation turns into the Wenzel equation [131, 132].

As an example, one wetting phenomenon that has attracted much attention in recent years is the Lotus effect, whereby water drops roll off the Lotus leaf surface under the slightest gravitational force while carrying away dirt particles with them. Such water-repellent solid surfaces are termed ‘‘super-hydrophobic” (hydrophobic surface with water contact angle above 150° is called ‘‘super-hydrophobic” surface [133, 134]). The Lotus effect is essentially a solid–(waterdrop)–air wetting phenomenon. However, it may inspire thinking about a similar mechanism in the solid– water–corrosive matters system, namely, prevention of corrosion by repelling corrosive matters from a surface, making them easily roll off by an external force [59].

It is also said that the behaviour of a liquid drop on a solid surface depends mainly on two dominant solid properties: the surface energy, determined by the chemical nature of the topmost molecular layer of the considered solid, and the surface roughness [135].

2.4 Hydrophobicity

The wetting of surfaces needs more investigation because of its important role in a wide range of daily phenomena and commercial applications. Surfaces with contact angles greater than 90° with water are named hydrophobic and surfaces with contact angles greater than 150° and low contact angle hysteresis (i.e. the difference between the advancing and the receding contact angle) are known as superhydrophobic. Superhydrophobicity is critical to the survival of many insects. Butterfly and cicada use superhydrophobicity to keep their wings dry and clean. A hydrophobic surface is non-wetting and a “super” hydrophobic surface is water repellent [136, 137].

Water striders have superhydrophobic legs with hierarchical structure with its numerous oriented microsetae that enable them to support themselves on the surface of the water (Figure 2-20) [138, 139]. Each seta has a nanoscale grooved surface texture. This multilevel surface texture allows the water strider to entrap a very high fraction of air at the leg/water interface. This interfacial air cushion prevents the legs from becoming wet, and helps the insect to overcome the gravity.

(a)

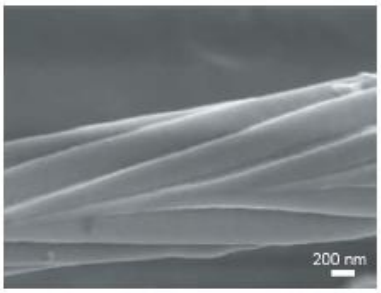

(b)

Figure 2-20 The hierarchical structure of a water strider's leg with numerous oriented microsetae. (b) Each seta has a nanoscale grooved surface texture [139].

Plant leaves provide the best-known examples of water-repellent surfaces in nature (Figure 2-21). The ability to remove water from the surface cleans the leaf, and minimizes the risk of infection to the plant.

Figure 2-21 Plant leaves with water-repellent surfaces [66].

Figure 2-22 shows this phenomenon in the lotus leaf. Similar to a water strider's leg, the lotus leaf has a multilevel surface roughness. Rose petals are similar to lotus leafs as another example of natural superhydrophobic surfaces. This superhydrophobic behaviour is attributed to the particular surface roughnesses. It is suggested that surface chemistry and roughness on multiple scales (microscale protuberances covered with a nanoscale, needle-like structure) on the lotus leaf's surface cause the trapping of air underneath the water droplet (heterogeneous wetting) and create a superhydrophobic surface with a water contact angle greater than 150°. Superhydrophobic surfaces are used for some purposes such as anti-sticking, self-cleaning, wettability improvement, anti-fouling, anti-corrosion and friction reduction [66].

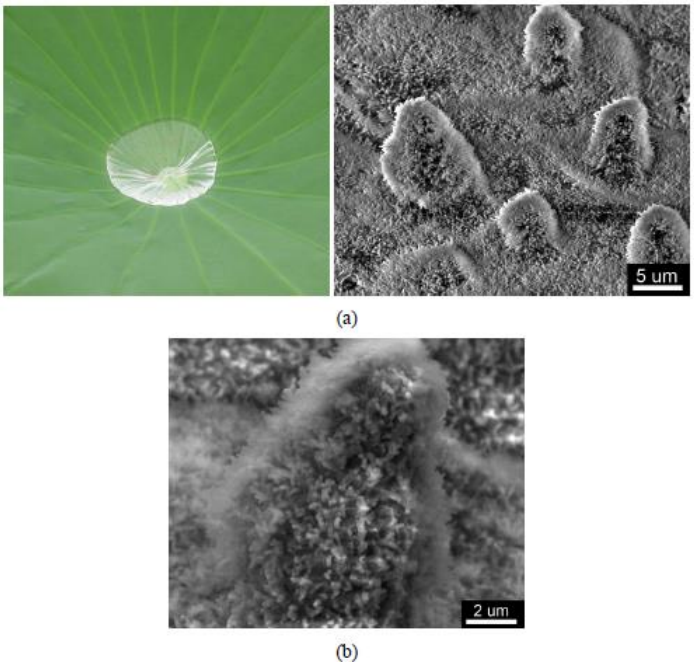

Figure 2-22 Microscale protuberances on the surface of a lotus leaf. (b) Each protuberance is covered with a nanoscale needle-like structure [66].

The successful advancement of micro-electro-mechanical systems (MEMS) with miniature moving parts, including micromotors, gears and transmissions, mechanical discriminators and optical microswitches, relies on the development of new materials and surfaces with high hydrophobicity (water repellency) and low adhesion and friction [140, 141].

Other possible applications for durable water repellent surfaces range from micro-fluidic devices [142] to bipolar plates in proton exchange membrane fuel cells (PEMFCs), because increasing hydrophobicity enhances the flow of both fluid and gas [143].

The natural world offers multiple examples of surfaces with optimized wettability, hydrophobicity and frictional properties through a combination of surface texture and chemistry. Some examples are the superhydrophobic lotus leaf, the water strider's leg, the cricket's attaching foot, the gecko's gripping foot, and the snake's textured skin, all of which suggest that nature offers effective ways of controlling wettability [67, 68, 139, 144-146]. The surface texture of the lotus leaf consists of microscopic protuberances covered in nanoscale, needle-like features with a waxy surface composition (Figure 2-23). This multilevel surface roughness is known as the source of the lotus leaf's superhydrophobicity [130, 138, 147].

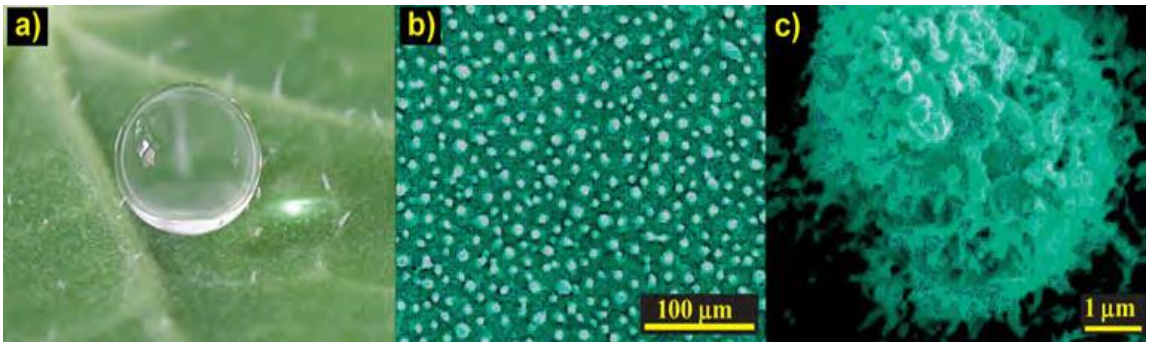

Figure 2-23 (a) An almost ballshaped water droplet on a non-wettable plant leaf.(b) Low- and (c) high-magnification scanning electron microscope images of the surface structures on the lotus leaf [148].

Superhydrophobic surfaces have attracted great interest because of their potential use in a variety of applications, such as self-cleaning, anti-sticky, anti-corrosion, and drag-reduction coatings [136, 149, 150]. Synthetic superhydrophobic surfaces are generally obtained by combining micro- or nanostructures with hydrophobic materials, on which air pockets are trapped below the water droplet in a typical Cassie or composite state, resulting in large contact angles (> 150 °) and low sliding angles (< 10 °) [151].

Methods for the preparation of the superhydrophobic surfaces include [152-157]:

- Layer-by-Layer and colloidal assembly
- Electrochemical reaction and deposition
- Sol-Gel Processing
- Etching and Lithography
- Chemical Vapor Deposition and Physical Vapor Deposition
- Electrospinning

2.5 Water repellant properties and corrosion

As previously mentioned, one of the applications of water repellant surfaces which has not attracted great attention is corrosion resistant surfaces. In reference [158], a superhydrophobic film was fabricated on copper (Cu) using a one-step electrolysis method. The film contacting with the solution presented a good protection effect due to the air trapped in the textures of the film. It was shown that the film was able to remain stable within a wide range of potential because of its excellent corrosion protection property and chemical stability. It was suggested that depending on the immersion depth in the NaCl solution, the hydrophobic surface can contact with the solution in two different methods (i.e., Cassie mode and Wenzel mode), which leads to different corrosion protection mechanisms [158]. The hydrophobic film in contact with the solution in the Cassie mode had a better corrosion protection property than in the Wenzel mode which was related to the trapped air in Cassie mode. This research also showed that using hydrophobic surfaces as corrosion protection strategy in aqueous solution is applicable to a system with a lower water pressure.

Corrosion resistance of non-wetting surfaces of Cu was also investigated in seawater and considerable improvement was observed [159]. Pretreated by a n-tetradecanoic acid etch, the super-hydrophobic film was formed on the copper surface. The film structure was probed with contact angle measurement and scanning electron microscopy (SEM). The results suggest that the structure of the film is similar to a haulm or flower and the seawater contact angle is larger than 150°. Moreover, the corrosion resistance of bare and modified samples in

seawater were investigated by cyclic voltammetry (CV) and electrochemical impedance spectroscopy (EIS). Experimental results show that the corrosion rate of Cu with super-hydrophobic surface decreases dramatically because of its special microstructure.

An alternative solution for controlling corrosion is the reduction of the contact area (by increasing the contact angle) between the affected surface and the corrosion agent/electrolyte. Due to the surface nature of the corrosion phenomenon, a reduction in the contact surface should lead to a significant reduction in the overall corrosion rate. A possible approach to reduce the contact surface between a solid and a fluid is by achieving heterogeneous wetting at the solid-liquid interface. As mentioned, heterogeneous wetting, known as the Cassie-Baxter state, is a suspended state where air/vapor is assumed to be trapped in the grooves of the surface, i.e., the liquid contacts with the composite surface of both air and solid. (Figure 2-24) The challenge in forming heterogeneous interfaces from hydrophilic materials lies in designing surface topographies that will lead to stable air/vapor entrapment [8, 160, 161].

There are two main parameters that are important for creating heterogeneous solid–liquid interfaces. One is the topology of the surface and the other is the nature of the surface layer. The mechanism of roughness-induced heterogeneous wetting is complicated and involves effects over various length scales [162]. There are different methods to convert a surface from hydrophilic or superhydrophilic to superhydrophobic such as using chemicals, coatings,

surfactants and surface patterning. A patterned surface with composite heterogeneous solid-liquid-air interface is notable as it has the features of liquid repellency and low surface energy. These two attributes have vast potential in various applications such as anti-sticking, self-cleaning, wettability improvement, anti-fouling, anti-corrosion, friction reduction, and heat transfer enhancement [4, 6, 53, 54, 122].

For example, in the case of corrosion properties on a patterned surface, if we have the reduction of the mass-loss rate, it could be attributed to one or a combination of the following three factors: a) change in the chemical composition of the surface (passivation for metals with the ability to form a passive layer); b) change of the microstructure of the metallic surface; c) reduction of the overall solid/electrolyte contact surface. The third item is the most important parameter in the surface patterning concept and this leads to the conclusion that the liquid electrolyte is not in contact with at least part of the surface of the patterned surface and therefore the regime of wetting is heterogeneous.

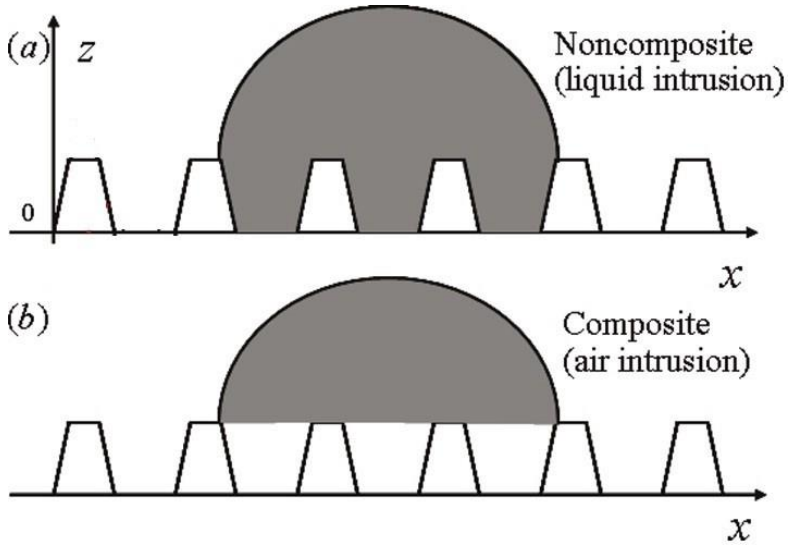

Figure 2-24 A typical 2-D microtexture: (a) noncomposite; (b) composite [163].

For engineering materials, undoubtedly, the resistance to the corrosive liquid will greatly enhance their anticorrosive ability, broaden their application environment and extend their service life. Superhydrophobic surfaces are able to withstand salt solutions in a wide range of concentrations, which may open a new avenue in applications especially for the marine engineering materials where salt resistance is required [164, 165]. These superhydrophobic engineering materials showed superhydrophobicity in nearly the entire pH range, so they can be used in strongly corrosive environments.

Thus by considering all the effective parameters on different properties of materials such as wear and corrosion resistance, this research was performed to investigate the effect of surface roughness and surface patterning on corrosion of metals. Another objective of the research was to study metals with different characteristics (nickel with ability to form a passive layer and mild steel with no

ability to form a passive layer) and to investigate the effect of the formation of a passive layer or corrosion products on corrosion resistance.

Chapter 3 EXPERIMENTAL PROCEDURES

3.1 Sample preparation of nickel and mild steel

The samples which were used in this study were high purity nickel (99.7%) and mild steel. One sheet of each metal was cut into smaller pieces of 15x15x1 mm using wire electrical discharge machining (EDM). All samples were first cold-mounted with a fiberglass resin and hardener.

To prepare the nickel samples for surface patterning process, the samples were ground and polished using different abrasive SiC grinding papers with grits of 60, 120, 180, 240, 320, 400, 600, 800 and 1200 respectively. This was then followed by rough polishing using a 9 μm diamond paste, and finally aluminum oxide ((Al_2O_3)) suspensions of 0.1 μm and 0.05 μm. After polishing, the samples were broken out of the cold mount and rapidly washed with ethanol and acetone and then dried.

Then the laser ablation process was performed on the surface to create different size patterns. Different diameter (D) circular holes were fabricated using the laser ablation technique. The inter-hole spacing (L), between the centres of the two neighbouring circular holes varied in the range of 2 to 30 μm. However, the ratios of (D/L) that are equal to 0.25, 0.5, and 1 are maintained constant for the different combinations of D and L. In addition, the arrangement of the holes forms adjacent equilateral triangles as shown in Figure 3-1. The depth of the holes is fixed and is equal to 5 μm.

3.1.1 **Laser ablation method**

To create specific surface textures on the surface of the samples, a laser ablation method was used as shown in Figure 2-4 in Chapter 2. A copper bromide (CuBr) laser was used and a single pulse was applied to create each hole. During laser ablation nitrogen gas (N_2) was blown to protect the surfaces from oxidation and also to clean melt splashes, and debris. The remained splashes will be removed by polishing with alumina suspension before corrosion tests. The pulse duration was selected as 30 ns which is common in laser ablation processes. For each hole size a different laser power was used which ranged from 20-80 W. In each case the most important parameter is the diameter of the hols which will affect the contact area of solution and substrate. Hole depth however, is almost the same and not important on the contact area of the electrolyte and the substrate. The laser process was completed in LMVL Bulgarian Academy of Science. The surface textures were created based on repetition of holes in form of an equilateral triangle in both X and Y directions on an area of 1.5 cm × 1.5 cm. Figure. 3-1 shows a schematic shape of the holes and the laser ablated area on the samples.

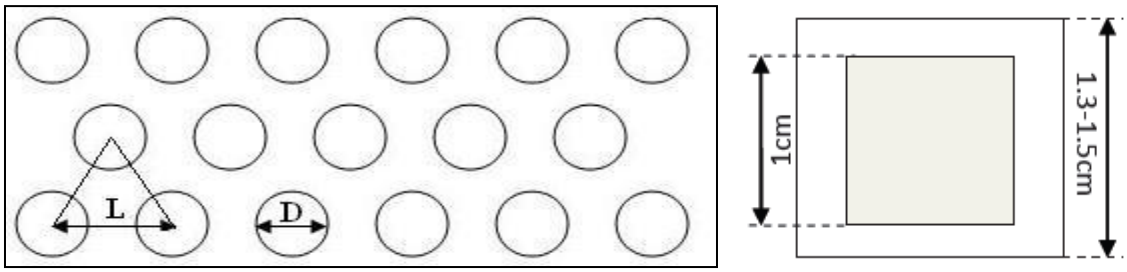

Figure. 3-1. Schematic of the proposed surface texture model; D is the hole diameter and L is the inter-hole spacing. The grey area is the laser ablated region.

Different characteristics of the patterns created on the nickel samples are listed in Table 3-1. L_1 to L_3 show the inter-hole spacing and D is the distance between the holes. The coding system which was used for identifying the samples includes these two letters and (D,L) is listed in Table 3-2.

Table 3-1. Hole sizes and distances between holes of the textures created on nickel

D (µm)	L_1 (µm)	L_2 (µm)	L_3 (µm)
2	2	4	8
3.5	3.5	7	14
5	5	10	20
10	10	20	30
20	20	30	40
30	30	60	-

Table 3-2. Sample coding system

D (µm)	L (µm)	Code
Polished sample (with no holes)		REF
2	2	D2L2
2	4	D2L4
2	8	D2L8
3.5	3.5	D3.5L3.5
3.5	7	D3.5L7
3.5	14	D3.5L14
5	5	D5L5
5	10	D5L10
5	20	D5L20
10	10	D10L10
10	20	D10L20
10	30	D10L30
20	20	D20L20
20	30	D20L30
20	40	D20L40
30	30	D30L30
30	60	D20L60

3.1.2 **Unidirectional roughness**

For preparation of the samples with unidirectional roughness, each sheet is placed in a sample holder and is ground with different SiC papers from grit 60 to 1200 to create different grooves with various depths and widths. The grinding was performed using a sample holder in a manner that produced unidirectional

roughness. All the roughnesses were measured using a profilometer before and after corrosion testing. A smaller grit number represents a rougher finish. For example sample G60 is the roughest and sample G1200 is the smoothest one. The letter G, in the used notation (G60 to G1200), stands for grit.

Figure 3-2 is a flowchart showing different experiments performed on nickel and mild steel samples with various surface roughnesses. More details about these experiments are given in Sections 3.2 to 3.4.

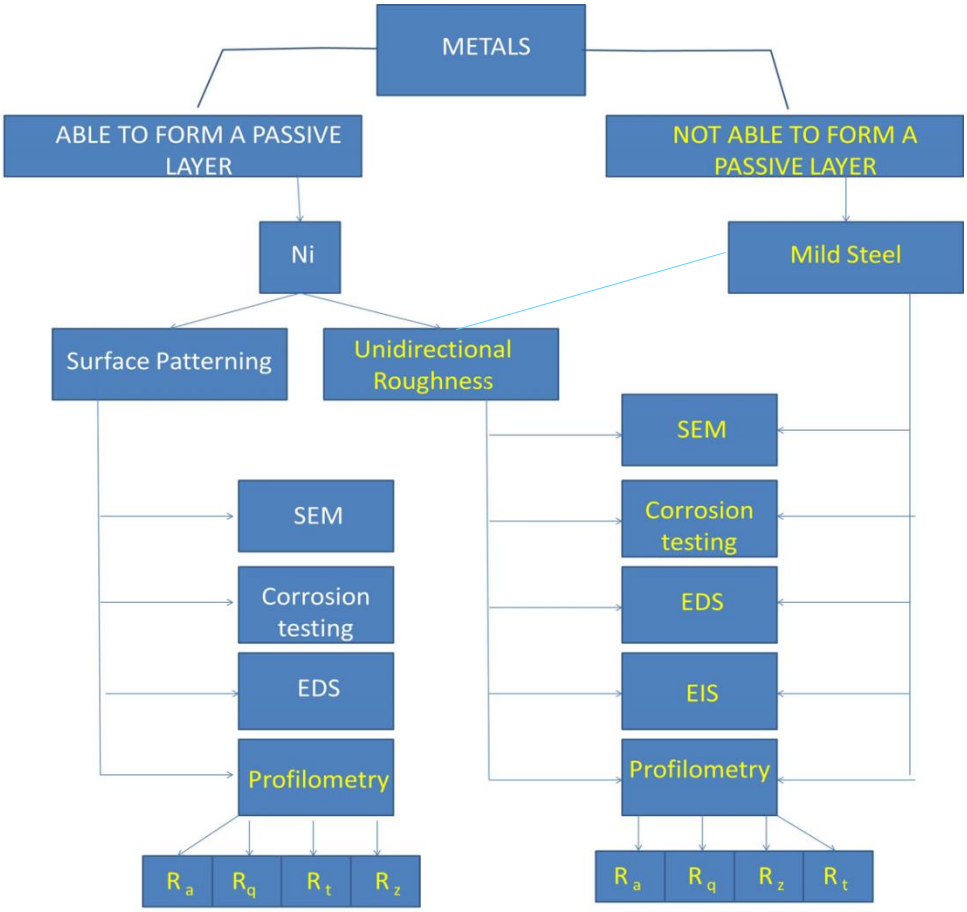

Figure 3-2. Flowchart of experimental procedures.

3.2 Corrosion Testing

3.2.1 Open circuit potential (OCP) and potentiodynamic polarization technique

The corrosion resistance of the samples was measured by a Solarton SI-1287 (electrochemical interface) using a potentiodynamic polarization technique in a 0.5M H_2SO_4 solution (pH=0.3) at room temperature (23±1°C). Samples were held for 30 min to reach a relatively stable open circuit potential and polarization curves were obtained at the OCP. A conventional three-electrode system was used in which a standard calomel electrode (SCE) served as the reference electrode and the counter electrode consisted of a platinum wire. The working electrodes were nickel and mild steel samples. The scan rate of the experiments was 1.0 mV/s. For the nickel samples the corrosion tests were performed in a potential range of -1 V to 1.5 V and for mild steel samples from -2.5 V to 2.5 V. Potential-current curves were then measured. For each corrosion test, a fresh 0.5M H_2SO_4 solution was prepared. The instrument measured the β_a, β_c, I_{corr} and corrosion rate values. Polarization resistance (R_p) of the nickel samples were calculated using the linear polarization method as obtained from Equation (3-1):

$$R_p=\beta_a\beta_c/2.3i_{corr}(\beta_a+\beta_c) \quad (3\text{-}1)$$

where β_a and β_c are cathodic and anodic Tafel constants and i_{corr} is the corrosion current density obtained from a potentiodynamic curve and R_p is defined in ohms (volts/ampers or millivolts/milliampers) [166].

3.2.2 **Electrochemical Impedance Spectroscopy (EIS)**

EIS is one of the most useful methods for a detailed analysis of electrochemical reactions mechanisms and kinetics and to evaluate the effect of surface roughness on the corrosion behaviour of metals [40].

Impedance diagrams provide data on the elementary steps occurring in an electrochemical reaction and on their kinetics. They also allow a thorough study of the role of intermediate species adsorbed on the surface and of reaction mechanisms, as well as a study of the properties of passive films [167]. The impedance characteristics of an electrode in acid solutions depend largely on the type of the surface pretreatment and surface roughness of the electrode [46, 86].

The EIS tests were performed using a Solarton 1255-B (Frequency Response Analyser). Different diagrams including Nyquist, Bode and Bode phase were plotted and corresponding equivalent circuits were designed to simulate the behaviour of the sample to calculate the EIS parameters. For EIS analysis, normally, the negative of imaginary impedance is plotted versus real impedance. Typically this yields a plot called Nyquist spectra. The Bode plot which gives a visual resolution of the resistive elements is a plot of absolute impedance versus frequency and frequency versus phase angle. To ensure a complete characterization of the electrode/electrolyte interface and corresponding processes, the impedance was measured at frequencies between 10^{-2} and 10^{4} Hz. Measurements were performed at room temperature in naturally aerated solutions. All the Nyquist plots were analysed by fitting the experimental data to an equivalent circuit model. Two different equivalent circuit

models were used for nickel and mild steel which will be presented in Chapters 5 and 6 respectively. Finally, all the equivalent circuit elements including charge transfer resistance (R_{ct}) were calculated and all the samples were compared. All the resistance values calculated from EIS analysis were then compared with the polarization resistance values calculated from potentiodynamic polarization technique.

3.3 Scanning Electron Microscopy (SEM) and Energy Dispersive Spectroscopy (EDS)

After creating different patterns by laser ablation and fabricating unidirectional surface roughnesses by SiC papers, all of the samples were examined by SEM (JEOL 5800 model). The EDS analysis was also used to check the chemical composition of the surfaces before corrosion testing. Finally, after corrosion tests the samples were again examined by SEM and EDS to evaluate any changes in surface morphology, appearance and composition. It is very important to keep the samples in a desiccator to prevent the samples from exposure to the air and any contaminations.

3.4 XRD

X-ray powder diffraction (XRD) analysis was performed on a Bruker D8 diffractometer using a monochromated $CuK\alpha_1$ radiation with accelerating voltage of 40 kV and a current of 30 mA to compare different compounds formed on the surface of different samples. The scan range was from 10-90 degrees in 2θ and the scan rate was 1.2 degree per min with a step size of 0.02 degree.

3.5 Roughness Measurements

The roughness was determined using a Wyko Surface Profiling System NT-1100 and magnifications from 10, 20 and 50X. The surface roughness data were processed with Vision software. The Wyko NT1100 can provide high resolution 3-dimensional topographical maps of the tested surfaces, from sub-nanometer roughness to millimeter-high steps. Different roughness parameters were calculated, including R_a, R_q, R_z and R_t. R_a is the average roughness on the surface. R_q is the root-mean-squared roughness calculated over the entire measured array. R_t is the peak-to-valley difference calculated over the entire measured array. R_z is the average of the ten greatest peak-to-valley separations on the sample.

The experiments reported in this investigation were repeated three times to check for reproducibility. In general the results were found to be quite reproducible. Error bars are shown for corrosion and roughness measurements which show the maximum and minimum limit of the data around the mean value. The impedance data were also simulated to the appropriate equivalent circuit, with a reasonable fit of an average error 2%. This error for resistance values was about 1% and for constant phase element and inductors reached a maximum of 3%.

Chapter 4 SURFACE PATTERNING OF NICKEL

The results of this study have previously been reported in the following two papers:

1)) Toloei, A. S, Stoilov, V, and Northwood, D. O. "A new approach to combating corrosion of metallic materials ", Applied Surface Science, 284 (2013) 242-247.

2) Toloei, A. S, Stoilov, V, and Northwood, D. O. "The effect of creating different size surface patterns on corrosion properties of Nickel", ASME, International Mechanical Engineering Congress & Exposition, 2012, Houston, Texas, USA, IMECE2012-89407, (IMECE) 3 (PARTS A, B, AND C) , pp. 1297-1303.

In this chapter all the results obtained from different experiments on nickel samples with patterned surfaces are presented and discussed.

4.1 Corrosion Testing Results

4.1.1 Potentiodynamic Polarization Technique

Figure 4-1 shows the polarization curves of the reference sample and the patterned samples in 0.5 M H_2SO_4 solution at room temperature.

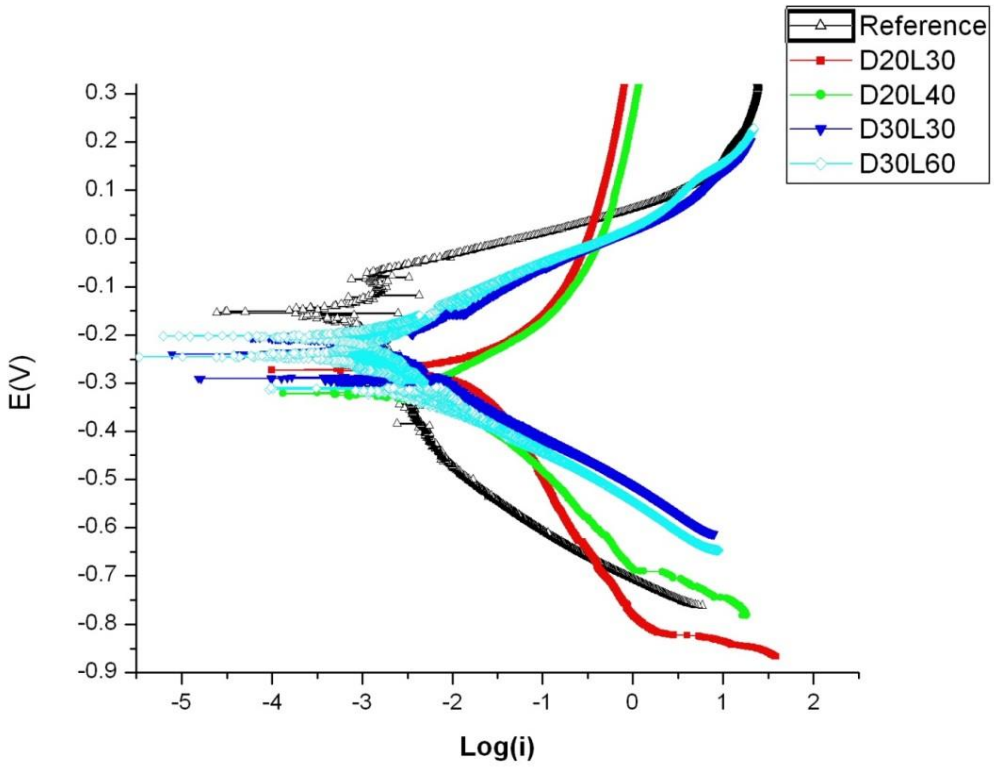

Figure 4-1 Potentiodynamic polarization curves for patterned samples (SCE).

I_{Corr} and E_{Corr} were calculated using Tafel extrapolation method on the anodic and cathodic branch of the curves. In this method the tangent lines are drawn and the intersection shows the corrosion potential and corrosion current density. The values of the I_{Corr} , R_p and E_{Corr} for samples with different hole diameters (D) and inter-hole spacings (L) are summarized in Table 4-1.

Table 4-1 Corrosion parameters for patterned nickel samples with different (D) and (L) values.

SAMPLE	β_a (mV)	β_c (mV)	R_p (Ω/cm^2)	I_{Corr} ($\mu A/cm^2$)	E_{Corr} (mV)
REF	148.40	298.56	1100	39.1	-153.6
D2L4	94.64	98.85	2107	9.9	-306.0
D2L8	69.13	90.03	4142	4.1	-274.7
D3.5L3.5	94.65	104.77	4472	4.8	-293. 0
D3.5L7	86.10	91.30	3560	5.4	-313. 1
D3.5L14	63.14	147.07	8337	2.3	-62.4
D5L5	103.57	125.65	1246	19.7	-299.9
D5L10	185.92	135.63	5751	5.9	-318.7
D5L20	187.24	363.99	33538	1.6	-242.2
D10L10	105.57	211.12	512	59.6	-215.4
D10L20	153.98	129.17	5046	6.2	-323.5
D10L30	166.52	119.45	4186	7.2	-321.8
D20L20	236.71	174.64	28070	1.2	-301.5
D20L30	123.96	242.06	2086	17.0	-271.9
D20L40	127.85	104.73	621494	0.04	-274.4
D30L30	105.51	127.76	16660	1.5	-220.9
D30L60	64.72	120.25	201638	0.09	-220.5

According to the current density values, I_{Corr}, the corrosion rate (mass-loss rate) in all patterned samples (except for D10L10), is significantly lower compared to the reference polished sample (REF). The reduction of the corrosion rate in 13 out of 16 patterned samples is between 4 and 500 times. The lowest corrosion rate was measured in two samples: D20L40 and D30L60. The magnitude of the corrosion current density is 0.04–0.09 $\mu A/cm^2$, which

corresponds to a corrosion rate more than two orders of magnitude smaller than the corrosion rate measured for the polished reference sample (39.1 $\mu A/cm^2$).

Figure 4-2, illustrates the variation of the I_{corr} for different hole diameters (1/D) in samples with the same ratio of patterned to non-patterned area D/L. Clearly samples with D = 20 µm (1/D = 0.05 μm^{-1}) show the lowest I_{corr}, and therefore better corrosion resistance. On the other hand, samples with D = 10 µm (1/D = 0.1 μm^{-1}) and smaller have the highest corrosion rates compared to any other samples with any pattern density (D/L = 0.25, D/L = 0.5 and D/L = 1.0). In addition, the corrosion resistance observed in samples with D = 20 µm exceeds the performance of the reference sample (1/D = 0.0 μm^{-1}) which is a significant improvement of the corrosion properties of the metal surface.

The observed trends in Figure 4-2 suggest that patterns with higher values of the hole diameter and inter-hole spacing were more corrosion resistant than the others. When it comes to a general comparison among all surface patterns, samples D20L40 and D30L60 stand out in the corrosion test results. Both of these samples have a (D/L) ratio of 0.5.

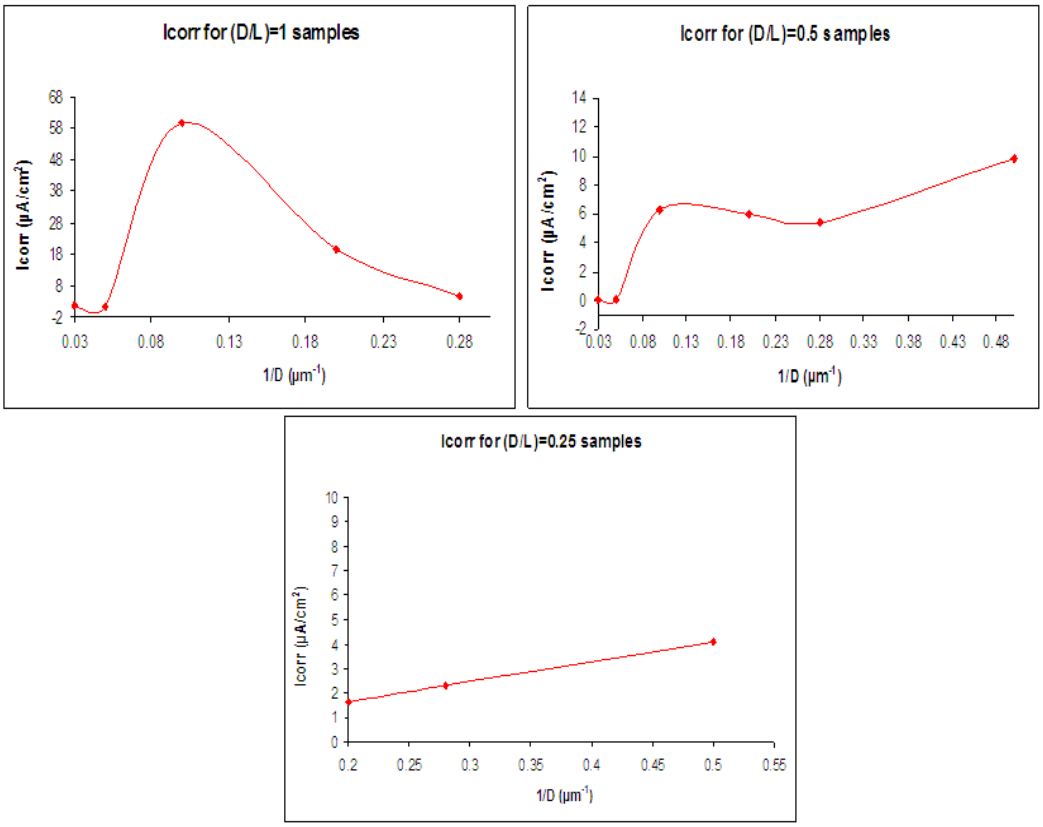

Figure 4-2 Current density of the patterned samples of nickel versus (1/D).

4.2 SEM Images

The surface topography of all patterned samples and the reference sample before and after corrosion tests were analyzed using SEM.

4.2.1 **Before corrosion:**

Figures 4-3 (a-q) show the reference sample and other samples with various D and L values before corrosion testing. Figure 4-3 (a) displays the reference sample of nickel with a flat surface which is prepared using alumina suspension to get a mirror like surface. Figure 4-3 (b) and (c) displays samples with hole diameters of 2 µm. In sample D2L4 the created holes are very close to each other but in sample D2L8 there is more space between the holes and it is easier to see the patterns on the surface. Figure 4-3 (d) shows sample D3.5L3.5 with a higher D value but in this case there was also some overlap between different holes because the distance between the holes is equal to the diameter of the holes. Thus, by creation of the splashes during laser ablation process and as a result of the small distance between the holes, it is difficult to see the patterns. Some defects seen in one of the micrographs are related to splashes from the holes on the surface (Figure 4-3 (d)).

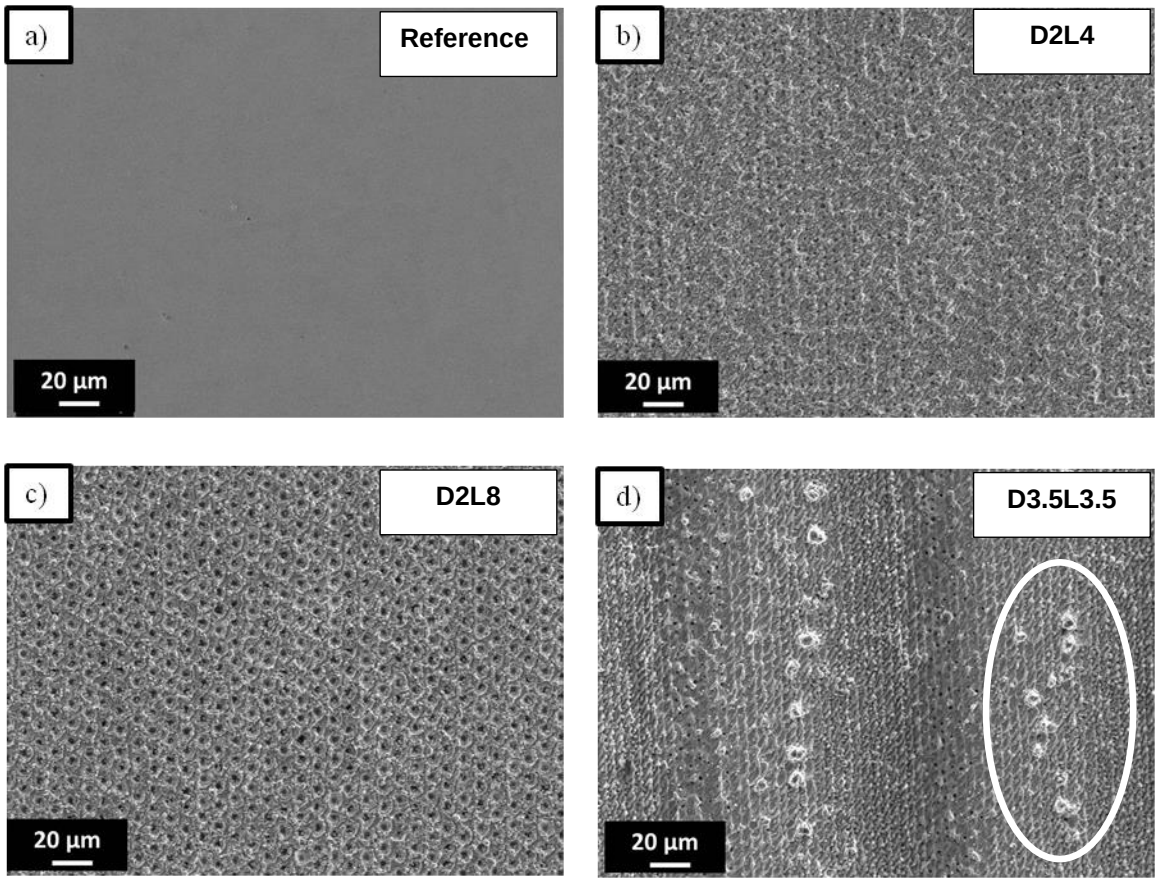

Figure 4-3 SEM micrographs of the patterned samples a) reference, b) D2L4, c) D2L8 and d) D3.5L3.5 before corrosion.

Figures 4-3 (e-h) illustrate two more samples with D=3.5 µm and samples with D=30 µm. In comparison with sample D3.5L3.5, it is easier to see the holes on the surface in sample D3.5L7 (Figure 4-3 (e)). There were no defects on the surface but there was still some overlap between holes. Figure 4-3 (f) shows different holes with more distances in sample D3.5L14. By increasing the hole diameter to sample D30L30 (Figure 4-3 (g)), it is seen that for the patterns with equal D and L values, the holes are very close together but in the case of this

sample a significant overlap is not seen on the surface. Figure 4-3 (h) displays some more details on sample D30L60 with more distance between the holes.

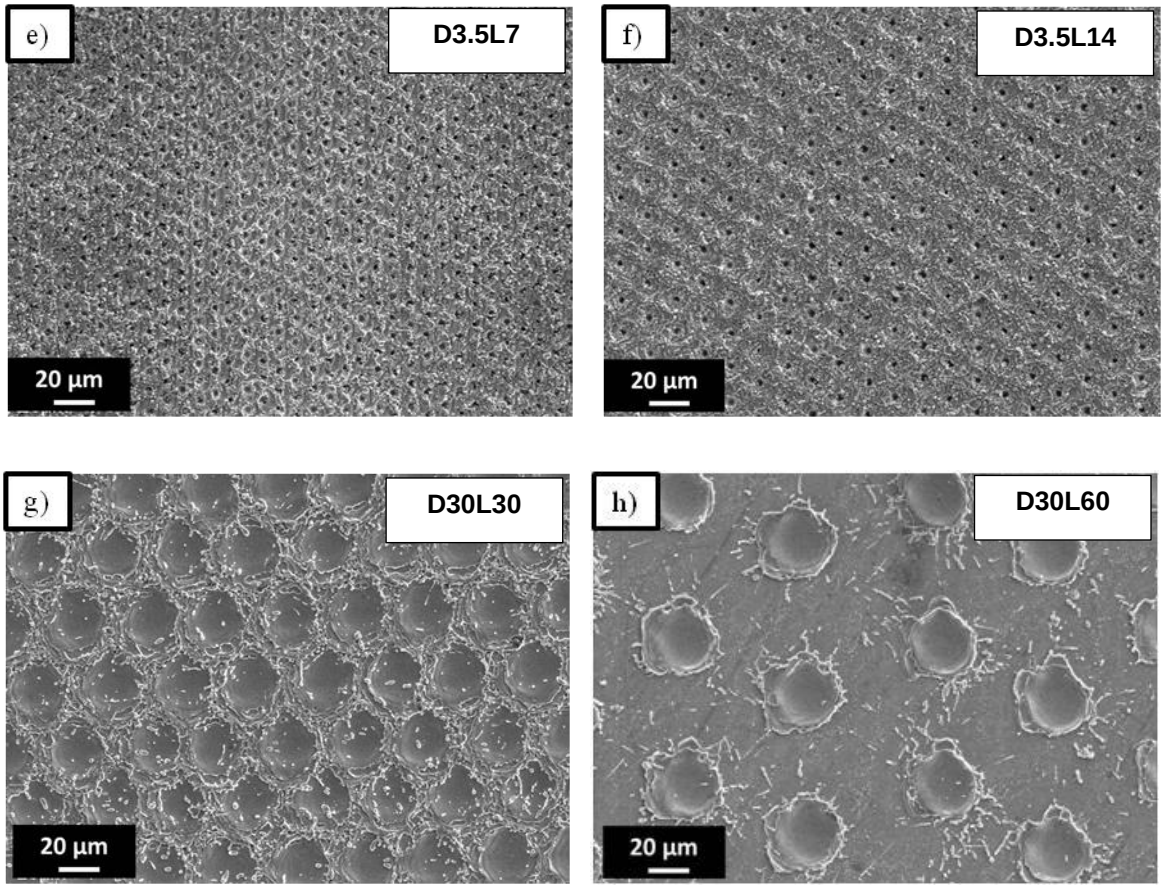

Figure 4-3 (Cont) SEM micrographs of the patterned samples e) D3.5L7, f) D3.5L14, g) D30L30 and h) D30L60 before corrosion.

Figure 4-3 (i) displays sample D5L5 before corrosion testing. As it is seen, similar to sample D3.5L3.5, which had a ratio of (D/L) = 1, there is overlap between the holes and it is not easy to see the individual holes. By increasing the inter-hole spacing in sample D5L10 (Figure 4-3 (j)), the holes are more obvious and also no overlap is observed on the surface. Figure 4-3 (k) shows sample D5L20, which doesn't show any significant overlap between the holes or splashes on the surface. By increasing the hole diameter to 10 µm in sample

D10L10 in Figure 4-3 (l), a significant overlap is seen between the holes and holes are not even as visible as previous samples with the same D/L ratio.

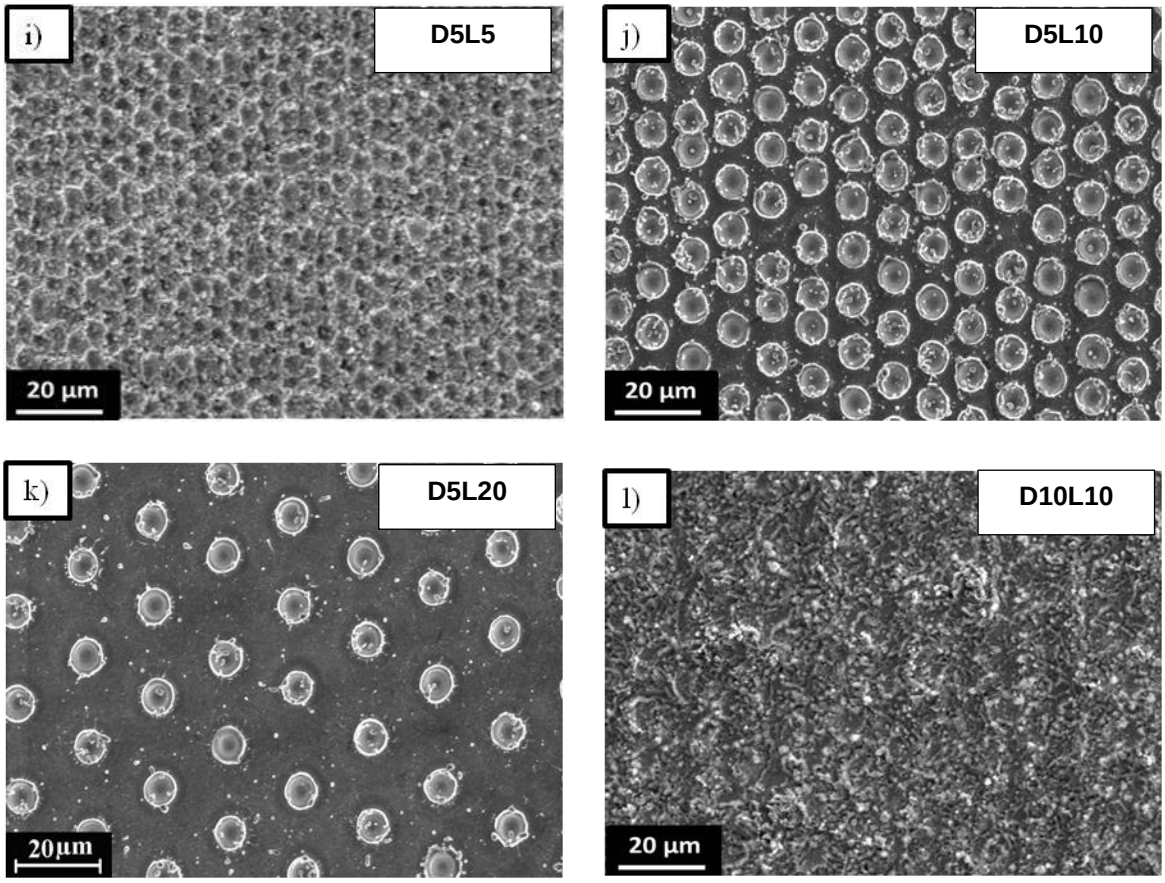

Figure 4-3 (Cont) SEM micrographs of the patterned samples i) D5L5, j) D5L10, k) D5L20 and l) D10L10 before corrosion.

Two other samples with D=10 namely D10L20 and D10L30 are presented in Figure 4-3 (m and n). In both cases specially sample D10L30 the holes are clearly identifiable. Sample D20L20 again with the ratio of (D/L) = 1 shows overlap between the holes as a result of the small inter-hole spacing on the surface (Figure 4-3 (o)). According to Figure 4-3 (p) by increasing the L value in sample D20L30 holes and also some splashes produced during creation of the patterns are recognizable. Finally, Figure 4-3 (q) displays an image from sample

D20L40 which clearly shows some holes with some splashes between the created patterns.

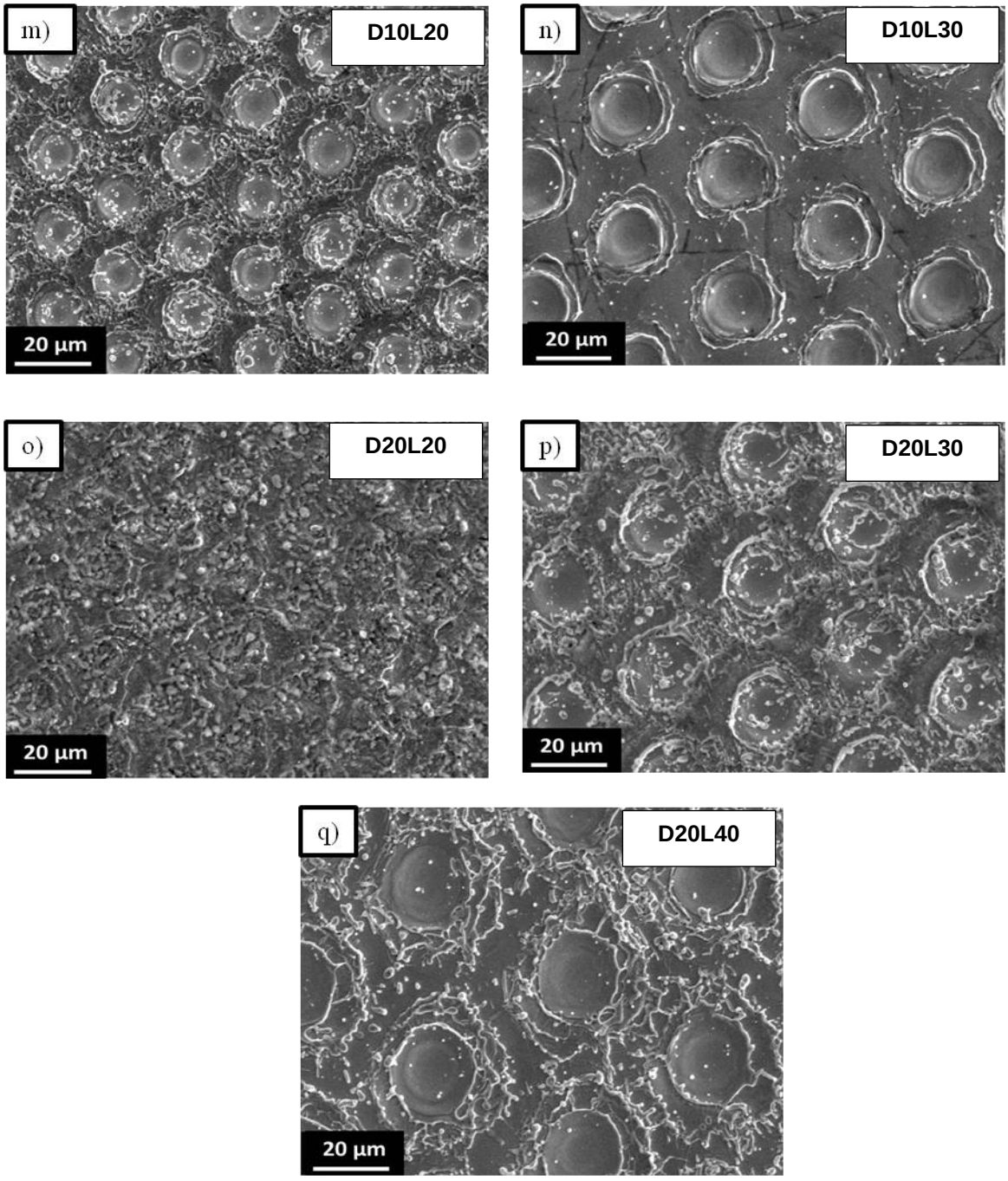

Figure 4-3 (Cont) SEM micrographs of the patterned samples m) D10L20, n) D10L30, o) D20L20, p) D20L30 and q) D20L40 before corrosion.

4.2.2 **After corrosion:**

Figures 4-4 (a-q) shows the reference and also different patterned samples after corrosion testing. Figure 4-4 (a) illustrates the reference sample after the corrosion testing. Severe localized corrosion, possibly pitting corrosion, was observed throughout the surface of this sample.

Figures 4-4 (b) and (c) compare samples with D=2 μm (D2L4 and D2L8) after corrosion testing. The patterned area showed a general type of corrosion with some small areas of more severe corrosion. Figure 4-4 (d) illustrates sample D3.5L3.5. Comparing Figures 4-4 (b-d), sample D2L4 Figure 4-4 (b) showed more corrosion. The corrosion test results, with a corrosion rate of 9.9 $\mu A/cm^2$ for sample D2L4, support the SEM results.

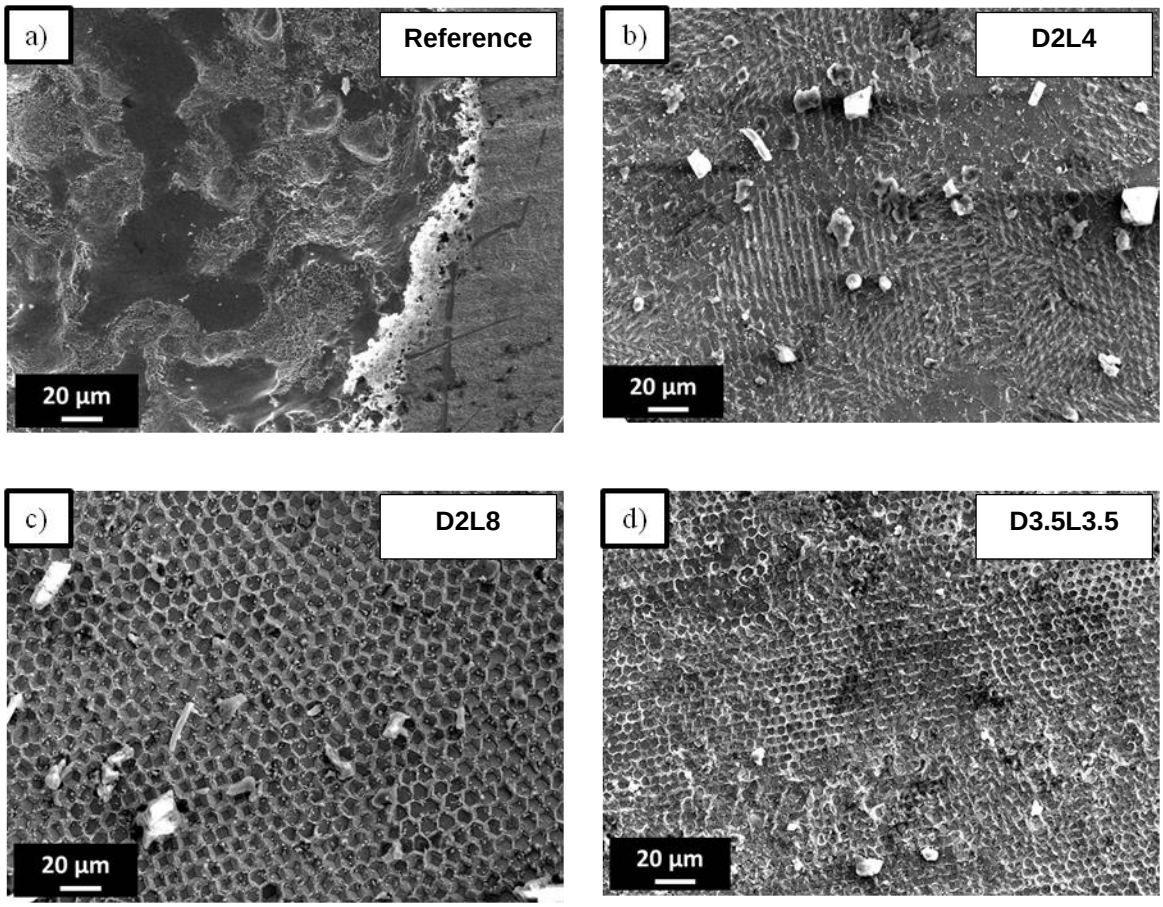

Figure 4-4 SEM micrographs of the patterned samples a) reference, b) D2L4, c) D2L8 and d) D3.5L3.5 after corrosion.

Figures 4-4 (e) and (f) show samples with D=3.5 µm after corrosion testing. In both cases some holes are filled with corrosion products but there are still some holes which have not experienced severe corrosion. Figure 4-4 (g) and (h) illustrate samples D30L30 and D30L60 as samples with the maximum value of D. In Figure 4-4 (g), sample D30L30 did not show a localized corroded area and the surface appeared darker compared to the surface before the corrosion test. This phenomenon is most likely a result of general corrosion on the surface and small pits in some parts of the patterned surface. This sample was one of the "better" patterns with an I_{corr} value (1.53 µA/cm^2) 25 times smaller than the I_{corr}

value for the reference sample. Figure 4-4 (h), shows one of the ideal patterns in this study from the corrosion resistance point of view, namely D30L60. This sample showed significantly lower I_{corr} values of 0.09 µA/cm^2 during the corrosion tests. A closer look at the SEM micrograph reveals no noticeable change in the sample appearance before and after the corrosion test which clearly demonstrates that no severe corrosion has taken place on the patterned area of the sample.

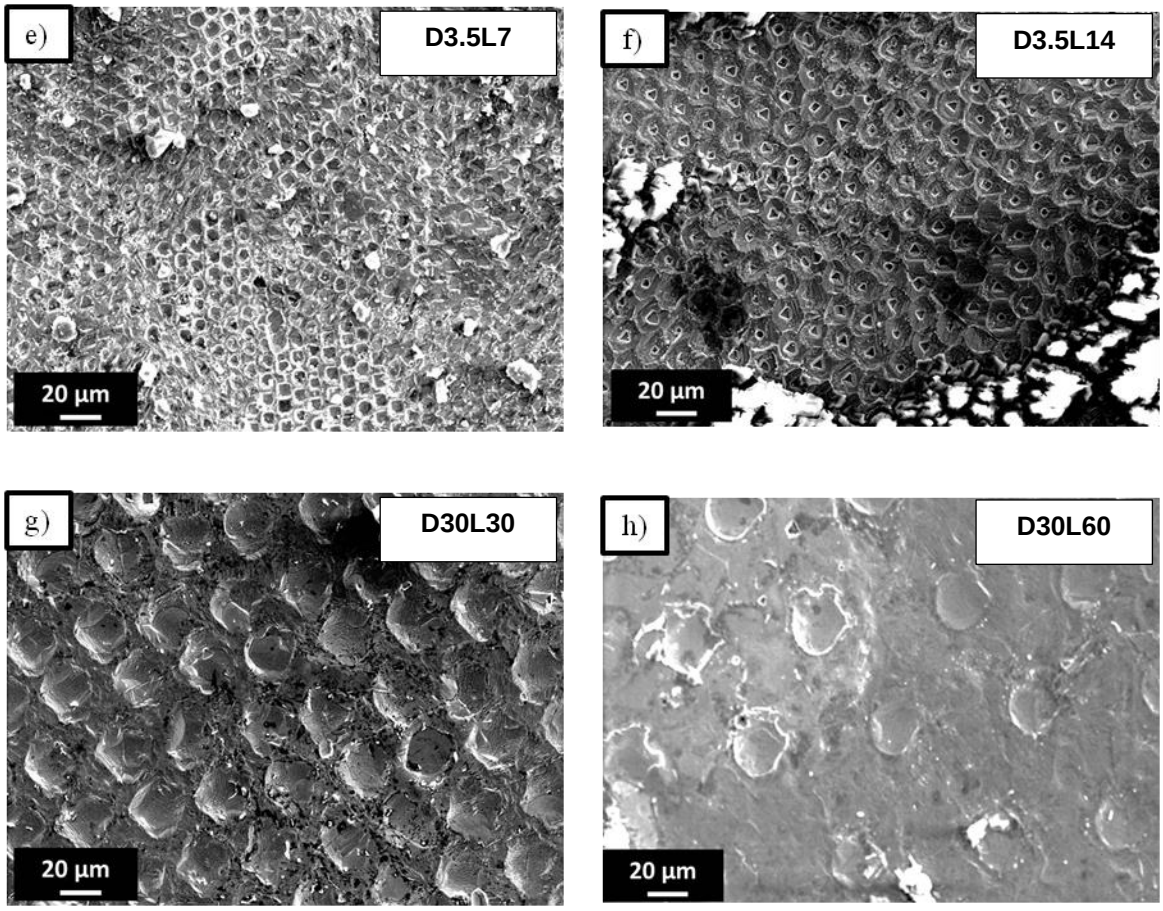

Figure 4-4 (Cont) SEM micrographs of the patterned samples e) D3.5L7, f) D3.5L14, g) D30L30 and h) D30L60 after corrosion.

According to corrosion test results and also the SEM micrographs, it can be considered that the corrosive solution has not reached the bottom of the holes and the contact area between the solution and substrate has decreased which has resulted in less corrosion of this sample.

Figures 4-4 (i-k) show samples D5L5, D5L10 and D5L20. For samples with D=5, sample with D/L = 1, D5L5 showed the highest corrosion rate and the SEM images confirm this. Among these samples, D5L10 showed less corrosion and sample D5L20 also showed some heavily corroded regions which are shown in Figure 4-4 (k).

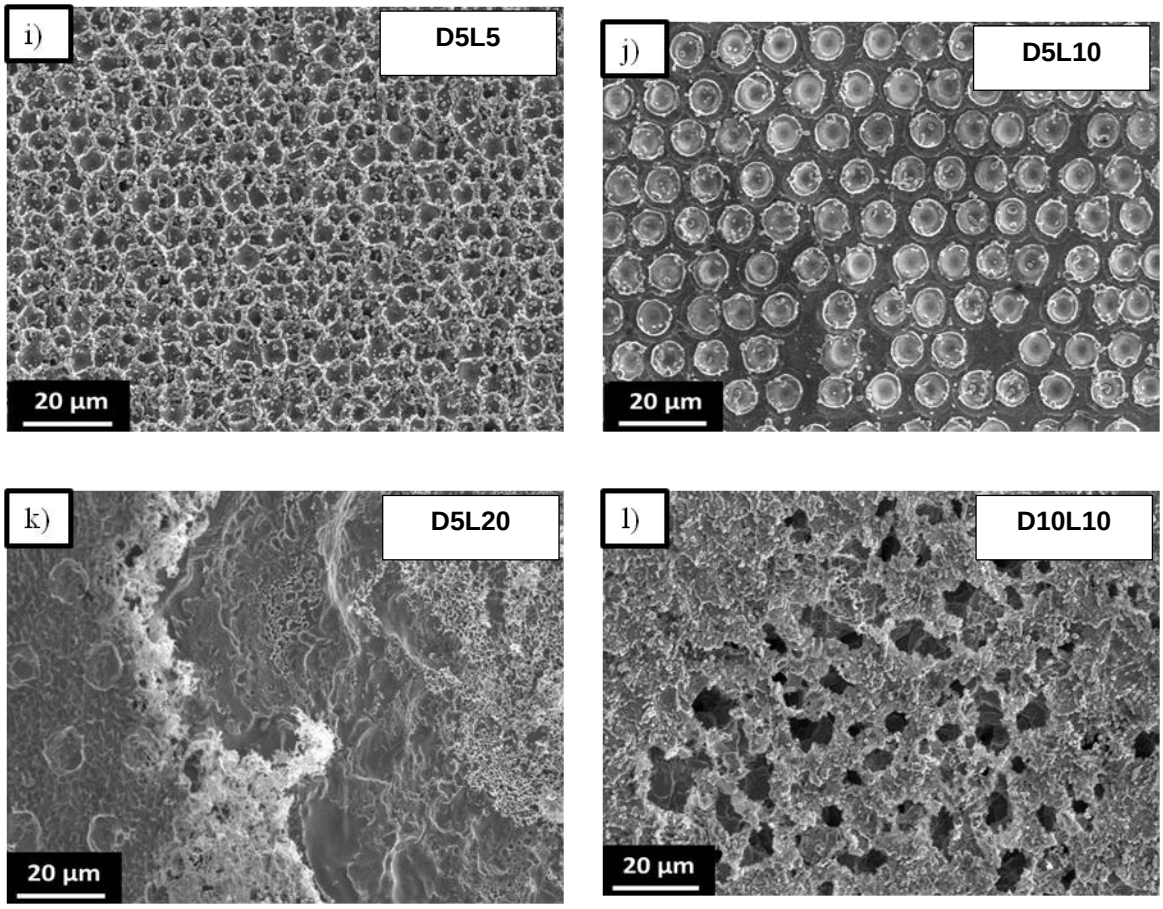

Figure 4-4 (Cont) SEM micrographs of the patterned samples i) D5L5, j) D5L10, k) D5L20 and l) D10L10 after corrosion.

The highest corrosion rate was observed in sample D10L10 as can be seen in Figure 4-4 (l). It seems that in this sample the corrosive electrolyte has been in contact with the whole substrate including the holes which has resulted in a complete change in the appearance of the surface.

Figure 4-4 (m) and (n) show samples with D=10 µm, namely D10L20 and D10L30. The first one with a ratio of with (D/L) = 0.5 showed less corrosion on the surface and less damage to the created patterns. In Figures 4-4 (o), (p) and (q) samples with D=20 are presented. With the exception of sample D20L30, all samples with D=20 and D=30 showed the lowest corrosion rate. Sample D20L30 is one of the samples with high corrosion current, I_{corr}, of 17.01 µA/cm^2. By comparing this sample before and after the corrosion test, it can be observed that the patterned area is corroded and the pattern's contrast (hole depth) is not as visible as before the test. This leads to the conclusion that in this sample the corrosive solution has reached the whole surface including the bottom of the holes. Figure 4-4 (q), show the most corrosion resistant sample in this study, namely D20L40. This sample showed significantly lower I_{corr} value of 0.04 µA/cm^2 in the corrosion tests. There is no noticeable change in the sample appearance after the corrosion test which clearly indicates that no severe corrosion has happened on the patterned area of the sample. In this sample, it seems that the electrolyte has not reached the bottom of the holes and didn't cause a severe corrosion on the surface.

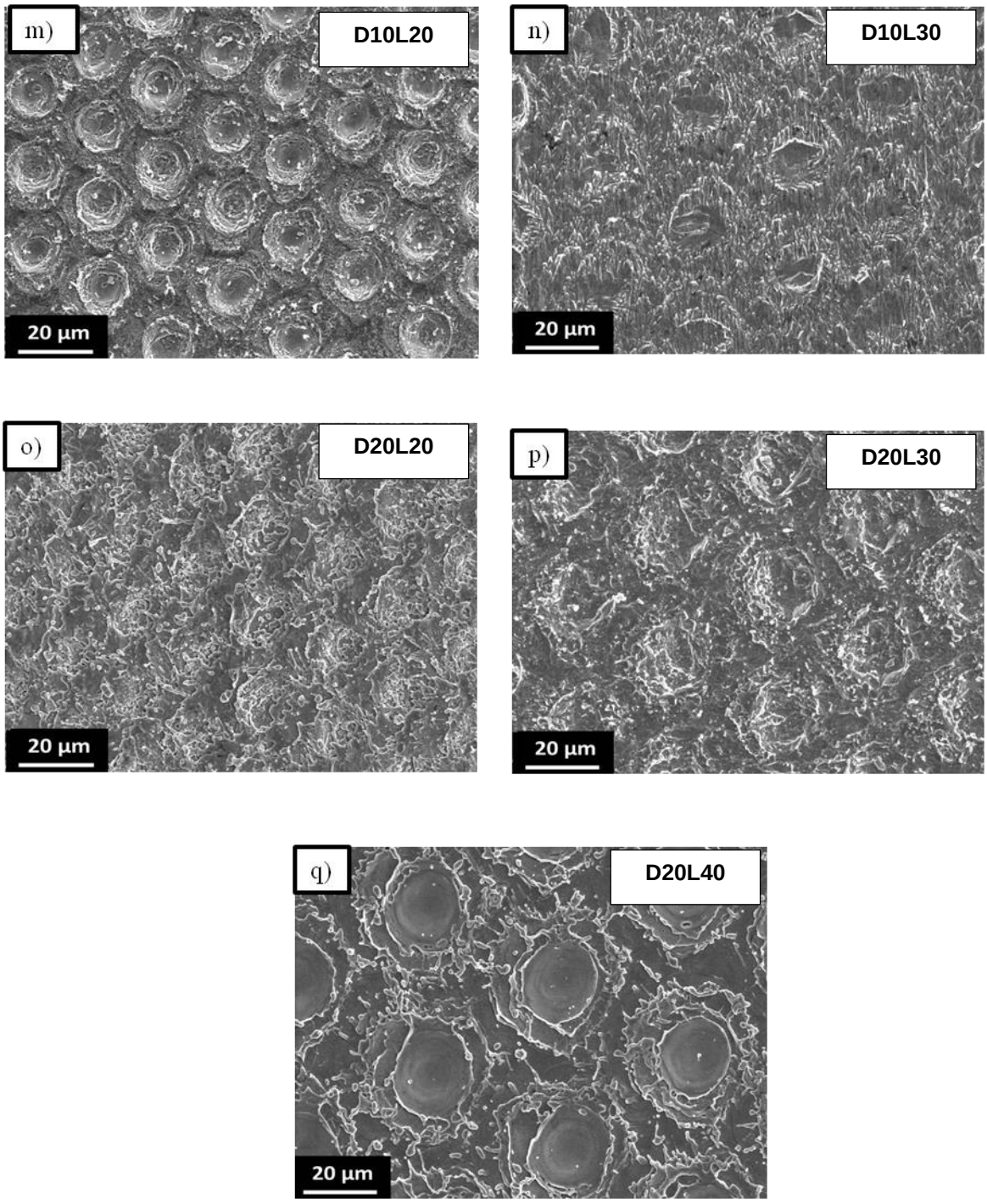

Figure 4-4 (Cont) SEM micrographs of the patterned samples m) D10L20, n) D10L30, o) D20L20, p) D20L30 and q) D20L40 after corrosion.

4.3 Roughness Measurement Results

4.3.1 Before corrosion

Figures 4-5 to 4-11 show 3D images related to nickel samples with different size patterns before corrosion testing. As it is seen, for smaller holes and holes with lower L values there might be some overlaps but by increasing the D values (D=30) or the L values (L=14, L=30 and L=60) the patterns are more obvious.

Figures 4-5 and 4-6 display samples with D=2 µm. In sample D2L8 compared to sample D2L4, the holes are more obvious and less overlap is seen on the surface of patterned sample because it has a larger inter-hole spacing between the holes.

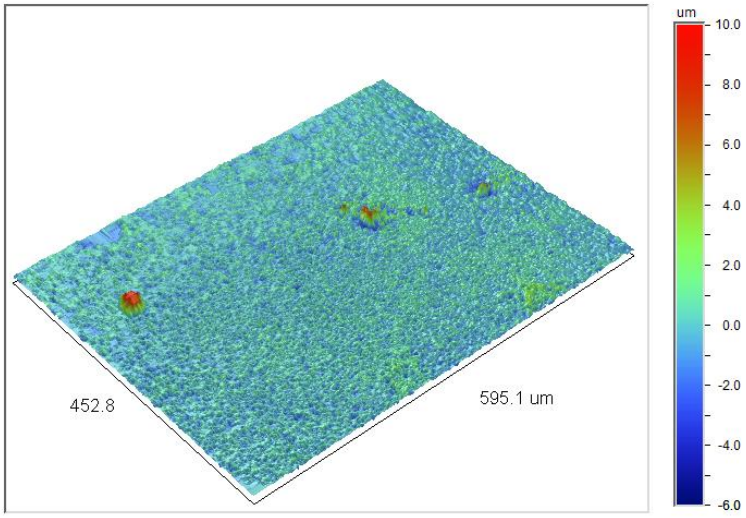

Figure 4-5 Sample D2L4 3D roughness before corrosion

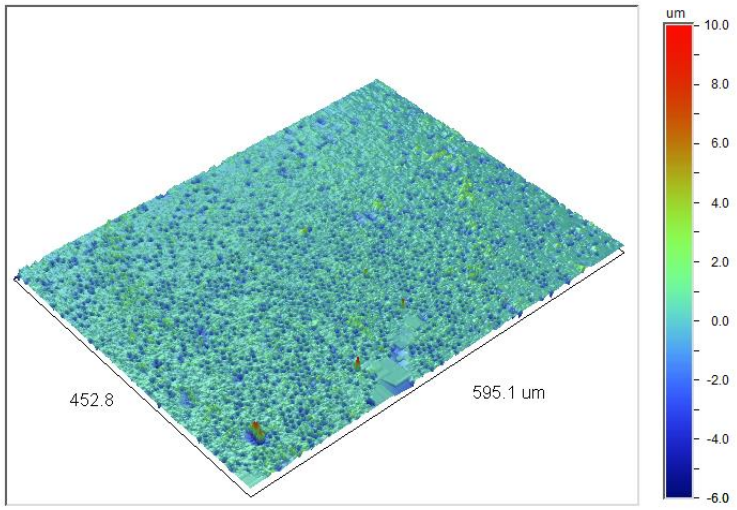

Figure 4-6 Sample D2L8 3D roughness before corrosion

For the samples with D=3.5 µm, there are three images which are presented in Figures 4-7 to 4-9. Similar to SEM results before corrosion, in sample D3.5L3.5 with D/L=1, there is much more overlap between the holes and by increasing the inter-hole spacing to sample D3.5L7, it is easier to see the patterns on the surface. Sample D3.5L14 however, doesn't show any overlap or splashes on the surface and there is enough space between the hole to make it easier to see the patterns compared to samples D3.5L3.5 and D3.5L7. In these images the appearance of the samples is similar to the SEM micrographs, but more details about the morphology of the surface can be observed.

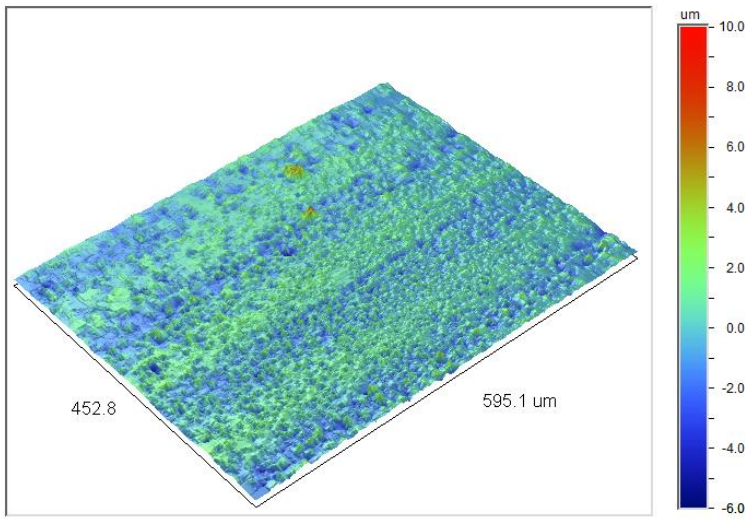

Figure 4-7 Sample D3.5L3.5 3D roughness before corrosion

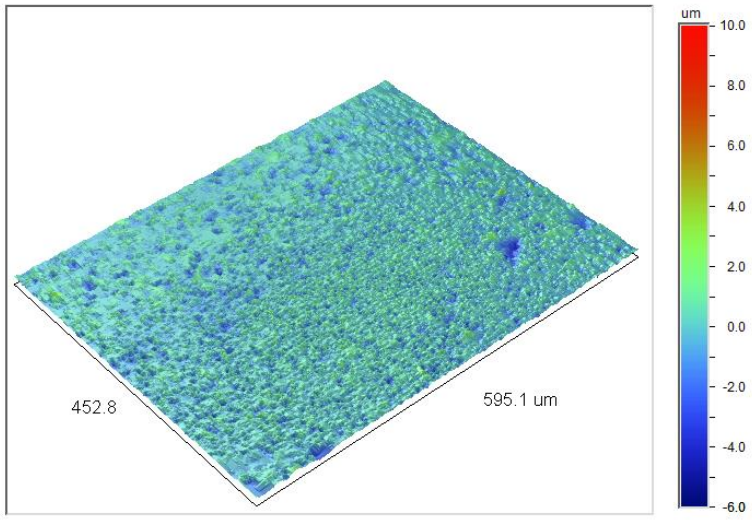

Figure 4-8 Sample D3.5L7 3D roughness before corrosion

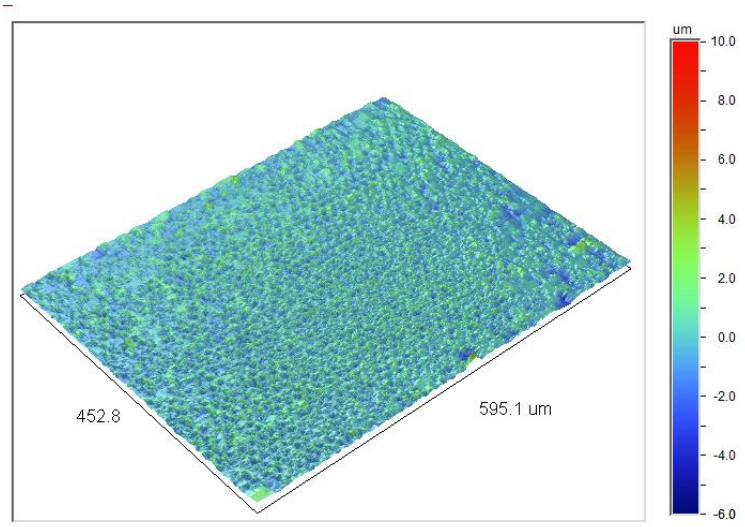

Figure 4-9 Sample D3.5L14 3D roughness before corrosion

For the two samples with D=30, namely D30L30 and D30L60, shown in Figures 4-10 and 4-11, the holes are large enough to be identifiable from each other and there is no overlap or too many splashes from the laser ablation process between the holes.

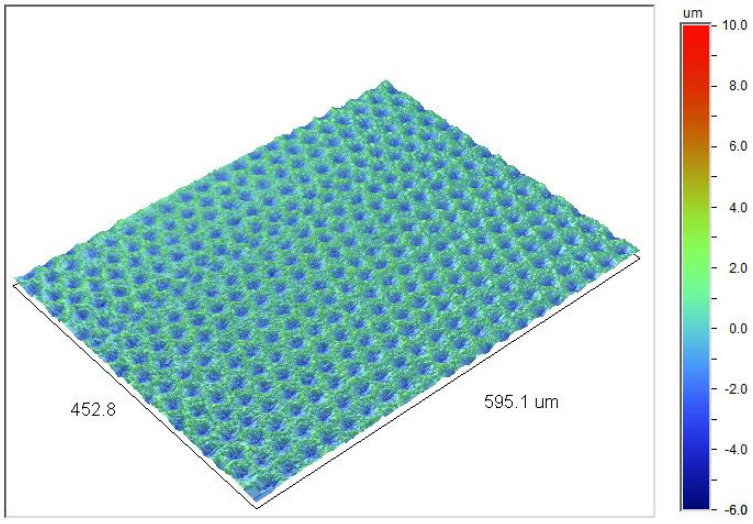

Figure 4-10 Sample D30L30 3D roughness before corrosion

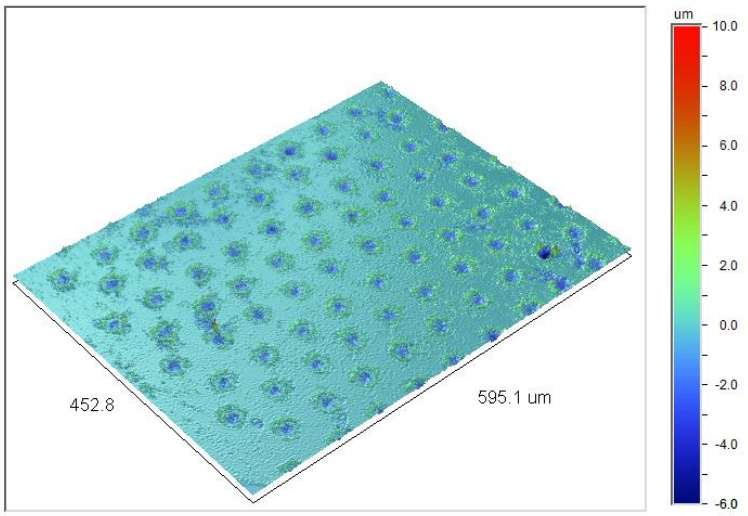

Figure 4-11 Sample D30L60 3D roughness before corrosion

4.3.2 **After corrosion:**

Figures 4-12 to 4-18 illustrate 3D images of patterned samples after corrosion testing. Amongst the samples with D=2µm, sample D2L8 and for samples with D=3.5 µm, sample D3.5L14, showed a better corrosion resistance both with D/L = 0.25. The 3D images confirm the potentiodynamic polarization test results and SEM. Samples with D=30 µm showed small changes compared to their appearance before corrosion testing. Corrosion results also indicated high corrosion resistance of these samples compared to other samples.

Figure 4-12 illustrates sample D2L4 after corrosion. In this sample it seems that some areas with higher height have formed which can be related to the passive layer formed on the surface outside the holes. Different deep holes created on the surface (identified with a circle around them) are some pits as signs of localized corrosion on metals such as nickel with ability to form a passive layer. By looking at corrosion results, it can be seen that creating the patterns

has decreased the corrosion of nickel compared to the reference sample but, the corrosion current density of this sample (9.9 µA/cm^2) is not as good as samples with D=20 or D=30, specifically D20L40 and D30L60 with values of 0.04 µA/cm^2 and 0.09 µA/cm^2, respectively. Therefore, it seems that the passive layer was not able to cover the whole surface including the bottom of the holes to decrease corrosion.

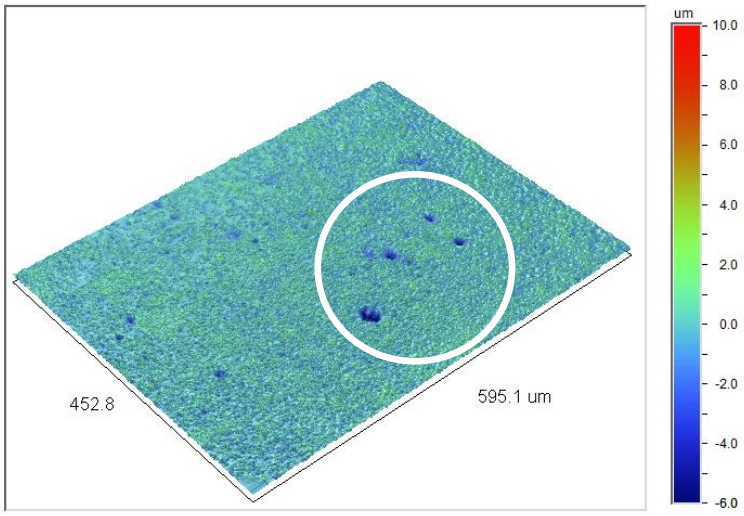

Figure 4-12 Sample D2L4 3D roughness after corrosion

By increasing the inter-hole spacing in sample D2L8 as shown in Figure 4-13, it seems that again there are some areas with higher height on the surface which can be related to the passive layer formed outside the holes. There are also a small amount of corrosion products on the surface. There are also some deep holes on the surface but the number of pits is less compared to sample D2L4. Corrosion testing results also revealed less corrosion current density for this sample (4.1 µA/cm^2).

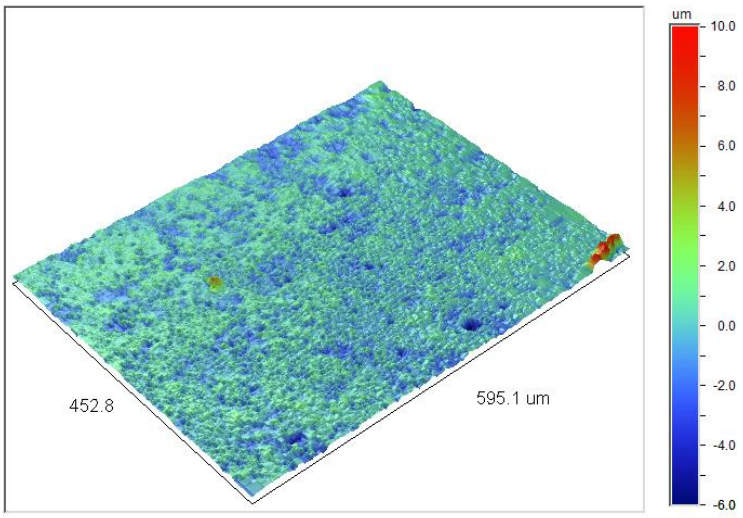

Figure 4-13 Sample D2L8 3D roughness after corrosion

Figure 4-14 shows sample D3.5L3.5 after corrosion testing. There are some deep holes on the surface and also the holes are not as visible as before corrosion (Figure 4-7). It seems that the passive layer has covered the whole surface including the holes and inter-hole spacings. Corrosion testing results also show a relatively low corrosion current density of 4.8 $\mu A/cm^2$ for this sample. Sample D3.5L7 in Figure 4-15 also illustrates regions with increased roughness with some deep holes on the surface. The corrosion results also confirmed almost similar value (5.4 $\mu A/cm^2$) for corrosion current density of this sample compared to sample D3.5L3.5. In both samples D3.5L3.5 and D3.5L7, it seems that the passive layer has formed on the surface and decreased corrosion but it seems that the decreasing contact area between the electrolyte and the substrate has not been as effective as for samples D20L40 and D30L60.

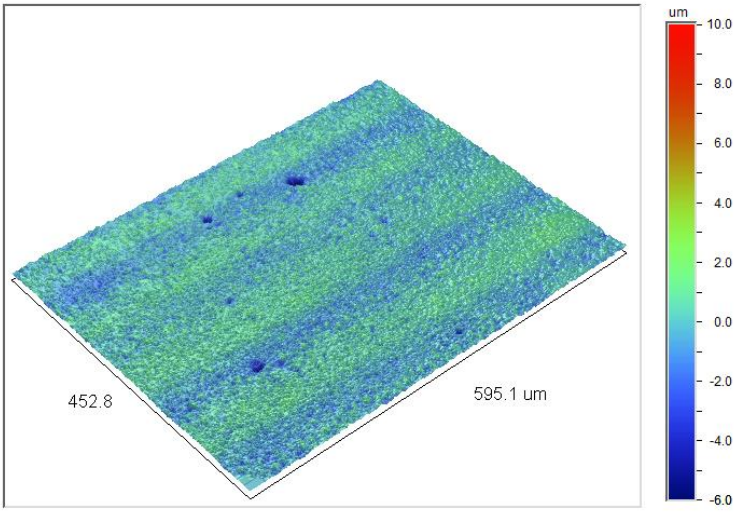

Figure 4-14 Sample D3.5L3.5 3D roughness after corrosion

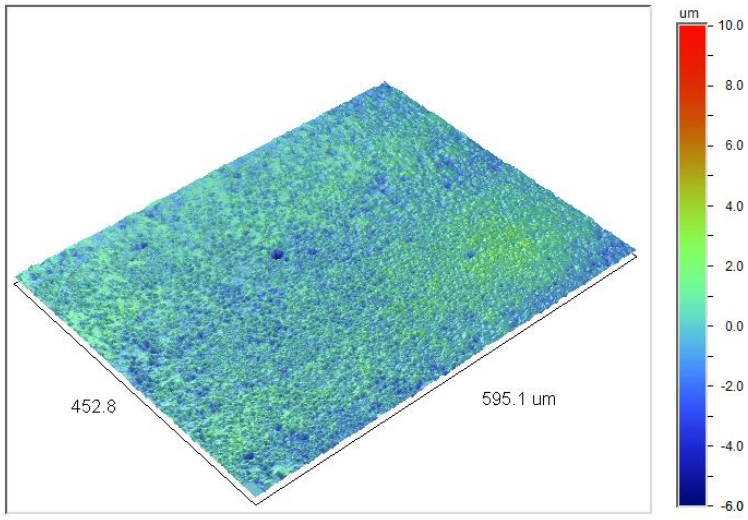

Figure 4-15 Sample D3.5L7 3D roughness after corrosion

Sample D3.5L14 is shown in Figure 4-16. In samples with D=3.5 µm also similar to samples with D=2 µm sample D3.5L14 with a (D/L) = 0.25 had the lowest corrosion current density (2.3 µA/cm^2). This value shows less corrosion on this sample and can be a result of the formation of a more stable passive layer

on the patterns including inside the holes. 3D images also didn't show any deep holes or significant corrosion products on the surface unlike samples D3.5L3.5 and D3.5L7.

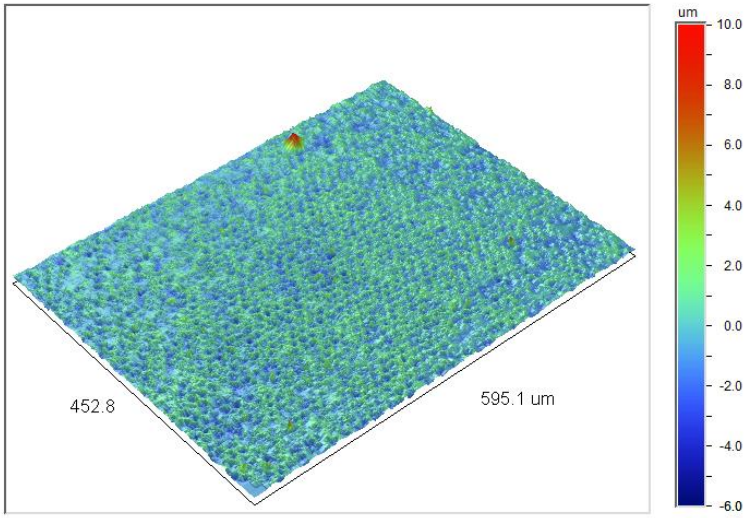

Figure 4-16 Sample D3.5L14 3D roughness after corrosion

Samples D30L30 and D30L60 are shown in Figures 4-17 and 4-18 as samples with the highest value of D, namely 30 µm. In the case of sample D30L60 however, the inter-hole spacing is two times larger compared to sample D30L30 and it is possible to see some corrosion on the surface outside the holes. In both cases the potentiodynamic polarization results showed very low corrosion current densities of 1.5 µA/cm^2 and 0.09 µA/cm^2 : See Table 4-1.

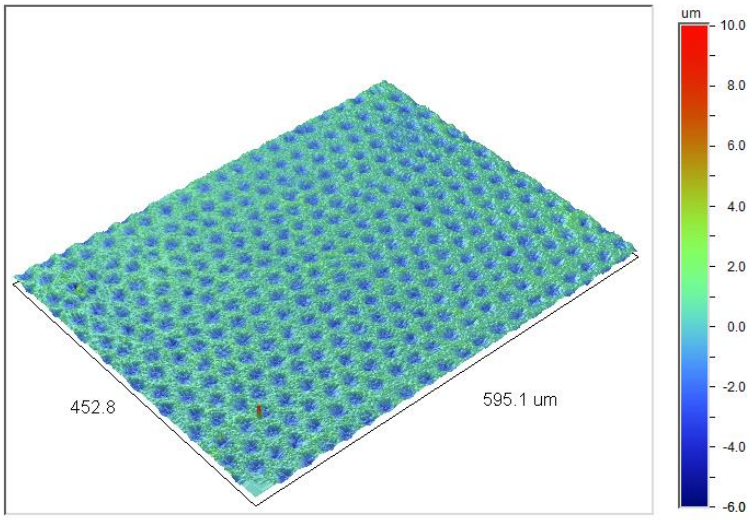

Figure 4-17 Sample D30L30 3D roughness after corrosion

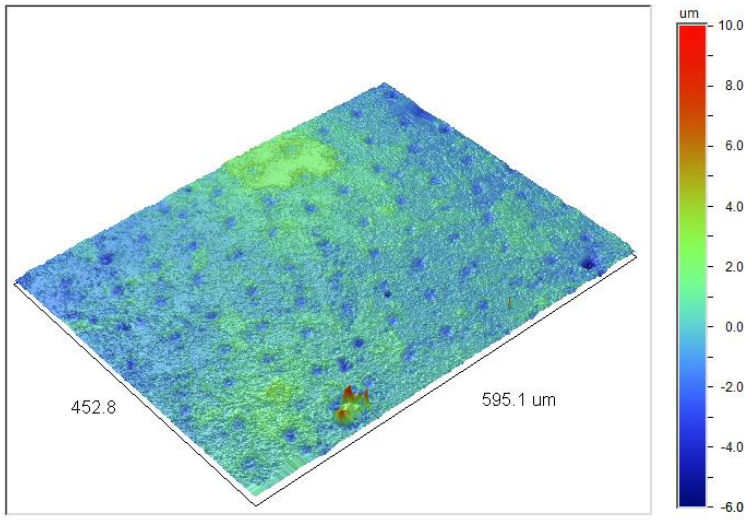

Figure 4-18 Sample D30L60 3D roughness after corrosion

4.4 EDS Results

In order to further investigate the reasons for the significant improvement of the corrosion resistance in some samples, energy-dispersive X-ray spectrometry (EDS) was used. The main goal was to evaluate the change in oxygen concentration both on the surface of the samples and inside the patterned holes. In the spectrum three elements, nickel (Ni), oxygen (O) and carbon (C) are observed. The intensity of the most intense peaks (Ni: L_{α}=0.851 and O: K_{α}=0.523 KeV) was used to calculate the oxygen concentration on the surface (see Table 4-2). Comparing the REF sample before and after testing (Table 4-2) shows that there is little change in the O concentration on the surface. The O concentration remained in the range of 2.3-2.8%, indicating that a stable passive oxide layer was not formed. Similar EDS spectra were obtained for all corrosion damaged samples. For instance the EDS spectra of sample D5L20 on the surface and in the hole before and after the corrosion test do not show a significant change in the O concentration, only 11% (Table 4-2). However, the EDS spectra for the patterned samples with the improved corrosion properties (D30L60) exhibit different behaviour.

Table 4-2. Oxygen concentration (wt. %) before and after corrosion testing

O, %wt	Before test	After test	% change
Surface (D30L60)	2.25	2.75	18
Hole bottom (D30L60)	2.17	4.24	49
Surface (D5L20)	2.45	2.75	11
Hole bottom (D5L20)	2.3	2.70	15
Reference (Polished)	2.29	2.75	17

The O concentration for sample D30L60 before and after the corrosion test are shown in Figures 4-19 to 4-22 and Table 4-2. The concentration of O on the surface before and after the corrosion test differs, which contrasts with the other corrosion damaged patterns. This is a clear indication that an oxide layer was formed on the patterned surface, including inside the holes, but only the oxides on the surface were dissolved by the electrolyte. A possible explanation of this phenomenon is the lack of convective motion of the electrolytic fluid at the bottom of the holes. However, such a hypothesis could be dismissed based on the fact that the dissolution of oxides at the hole bottom was observed in patterns with hole diameters much smaller than 30 μm, e.g. 5 μm in D5L20. One would expect that a hole with a 5 μm diameter would exert more severe constraint on the convective fluid flow than a 30 μm diameter hole with the same depth. However the EDS measurements in D5L20 show no significant change (11–15%) in the O concentration on the surface and the hole bottom after the corrosion test (Table 4-2). Therefore, the retention of the passive oxide layer inside the patterned holes is consistent with the fluid not actually reaching the

bottom of the patterned hole. In other words, in the samples with better corrosion resistance, the contact between the electrolyte and the metal surface is heterogeneous wetting – alternating solid–liquid zones and stable air/vapor pockets. These air/vapor pockets allow the formation of the passive oxide layer but prevent its dissolution by the electrolyte. The heterogeneous interface formed between the solution and the surface, significantly decreases the overall contact area between the surface and the electrolyte, thus significantly decreasing the corrosion rate.

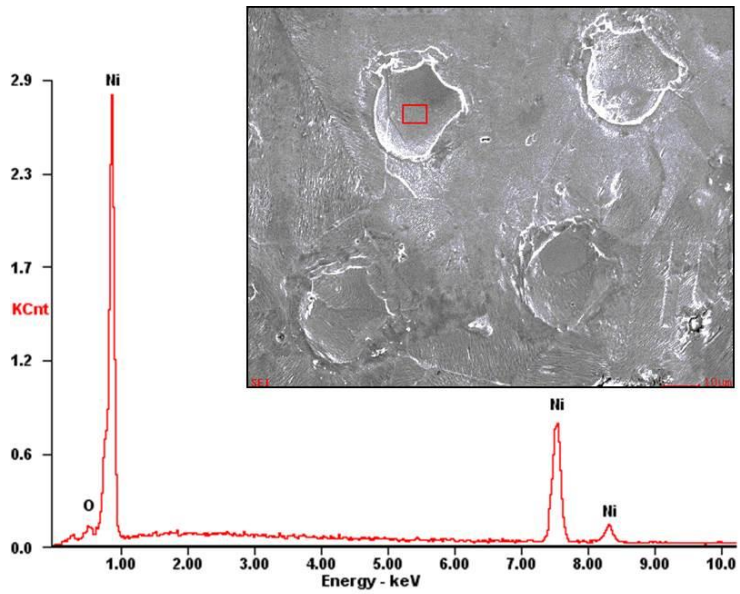

Figure 4-19 EDS analysis of sample D30L60 before the corrosion test inside the hole

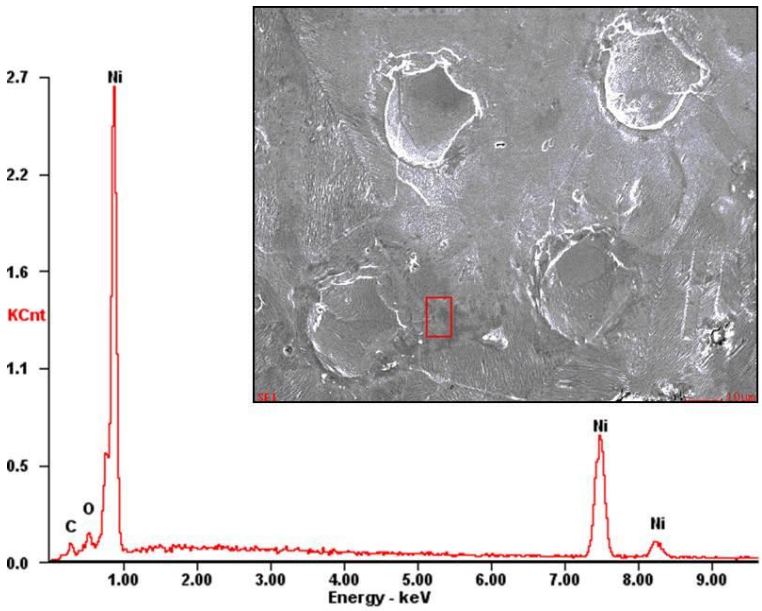

Figure 4-20 EDS analysis of sample D30L60 before the corrosion test outside the hole.

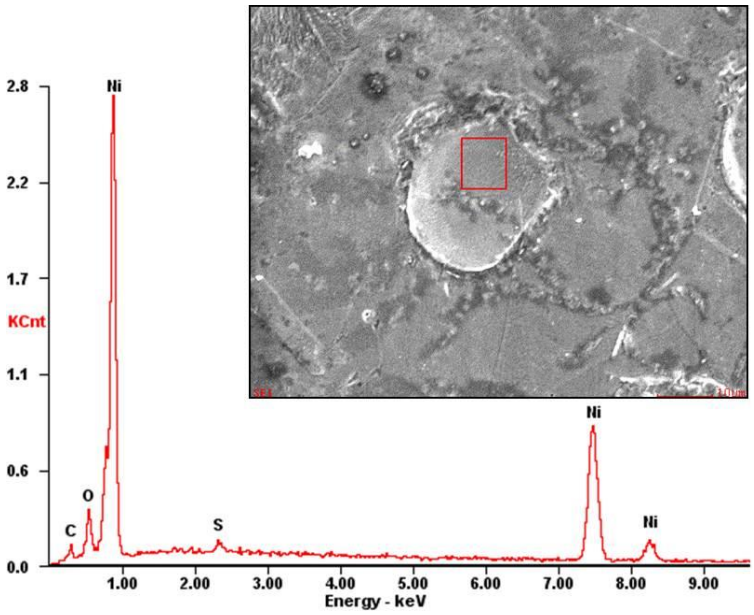

Figure 4-21 EDS analysis of sample D30L60 after the corrosion test inside the hole.

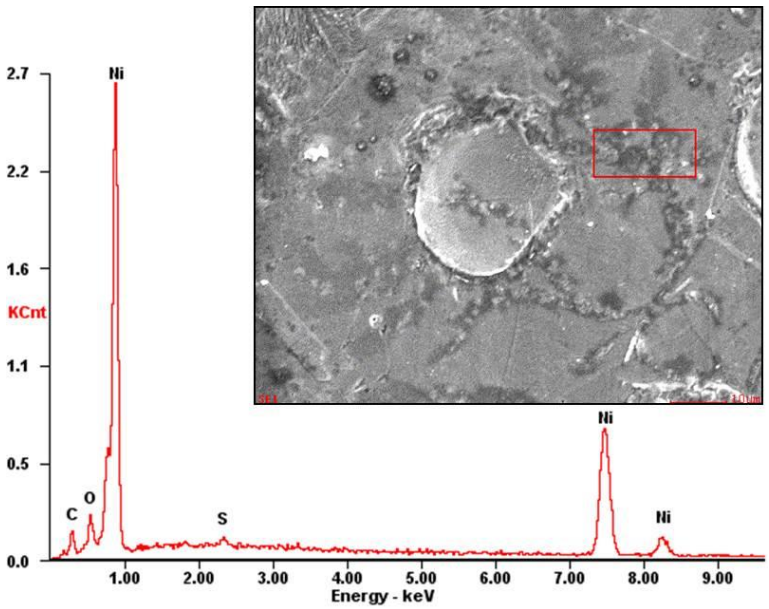

Figure 4-22 EDS analysis of sample D30L60 after the corrosion test outside the hole.

Therefore, an explanation for the low corrosion rate in samples with the pattern density of (D/L) with hole diameter of D≥20μm is that the contact area between the nickel surface and the electrolyte solution has decreased due to the existence of a heterogeneous interface. Therefore, one of the important parameters which is necessary for corrosion i.e. contact between the corrosive solution and the material, has been interrupted which has resulted in smaller overall mass-loss/corrosion rate from the patterned nickel surface. Consequently, it has led to a higher corrosion resistance of the samples.

According to the mechanism explained in corrosion results in this chapter, the very low value of corrosion current density in sample D30L60 is a result of formation of a more stable protective passive layer on the patterns including inside the holes. Inside the holes the existence of air pockets also has prevented

the dissolution of the formed passive layer and has decreased the contact of the corrosive solution and the bottom of the holes. EDS results also showed a significant increase in oxygen content at the bottom of the holes compared to outside area. More oxygen in the holes means that a more stable passive layer is present at the bottom of the holes; and that a heterogeneous wetting process, which is a result of the existence of air pockets inside the holes, has protected the bottom of the holes and thereby decreased the total contact area of electrolyte and the substrate. SEM and 3D images also showed no noticeable change in the appearance of the samples with lower corrosion rates. (D30L30, D30L60, D20L20 and D20L40)

Chapter 5 UNIDIRECTIONAL ROUGHNESS ON NICKEL

The results of this study have previously been reported in the following two papers:

1) Toloei, A. S., Stoilov, V., and Northwood, D. O. "The Effect of Different Surface Topographies on the Corrosion Behaviour of Nickel," WIT Transactions on Engineering Science, 77(2013) 193-204.

2) Toloei, A. S., Stoilov, V., and Northwood, D. O. "The relationship between surface roughness and corrosion" ASME International Mechanical Engineering Congress & Exposition, 2013, San Diego, California, USA.

In this chapter the results related to nickel samples with unidirectional surface roughnesses are presented.

5.1 Corrosion Testing Results

Two different corrosion testing methods including potentiodynamic polarization and electrochemical impedance spectroscopy were used and are presented in Sections 5.1.1 and 5.1.2, respectively.

5.1.1 Potentiodynamic Polarization Technique Results

A typical potentiodynamic polarization curve obtained at increasing potential for nickel immersed in 0.5 M H_2SO_4 is shown in Figure 5-1. As can be seen, there are three different regions: active, passive and transpassive. In the active region the corrosion increases. In the passive region it decreases and

reaches an approximately constant value before reaching the pitting potential. Finally, as a result of the removal of any passive layer, the metal goes into the transpassive region and the corrosion rate increases.

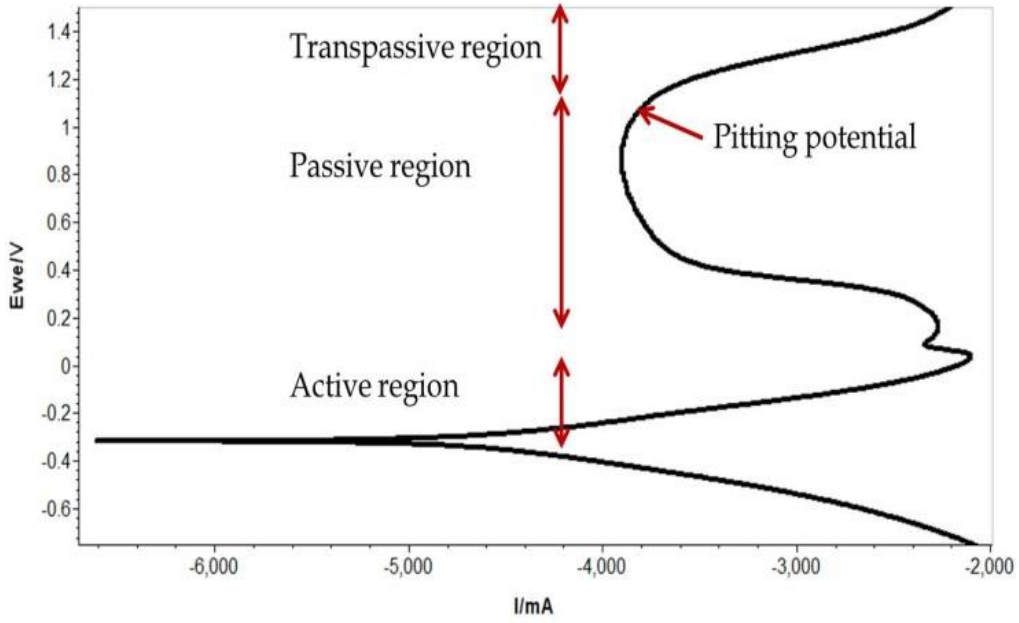

Figure 5-1: Typical polarization curves for nickel in 0.5M H_2SO_4.

Selected polarization curves of nickel samples with different surface roughness, are shown in Figure 5-2. Potentiodynamic polarization curves revealed that the roughnesses affected the corrosion processes because changing the roughness resulted in some shifts in the curves. The results showed that corrosion resistance increases with increasing the grit number of silicon carbide paper.

There was no significant difference in the cathodic branch of the polarization curves for samples with different surface roughness. This suggests that any corrosion rate changes were solely due to the anodic behaviour of the

sample. As can be seen in Figure 5-2, the potential for samples to shift from the passive region to the trans-passive region (pitting potential) increased with decreasing surface roughness from sample G60 to G1200 which is an indication of a higher pitting resistance [79].

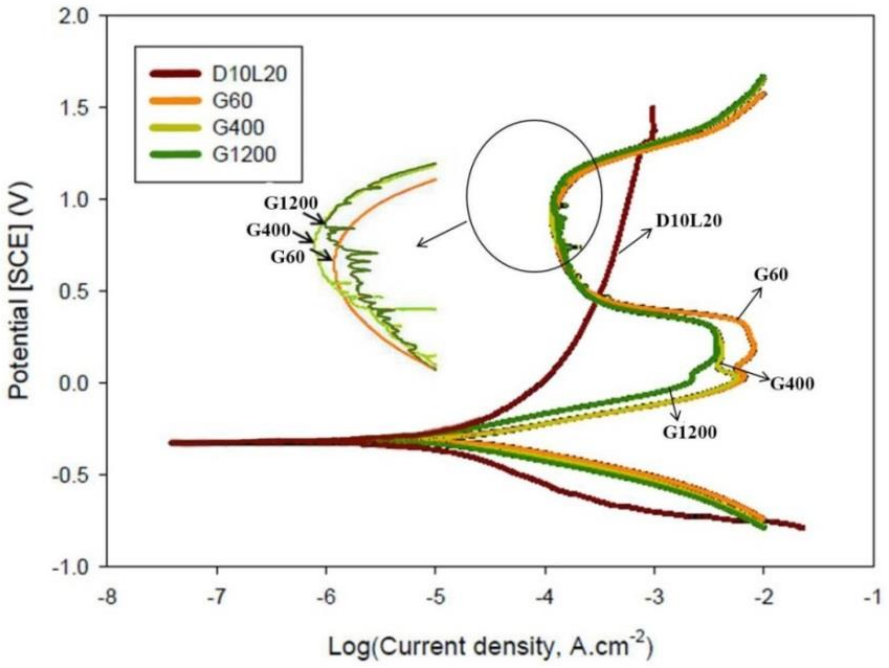

Figure 5-2: Polarization curves for samples G60, G400, G1200 and D10L20.

Table 5-1 presents the electrochemical corrosion parameters i.e. corrosion potential (E_{corr}), cathodic and anodic Tafel slopes (b_a, b_c) and corrosion current density (i_{corr}) obtained from the extrapolated polarization curves. In Table 5-1, P_i, the corrosion rate, has been calculated in mils per year (mpy) from i_{corr} using equation (5-1):

$$P_i = K\,(i_{corr})\,EW/\,\rho \qquad (5\text{-}1)$$

where K = constant for converting units, i_{corr} = corrosion current density (microamp/cm^2), ρ = alloy density (gram/cm^3), and EW = alloy equivalent weight (gram/equivalent).

The results of two patterned samples have been included in order to study the effect of patterning and unidirectional roughnesses in nickel. Obviously, patterning has improved the corrosion resistance especially for samples D20L20, D20L40 and D30L60, as discussed in Chapter 4.

Table 5-1: Corrosion parameters obtained from dynamic polarization measurements for nickel.

Sample	E_{corr} (mV)	β_a (mV)	β_c (mV)	i_{corr} (μA.cm^{-2})	R_p (Ω/cm^2)	P_i (mil $year^{-1}$)
G60	-319	104.7	114.6	21.93	1086	9.53
G120	-321.8	109.5	118.3	21.64	1144	9.40
G180	-325.5	111.2	113.8	19.22	1275	8.35
G240	-310.5	110.0	116.8	19.27	1275	8.37
G320	-300.8	100.0	112.1	18.32	1255	7.96
G400	-313.9	112.1	113.3	17.26	1419	7.50
G600	-312.6	123.8	111.1	14.67	1735	6.37
G800	-272.9	82.3	107.9	12.60	1614	5.48
G1200	-272.7	120.3	105.3	8.43	2899	3.66
D10L20	-327.4	153.4	128.5	6.01	5046	2.61
D20L20	-303.3	132.6	173.3	1.16	28070	0.50

Figures 5-3 to 5-6 illustrates the change in different corrosion parameters of nickel including corrosion current density (I_{corr}), corrosion potential (E_{corr}), corrosion rate (CR) and polarization resistance (R_p) versus surface finish. Two

patterned samples of nickel also have been compared with the unidirectional surfaces. As it can be seen, the corrosion current density and corrosion rate decrease with decreasing roughness (Figures 5-3 and 5-4). Patterned samples showed the best corrosion resistance. As it is seen, the rougher samples (G60 and G120) have the highest corrosion current density and corrosion rate and by decreasing roughness toward sample G180, a considerable decrease is observed in both parameters. From sample G240, the corrosion current density and corrosion rate decrease slowly and then for the smoothest sample, G1200, a significant drop is seen in these parameters. Patterned samples, specially the one with D=20, showed the lowest corrosion current density and corrosion rate compared to all samples with unidirectional roughnesses.

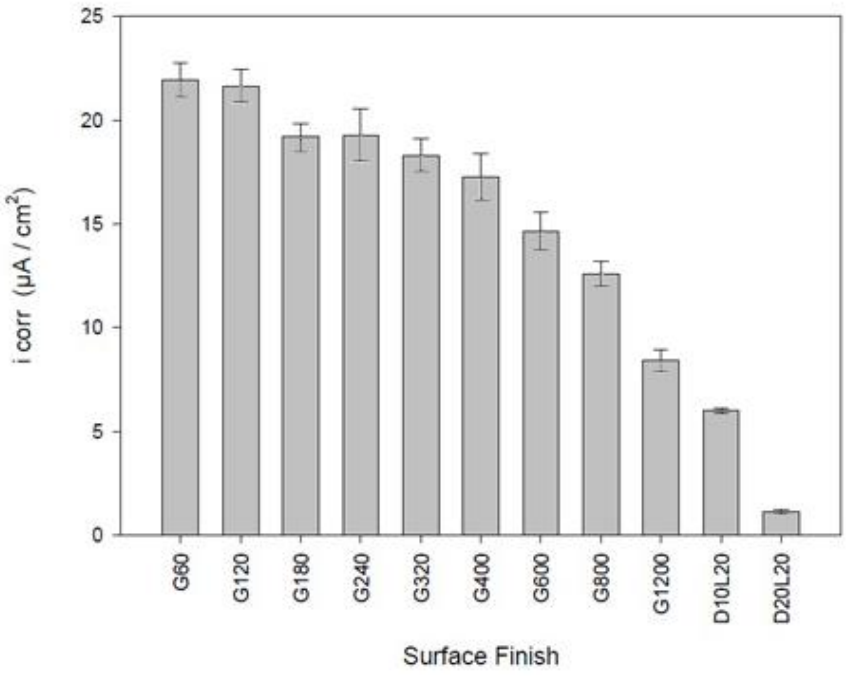

Figure 5-3 Dependence of i_{corr} on surface finish of nickel

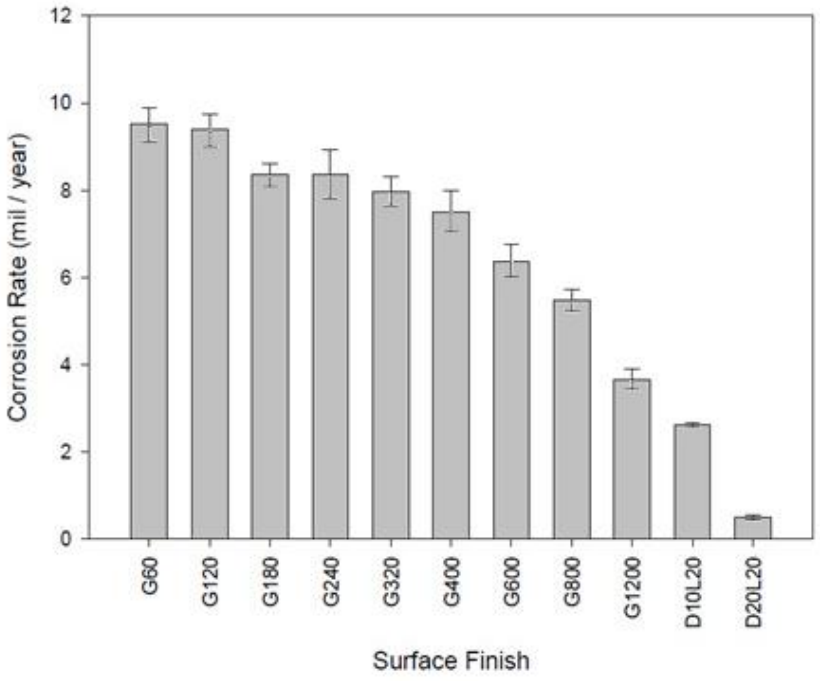

Figure 5-4 Dependence of CR on surface finish of nickel

All samples with unidirectional roughnesses had almost the same corrosion potential, E_{Corr}, values except for G800 and G1200, the smoothest samples, where E_{Corr} was less negative, i.e. more noble. As also can be seen in Figure 5-5, the patterned samples had similar E_{Corr} as the unidirectional roughness samples for G60 to G600.

Polarization resistance values had a reverse trend compared to corrosion current density and corrosion rate values, as would be expected (Figure 5-6). By decreasing the roughness, the polarization resistance increased, which means more corrosion on the rougher surfaces. Patterned samples had the highest polarization resistance values.

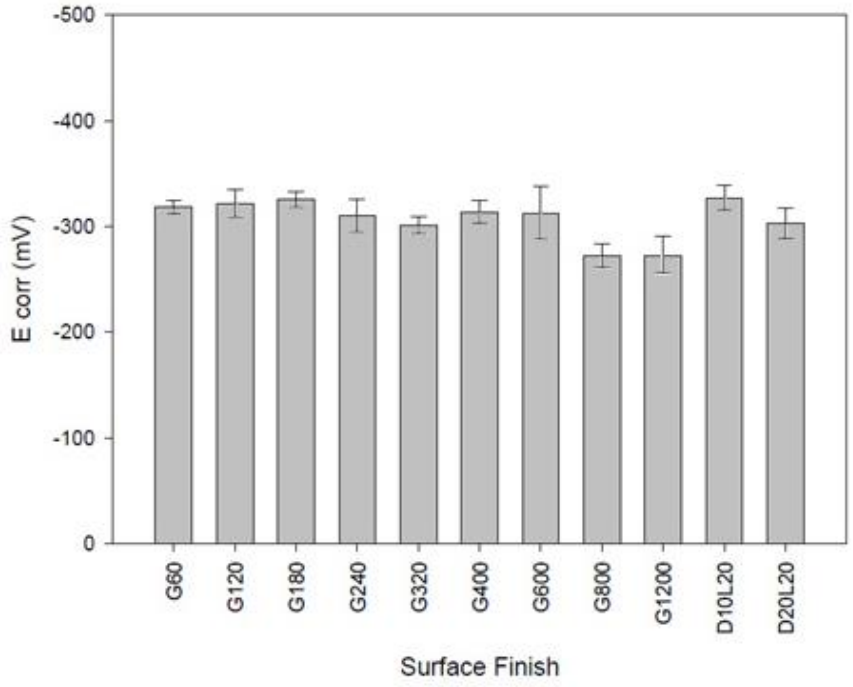

Figure 5-5 E_{corr} vs surface finish on nickel (including patterned samples)

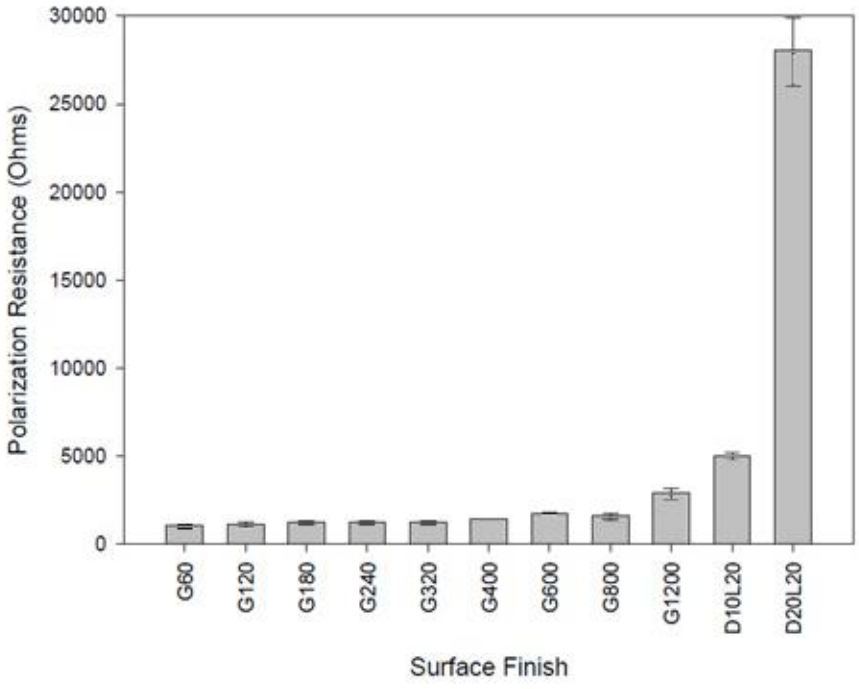

Figure 5-6 Dependence of R_p on surface finish of nickel

5.1.2 **EIS Results**

EIS measurements can provide additional electrochemical information about the kinetics of Ni corrosion in H_2SO_4 solutions with different surface roughnesses.

For the electrochemical impedance spectroscopy measurements, the impedance was measured at frequencies between 10^{-2} and 10^{4} Hz in order to ensure a complete characterization of the electrode/electrolyte interface and corresponding processes. All the Nyquist plots were analyzed by fitting the experimental data to an equivalent circuit model. The model chosen for the fitting was a commonly used model for nickel in sulphuric acid [168], Figure 5-7. In this circuit, R_s represents the solution resistance; R_{ct} is the charge transfer resistance and CPE is constant phase element related to the double-layer capacitance. The impedance, Z, of CPE is calculated from equation (5-2):

$$Z_{CPE} = [\, Q\, (j\omega)]^{-n} \qquad (5\text{-}2)$$

Depending on the value of n, CPE can represent resistance (n = 0, Q = 1/R), capacitance (n = 1, Q = C), inductance (n = -1, Q = 1/L) or Warburg impedance (n = 0.5, Q = W) [45].

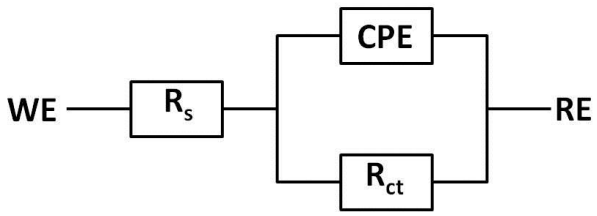

Figure 5-7: Equivalent circuit model.

Two values, Q and n, define the CPE. Q is the CPE constant, which is a combination of properties related to the surface and electro-active species, $j^2 = -1$ the imaginary number, ω the angular frequency and n is a CPE exponent which can be used as a measure of the heterogeneity or roughness of the surface.

Therefore, a constant phase element (CPE), which is an empirical impedance function that has proved of considerable value in data fitting instead of a capacitive element, is used to account for the physical adsorption and formation of barrier film on the metal surface and to give a more accurate fit on experimental data as the resulting capacitive loop is depressed semicircle rather the one with the same scale on the X-axis and Y-axis (Figure 5-7) [169]. It is known that the depression in the semicircles, which is referred to as frequency dispersion, is usually attributed to roughness and inhomogeneities of the solid surface in acidic systems [170]. The CPE sums up the impedance response of the distributed process in a single expression. CPE reflects the distributed surface reactivity, surface roughness, electrode porosity, and current and potential distributions associated with electrode geometry [170].

Figure 5-8 presents the Nyquist diagrams for the different surface roughnesses. The diagrams consist of a large capacitive loop at high frequency (HF). The HF capacitive loop is related to the charge transfer process in metal corrosion and the double layer behaviour at the film/solution interface. The semicircle diameter increases with decreasing roughness, indicating that the corrosion is mainly a charge transfer process [171] which results in a higher R_{ct}

value. The patterned sample (D10L20) has the largest capacitive loop reflecting the highest R_{ct} value and consequently more corrosion resistance.

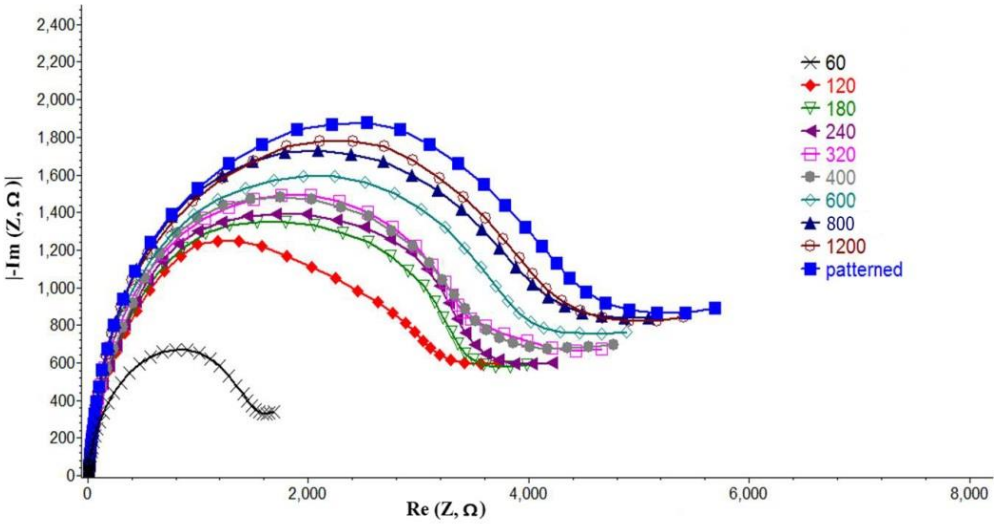

Figure 5-8: Nyquist diagrams for nickel with different roughnesses.

An increase in R_{ct} value has been ascribed to a decrease in the dielectric constant and/or an increase in the double electric layer thickness [172]. It is considered that surface pre-treatment and surface roughness are the most important parameters determining the impedance characteristics of a metal [173]. It is also considered that the formation of a continuous protective film would be higher on a smooth surface than on an irregular surface [81]. Hence, the sample with relatively high surface roughness showed the least evidence of a stable passive layer and indicated more susceptibility to corrosion. A smooth surface exhibits a higher passivation tendency and pitting resistance than the high surface roughness alloy.

Patterned sample D10L20 has the largest capacitive loop. As discussed in Chapter 4, there is a different protection mechanism, namely heterogeneous wetting, operative in this case.

Figure 5-9 shows the examples of Bode and Bode phase plots for one of the samples, G60. The Bode phase plot, Figure 5-9b, shows only one phase maximum at intermediate frequencies. This result indicates that the corrosion process occurs via a one-step process corresponding to one time constant. The maximum phase angle θ_{max} also is less than 80° which is generally considered to be a result of the roughness of the electrode surface [43].

All data were curve-fitted and analyzed using an EIS spectrum analyzer. A combination of randomize followed by the most widely used optimization algorithm, Levenberg-Marquardt fitting, was used to fit the results [174]. A good fit was observed between the experimental data and the simulated values as it can be seen in Figure 5-9 for the Bode plots. The accuracy of the selected equivalent circuit can be observed by comparing the fitted line with experimental results. It is said that by increasing the roughness of the electrode surface the value of θ_{max} is reduced [43]. The same result was observed in our research. In the case of nickel and smoother surfaces, they showed a higher value for θ_{max}. The θ_{max} values started from 68 for sample G60 and increased to 75 for sample 1200 (Table 5-2).

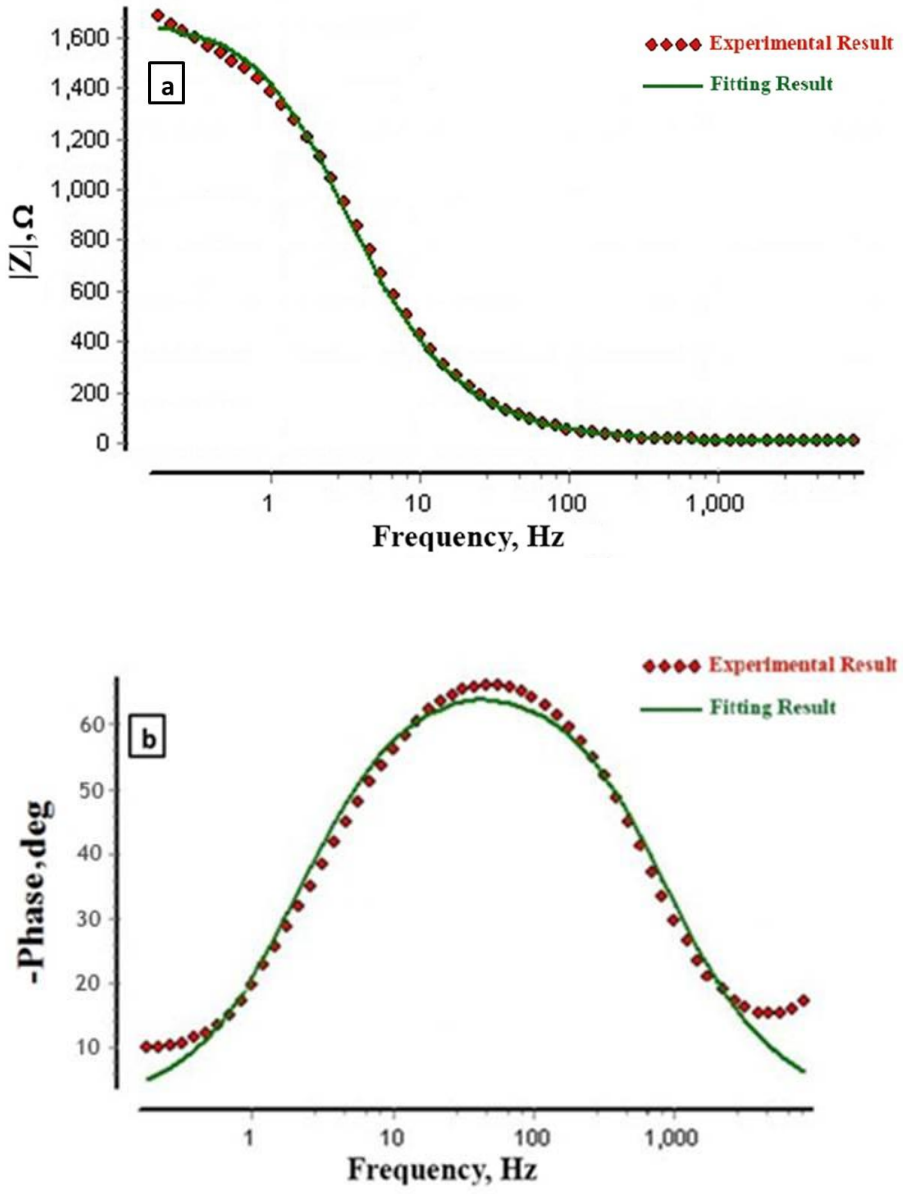

Figure 5-9: (a) Bode magnitude and (b) Bode phase plots for fitted and experimental results for sample G60 of nickel.

The values of the equivalent circuit elements for the corrosion of nickel for various surface roughnesses are summarized in Table 5-2. The different values obtained for the n and CPE exponent can be related to the roughness of the

surface of nickel [40]. The rougher the samples, the lower the n value and the higher the CPE values. Generally, unchanged n values for samples G180 to G1200 suggest the formation of the same passive layer on the surface.

Table 5-2: Equivalent circuit elements for nickel with various surface roughnesses.

Sample	R_s ($\Omega.cm^2$)	R_{ct} ($\Omega.cm^2$)	θ_{max} (deg)	CPE ($\Omega^{-1}cm^{-2}S^n$)	n
G60	7.99	1664.2	68	5.58×10^{-5}	0.898
G120	8.46	3220.5	70	4.73×10^{-5}	0.916
G180	9.21	3514.7	71	3.76×10^{-5}	0.922
G240	9.01	3655.7	71	4.51×10^{-5}	0.921
G320	8.56	3764	70	4.51×10^{-5}	0.920
G400	8.84	3838.4	70	4.56×10^{-5}	0.920
G600	8.32	4114.9	71	4.03×10^{-5}	0.922
G800	8.68	4463.1	73	4.57×10^{-5}	0.921
G1200	8.56	4498.7	75	4.73×10^{-5}	0.923
D10L20	8.98	4733.5	70	4.52×10^{-5}	0.922

According to Table 5-2, the values of R_{ct} and (n) increased generally from sample G60 to G1200. R_{ct} is a measure of electron transfer across the surface, and inversely proportional to the corrosion rate [44]. The decrease in the CPE value or increase in n value can be attributed to the formation of passive layer at the metal surface [44].

The change in CPE and n values vs roughness is presented in Figure 5-10 and 5-11. As it can be seen, by increasing the roughness, n decreased and

CPE increased. The observed trend in decreasing n by increasing roughness, is the same as trend for R_{ct} and proportional to corrosion rate.

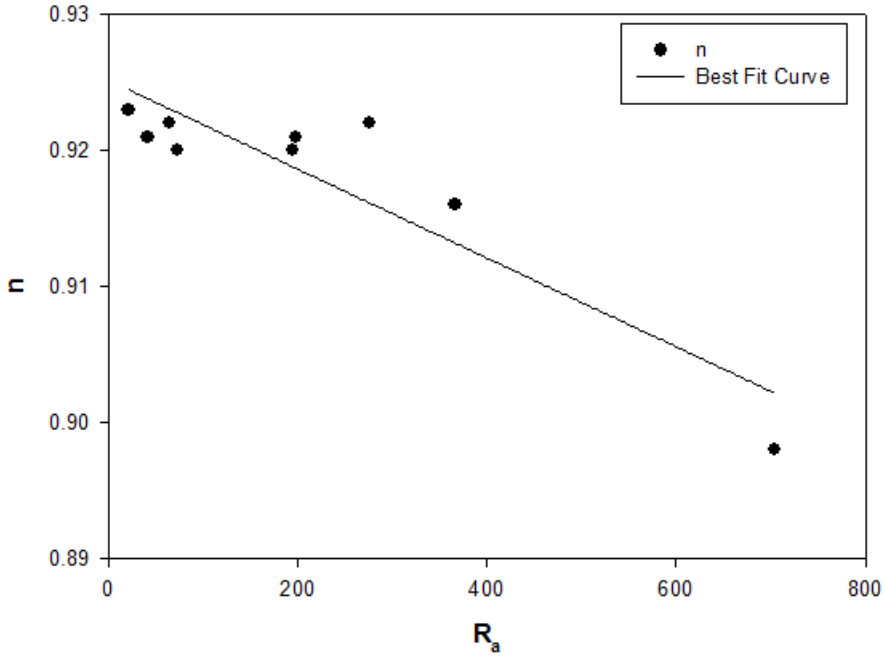

Figure 5-10: Change in n with surface roughness of nickel

However, CPE showed a reverse trend compared to n and samples with higher corrosion rates (rougher samples) showed higher CPE value. As mentioned before, CPE is used instead of a capacitor in the case of nickel in sulphuric acid solution to get a better fitting in simulations. CPE reflects the distributed surface reactivity and as seen in Table 5-2, sample G60 shows the highest value which means more surface reactivity and consequently more corrosion for this sample.

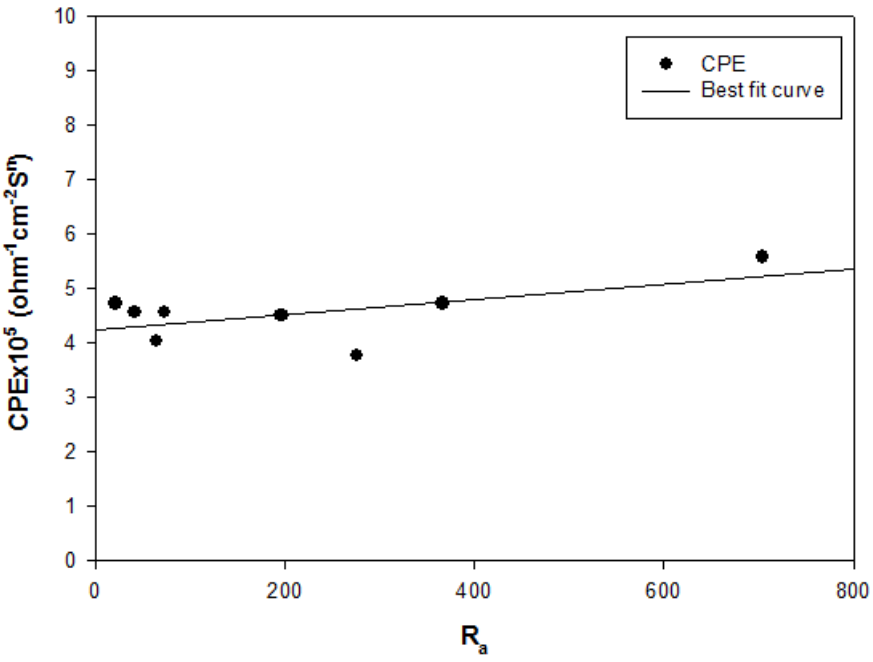

Figure 5-11: Change in CPE with surface roughness of nickel

Therefore, EIS results are in agreement with potentiodynamic polarization technique results and other studies which investigated the effect of roughness on corrosion properties of metals with ability to form a passive layer [71, 78-80]. In both corrosion measurement techniques in this research, surfaces with higher roughness showed more corrosion because these surfaces provide more area of contact with corrosive solution. Other studies have also shown an earlier formation of passive layer on smoother surfaces [79].

5.2 SEM Images

SEM was used to characterize the surface of nickel samples with different unidirectional roughness both before and after corrosion testing.

5.2.1 **Before corrosion:**

Figures 5-12 (a-i) present SEM micrographs of the unidirectional roughness samples of nickel (G1200 to G60) before corrosion testing. As seen, the grooves are very thin in sample G1200 and on increasing the roughness towards sample G60, the grooves become more evident. Figure 5-12(a) shows sample G1200. In this sample, the grooves are very fine. By increasing the roughness toward samples G800, G600 and G400 in Figure 5-12(b-d), the unidirectional roughnesses (grooves) become wider and deeper.

Figures 5-12 (e-h) illustrate SEM micrographs for samples G320 to G120 as samples with surfaces contained medium to high roughness. By increasing the roughness from sample G320 to sample G120, the grooves become wider and deeper compared to previous samples. In some cases, especially in samples G180 and G120, there are some deeper grooves or scratches which are formed during the grinding process.

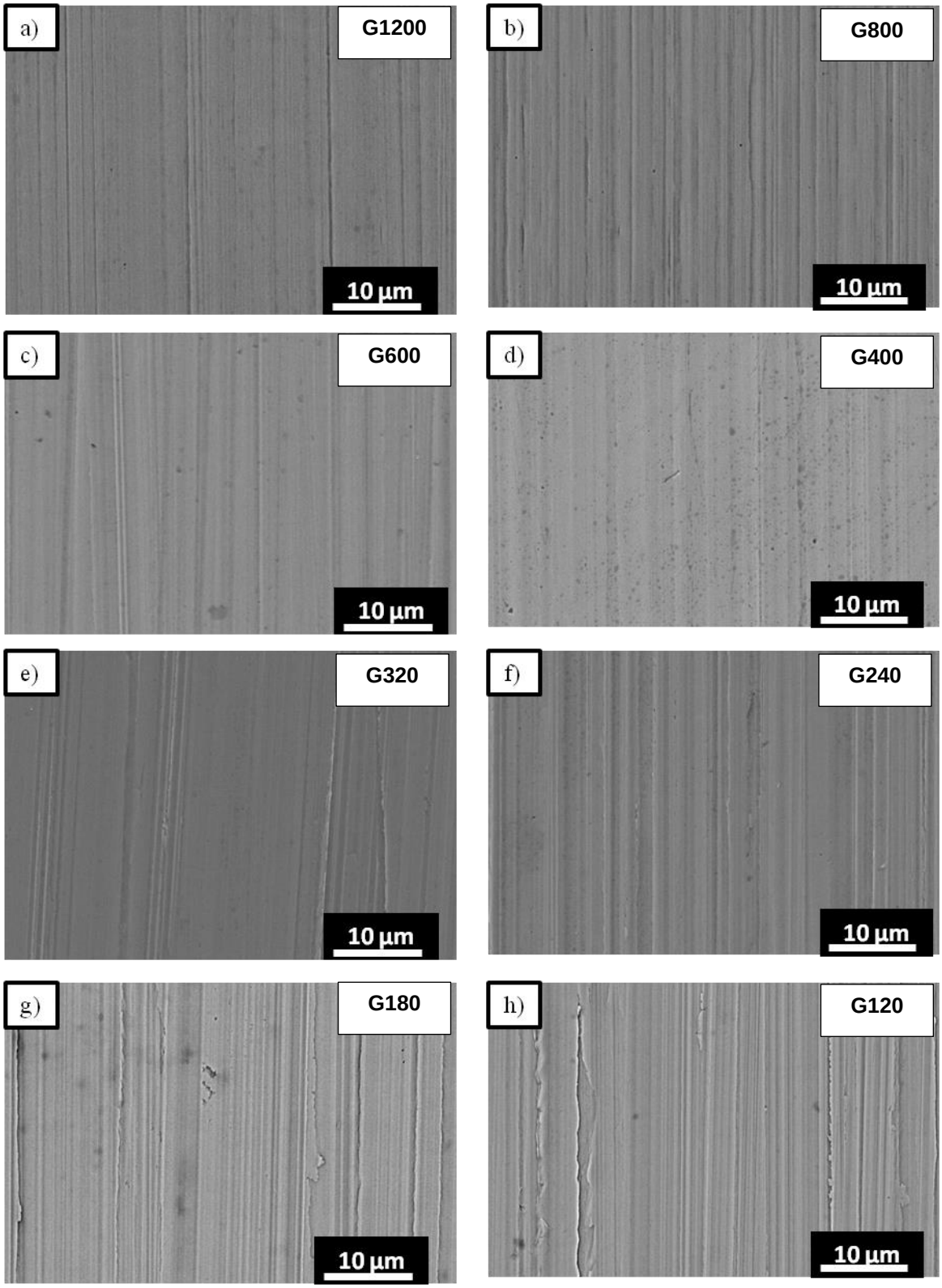

Figure 5-12 SEM micrographs of nickel samples with unidirectional roughnesses a)G1200, b)G800, c)G600, d)G400, e)G320, f)G240, g)G180 and h)G120 before corrosion

Figure 5-12 (i) shows the SEM micrograph for sample G60 as the roughest sample of this study. As seen, the grooves are not as uniform as previous samples. Additionally, the removal of the metal with the roughest SiC paper for sample G60 during the grinding process also has led to some damage or deeper grooves on the surface.

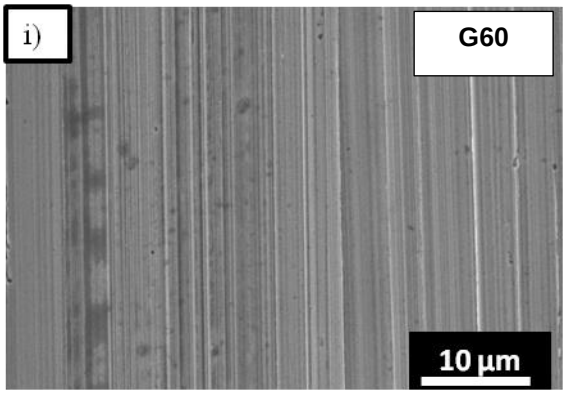

Figure 5-12 (cont) SEM micrograph of nickel sample with unidirectional roughness i)G60 before corrosion

5.2.2 **After corrosion:**

Figures 5-13 (a-i) illustrate the SEM micrographs of the surface of nickel samples after corrosion testing. In Figures 5-13 (a-d) SEM micrographs for sample G1200, G800, G600 and G400 show a completely different structure compared to unidirectional roughness on the surface, which is the passive film that forms quickly on the smoother surfaces. As can be seen, the whole surface, including inside the grooves and the peaks, is covered with the protective layer. For the G800 sample, the grooves were fine before corrosion, and are much less obvious after corrosion compared to samples G600 and G400. However, there is evidence of heavy corrosion along what is presumed to be one of the deeper grooves formed during the initial unidirectional grinding.

By increasing the roughness to samples G320, G240, G180 and G120 (Figures 5-13 (e-h)), the grooves appear to have both the passive layer and corrosion products, and the corrosion seems to be more concentrated along the grooves, especially for samples G180 and G120.

Figure 5-13 (i) is the SEM micrograph for sample G60, the roughest sample in the experiments. As it is seen, some grooves are still visible after corrosion and a severe corrosion is observed specially along the grooves. Corrosion is also observed at the bottom of the grooves and on the peaks (indicated by arrows).

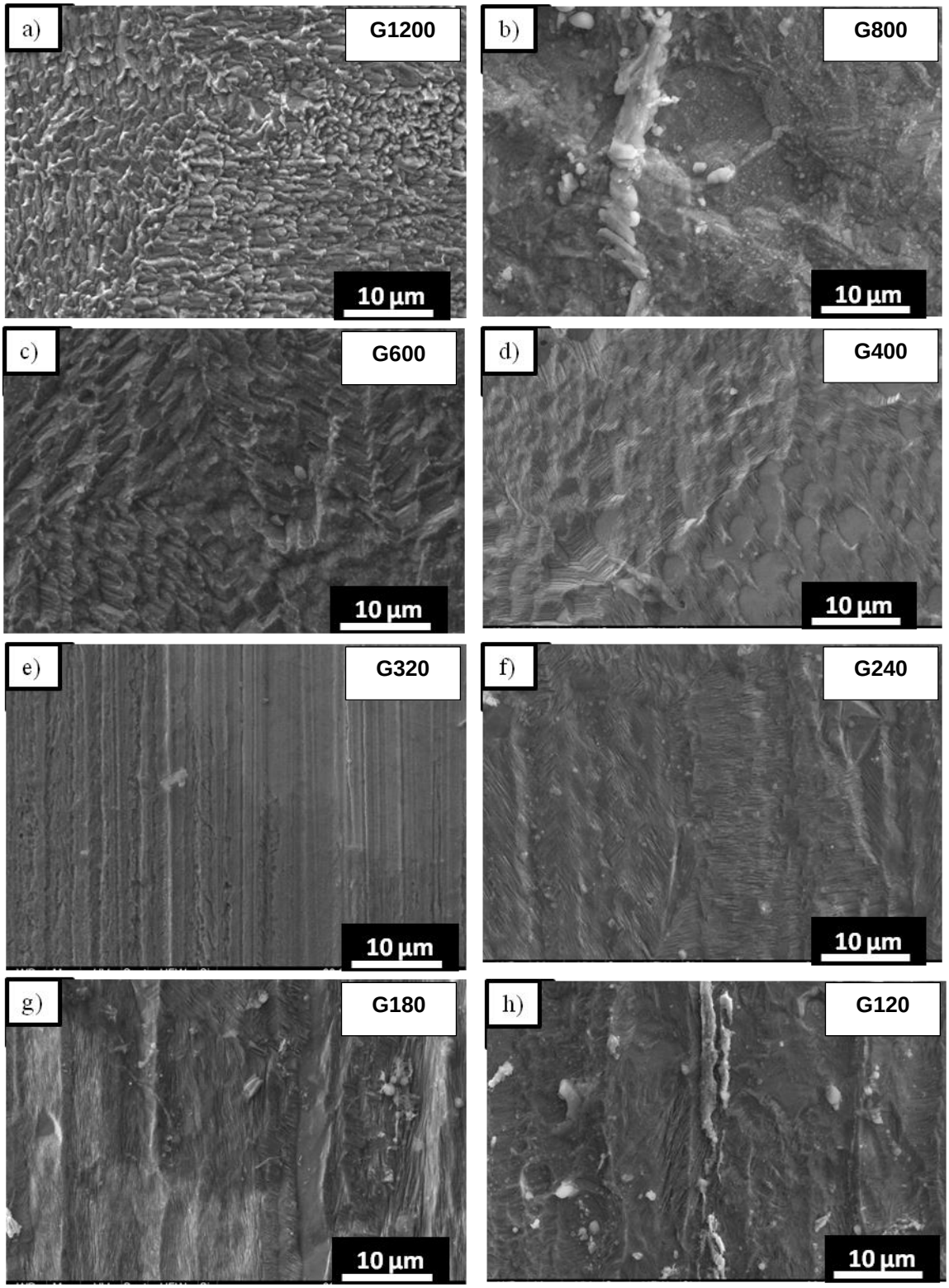

Figure 5-13 SEM micrographs of nickel samples with unidirectional roughness a)G1200, b)G800, c)G600, d)G400, e)G320, f)G240, g)G180 and h)G120 after corrosion

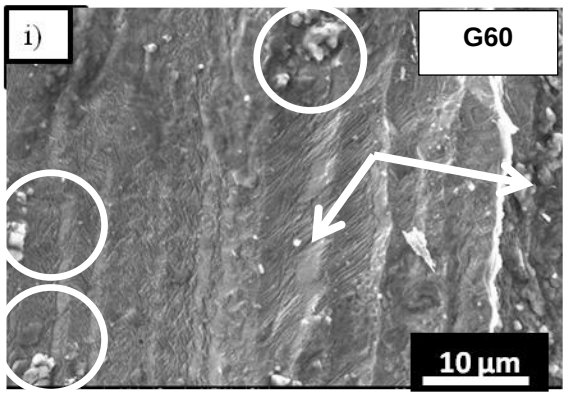

Figure 5-13 (Cont) SEM micrograph of nickel sample with unidirectional roughness i)G60 after corrosion

Another interesting point is that some corrosion products can also be seen on the rougher surfaces including G180, G120 and G60 (inside the circles) indicating more corrosion on rougher surfaces of nickel.

In general, on smoother samples (G1200 to G400), the earlier formation of passive layer has decreased the corrosion, but on rougher surfaces (G320 to G60) deeper grooves and more contact surface has led to more corrosion in the samples. By considering all evidence, including corrosion measurements and SEM images, it seems that the corrosive solution has reached the whole surface and has completely changed the appearance of rougher samples.

5.3 Roughness Measurement Results

Surface characterization was performed and different roughness parameters including R_a, R_q, R_z and R_t both before and after corrosion testing were measured using a profilometry method.

Tables 5-3 to 5-6 summarize the measured values for roughness parameters before and after corrosion testing. For all samples, the roughness has increased after corrosion. For samples with lower roughnesses, the values of roughness after corrosion are relatively lower, which suggests less corrosion products, a more stable passive layer on the surface and consequently less corrosion of metal. In Table 5-3 for R_a, sample G60 shows the maximum value for the average roughness (704 nm) before corrosion which changed to 1680 nm after corrosion; and sample G1200 with a roughness value of 21 nm is the smoothest sample and an average roughness of 147 nm after corrosion.

Table 5-3 R_a values before and after corrosion testing of nickel

Sample	Roughness values	
	R_a (Before Corrosion Testing) (nm)	R_a (After Corrosion Testing) (nm)
G60	704	1680
G120	366	1351
G180	276	802
G240	197	416
G320	194	552
G400	73	285
G600	64	408
G800	41	290
G1200	21	147
D10L20	526	778
D20L20	766	779

Table 5-4 presents the root-mean-squared roughness, R_q values before and after corrosion. Higher roughnesses are obtained compared to the average roughness both before and after corrosion and the same trend as for R_a is observed. Samples G60 and G1200, as the roughest and the smoothest surfaces, have roughnesses of 924 nm and 30 nm respectively. After corrosion, these values change to 2510 and 323 nm. In this case also all roughnesses increased after corrosion.

Table 5-4 R_q values before and after corrosion testing of nickel

Sample	Roughness values	
	R_q (Before Corrosion Testing) (nm)	R_q (After Corrosion Testing) (nm)
G60	924	2510
G120	467	1707
G180	354	1031
G240	264	611
G320	246	959
G400	94	389
G600	87	1031
G800	52	434
G1200	30	323
D10L20	819	1024
D20L20	1024	1036

Tables 5-5 and 5-6 present the R_z and R_t values before and after corrosion. The values are very similar and all have increased after corrosion. Patterned samples again have high initial roughnesses and samples with larger D value showed less increase in roughness.

Table 5-5 R_z values before and after corrosion testing of nickel

Sample	Roughness values	
	R_z (Before Corrosion Testing) (µm)	R_z (After Corrosion Testing) (µm)
G60	6.73	41.99
G120	4.44	20.93
G180	3.05	11.80
G240	2.84	14.40
G320	3.07	22.80
G400	1.05	9.18
G600	1.42	30.96
G800	0.93	18.04
G1200	1.06	6.22
D10L20	5.33	7.23
D20L20	7.14	7.22

Table 5-6 R_t values before and after corrosion testing of nickel

Sample	Roughness values	
	R_t (Before Corrosion Testing) (µm)	R_t (After Corrosion Testing) (µm)
G60	7.84	50.30
G120	4.81	27.96
G180	3.68	28.93
G240	3.33	19.13
G320	3.60	25.51
G400	1.40	21.48
G600	1.83	38.36
G800	1.54	24.96
G1200	3.37	6.62
D10L20	5.56	8.62
D20L20	8.52	8.60

By considering all the roughness parameters, it is seen that all the roughnesses have increased after corrosion, especially for initially smoother samples. Thus, the protective layer and also the corrosion products have formed on the whole surface, including inside the grooves and on peaks. In the case of

rougher surfaces, according to the SEM images and also the study of Suter et al, [79], corrosion is more concentrated along the grooves which will cause an increase in depth of the grooves and increasing the roughness parameters. In the case of smoother samples that have a faster formation of passive layer, however, the passive layer increased the roughness parameters compared to before corrosion but the measured values are smaller than rougher surfaces.

Patterned samples have high roughnesses which are the result of creating holes and the splashes in the laser ablation process. The roughness also increased for these samples but smaller increase was observed for samples with larger diameter.

5.4 Roughness profiles before and after corrosion

In this section different roughness profiles including 2D images, 3D textures, X and Y profiles and histogram data obtained from the profilometry analysis before and after corrosion testing are presented. Changes observed for samples with different roughnesses are discussed. For the sake of brevity, the images of profilometry analysis for one of the roughest samples (G120) and one of the smoothest samples (G1200) are presented and the general trend for all samples is explained. Images related to other samples are provided in Appendix A_1-A_3.

Figure 5-14 to 5-17 display 2D images and 3D textures for sample G120 before and after corrosion. Wide and deep grooves are present and all grooves appear similar width and depth before corrosion. By decreasing the roughness from sample G60 to G1200, finer grooves are observed in 2D and 3D images. For smoother samples, 2D and 3D images of the surface illustrate a more uniform unidirectional roughness structure without any scratches or deeper grooves with significantly different depth.

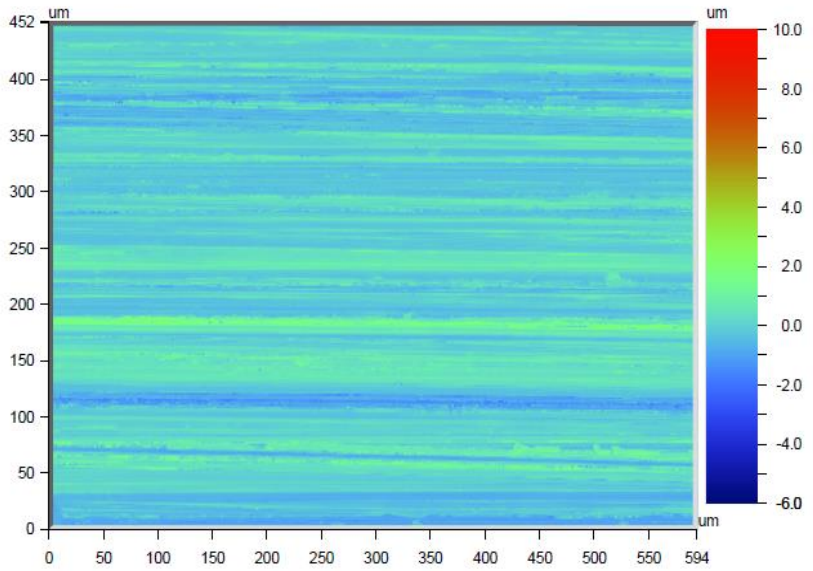

Figure 5-14 Sample G120 2D roughness before corrosion

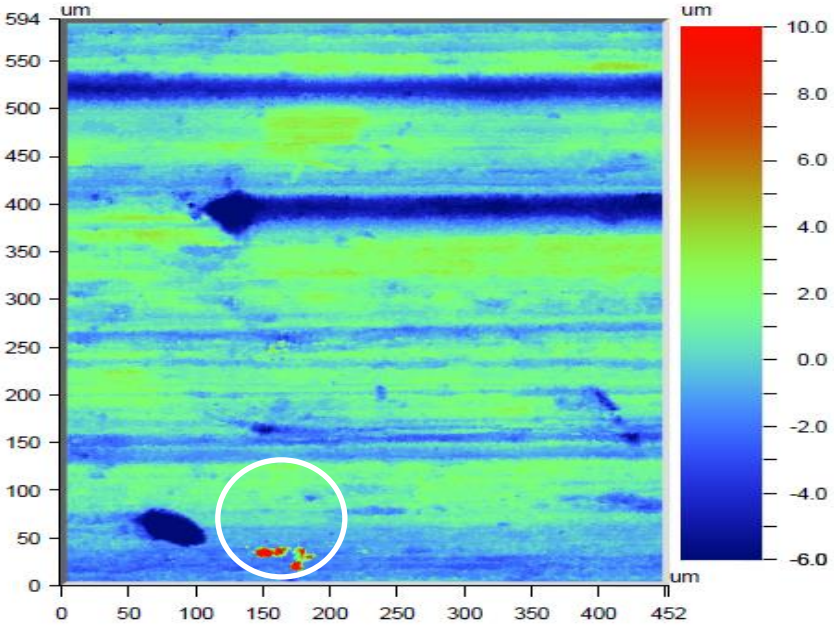

Figure 5-15 Sample G120 2D roughness after corrosion

As it is seen in sample G120 (in Figures 5-15 and 5-17), there are some corrosion products (inside the circle) after corrosion on the surface. There are also some grooves which are still visible after corrosion but two deeper grooves show a significant increase in their depth compared to the surface before the corrosion testing. From 2D and 3D images, less corrosion products and less corrosion along the grooves are also observed (inside the circle in Figure 5-17) on the surface of sample G120 compared to sample G60 (Appendix A_1). As it is seen in 2D and 3D images after corrosion, peaks and valleys are more pronounced on the surface and deeper grooves are formed confirmed by R_z and R_t. The whole surface, including the valleys and peaks, have increased in roughness. These observations confirm the roughness data presented in Section 5.3.

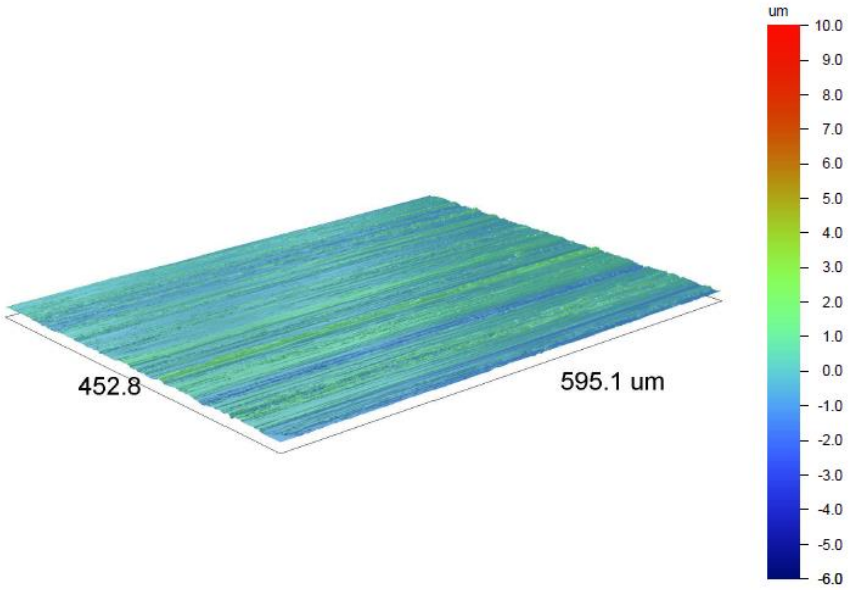

Figure 5-16 Sample G120 3D roughness before corrosion

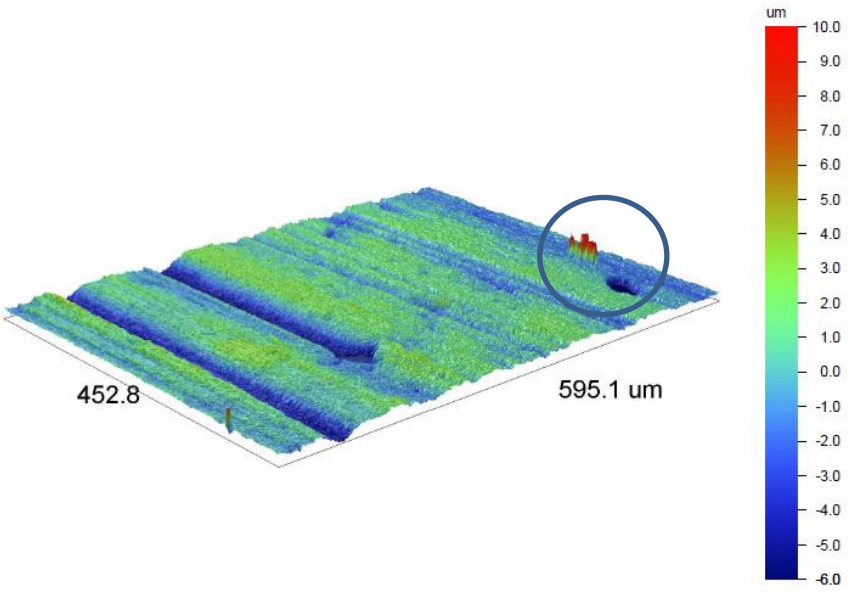

Figure 5-17 Sample G120 3D roughness after corrosion

In addition to the faster formation of passive layer on smoother surfaces of active-passive metals [79], there is another reason for more corrosion on rougher surfaces. On rougher surfaces more contact area is available for the corrosive solution with the substrate, and trapping the corrosive ions results in more severe corrosion compared to the smoother surfaces.

After corrosion, by decreasing the roughness from sample G60 to G1200, less deep grooves are seen in 2D and 3D images especially in the smoothest samples (G1200) which is an indication of a more severe corrosion on samples with higher roughnesses. R_t and R_z which give us information about the peaks and valleys from Table 5-5 and 5-6 also confirmed an increase in peak to valley difference after corrosion. By comparing smoother surfaces with sample G120, it is seen that the surface is more uniform after corrosion. It is suggested that the faster formation of passive layer both inside and outside the grooves has resulted

in less corrosion along the grooves in smoother surfaces which have smaller depth of valley compared to rougher samples (samples G120). No unidirectional roughness is observed on smoother surfaces especially samples G600 to G1200 after corrosion (Appendix A_1) and it means there is less corrosion along the fine grooves in these samples (unlike rougher samples) or easily filled grooves with passive layer. There are just a few corrosion products on the surface and the whole area of the sample has been covered with the passive layer. Corrosion results confirmed the fast formation of passive layer on smoother surfaces. It means that the protective passive layer has filled all the grooves and also covered the peaks of the unidirectional roughnesses and resulted in an increase in height of the points on the surface. Therefore, the different roughness parameters increased after corrosion (more results are presented in Section 5.3).

2D images and 3D textures for sample G1200 are presented in Figures 5-18 to 5-21, both before and after corrosion. This sample had the smoothest surface before corrosion testing and, similar to other samples, showed some increase in surface roughness after corrosion. According to the 2D and 3D images, the surface was covered with the protective layer. There are some damaged areas which are more pronounced compared to other samples. This is because the surface is very smooth and more sensitive to small defects and localized corrosion. The R_z value for this sample also showed an increase of peak to valley difference as shown in Table 5-5. This implies the formation of the passive layer inside the grooves and on the peaks. Generally, the observations

are in agreement with SEM and corrosion testing results that confirmed less corrosion on smoother samples.

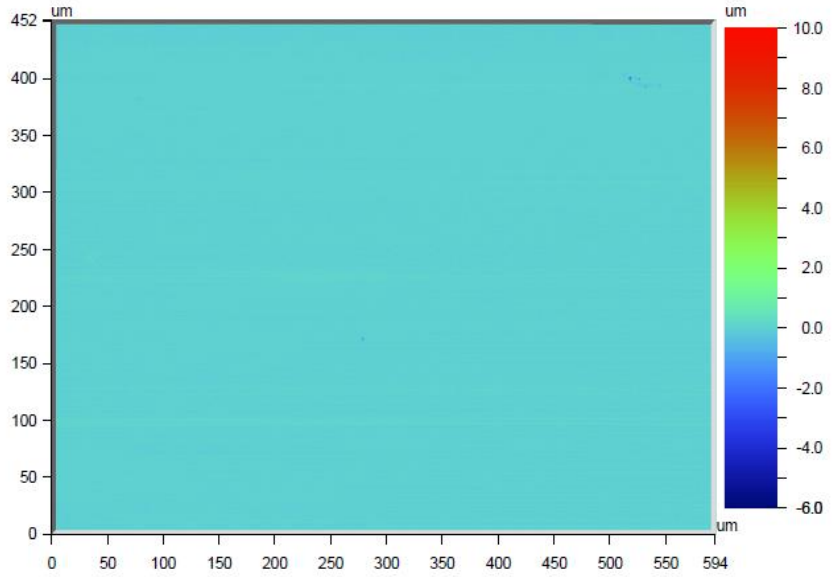

Figure 5-18 Sample G1200 2D roughness before corrosion

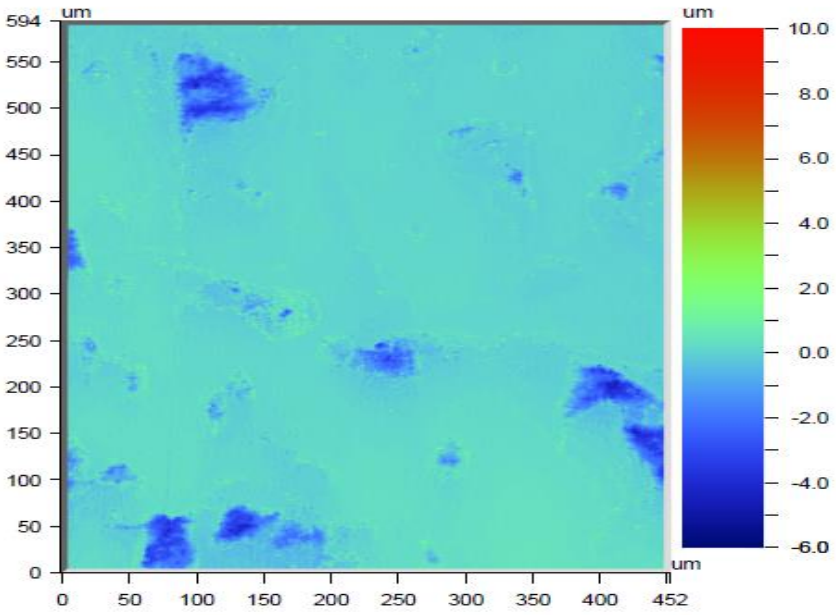

Figure 5-19 Sample G1200 2D roughness after corrosion

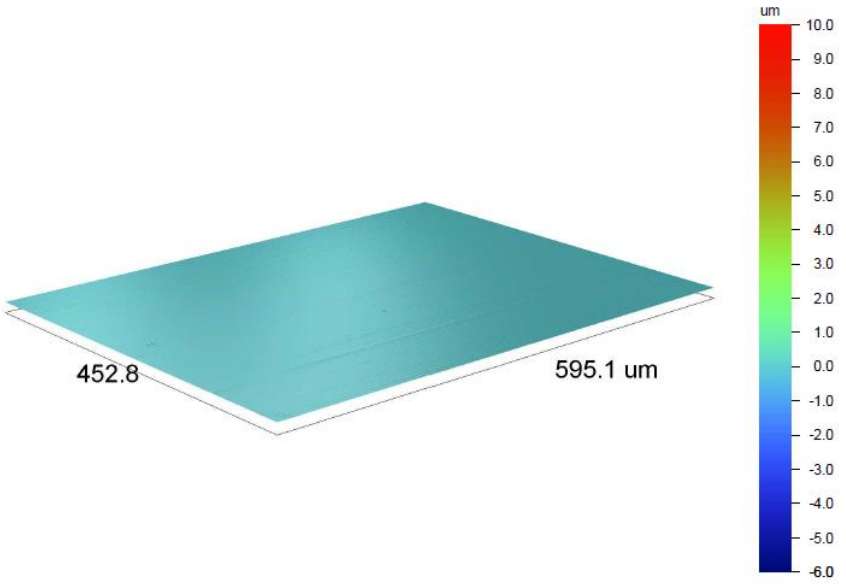

Figure 5-20 Sample G1200 3D roughness before corrosion

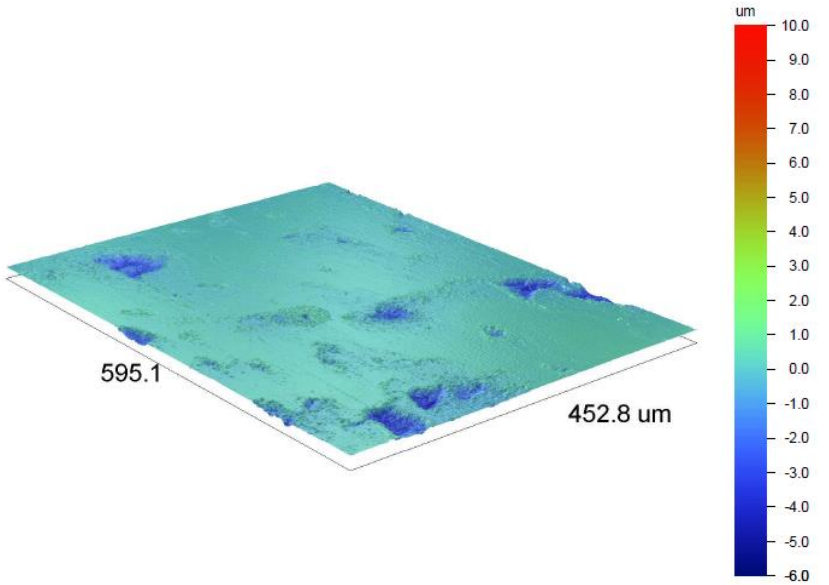

Figure 5-21 Sample G1200 3D roughness after corrosion

X and Y profiles before corrosion for sample G120 as an example of a rough surface, are presented in Figure 5-22. As can be seen, there are some changes in the height of the points, which means deep valleys and sharp peaks existed on the surface in X and Y directions. Some sharper peaks in both profiles deeper grooves created during the polishing process. X and Y profiles for other samples are presented in Appendix A_2. Generally, by decreasing the roughness from sample G60 to G1200, the number of smaller fluctuations increased and less sharp peaks than before corrosion are observed. In smoother surfaces also there are less variation in height of the points in X and Y direction compared to rougher surfaces. It is important to notice that on smooth surfaces (G600-G1200), the surface is very sensitive to small damages or deeper grooves or sharper peaks. Therefore, even a small irregularity will result in peaks or valleys in the X and Y profile.

After corrosion, however, some of the peaks have disappeared on sample G120 and there are two major valleys which are related to two deeper grooves created on the surface which were seen in 2D and 3D images. Figure 5-23 shows X and Y profiles for sample G120 after corrosion. By decreasing the roughness, X and Y profiles also show less variation of the heights of the points compared to rougher samples. Thus, the passive layer seem to cover the grooves and also peaks on the surface and have increased the roughness at the same time and prevented the formation of more deeper grooves (unlike samples G60 and G120 with deeper grooves after corrosion).

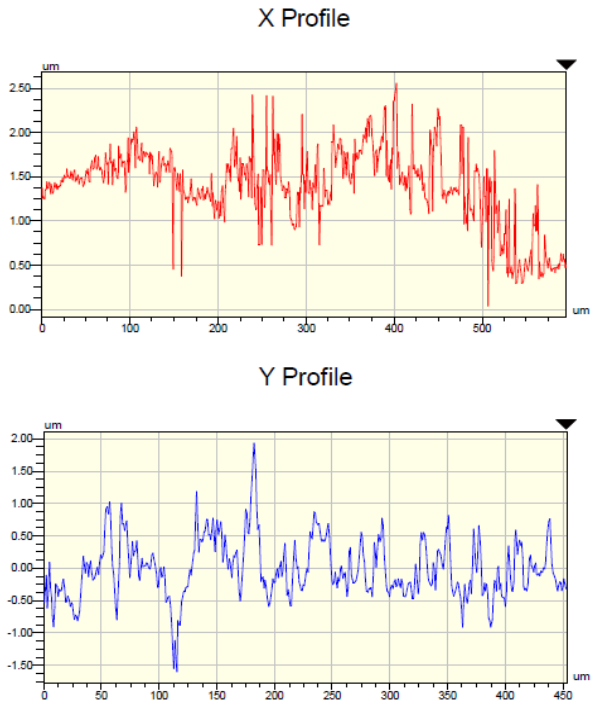

Figure 5-22 X-profile and Y-profile of sample G120 before corrosion

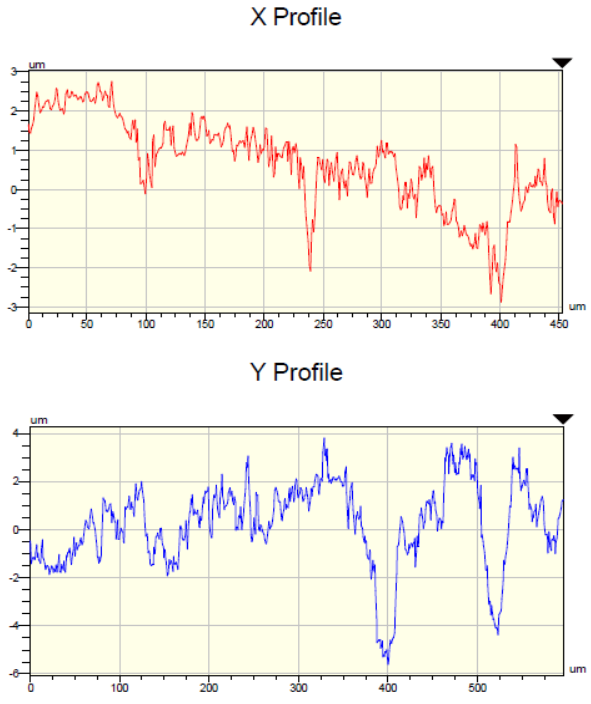

Figure 5-23 X-profile and Y-profile of sample G120 after corrosion

Figures 5-24 and 5-25 display X and Y profiles for sample G1200 as the smoothest surface before and after corrosion. As it is seen, there are so many small fluctuations which confirm the lower roughness parameters calculated for this sample in Section 5-3. The X profile displays small deviations for each point compared to adjacent points and the Y profile shows two peaks and one valley on the surface with some other grooves resulting from the grinding process. After corrosion, the X and Y profiles result show sharp peaks in all samples which are indications of points with increased depth or height on the surface. These sharp peaks are fewer in smooth samples, G600 to G1200, which can be some grooves with localized corrosion.

Fluctuations in the X and Y profiles disappeared after corrosion which will result in an almost smooth surface. The observations approve four different roughness parameters calculated in Section 5-3. The results also are in agreement with SEM observations and corrosion testing confirming the formation of a more stable protective layer on smoother surfaces. This layer covers the grooves the peaks of the unidirectional roughnesses and will result in increased roughness.

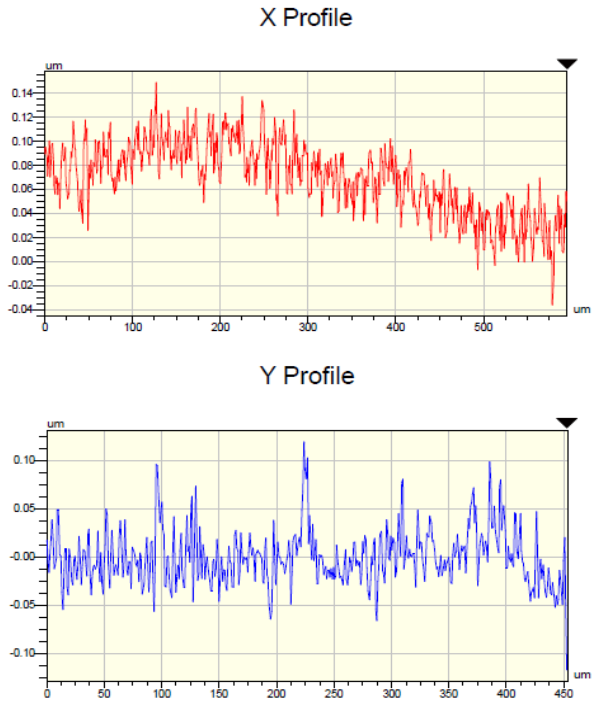

Figure 5-24 X-profile and Y-profile of sample G1200 before corrosion

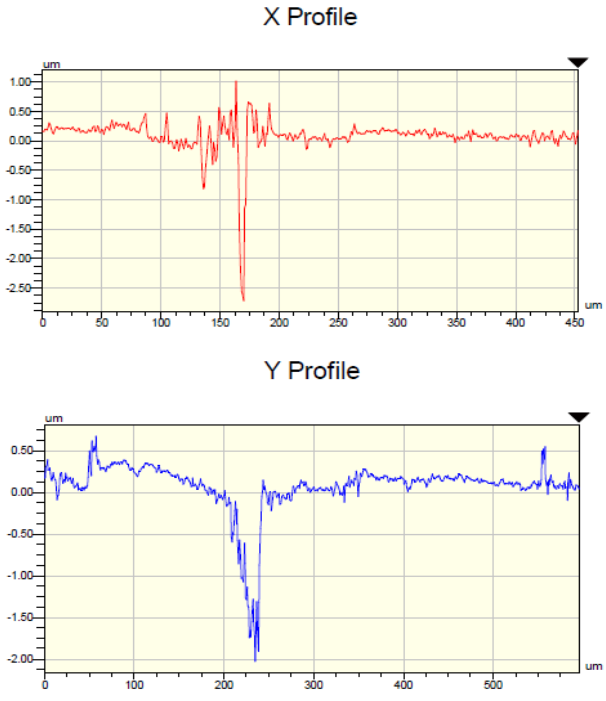

Figure 5-25 X-profile and Y-profile of sample G1200 after corrosion

As can be seen in Appendix A_3, the histogram curves go toward a uniform and normal shape with a decreased width from sample G60 to G1200 confirms the existence of fewer valleys and tops (negative and positive values around zero respectively). Therefore, the average roughness of the samples is decreasing. By decreasing the roughness also the data are around zero and there is a normal distribution of roughness on the surface which was expected for smoother surfaces. The histogram curves of rougher samples (sample G60 and G120) are a bit different from smoother samples. In these histograms it is possible to observe some irregularities that are related to scratches or deeper grooves on the surface. Figure 5-26 shows the histogram for sample G120 as one of the roughest samples before corrosion testing. Histograms for other samples are presented in Appendix A_3. As it is seen in Appendix A_3, the height of different points for sample G60 shows a completely random shape which is not around zero and symmetrical. It shows different points with variety of heights with irregularities that are the results of deeper grooves in some parts. But for sample G120 as is shown in Figure 5-26, the histogram shows a more uniform shape compared to sample G60 but still with some deviations around zero and with an unsymmetrical shape. A complete uniform distribution of roughness still cannot be seen on the surface of this sample. The width of the histogram also decreased compared to sample G60 indicating more points with lower height and depth values.

Figure 5-27 shows the histogram for sample G120 after corrosion. The histogram of this sample has been changed in comparison to before corrosion,

Figure 5-26, and the point's height distribution is larger. It means that there are more points on the surface with height difference compared to the polished surface (height of zero). As it is seen, in this sample 95% of data was reported to be between 1200 and 240 nm before corrosion. But after corrosion, 95% of data was reported to be between -1440 to 4400 nm which has increased the width of the histogram. There is a deviation on the left side of the histogram showing more points with negative height values (deep areas) which is as a result of the formation of deeper grooves on the surface. Therefore, the non-uniform shape of the histogram is due to the deeper grooves and corrosion along the grooves not the corrosion products on the surface (corrosion products can cause deviation on the right side of the histogram). Thus, there is not a significant formation of corrosion products on the surface and corrosion has concentrated more in the deep grooves. It can be concluded that corrosion in the grooves has increased the depth of the unidirectional roughnesses and consequently the surface roughness.

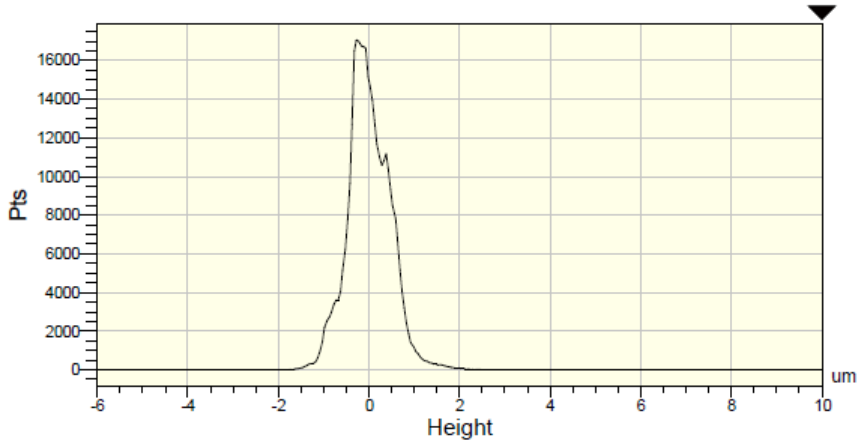

95% of data is between 1200.00 and 2640.00 nm (pv:1440.00)
90% of data is between 1320.00 and 2520.00 nm (pv:1200.00)
85% of data is between 1480.00 and 2480.00 nm (pv:1000.00)
80% of data is between 1560.00 and 2440.00 nm (pv:880.00)

Figure 5-26 Histogram curve of sample G120 before corrosion

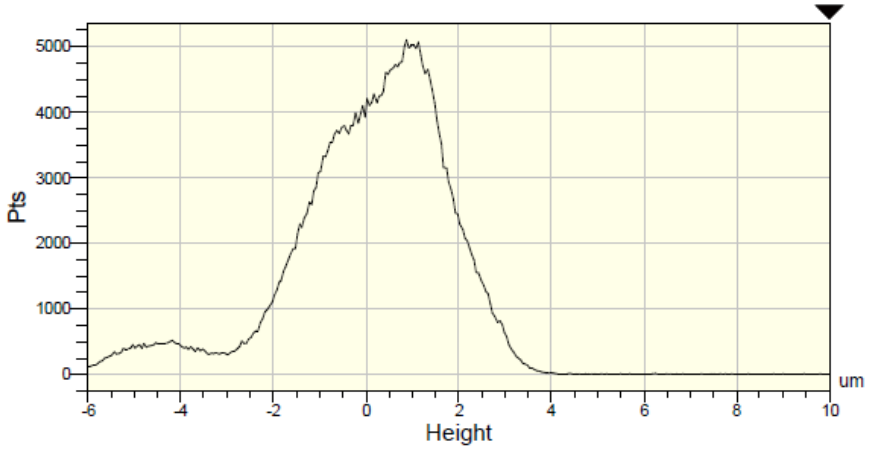

95% of data is between -1440.00 and 4400.00 nm (pv:5840.00)
90% of data is between 40.00 and 4240.00 nm (pv:4200.00)
85% of data is between 480.00 and 3960.00 nm (pv:3480.00)
80% of data is between 560.00 and 3640.00 nm (pv:3080.00)

Figure 5-27 Histogram curve of sample G120 after corrosion

After corrosion the histogram curves have an approximately uniform and normal shape for samples G180 to G1200 (Appendix A_3). For all the samples, there is an approximately normal distribution of roughness on the surface but for samples G60 and G120 as a result of more corrosion (which was confirmed on rougher surfaces through SEM and corrosion measurements in Sections 5.1 and 5.2) and having deeper grooves, no normal distribution of roughness is observed. For other surfaces there is a more uniform surface with a normal distribution of heights around zero (Appendix A_3).

After corrosion also, generally the point's distribution was extended (higher width of the histogram) which is due to increase in height or depth at some points on the surface which is an indication of roughness increase and confirms different roughness parameters (R_a, R_q, R_t and R_z) measured in Section 5.3. Some irregularities in the histogram curves after the corrosion testing also refer to some local corroded areas [175]. For all samples, this extension in width of the histogram, unlike samples G60 and G120, is symmetric which means that there are two points with positive and negative height on the surface. It can be concluded that on smoother surfaces both corrosion and also protection of the surface are existed on the surface and formation of passive film has affected the whole surface and prevented the concentration of corrosion just along the grooves (unlike samples G60 and G120 that deeper grooves were produced after corrosion).

Figure 5-28 and 5-29 show the histogram for sample G1200 before and after corrosion. As it is seen, before corrosion the histogram shows a perfect symmetry around zero indicating a uniform distribution of points with low roughnesses on the surface. The width of the histogram is also even less compared to other samples indicating less variety of data and less difference between the heights of the points on the surface which proves the lower roughness and flatness of the surface. The distribution of the height of the points is more uniform compared to all samples and with the least difference compared to the surface (height of zero) indicating lowest roughness of the surface. After corrosion, the histogram is symmetric around zero with extended width compared to before corrosion indicating points with higher height and depth values. It means that the protective passive layer has covered the grooves and also the peaks and resulted in an increase in the roughness of the surface. The symmetry in the histogram also shows a uniform distribution of points with different heights on the surface.

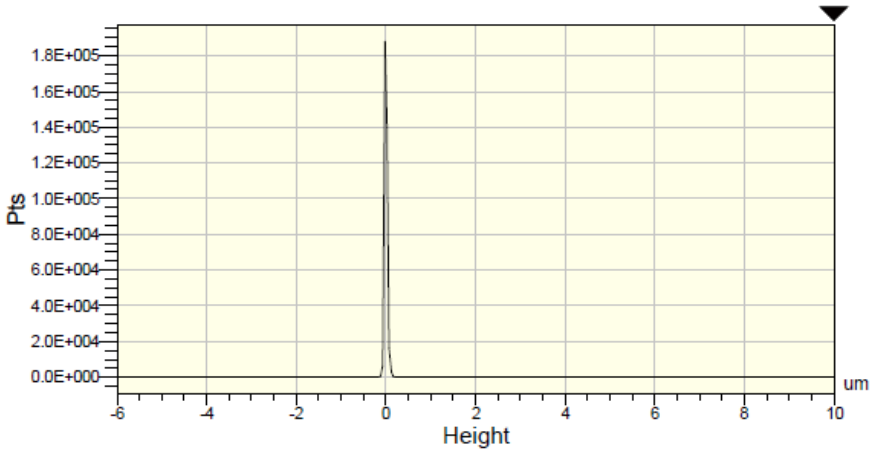

95% of data is between 1960.00 and 2040.00 nm (pv:80.00)
90% of data is between 1960.00 and 2000.00 nm (pv:40.00)
85% of data is between 1960.00 and 2000.00 nm (pv:40.00)
80% of data is between 1960.00 and 2000.00 nm (pv:40.00)

Figure 5-28 Histogram curve of sample G1200 before corrosion

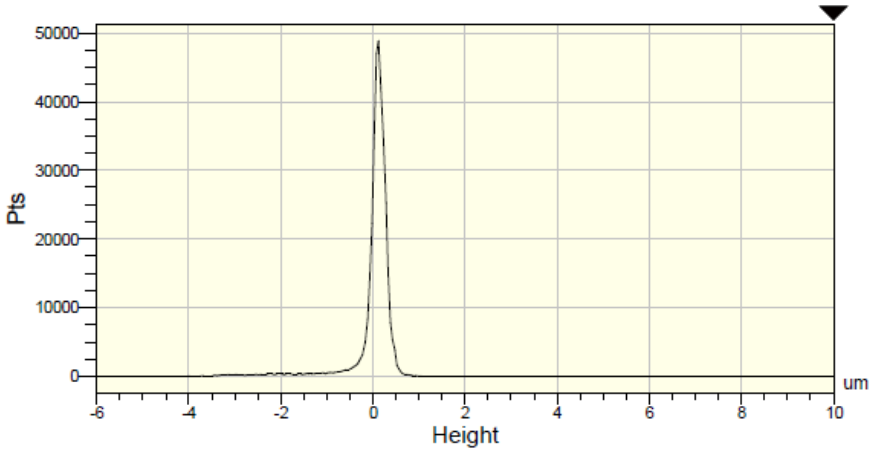

95% of data is between 1080.00 and 2400.00 nm (pv:1320.00)
90% of data is between 1760.00 and 2360.00 nm (pv:600.00)
85% of data is between 1840.00 and 2280.00 nm (pv:440.00)
80% of data is between 1920.00 and 2240.00 nm (pv:320.00)

Figure 5-29 Histogram curve of sample G1200 after corrosion

5.5 EDS Results

EDS was used to measure the change in oxygen concentration on the surface of the samples before and after corrosion testing.

5.5.1 Before corrosion

Figure 5-30 illustrates the EDS analysis results on sample G600 of nickel before corrosion testing. Results related to other samples with different roughnesses are presented in Appendix B_1. As is expected, peaks of Ni are observed with some oxygen and a very small amount of carbon. All the chemical composition analysis before the corrosion testing had almost identical results with the same elements including Ni, O and C.

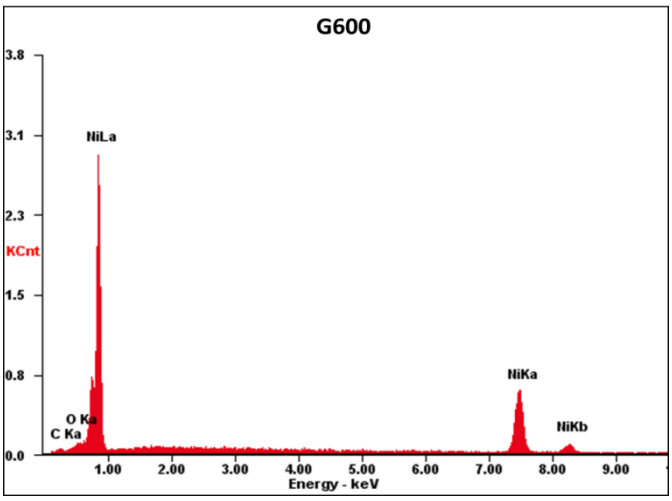

Figure 5-30 EDS analysis of sample G600 of nickel before corrosion.

5.5.2 **After corrosion:**

Figure 5-31 illustrates the EDS analysis result related to sample G600 of nickel after corrosion testing. In all samples (Appendix B_2), especially samples G60 to G120, there is a significant increase in oxygen content which is possibly related to corrosion products as a result of corrosion on the surface which justify higher corrosion rates obtained in potentiodynamic polarization tests. SEM and profilometry also confirmed more corrosion on rougher samples. A similar trend is observed for smoother surfaces (G600 and G1200) but in these cases the higher content of oxygen is related to a more stable protective passive layer [79]. The increase in oxygen content is also obvious from the peaks after corrosion.

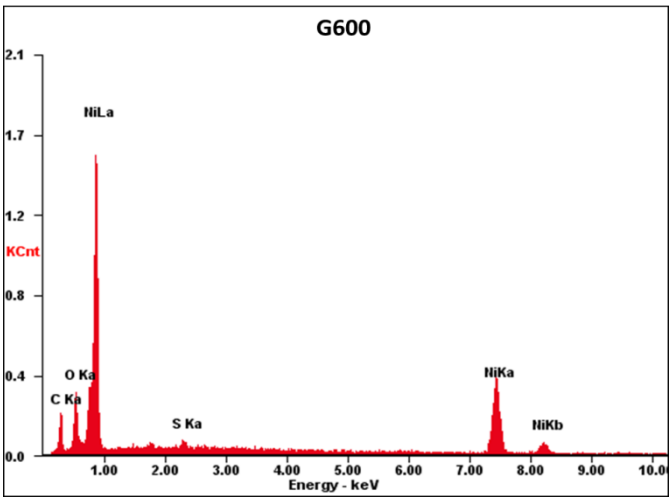

Figure 5-31 EDS analysis of sample G600 of nickel after corrosion.

The results of EDS are summarized in Table 5-7. All samples, except the patterned ones, had similar oxygen contents before corrosion testing but the oxygen content increased for all samples after corrosion. Looking at the increase

in oxygen content of the surface, the largest increases were for the two roughest samples (G60 and G120). For intermediate roughness samples (G180-G400) there was a much smaller increase in oxygen content. For the smoothest samples (G600-G1200) the increase in oxygen content stabilized at about 2.2wt% O. As demonstrated from the electrochemical results, G60 and G120 exhibited the highest corrosion rates, and the corrosion rate decreased with decreasing roughness. For samples G600- G1200, where the final oxygen content was ~3.7wt% O, this could be indicative of the formation of a stable passive film as suggested by Suter et al. [79] for high purity aluminum. But for rougher steel samples, the reason is reported to be the autocatalytic diffusion and corrosion happened within the deep grooves which resulted in a higher corrosion rate of the metal [73].

In the patterned samples, which was discussed in Chapter 4, as a result of the laser ablation process and possible oxidation there is more oxygen both inside and outside the holes before corrosion testing. After corrosion testing, the oxygen content has increased inside and outside the holes but the existence of air pockets inside the holes and heterogeneous wetting process, as was explained in Chapter 4, has prevented the dissolution of protective film inside the holes. Therefore, there is more oxygen inside the hole that is related to a more stable passive layer which will result in less contact between solution and substrate and consequently less corrosion of the patterned sample.

Table 5-7: Oxygen contents on the surface of the nickel samples before and after corrosion testing.

Sample	Oxygen wt% before corrosion	Oxygen wt% after corrosion	Oxygen wt% difference
G60	1.17	4.60	3.43
G120	1.37	4.71	3.34
G180	1.19	2.07	0.88
G240	1.20	2.6	1.40
G320	1.18	2.52	1.34
G400	1.20	2.11	0.91
G600	1.48	3.69	2.21
G800	1.54	3.69	2.15
G1200	1.49	3.75	2.26
D10L20 (outside the hole)	2.2	2.5	0.3
D10L20 (inside the hole)	2.2	4.2	2

5.6 Roughness parameters before and after corrosion

Figures 5-32 to 5-35 illustrate different surface roughness parameters including R_a, R_q, R_z and R_t for all unidirectionally ground samples before and after corrosion testing. In all cases, by increasing the grit number from G60 to G1200, the roughness decreases systematically before corrosion testing and in all samples the value of various roughness parameters has increased after corrosion. The roughness after corrosion doesn't show the same trend as before corrosion but shows almost the same trend for R_a, R_q. Patterned samples showed high roughnesses before corrosion with a slight increase after corrosion testing.

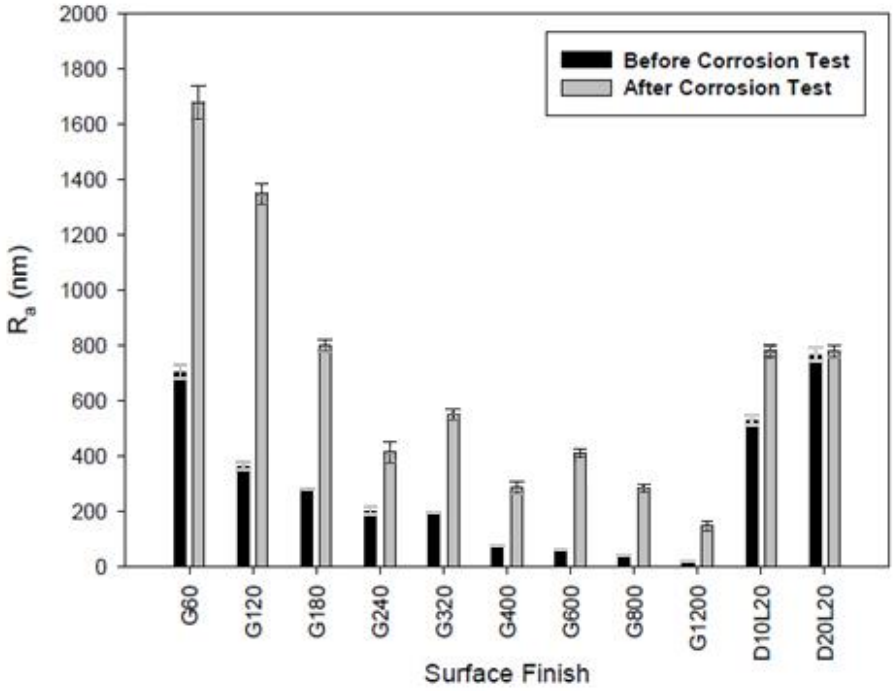

Figure 5-32 R_a values for nickel before and after corrosion testing.

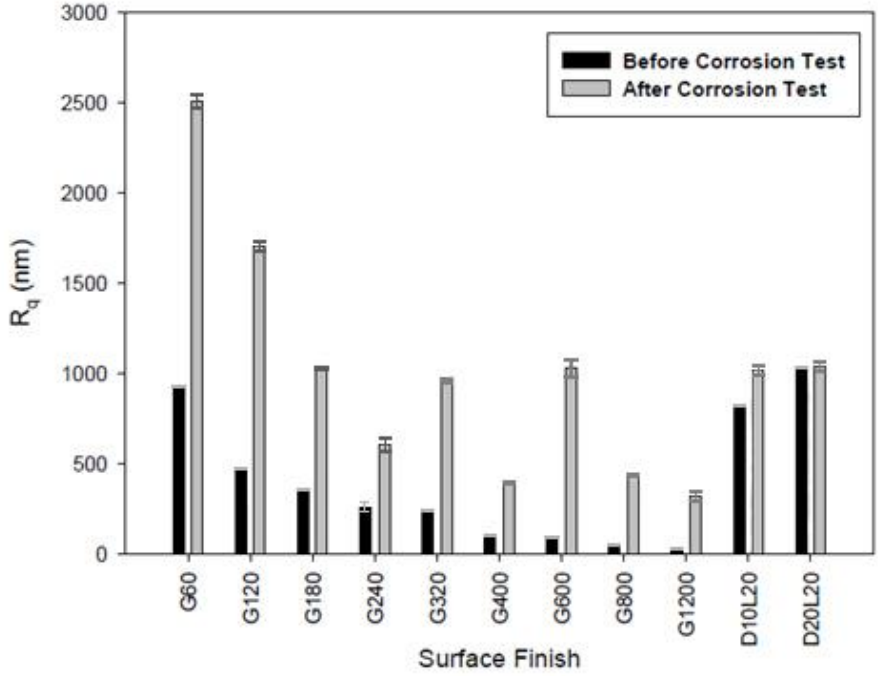

Figure 5-33 R_q values for nickel before and after corrosion testing.

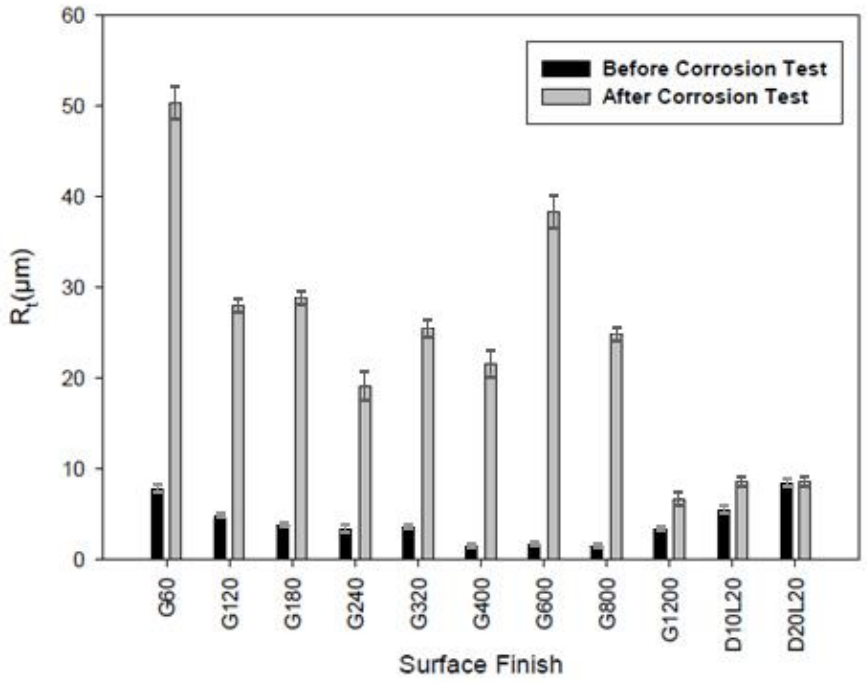

Figure 5-34 R_t values for nickel before and after corrosion testing.

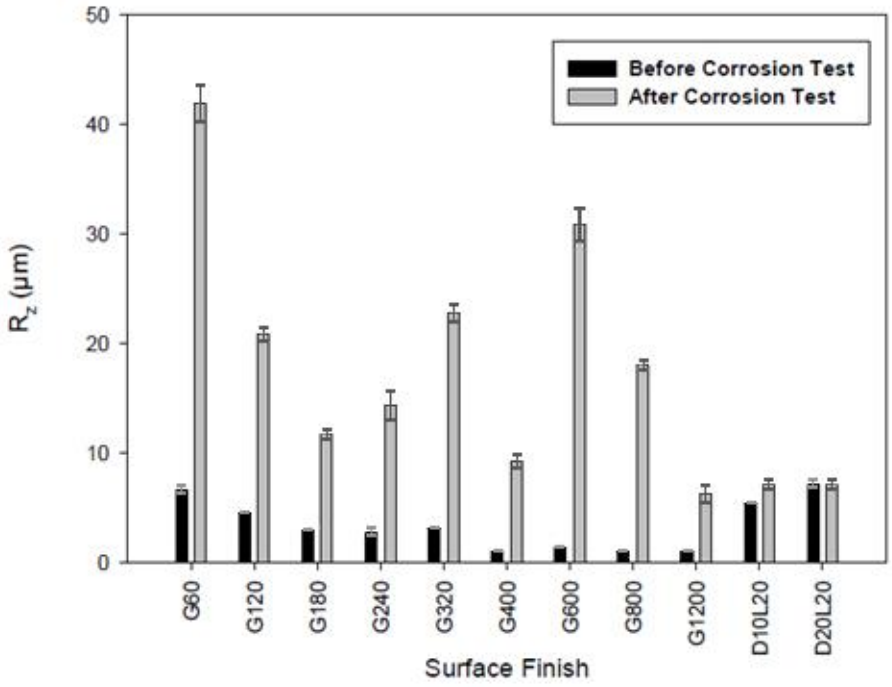

Figure 5-35 R_z values for nickel before and after corrosion testing.

5.7 Relationship between corrosion rate and different roughness parameters

Figures 5-36 to 5-39 show the change in corrosion rate as determined by potentiodynamic polarization tests versus various surface roughness parameters (R_a in Figure 5-36, R_q in Figure 5-37, R_t in Figure 5-38, and R_z in Figure 5-39). As can be readily seen, all plots show almost the same general trend and in all cases by increasing the surface roughness, the corrosion rate increased. These scratches can increase the R_z value of the surface compared to a surface with no scratches. These results are in agreement with previous results on morphology, oxygen concentration and roughness parameters. As noted in the literature survey in Chapter 2, this is a general trend seen for corrosion of metals with the ability to form a passive layer [75, 78-80]. This trend is opposite to metals with no ability to form a protective passive film [73].

Looking at the general shape of the plot, we can see that up to a limit, increasing the surface roughness dramatically increases the corrosion rate. After that limit, it doesn't have a significant effect. The rate of change of corrosion rate with roughness decreases after this limit and, for the highest roughnesses, the corrosion rate appears to reach a plateau. This kind of behaviour shows that corrosion doesn't change at higher roughnesses significantly (after 200 nm for R_a and R_q). The same trend was reported by Li and Li [80] for Cu in a 3.5% NaCl solution which was expected as a result of the faster formation of a protective layer on the smoother surfaces.

In all cases the patterned samples have high roughnesses and lower corrosion rates as shown with blue triangles. This strongly suggests a different corrosion protection mechanism for the patterned samples namely heterogeneous wetting, as discussed in Chapter 4.

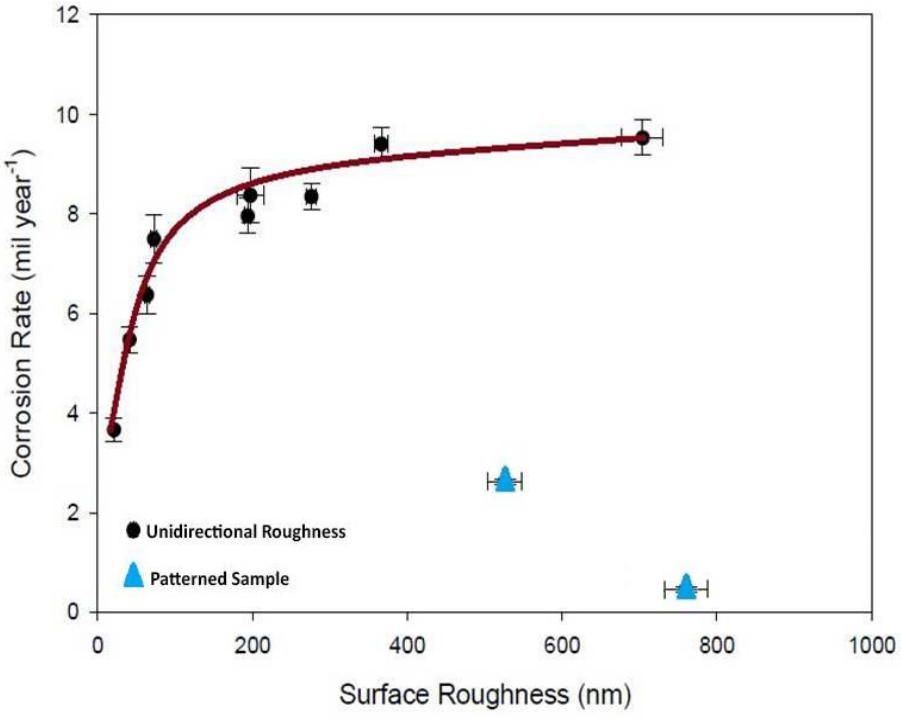

Figure 5-36 Dependence of corrosion rate on (R_a) for nickel

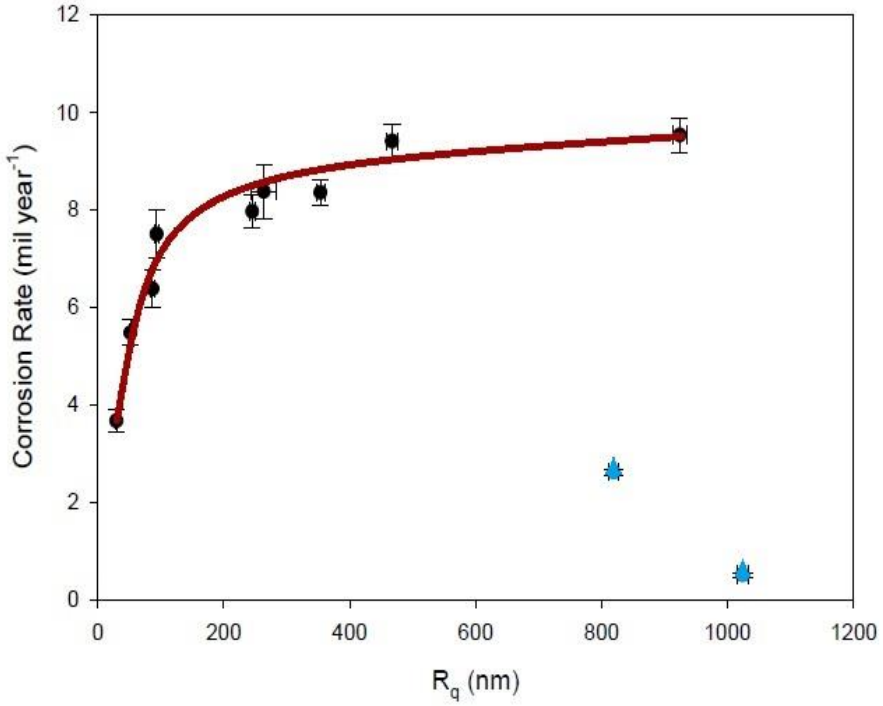

Figure 5-37 Dependence of corrosion rate on (R_q) for nickel

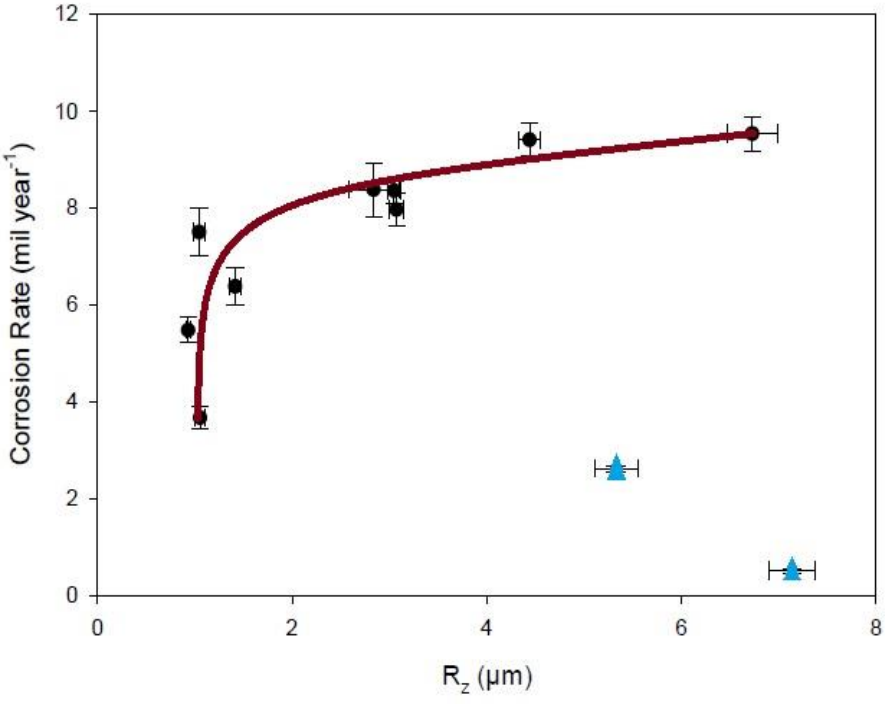

Figure 5-38 Dependence of corrosion rate on (R_z) for nickel

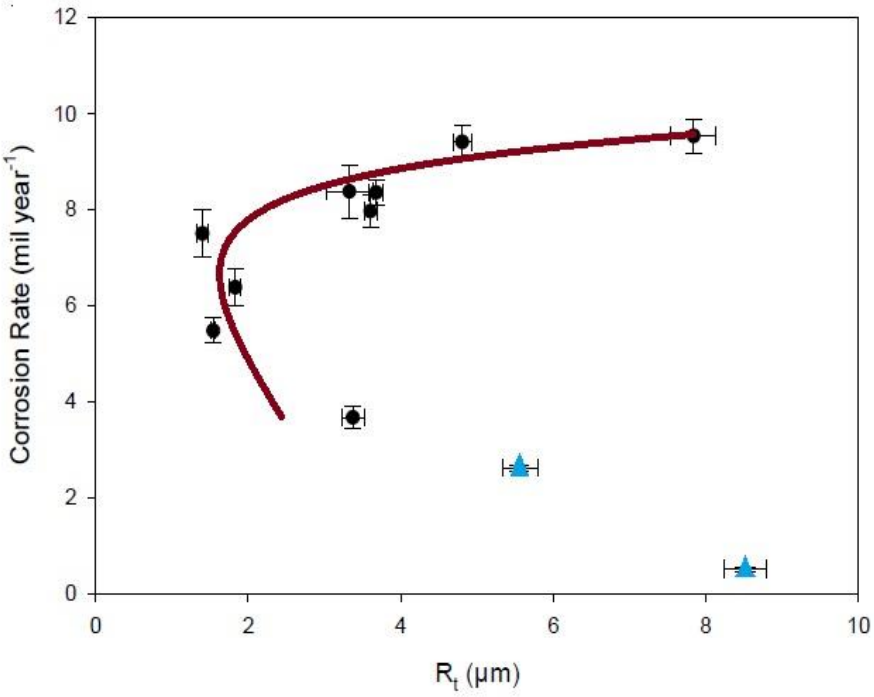

Figure 5-39 Dependence of corrosion rate on (R_t) for nickel

Figure 5-40 illustrates the change in R_p and R_{ct} calculated from potentiodynamic polarization technique and EIS analysis, respectively with change in average surface roughness R_a. Both R_p and R_{ct} decrease with increasing surface roughness, and consequently there is an increase in corrosion rate with increasing surface roughness.

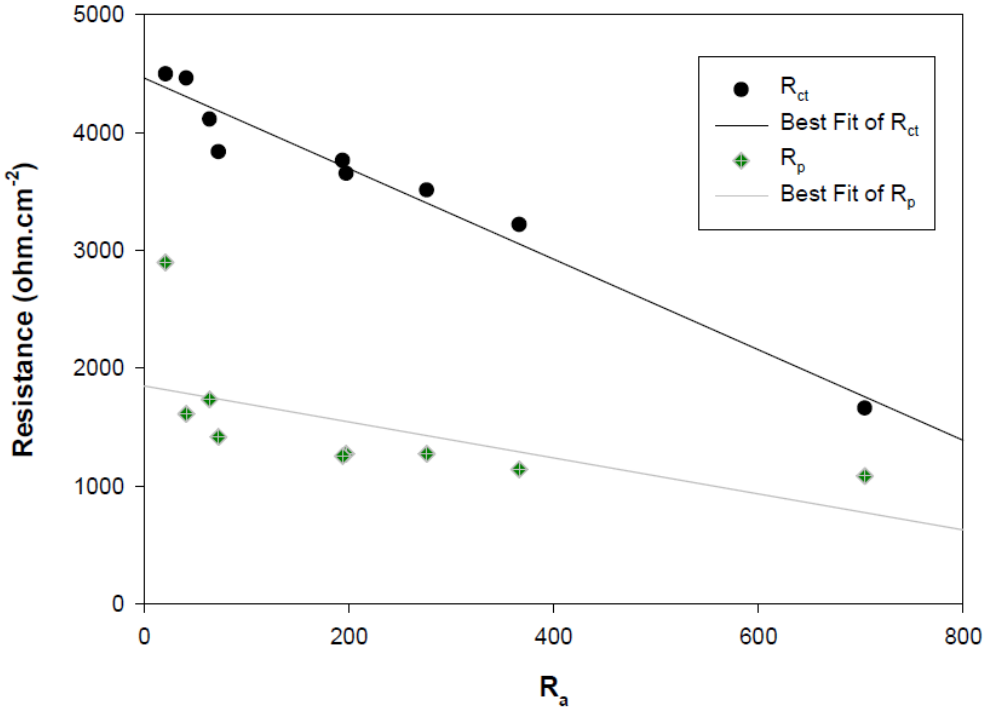

Figure 5-40: The effect of average roughness on R_p and R_{ct} for nickel.

This behaviour, ie decreasing R_p and R_{ct} with increasing roughness, can be explained in the following manner. In samples with rougher surfaces, there is a larger contact area between the sulphuric acid solution and nickel. Also, in the case of metals with an ability to form a passive layer, there can be trapping of the corrosive ions in the deep grooves, possibly leading to an autocatalytic process such as pitting [176]. Both phenomena would increase the corrosion rate. Also deep grooves are suitable places for corrosion initiation [84]. That's why in the SEM micrographs of rough samples (especially from samples G320 to G60 in Figure 5-13) corrosion seems to be more concentrated along the grooves. These observations are in agreement with the finding that stainless steel samples with deep grooves i.e. those with higher reduced valley depth (R_{vk}) values, show

poorer corrosion resistance [84] and the observations of Suter et al.'s [79] that these deeper grooves on aluminium trap the corrosion products leading to more corrosion in NaCl solution [79]. Potentiodynamic polarization testing and EIS analysis in this research also showed a higher corrosion rate on rougher samples. According to SEM and corrosion test results, a possible explanation for this phenomenon can be the unstable passive layer formed on rougher surfaces and the lower passive layer break-down potential compared to smoother surfaces (Figure 5-2).

The rougher surface also has relatively deep grooves in comparison with the smooth surface which will cause the accumulation of corrosive ions. The rough surfaces show much larger and deeper pits, and the surrounding areas also show signs of general corrosion. By contacting the corrosive solution with the substrate, passive layers are formed quickly on rough and smooth surfaces. Then the passive layer is dissolved by the corrosive ions in the electrolyte. However, on rough surfaces as a result of the existence of the deep grooves, pH drops locally inside the grooves [177]. But on the smooth surface there is no pH drop and no dissolution of the passive layer occurs. Therefore, the repassivation happens and prevents the breakdown of the passive layer. The pits on the rough surfaces grow faster and a significant general and localised corrosion will be the result of the whole process. In contrast, on smooth surface there are areas with localised corrosion and the rest of the sample is protected by the passive layer [177]. For metals with the ability to form a passive film, on smooth surfaces the

formation of a stable passive film is also fast and more likely to occur, resulting in a decreased corrosion rate [49, 79].

This trend is also consistent with the results of Li and Li [80] that investigated the effect of surface roughness on the electron work function (EWF) of Cu. They found that the EWF decreased with increasing roughness. Therefore, a rougher surface, could more readily release electrons which would result in a higher corrosion rate.

Another important observation related to the trend observed for nickel samples is the EDS results which measured oxygen content on the surface after corrosion and was discussed in this chapter. As was discussed, samples G600 to G1200 as smoother surfaces showed a higher oxygen content indicative of the formation of a stable passive film that will result in a better corrosion protection. In the patterned samples, as discussed in Chapter 4, there is a different mechanism and heterogeneous wetting decreases the surface area exposed to the sulphuric acid solution, thus reducing the corrosion rate.

Chapter 6 UNIDIRECTIONAL ROUGHNESS ON MILD STEEL

In this chapter the results of the effect on corrosion resistance of creating unidirectional surface roughness on mild steel are presented. It is well known that during the corrosion of mild steel, anodic and cathodic areas develop over the corroded surface. These areas change in shape and move across the surface, resulting in corrosion that is approximately uniform [16]. In this chapter we will see that the surface roughness affects the corrosion resistance to some extent. This implies that it may be possible to decrease corrosion by specifying the proper surface finish rather than by upgrading the chosen alloy.

6.1 Corrosion Testing Results

6.1.1 Potentiodynamic Polarization Technique

The polarization curves for samples G60, G400 and G1200 are presented in Figure 6-1.

Anodic and cathodic reactions happening for dissolution of mild steel in acidic solution are according to equations (6-1) and (6-2).

$$Fe \rightarrow Fe^{2+} + 2e^{-} \quad (6\text{-}1)$$

$$2H^{+} + 2e^{-} \rightarrow H_2 \quad (6\text{-}2)$$

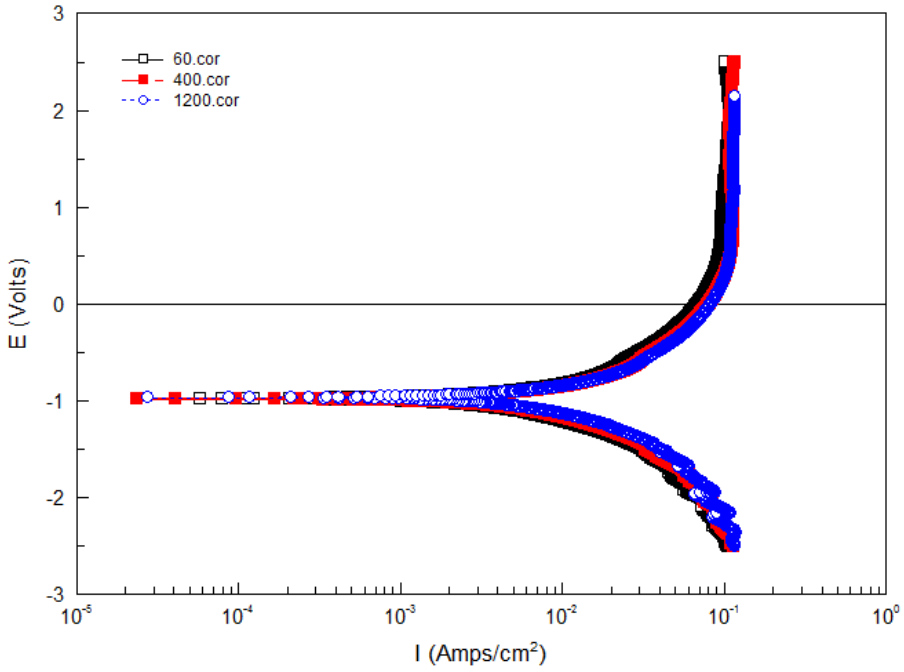

Figure 6-1 Polarization curves for samples G60, G400 and G1200 (SCE).

As can be seen, by increasing the roughness from sample G1200 to G60, the curves are shifted to the left which means that corrosion current density has decreased and therefore the corrosion rate will be decreased. It means that the increasing roughness reduced anodic dissolution (equation 6-1) and also retarded the hydrogen evolution reaction (equation 6-2).

Table 6-1 presents the electrochemical corrosion parameters i.e. corrosion potential (E_{corr}), cathodic and anodic Tafel slopes (b_a, b_c) and corrosion current density (i_{corr}) obtained from the extrapolation of the polarization curves. Details on the calculation of the corrosion rate and other electrochemical parameters listed in Table 6-1 are given in Section 5.1.1.

Table 6-1 Different corrosion parameters obtained from potentiodynamic polarization technique

Sample	E_{corr} (V)	i_{corr} ($\mu A/cm^2$)	β_a (V)	β_c (V)	R_p (Ω/cm^2)	P_i (mil/year)
G60	-0.968	4140.86	0.295	0.570	20.46	1886
G120	-0.971	4372.53	0.290	0.507	18.37	1991
G180	-0.973	4431.88	0.305	0.457	17.93	2018
G240	-0.974	4723.77	0.291	0.513	17.05	2151
G320	-0.973	5027.15	0.306	0.543	16.93	2289
G400	-0.974	6112.51	0.349	0.690	16.49	2784
G600	-0.974	6254.88	0.358	0.688	16.35	2848
G800	-0.973	7239.01	0.388	0.628	14.44	3297
G1200	-0.973	7498.72	0.374	0.740	14.41	3415

According to Table 6-1, the corrosion rate increases with increasing grit size i.e. rougher surfaces are more corrosion resistant. According to the measurements, the lowest corrosion rate of 1886 (mil/year) was related to the roughest sample (G60) and by decreasing the roughness, an increase of 81% was observed in corrosion rate of sample G1200 which showed the value of 3415 (mil/year).

Figures 6-2 to 6-5 show the bar charts, with associated error bars related to the change in corrosion current density (I_{corr}), corrosion potential (E_{corr}),

corrosion rate (CR) and polarization resistance (R_p) versus surface finish for mild steel.

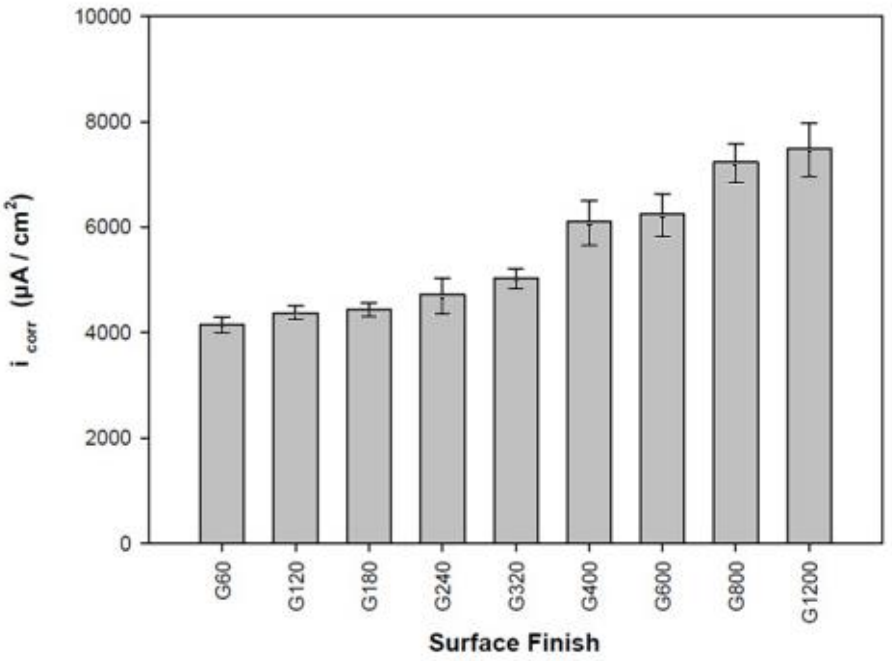

Figure 6-2 Dependence of i_{corr} on surface finish of mild steel

As it is seen in the bar chart, corrosion current density values have increased by decreasing the roughness for different samples. The values increased slowly from sample G60 to G320 and then more increase was observed for smoother samples toward sample G1200.

All samples with unidirectional roughnesses had almost the same corrosion potential values (around -0.9 V), within the scatter range of triple tests. In this case, the error bar representing the E_{corr} variation in for the three samples tested was larger for rougher surfaces. Similar values for E_{corr} show that variation of the roughness for different samples has not changed the corrosion

mechanism and just affected the tendency of material for corrosion. It means that by creating the unidirectional roughnesses we were able to change the corrosion resistance of the mild steel surface. The reported corrosion current density values also confirm the change of corrosion resistance by changing roughness.

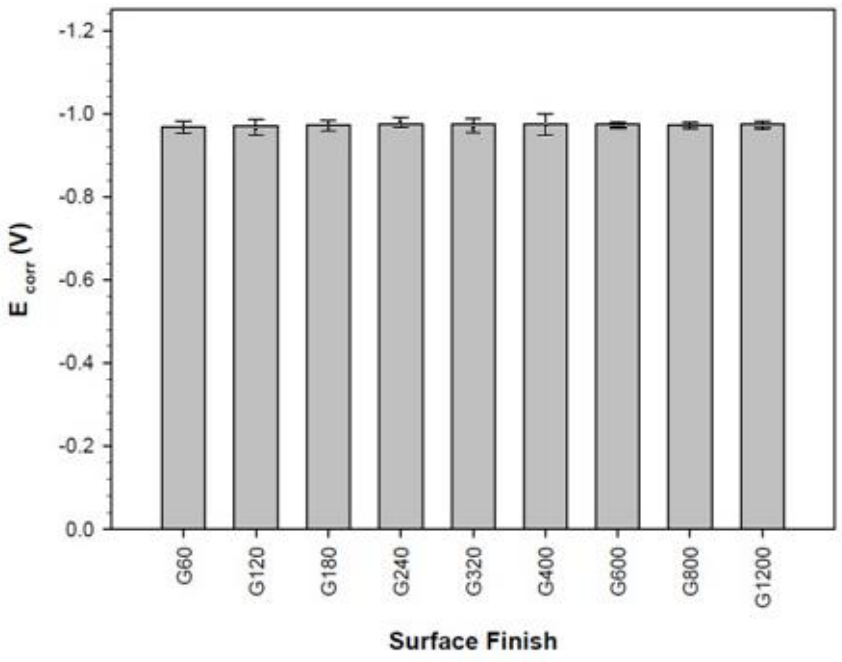

Figure 6-3 Dependence of E_{corr} on surface finish of mild steel

Corrosion rate which is calculated directly from i_{corr}, also showed the same trend as corrosion current density. From the rougher sample (G60) to sample G320, the increase in corrosion rate with decreasing roughness is gradual. Then, by decreasing the roughness from sample G400 to G1200, more increase in corrosion rate was recorded for different samples.

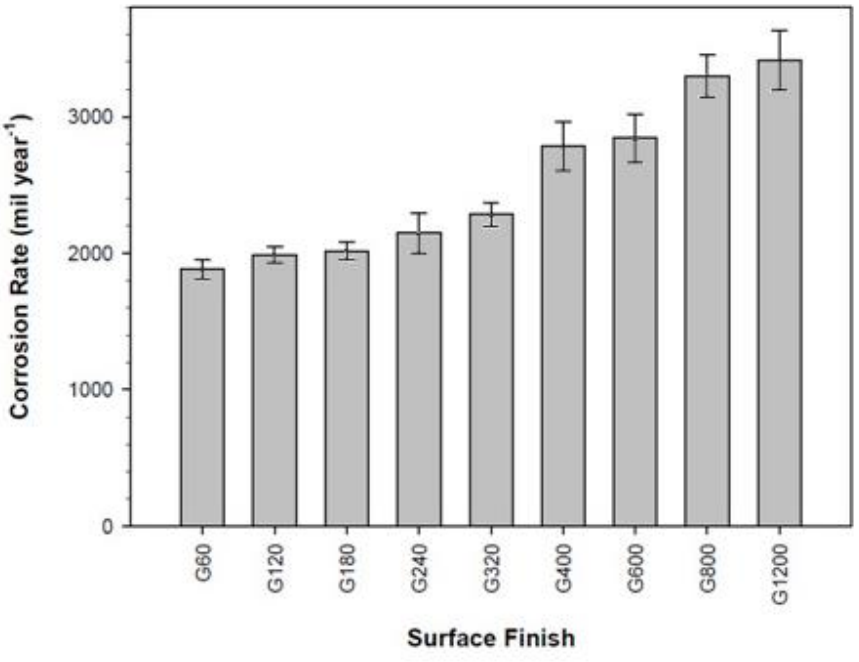

Figure 6-4 Dependence of corrosion rate on surface finish of mild steel

Polarization resistance is calculated from corrosion current density values. Polarization resistance values show a reverse trend compared to corrosion current density and corrosion rate values: by decreasing the roughness, the polarization resistance values decreased which means a higher corrosion rate for the smoother surfaces (Figure 6-5).

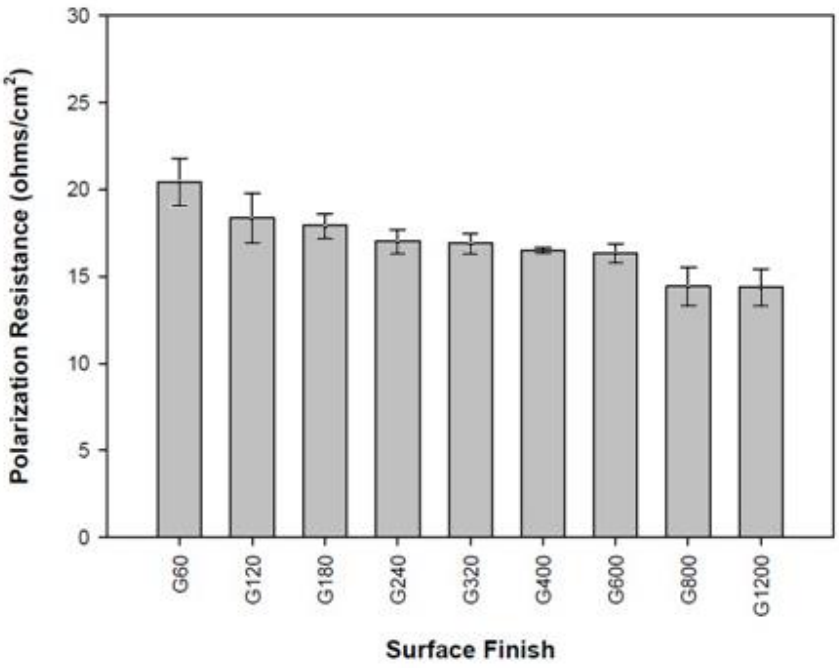

Figure 6-5 Dependence of R_p on surface finish of mild steel

6.1.2 **EIS Results**

EIS provides information about kinetics of the electrode processes and simultaneously about the surface properties of the investigated system [36]. Studying different circuit element behaviour in EIS such as the double layer behaviour of the electrode surface is also a more quantitative mean to study the surface roughness [178]. In this simulation, the double layer refers to two layers of charges, due to an electrical potential formed on the surface of electrode, which behaves like a capacitor [179]. It is said that the double layer capacitance is proportional to the effective surface area of an electrode. Therefore, it has been used as a means to reflect the roughness of an electrode surface [178].

To calculate the impedance of the electrode, an analogous circuit should be used to describe the impedance. In this circuit, R_{ct} is the charge transfer resistance, which is also noted as the reaction resistance and CPE is a constant phase element which is generally used to replace the double layer capacitance for a better fitting when an electrode does not behave as a pure capacitor [180]. It is also said that a constant phase element is used in place of pure capacitor to account for non-homogeneity of the system [177].

The model chosen for the fitting in this research was a commonly used model for mild steel because it gives the best fit between the experimental and simulated results [33, 181, 182]. In this circuit, R_1=R_s represents the solution resistance; R_2=R_{ct} is the charge transfer resistance and CPE is related to the double-layer capacitance. The impedance, Z, of CPE can be calculated according to equation 5-2 in Chapter 5.

The chosen electrical equivalent circuit describes the impedance of the electrode as a combination of a solution resistance R_s, in series with a parallel connection between R_{ct} and CPE. R_{ct} is also in series with a parallel connection between inductive elements (L and R_L). (L) is inductance related to adsorbed intermediates of specimen corrosion and R_L is the inductor resistance (Figure 6-6).

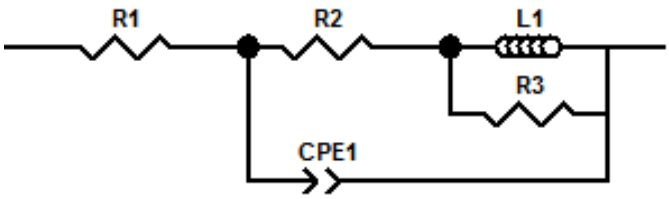

Figure 6-6 Equivalent circuit model for mild steel

The physical meaning of other elements of this circuit is that, the solution resistance only occurs in the solution. While the charge transfer resistance or reaction resistance combined with the double layer capacitor in a parallel way because they coexist on the surface of electrode. After selecting the best equivalent circuit, the impedance is recorded experimentally and plotted in a complex plane (Argand diagram), known as the Nyquist plot [183]. The Nyquist plot is typically a semicircle plot or consist of a semicircle on a complex plane. The X-axis is the real and the Y-axis is the imaginary part of the impedance, which characterise the magnitude of the impedance and the phase shift between the recorded potential and current [179]. Usually a depressed semicircle (rather than a perfect semicircle) occurs on a Nyquist plot due to the fact that most of the electrodes do not behave exactly as a pure capacitor. Another reason for the depression of the large semicircle in the complex impedance plane of the Nyquist plot which is often referred to as frequency depression, is attributed to roughness and in-homogeneities of the solid surface [184]. When a depressed semicircle occurs, the CPE is usually introduced to get a more accurate fit of experimental data sets using generally more complicated equivalent circuit [179].

Combining the model and experimental results, the impedance fitting was performed following a non-linear least square fitting procedure [185], allowing the best values with least errors of the electrical components in the analogous circuit to be obtained with minimised deviations between the experimental and curve-fitted impedance data. An example of the curve-fitted impedances are presented in Figure 6-7 which shows a good fit between the experimental data and simulated values. The CPE or double layer capacitance values can then be calculated from the fitted values of the electrical components in the analogous circuit [186]. Similar Nyquist plots were observed in the studies of Momoh et al [181] for mild steel and Heydari et al for low alloy steel, both in sulphuric acid [182].

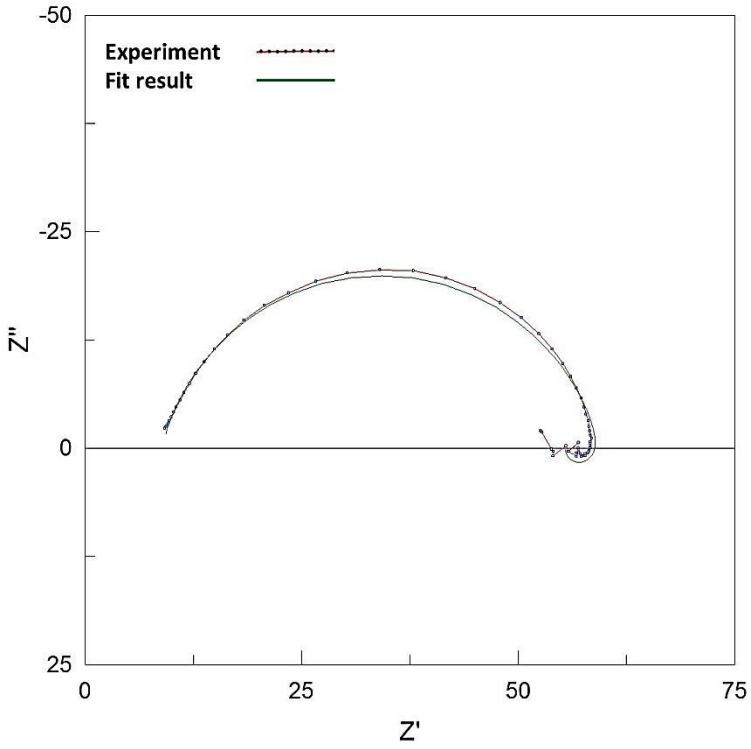

Figure 6-7 Nyquist curve-fitted impedance results for sample G600

Figure 6-8 also shows the curve-fitted results of impedance in Bode, Figure 6-8(a) and Bode- Phase, Figure 6-8(b) representations. Both plots show good agreement between the experimental and simulated (fitted) results.

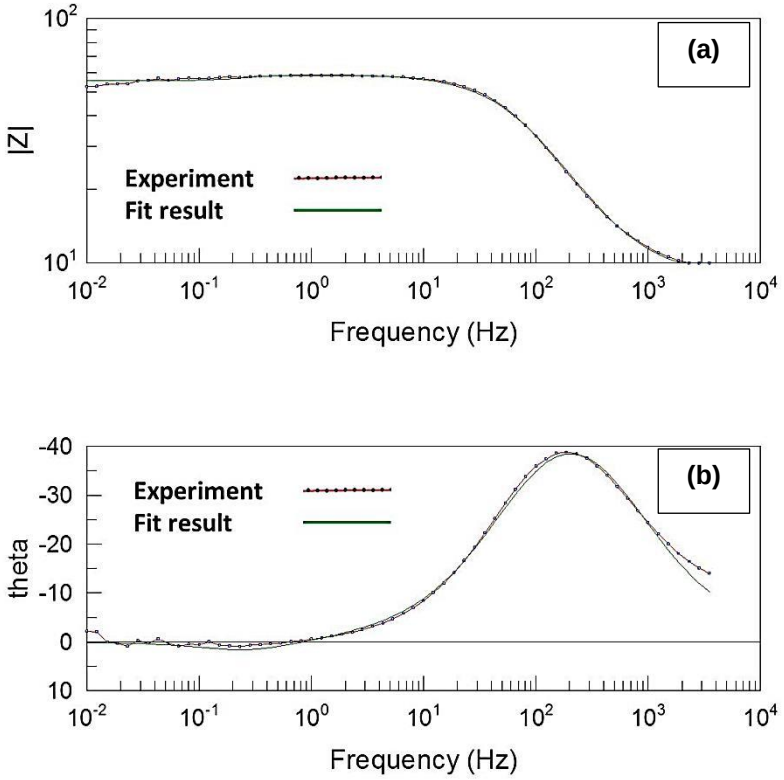

Figure 6-8 (a)Bode (b)Bode phase curve-fitted impedance results for sample G600

Figure 6-9 shows the Nyquist diagrams related to mild steel in 0.5M H_2SO_4 solution for different surface roughnesses. The diagrams consist of a large capacitive loop at high frequency (HF). The HF capacitive loop is related to the charge transfer process in metal corrosion and the double layer behaviour at the film/solution interface. An inductive loop is also observed in the Nyquist at low frequency (at the end of the plot). The presence of inductor (L) in the impedance spectra is said to be as a result of the dissolving the metal by the direct charge

transfer on the surface [36, 187]. The inductive loop which appeared following the disappearance of the mid frequency capacitive loop, exists at lower frequency range has been reported to indicate localized and sometimes uniform type of corrosion [177, 187]. The inductive behaviour at low frequency is due to the consequence of the layer stabilization by products of the corrosion reaction on the electrode surface. It may also be attributed to the re-dissolution of unstable passivated layer [184]. The inductance in our system in H_2SO_4 solution is also interpreted as coming mainly from the adsorption of reaction species such as $(SO_4^{2-})_{ads}$ and $(H^+)_{ads}$ or the intermediate reaction product $(Fe(OH)_{ads})$ [33, 36, 182].

As it is seen, by increasing the roughness the diameter of semicircle which shows charge transfer resistance has increased and consequently corrosion resistance will increase [171]. This plot shows that sample G60 which is the roughest sample has the largest semicircle diameter compared to other samples and sample G1200 which is the smoothest one shows the smallest diameter confirming more corrosion resistance of the roughest sample. Figure 6-10 (a and b) also displays Bode and Bode-Phase plots of the same samples respectively. All the samples have the same trend but samples with higher roughnesses show higher impedance values by changing frequency which results in higher corrosion resistance of these samples. Sample G60 in this plot also shows the highest value of impedance. The maximum phase angle θ_{max} in Bode-Phase plot also is less than 80° which is considered to be a result of the roughness of the electrode surface [43]. The θ_{max} values start from 26 and reaches 44 for the

roughest sample (G60). All the values are listed in Table 6-2. The values of the equivalent circuit elements for the corrosion of mild steel for various surface roughnesses are also summarized in Table 6-2. Different values obtained for the n which is the CPE exponent can be related to the roughness of the surface of mild steel [40]. As it can be seen, generally by decreasing the roughness, n increased from sample G60 to G1200.

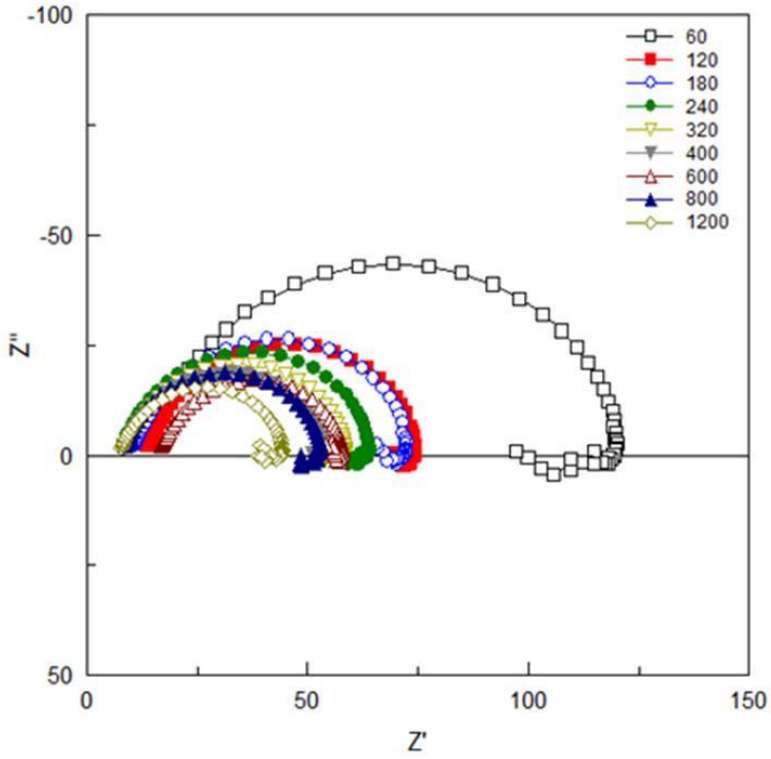

Figure 6-9 Nyquist plots of mild steel samples with different roughnesses

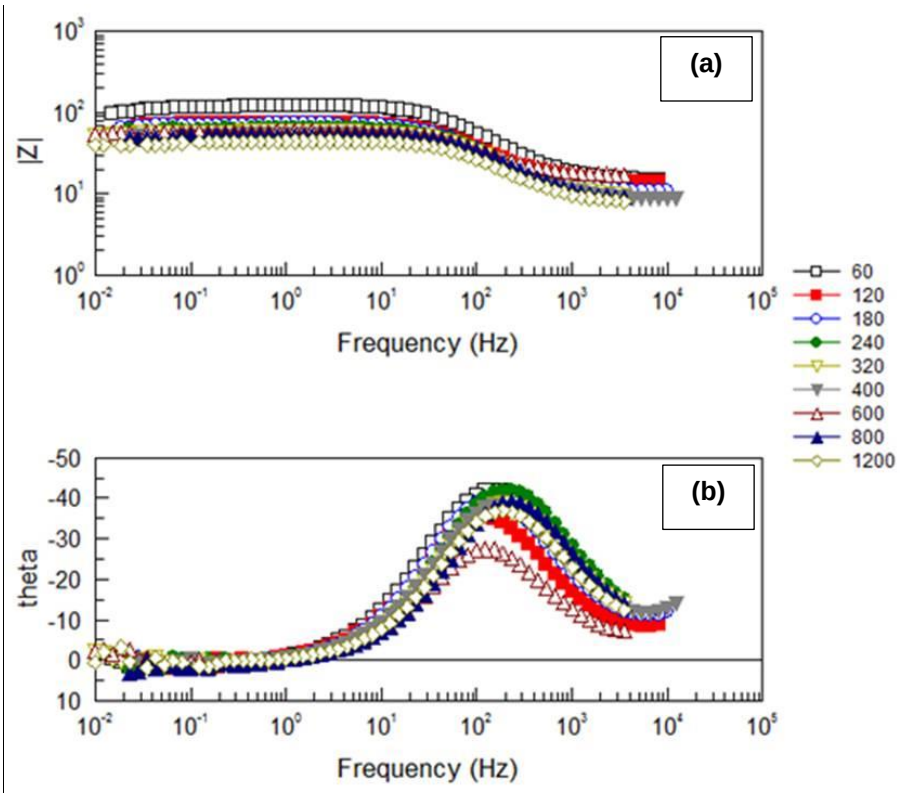

Figure 6-10 (a)Bode and (b)Bode-Phase plots for mild steel with different roughnesses

Thus the EIS results confirm the potentiodynamic polarization technique results and show more corrosion on smoother surfaces. To better understand the mechanisms governing the process, SEM, different profilometry techniques, EDS and XRD data are presented in Sections 6-2 to 6-5.

Table 6-2 shows the EIS analysis data obtained from Nyquist curves. All the Nyquist plots were analyzed by fitting the experimental data to an equivalent circuit model as was shown in Figure 6-6.

Table 6-2 EIS data for mild steel samples with different roughnesses

Sample	R_s ($\Omega.cm^2$)	R_{ct} ($\Omega.cm^2$)	L_1	R_L ($\Omega.cm^2$)	θ_{max} (deg)	CPE ($\Omega^{-1}cm^{-2}S^n$)	n
G60	13.87	93.98	18.53	15.19	44	9.10×10^{-5}	0.820
G120	13.63	58.06	0.22	11	35	13.33×10^{-5}	0.837
G180	10.47	57	4.08	7.7	43	12.88×10^{-5}	0.836
G240	7.74	54.24	0.83	3.88	43	11.10×10^{-5}	0.845
G320	8.80	46.66	2.30	4.05	38	11.9×10^{-5}	0.848
G400	7.98	45.32	0.11	9.03	37	24.09×10^{-5}	0.850
G600	16.51	39.53	1.04	2.7	26	14.13×10^{-5}	0.851
G800	8.24	36.58	6.09	4.60	37	9.61×10^{-5}	0.867
G1200	7.53	33.09	3.99	4.18	35	14.29×10^{-5}	0.855

According to Table 6-2, the values of R_{ct} decreased by decreasing the roughness toward sample G1200. Sample G60 as the roughest sample has a charge transfer resistance of 93.98 $\Omega.cm^2$ and this value deceased to 33.09 $\Omega.cm^2$ for the smoothest sample (G1200). As mentioned before, R_{ct} is a measure of electron transfer across the surface, and inversely proportional to the corrosion rate [44]. Thus, it means that corrosion rate has decreased by increasing surface roughness and sample G60 is the most corrosion resistant sample.

6.2 SEM Images

Scanning Electron Microscopy (SEM) was used to characterize the surface of mild steel samples with different unidirectional roughnesses both before and after corrosion testing. For all samples, the trend observed in corrosion of micrographs after corrosion is compared with the results of corrosion tests (potentiodynamic polarization technique and EIS).

6.2.1 **Before Corrosion:**

Figures 6-11 (a-i) present SEM micrographs of the unidirectional roughness samples (G1200 to G60) of mild steel before corrosion testing. In sample G1200 (Figure 6-11(a)), the grooves are very fine and it is difficult to see the grooves created with SiC papers. By increasing the roughness toward sample G800 in Figure 6-11(b), very fine grooves are appeared. In samples G600 and G400 the unidirectional roughnesses are readily visible, Figure 6-11(c,d).

Figures 6-11 (e-h) display SEM micrographs for samples G320 to G120. By increasing the roughness from sample G320 to sample G120 the grooves are getting wider and deeper and in some cases there are some deeper grooves or scratches which are formed during the polishing process. Some of these grooves or scratches are visible in samples G180 and G120.

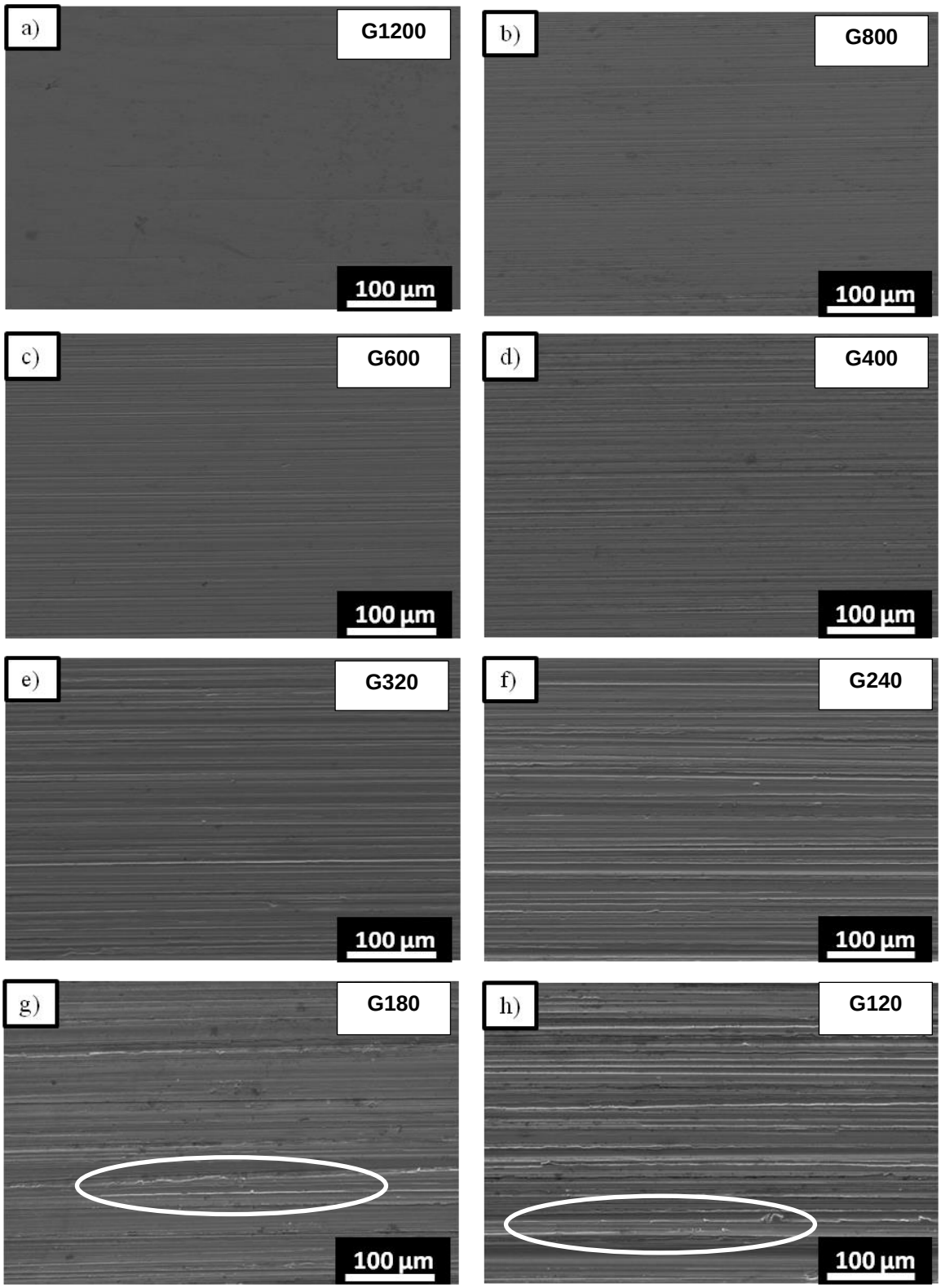

Figure 6-11 SEM micrographs of mild steel samples a) G1200, b) G800, c) G600, d) G400, e) G320, f) G240, g) G180 and h) G120 before corrosion

Figure 6-11 (i) shows the SEM micrograph for sample G60 which is the roughest sample of this study. As it is seen, the grooves are not as fine as previous samples and removal of the metal during the grinding process also has led to some deeper grooves.

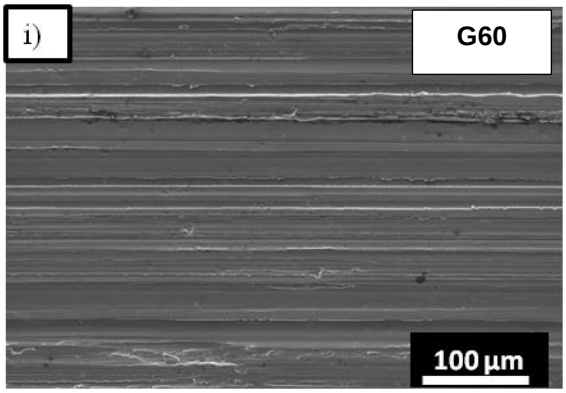

Figure 6-11 (Cont) SEM micrograph of mild steel sample i) G60 before corrosion

6.2.2 **After Corrosion:**

Figures 6-12 (a-i) illustrate the SEM micrographs of the surface of mild steel samples after corrosion testing. Looking at the SEM micrographs for sample G1200, G800 and G600 in Figures 6-12 (a-c), we can readily see that corrosion has taken place over the total sample surface. As it is seen, for these samples no grooves remain after corrosion which can be an indication of general corrosion throughout the surface. In these samples corrosion products have filled the grooves and the peaks are dissolved and there is no sign of the unidirectional roughnesses after corrosion. By increasing the roughness to sample G400,

Figure 6-12 (d) shows the first sample in this set that some signs of unidirectional roughnesses are still visible after corrosion.

As the roughness increases to sample G320 (Figure 6-12(e)), some more grooves are visible and these grooves are increased for the next rougher samples (samples G240, G180 and G120) in Figures 6-12(f-h). In these samples also corrosion products have filled the grooves but in some parts are formed not only at the bottom of the grooves but also on peak areas.

Figure 6-12 (i) displays the SEM micrograph for sample G60. As it is seen, the grooves are still visible after corrosion on almost the total area and corrosion products have been formed on the surface including along the grooves, bottom of the grooves and peaks.

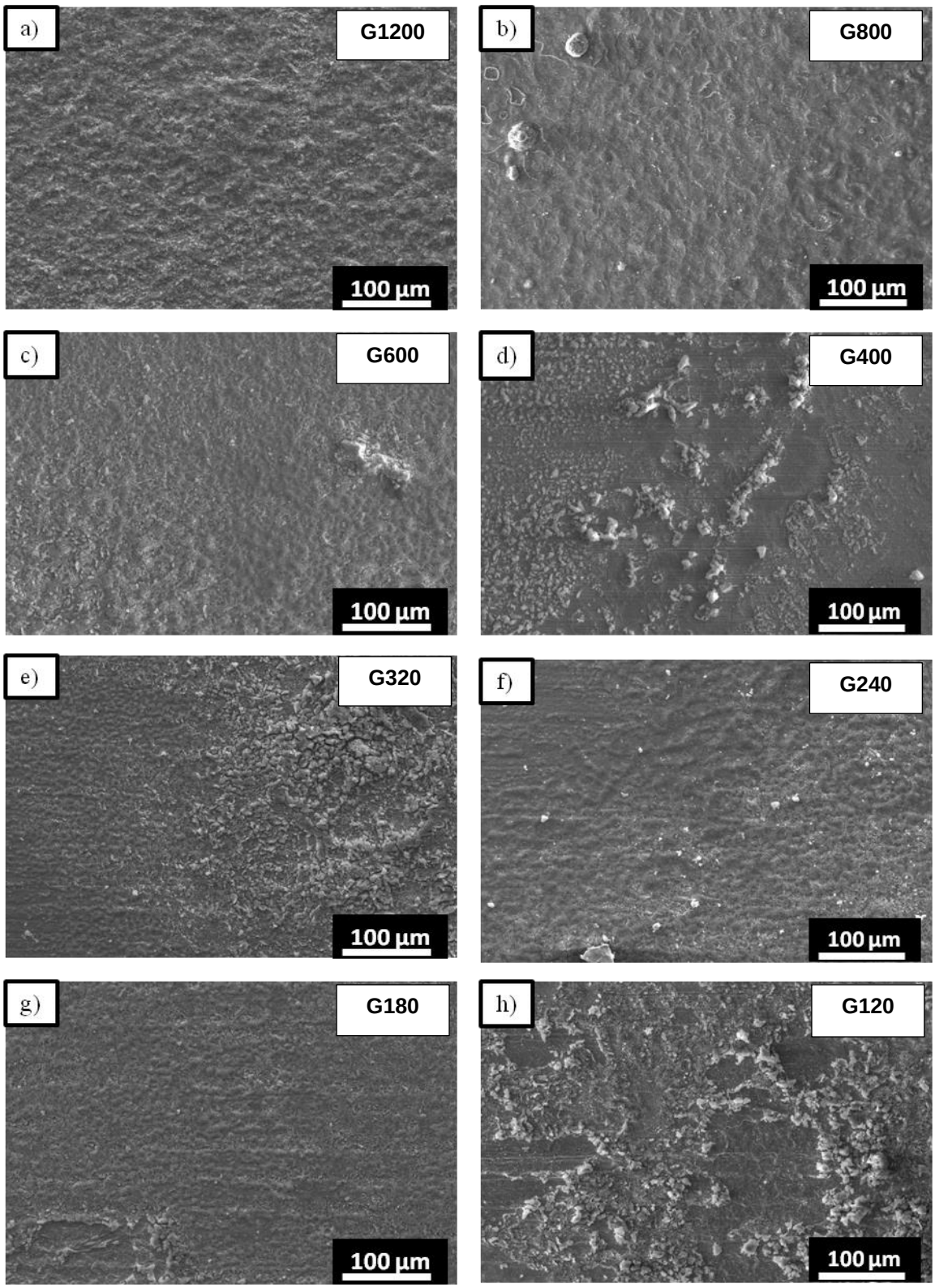

Figure 6-12 SEM micrographs of mild steel samples a) G1200, b) G800, c) G600, d) G400, e) G320, f) G240, g) G180 and h) G120 after corrosion

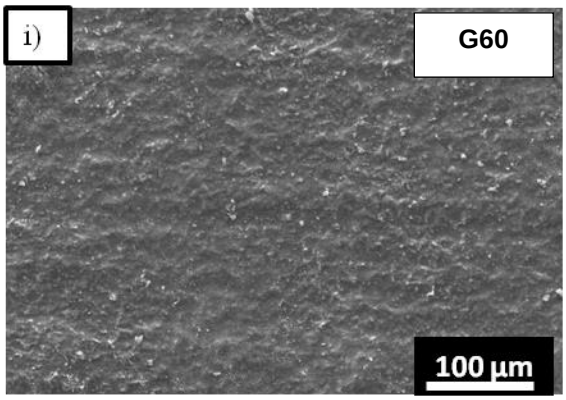

Figure 6-12 (Cont) SEM micrograph of mild steel sample i) G60 after corrosion

Therefore, according to SEM micrographs, for samples G1200, G800 and G600 (Figures 6-12 (a-c)) there is no evidence of any remaining unidirectional roughness (grooves) and there is a uniform deposition of corrosion products. For sample G400 in Figure 6-12 (d), some evidence of remaining unidirectional roughness is observed. Corrosion products in this case are not as uniform as previous samples. Samples G320-G120 (Figures 6-12 (e-h)), showed more evidence of unidirectional roughness but at a larger scale than grooves in as-ground specimens. Finally, sample G60, (Figure 6-12 (i)), is the most pronounced evidence of original grooves but in a larger scale.

6.3 Roughness Measurement Results

Profilometry (Wyko Surface Profiling System NT-1100) was used to characterize the surface and measure the average surface roughness (R_a), root-mean-squared roughness (R_q), the average of the ten greatest peak-to-valley separations (R_z) and the peak-to-valley difference calculated over the entire measured array (R_t) both before and after corrosion testing. Tables 6-3 to 6-6 summarize the calculated values for R_a , R_q, R_z and R_t before and after corrosion testing. In all roughness parameters, the roughness has increased after corrosion. For samples with lower roughnesses, the increase in roughness after corrosion is more significant which can be related to more corrosion products on the surface. In all cases, sample G60 has the lowest change in roughness after corrosion. The average roughness according to Table 6-3 is 1446 nm for the roughest sample (G60) which decreased to 128 nm for the smoothest sample (G1200). After corrosion however, both values have increased. This increase for sample G60 is 7% but for sample G1200 is 878%.

Table 6-3 R_a values for mild steel before and after corrosion testing

Sample	Roughness values		Roughness change %
	R_a (Before Corrosion Testing) (nm)	R_a (After Corrosion Testing) (nm)	
G60	1446	1550	7
G120	916	1688	84
G180	819	1725	110
G240	401	1384	245
G320	272	1460	436
G400	217	1578	625
G600	185	1586	753
G800	171	1588	826
G1200	128	1254	879

As it is seen, by decreasing the roughness, the resultant change in roughness after corrosion is increased which indicate more corrosion products or relatively deeper areas formed on the surface of smoother mild steel samples. Corrosion products result in an increase in height of different points especially outside the grooves on the surface and can increase the average roughness.

R_q values are presented in Table 6-4. The roughness parameters have higher values compared to R_a and in this case the roughness for sample G60 is 1792 nm and by decreasing the roughness, R_q decreases to 162 nm. These values increased to 1944 nm and 1600 nm after corrosion respectively. For R_q also similar to R_a, the change in roughness after corrosion is less for sample G60 (9%) and by decreasing the roughness more change is observed. For this parameter also, sample G1200 has the highest change in roughness after corrosion (886%).

Table 6-4 R_q values for mild steel before and after corrosion testing

Sample	Roughness values		Roughness change %
	R_q (Before Corrosion Testing) (nm)	R_q (After Corrosion Testing) (nm)	
G60	1792	1944	9
G120	1211	2116	75
G180	1028	2235	117
G240	507	1750	245
G320	345	1866	440
G400	273	2008	634
G600	230	1984	759
G800	209	1998	855
G1200	162	1600	886

In the case of R_q also, the increase in roughness after corrosion can be related to corrosion products formed on the surface (especially outside the grooves) or deeper grooves after corrosion. Both factors result in areas with positive and negative height values (peaks and valleys respectively) and increase the roughness.

Table 6-5 presents the R_z values for samples with different roughnesses before and after corrosion. The R_z for sample G60 showed an increase of about 43% in roughness. In the case of the smoothest sample (G1200) however, an increase of 873% in roughness after corrosion was observed. Therefore, by considering all the samples, it is seen that the change in roughness is higher for smoother surfaces. According to the values of R_z which is calculated based on the ten greatest peaks to valleys on the surface also, the increase in R_z indicates an increase in height of the peaks or depth of the valleys or both. Results are in

agreement with R_a and R_q confirming more corrosion products or deeper grooves on smoother surfaces.

Table 6-5 R_z values for mild steel before and after corrosion testing

Sample	Roughness values		Roughness change %
	R_z (Before Corrosion Testing) (µm)	R_z (After Corrosion Testing) (µm)	
G60	10.65	15.18	43
G120	9.39	17.25	84
G180	7.94	16.36	106
G240	4.42	15.85	259
G320	2.96	14.64	395
G400	2.83	15.82	459
G600	1.95	14.67	653
G800	1.62	15.44	854
G1200	1.44	13.97	873

R_t is the last roughness parameter listed in Table 6-6 for mild steel samples before and after corrosion. The values are almost in the same range as R_z and in this case also less increase in roughness is observed for sample G60 (48%) and more increase in roughness after corrosion is seen for samples G800 and G1200 which are the smoothest samples (862% and 830% respectively). Based on the definition of this parameter which is peak to valley difference over the entire area, an increase in R_t after corrosion means that the height of the peaks has increased which is because of corrosion products formed on the surface. Other possibility for increased R_t after corrosion is increase in depth of some grooves.

Considering both R_z and R_t, it can be seen that in each case the roughness after corrosion ended up with almost the same values regardless of value before corrosion. However, more increase was observed after corrosion on smoother samples. The results of R_z and R_t measurement are in agreement with R_a and R_q values showing almost the same roughness parameter for the surfaces covered with corrosion products.

Table 6-6 R_t values for mild steel before and after corrosion testing

Sample	Roughness values		Roughness change %
	R_t (Before Corrosion Testing) (µm)	R_t (After Corrosion Testing) (µm)	
G60	12.22	18.13	48
G120	10.67	19.66	84
G180	8.70	18.78	116
G240	5.39	18.09	236
G320	3.39	16.32	381
G400	3.38	18.86	458
G600	2.22	16.46	641
G800	1.81	17.38	863
G1200	1.67	15.54	830

6.4 Roughness profiles before and after corrosion

2D images, 3D textures, X and Y profiles and histogram data before and after corrosion testing were analyzed. Among samples G60 to G1200 with different roughnesses, images related to two samples (G60 and G800) are presented as two examples of surfaces with high and low roughness respectively and the general trend for all samples is explained. The results, before and after corrosion, for the other samples can be found in Appendix C_1-C_3.

2D surface image and 3D surface texture of sample G60 are presented in Figures 6-13 to 6-16, before and after corrosion testing. In sample G60, the coarse surface with wide and deep grooves is shown in both 2D and 3D images before corrosion (Figures 6-13 and 6-15). From sample G180 which is one of the rough surfaces until sample G1200 which is the smoothest sample, the surface looks more uniform without any deeper grooves compared to samples G60 and G120 (Appendix C_1). Generally, by decreasing the roughness from sample G60 to G1200, finer grooves are observed in 2D and 3D images before corrosion.

2D and 3D images for sample G60 after corrosion are shown in Figures 6-14 and 6-16. The images after corrosion are not from exactly the same area of the sample that we analyzed before corrosion, so changes seen can be described in a qualitative fashion. The images after corrosion also show the remaining grooves much better than SEM. After corrosion, by decreasing the roughness from sample G60 to G1200, no grooves are seen in 2D and 3D

images especially for smoother surfaces which is an indication of uniform and more severe corrosion on samples with lower roughnesses. The reason for more corrosion on smoother surfaces is direct contact between solution and the substrate (In contrast with rougher surfaces that corrosion products fill the grooves and partially protect the substrate).On rougher surfaces however (samples G60 and G120), some grooves are still remained after corrosion but in a larger scale. By decreasing the roughness, the number of remained grooves is decreased after corrosion compared to sample G60 and there is nothing remained from the unidirectional roughnesses created on the surface of mild steel (Appendix C_1). 2D image and 3D surface texture show a surface covered with corrosion products with the formation of corrosion products both at the bottom of the grooves (valleys) and also on the peaks of the surface. In addition, on smooth surfaces different deep areas which shows corroded surface can be observed. These results are in agreement with SEM observations (Figure 6-11). In SEM also rougher surface (G60), showed less corrosion and some hints of the unidirectional roughnesses still remain after corrosion. As discussed in the potentiodynamic polarization results in Section 6.1.1, corrosion products formed on the rougher surfaces can partially protect the surface which will result in less corrosion rate on rougher surfaces compared to smooth ones. Thus, the 3D images confirm the findings from SEM.

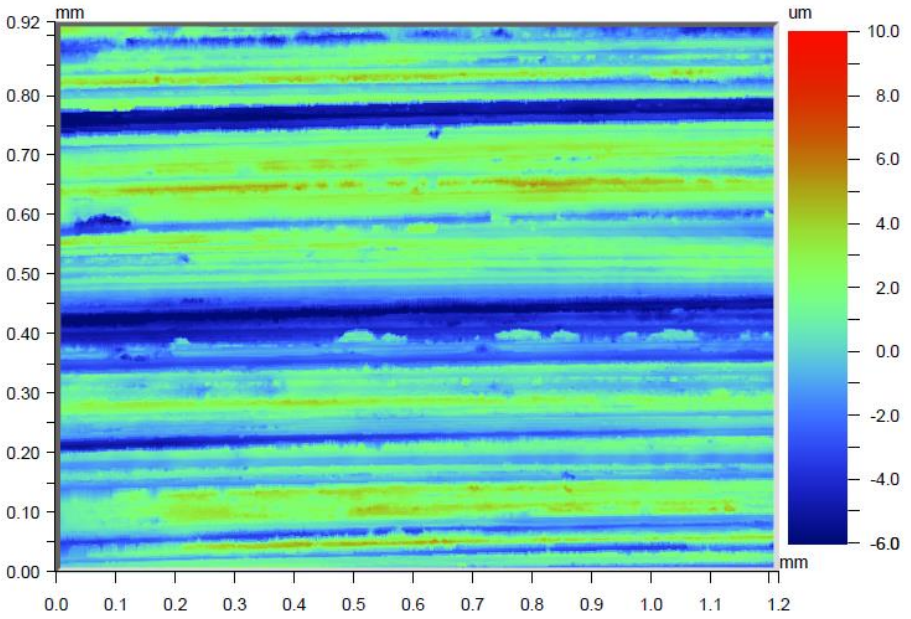

Figure 6-13 Sample G60 2D roughness before corrosion

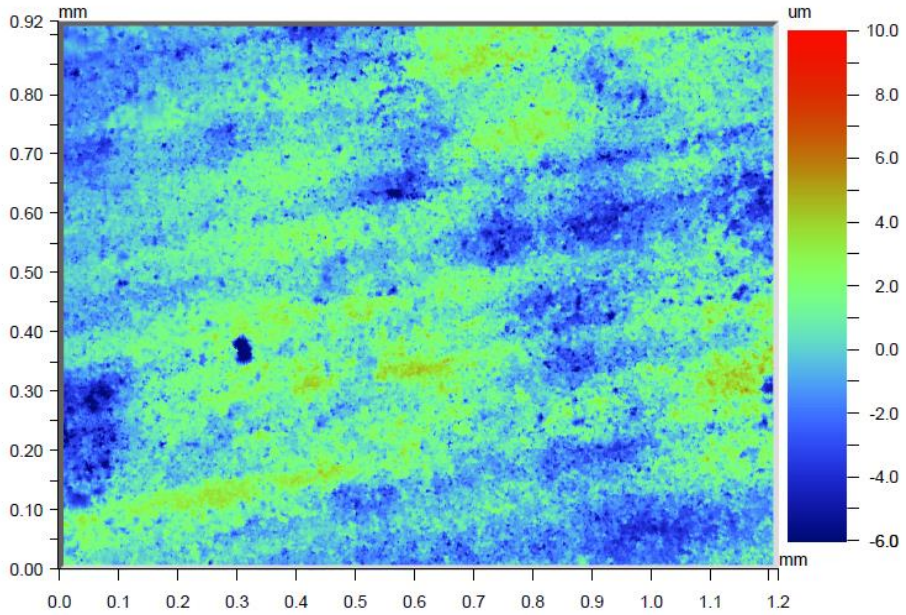

Figure 6-14 Sample G60 2D roughness after corrosion

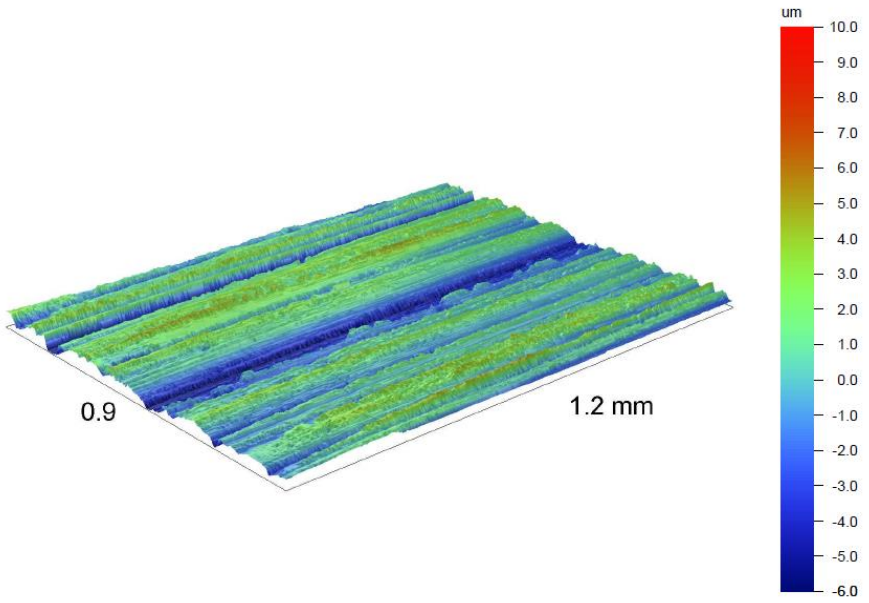

Figure 6-15 Sample G60 3D roughness before corrosion

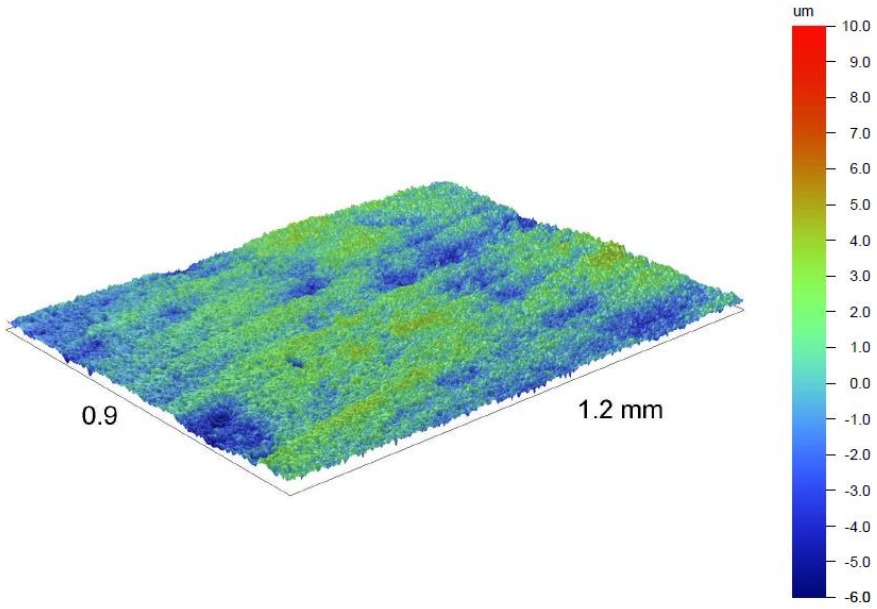

Figure 6-16 Sample G60 3D roughness after corrosion

On both smooth and rough surfaces the roughness increased because of the formation of corrosion products after corrosion to a level dependant on the surface morphology of the corrosion products. But on rougher surfaces (such as

G60), corrosion products fill the grooves and also cover the peaks and will result in less increase of the roughness. The results are in agreement with different roughness parameters measured in Section 6.3. In Section 6.3, the highest increase in roughness was measured for smoother samples.

Sample G800 is a sample with smooth surface. 2D and 3D images show an almost flat surface without any defects or scratches before corrosion. 2D and 3D images for sample G800 before and after corrosion are shown in Figures 6-17 to 6-20. The only things which are seen are very fine unidirectional roughnesses on the surface before corrosion. For the smoothest sample (G1200), 2D image and 3D surface texture show the surface appearance with some fine grooves before corrosion (Appendix C_1). The scanned area was selected in a manner to show the flatness and sensitivity of the surface to some grooves which are seen at the bottom of 2D image in Figure 6-17. The differences between the average roughnesses of these grooves are on a nanometer scale.

After corrosion on smooth surfaces, the grooves have been corroded away, some corrosion products have filled some of the grooves, and deep corroded areas are created and resulted in a significant increase in roughness of the surface (The results were reported in Section 6.3). For each sample five different spots were analysed. This increase in roughness is more on smoother surfaces due to more deep areas (inside the circle in Figure 6-20) and corrosion products formed on the surface (shown by arrows in Figure 6-20). As it can be

seen, the surface has changed a lot and there is no sign of unidirectional roughnesses remained from before corrosion (Figures 6-18 and 6-20).

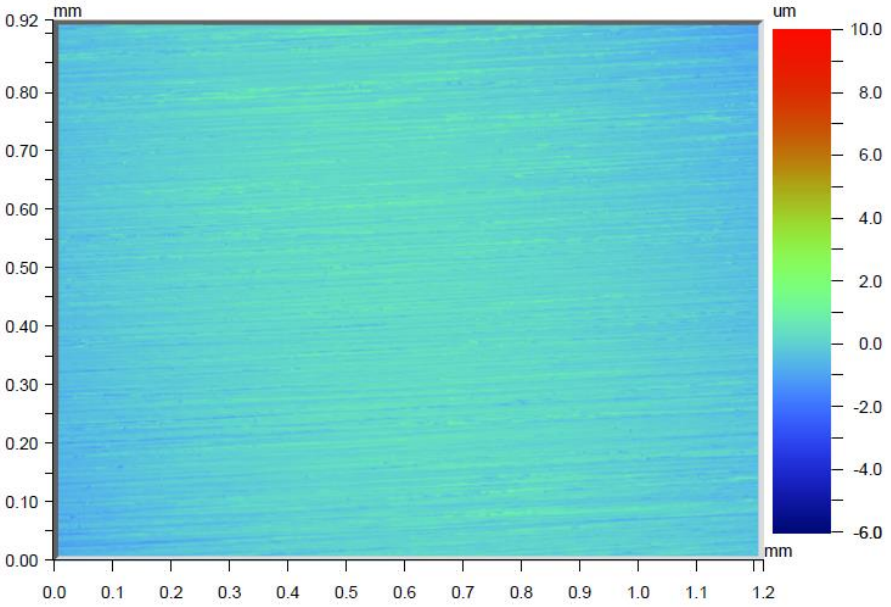

Figure 6-17 Sample G800 2D roughness before corrosion

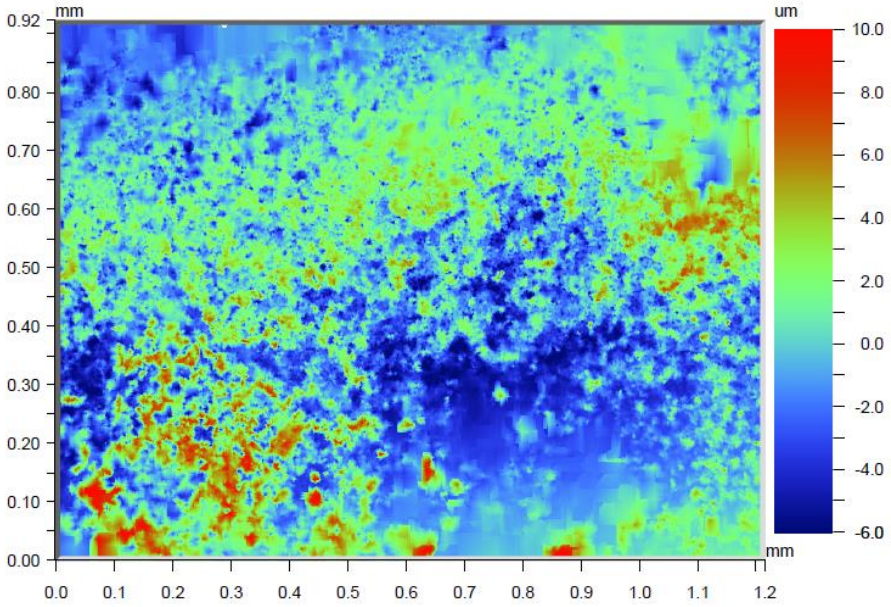

Figure 6-18 Sample G800 2D roughness after corrosion

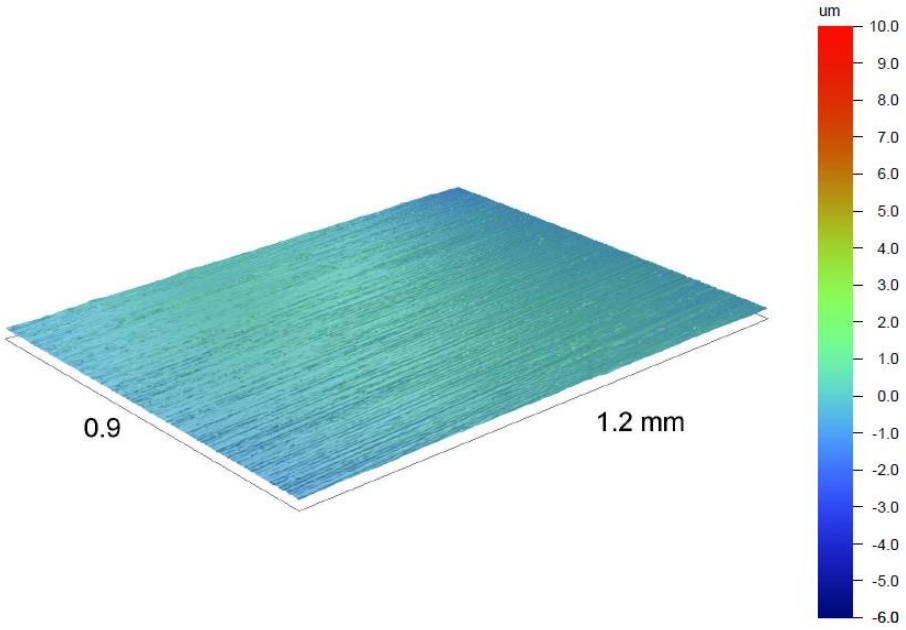

Figure 6-19 Sample G800 3D roughness before corrosion

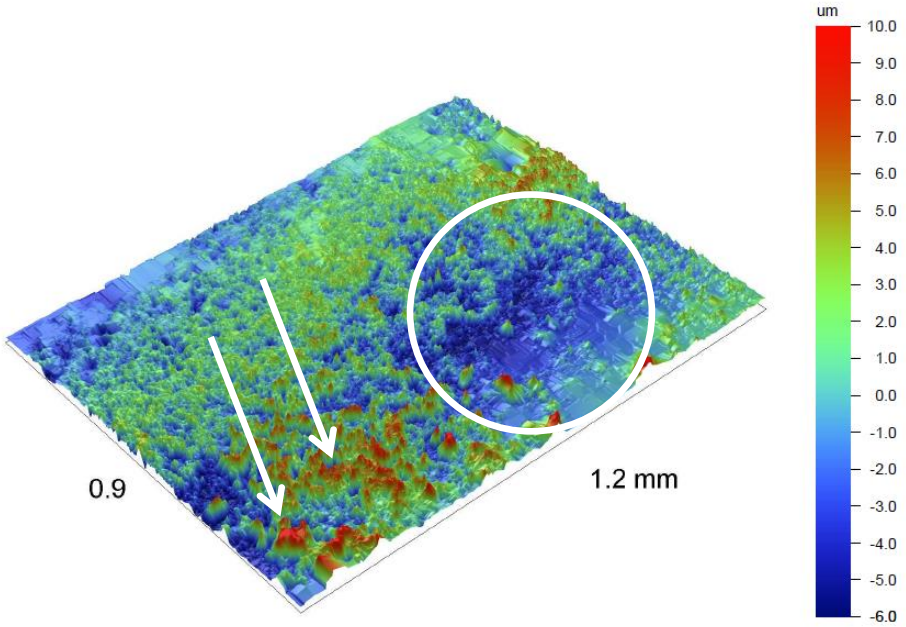

Figure 6-20 Sample G800 3D roughness after corrosion

X and Y profiles show some sharp peaks which stand for points with different heights (valleys or peaks) on the surface for all samples before corrosion. In some cases these peaks are related to a deeper groove or a scratch. Generally, the number of fluctuations and magnitude of the peak/valley is reduced after corrosion with some disappearing and the rest getting smaller. In sample G60, the X and Y profiles display a significant change in point's height which is an indication of deep grooves and also so many sharp peaks on the surface (Figure 6-21). By decreasing the roughness from samples G120 to G1200, the X and Y profiles show less change in height of the points compared to sample G60 (smaller fluctuations) which means less deep valleys and sharp peaks on the surface (Appendix C_2). In the smooth surfaces such as G600, G800 and G1200, the surface is very sensitive to even small scratches or deeper grooves or peaks so; even a small deviation from adjacent height values on the surface will result in peaks or valleys in the X and Y profile.

X and Y profiles for sample G60 after corrosion, Figure 6-22, also display less sharp deviations (with smaller fluctuations) indicating a more uniform surface compared to before corrosion. It means that corrosion products have filled the grooves to some extent and the peaks have been resolved. The hints in 2D and 3D images remained from unidirectional roughnesses after corrosion also confirm an almost uniform surface covered by corrosion products.

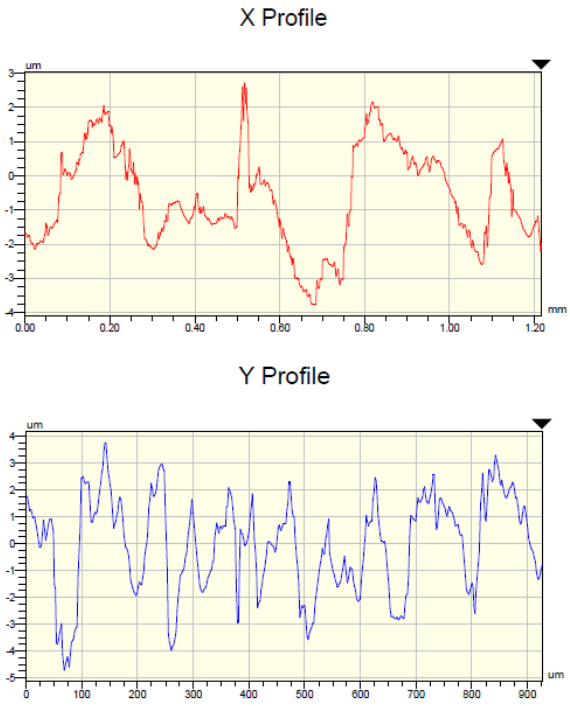

Figure 6-21 X-profile and Y-profile of sample G60 before corrosion

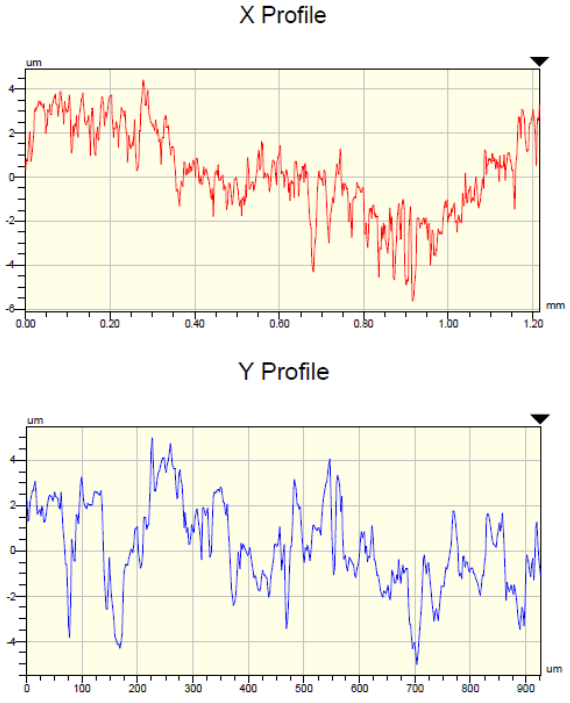

Figure 6-22 X-profile and Y-profile of sample G60 after corrosion

The X and Y profiles of sample G800 before corrosion are shown in Figure 6-23. In sample G800, X and Y profile display a normal distribution of data (without so many sharp peaks and valleys) before corrosion with one or two deviations from other values indicating a uniform surface with very fine valleys and peaks. As mentioned in the case of smoother samples, the surface is more sensitive to small changes in roughness so; two sharp peaks are magnified in the Y profile.

By decreasing the roughness, X and Y profiles display more peaks and valleys after corrosion which indicates corrosion products and corroded areas on the surface. Figure 6-24 also displays X and Y profiles for sample G800 after corrosion. X and Y profiles display more deviation around zero and sharper peaks and valleys compared to before corrosion on the scanned area. No evidence of small fluctuations can be seen from before corrosion indicating the increased roughness on the surface which agrees with the four different roughness parameters reported in Section 6-3.

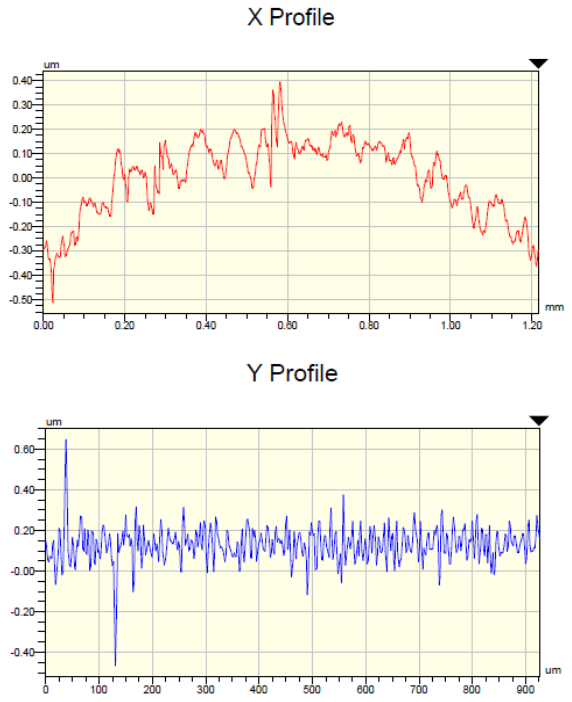

Figure 6-23 X-profile and Y-profile of sample G800 before corrosion

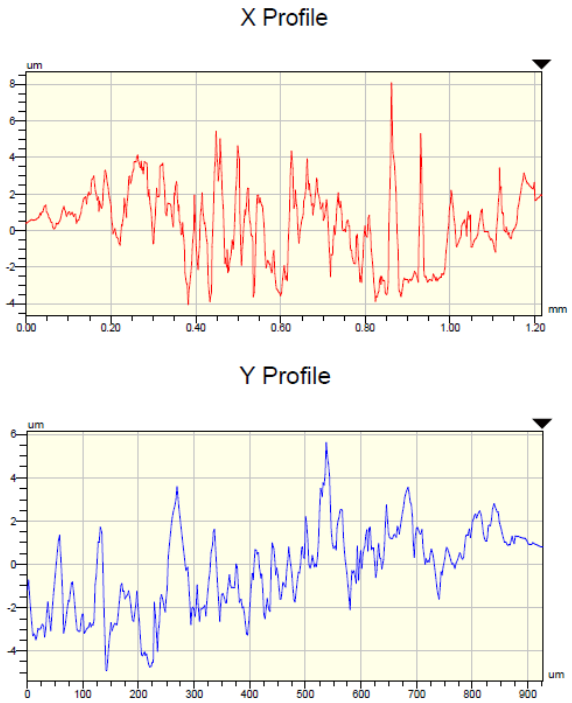

Figure 6-24 X-profile and Y-profile of sample G800 after corrosion

Figure 6-25 shows the histogram result for sample G60 before corrosion. This histogram shows the height of different points and a completely uncommon shape which is not around zero and symmetrical. It shows different points with variety of heights with irregularities that are the results of deeper grooves and sharp peaks in some parts.

By changing the roughness from sample G60 to G1200, the histogram curves seem to be more uniform before corrosion and in a normal distribution. It confirms that the average roughness of these samples is decreasing (Appendix C_3). By decreasing the roughness also the data are around zero and there is a normal distribution of roughness on the surface which was expected for smoother surfaces before corrosion. The histogram curve of rougher samples is different from smoother samples and it is possible to observe some points with different heights in the histogram (some irregularities). From sample G240 to G1200 there is almost no irregularity in the histogram and also the width of the histogram is decreased compared to rougher samples indicating less variation of points height on the surface. The histograms for samples G240 to G1200 show symmetry around zero which indicates a normal distribution of roughness on the surface.

After corrosion, the histogram curves have an approximately uniform and normal shape for sample G60 to G1200. For all the samples, there is a normal distribution of roughness on the surface which can be as a result of corrosion products that filled the grooves and have led to a more uniform surface with a normal distribution of heights around zero. As it is observed, the height

distribution is more uniform compared to that of the initial rough sample (G60) and less uniform in comparison with samples G240 to G1200 (Appendix C_3). This is an indication of filled grooves on rougher surfaces and increasing roughness as a result of production of corrosion products at the same time.

After corrosion, the distribution of points was extended (increased width in histograms) which is due to increase in height or depth at some areas on the surface. After corrosion also 95% of data is between -1320 and 4920 nm which shows a wider range of data compared to before corrosion (95% of data was between -1040 and 4280 nm). It shows an increase in roughness and confirms different roughness parameters measured in Section 5.3. Some irregularities in the histogram curves such as samples G400, G600 and G800 after the corrosion testing can be refer to some local corroded areas and corrosion products on the surface of the samples.

In sample G60, histogram also show a more uniform shape after corrosion compared to before corrosion testing indicating filled grooves with corrosion products and less irregularities in the points distribution (Figure 6-26). By decreasing roughness toward sample G120, the width of the histogram also shows an increase which means that there are more points on the surface with height difference compared to the flat surface (height of zero) (Appendix C_3). It can be concluded that corrosion products and also some corroded areas have increased the surface roughness. This increase is roughness was much more on smoother surfaces because the final roughness is primarily corrosion products.

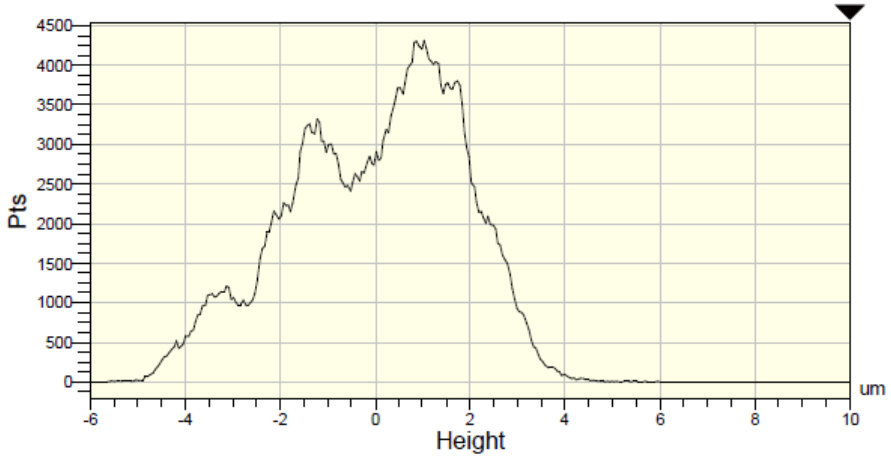

Figure 6-25 Histogram curve of sample G60 before corrosion

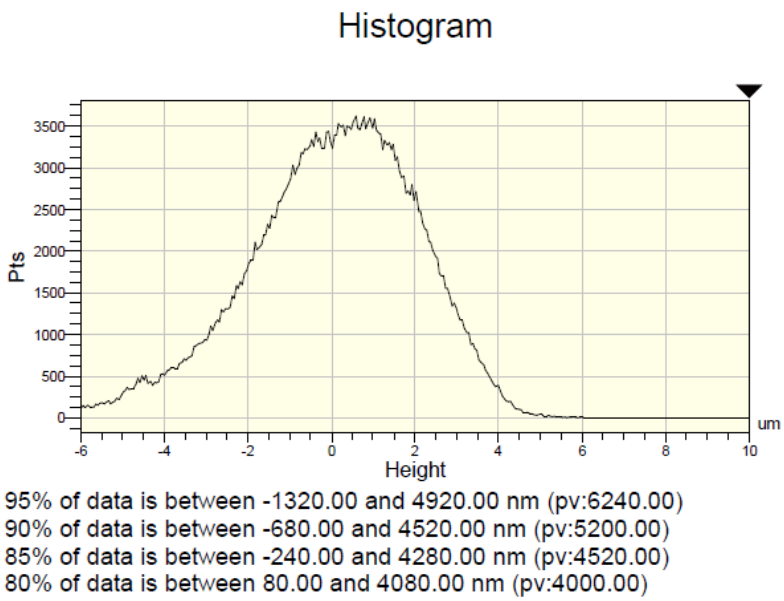

Figure 6-26 Histogram curve of sample G60 after corrosion

Figure 6-27 shows the histogram result for sample G800 before corrosion. Histogram has a perfect symmetry shape with data close to zero which means a normal distribution of points with low heights and depth on the surface. The width of the histogram is also less compared to previous samples indicating less variety of data and less difference between the heights of the points on the surface which proves the lower roughness and flatness of the surface.

Figure 6-28 shows the histogram result for sample G800 after corrosion. Histogram also displays a wider bell shape plot with some irregularities due to corrosion products morphology and indicating some local corroded areas and corrosion products. By decreasing the roughness toward sample G800, a significant increase is observed in the width of the histograms compared to before corrosion telling that the height and depth of the points have increased and the data are far from zero (flat surface) in the histograms. It means that corrosion has happened on the surface and resulted in deeper areas (inside the circle in Figure 6-20) especially on smoother surfaces and the corrosion products (shown by arrows in Figure 6-20) have increased the height of the peaks in other areas. Both parameters resulted in a greater increase in roughness of smoother surfaces (G800 and G1200) as detailed in Section 6-3.

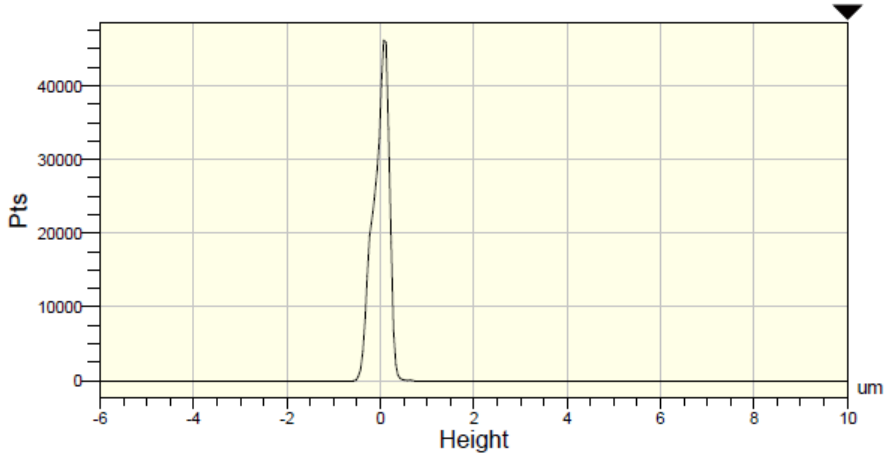

95% of data is between 1720.00 and 2160.00 nm (pv:440.00)
90% of data is between 1760.00 and 2160.00 nm (pv:400.00)
85% of data is between 1760.00 and 2120.00 nm (pv:360.00)
80% of data is between 1800.00 and 2120.00 nm (pv:320.00)

Figure 6-27 Histogram curve of sample G800 before corrosion

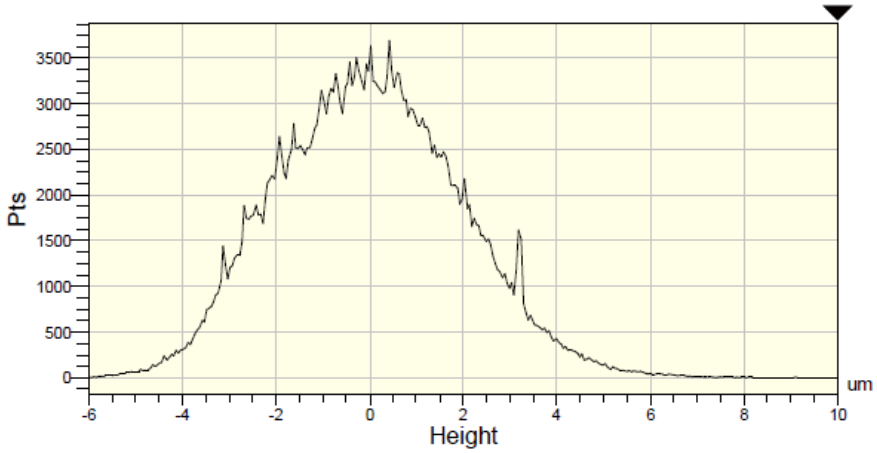

95% of data is between -1080.00 and 4800.00 nm (pv:5880.00)
90% of data is between -480.00 and 4520.00 nm (pv:5000.00)
85% of data is between -440.00 and 4000.00 nm (pv:4440.00)
80% of data is between -320.00 and 3680.00 nm (pv:4000.00)

Figure 6-28 Histogram curve of sample G800 after corrosion

6.5 EDS Results

Energy dispersive spectroscopy (EDS) was used to measure the oxygen and sulphur content of the surface both before and after corrosion testing. Table 6-7 presents oxygen concentration both before and after corrosion on surfaces with different roughnesses. All samples had similar oxygen contents before corrosion testing but the oxygen content increased significantly for all samples after corrosion.

Looking at the oxygen content increase of the surface, all samples show a significant increase. For the roughest samples (G60-G120) the increase in oxygen content is less compared to other samples. As demonstrated from the electrochemical results, G60 and G120 exhibited the lowest corrosion rates, and the corrosion rate decreased with increasing roughness. It is known that mild steel has no ability to form a passive layer therefore; the increase in oxygen content is related to corrosion products on the surface which protect the surface partially especially on rougher surfaces. Profilometry results also confirmed less increase in roughness of rough samples of mild steel and showed a uniform corrosion product layer formed on rough samples.

The sulphur content, expressed as the ratio of intensities of the $S_{k\alpha}$ to $Fe_{k\alpha}$ peaks, is also shown in Table 6-7. As it is seen, generally rougher samples (G60-G180) had higher sulphur contents compared to smoother surfaces (G600-G1200). This trend also confirms the SEM, profilometry and corrosion testing result indicating the formation of corrosion products on rougher surfaces. More

sulphur content of the corrosion product layer on rougher samples confirms the mechanism explained in the corrosion and SEM sections (Sections 6.1.1 and 6.2.2) indicating partial protection against corrosion of rough surfaces by the corrosion products.

Table 6-7 Oxygen and sulphur contents on the surface of mild steel samples before and after corrosion testing.

Sample	Oxygen wt% before corrosion	Oxygen wt% after corrosion	Oxygen wt% difference	(S/Fe)
G60	2.51	24.63	22.12	0.140
G120	2.92	20.36	17.44	0.136
G180	2.93	31.61	28.68	0.126
G240	2.55	30.49	27.94	0.125
G320	2.38	33.67	31.29	0.134
G400	2.35	26.28	23.93	0.133
G600	2.23	31.95	29.72	0.093
G800	2.63	26.95	24.32	0.085
G1200	2.37	28.85	26.48	0.091

6.5.1 **Before Corrosion:**

Figure 6-29 illustrates the EDS spectra on mild steel sample G320 before corrosion testing. The results for other samples are presented in Appendix D_1. As is expected, strong Fe peaks are observed with some oxygen and very small amount of carbon. All the chemical composition analysis before the corrosion testing showed the same elements including Fe, O and C.

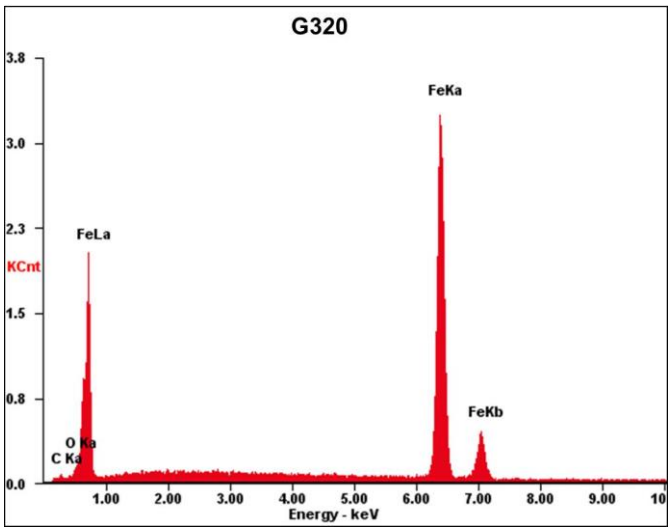

Figure 6-29 EDS analysis of sample G320 before corrosion testing

6.5.2 **After Corrosion**

Figure 6-30 illustrates the EDS analysis results on mild steel sample G320 after corrosion testing. The results for other samples are presented in Appendix D_2. In all samples especially samples G180 to G1200 there is a significant increase in oxygen content which is related to a severe general corrosion and the corrosion products formed on the surface. The same thing has happened for rougher surfaces (G60 and G120) but with lower amounts of oxygen and less degree of corrosion. The increase in oxygen content is obvious from the peaks after corrosion. A sulphur peak is also observed in the EDS analysis result which is related to the solution used for the experiments.

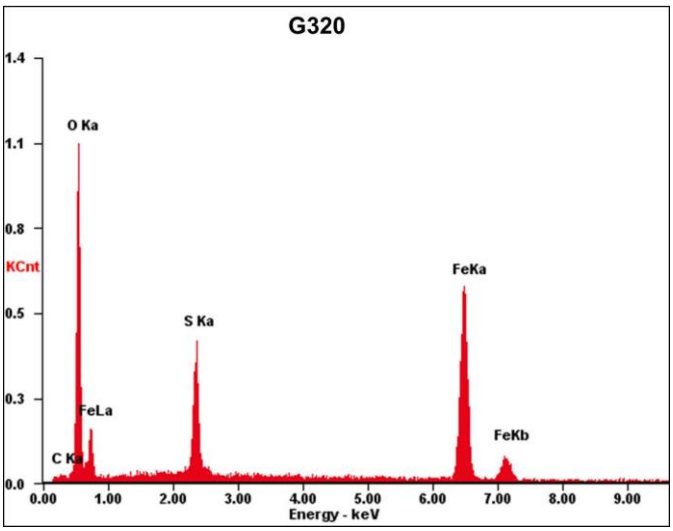

Figure 6-30 EDS analysis of sample G320 after corrosion testing

6.6 XRD

XRD was also performed in order to characterise different compounds formed on the surface after corrosion. Figure 6-31 displays XRD results for the roughest (G60) and the smoothest (G1200) samples as two examples. The important point is that roughness has not had any effect on the corrosion products and all the samples with different unidirectional surface roughnesses had similar surface compounds after corrosion testing. Interestingly the results approve almost the same corrosion potentials values achieved in potentiodynamic polarization technique in this chapter for all the surfaces with different roughness values. The result also is in agreement with EDS analysis about the elements exists on the surface of the sample (oxygen and sulphur).

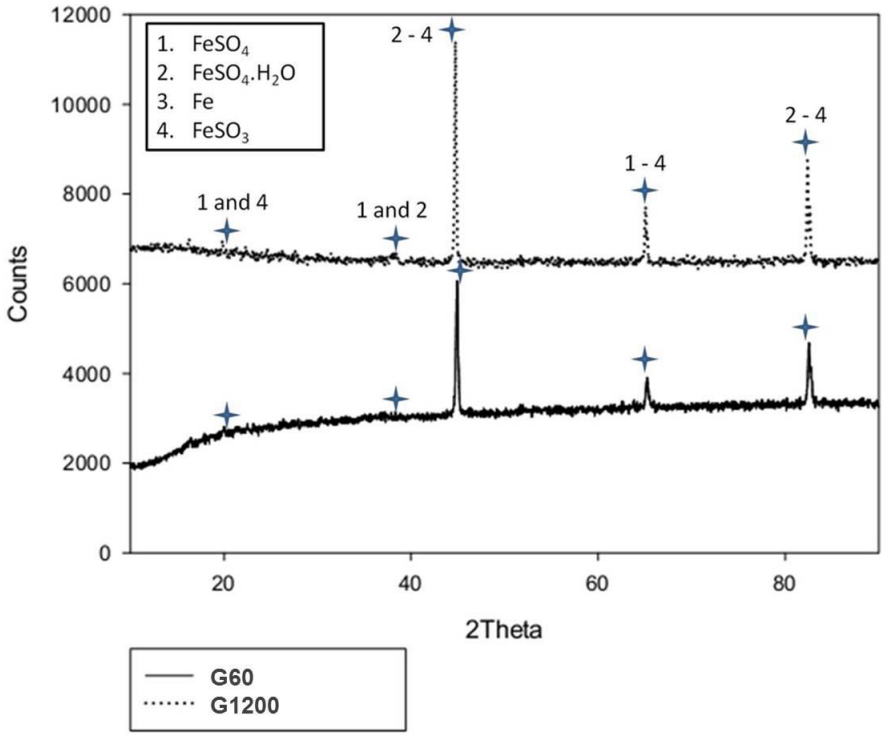

Figure 6-31 XRD analysis of samples G1200 and G60 after corrosion

6.7 Roughness parameters before and after corrosion

Figures 6-32 to 6-35 display different surface roughness parameters including R_a, R_q, R_z and R_t of all unidirectionally ground samples before and after corrosion testing. In all cases, by increasing the grit number from G60 to G1200, the roughness decreases systematically before corrosion testing and in all samples the value of various roughness parameters has increased after corrosion. This increase is lower for rougher samples indicating less change in roughness and probably less corrosion products on the surface because SEM and EDS results showed that on rougher samples some grooves are visible after corrosion and corrosion testing also showed less corrosion on rougher samples.

The values of R_a, R_q, R_z and R_t measured for mild steel before corrosion testing are two times larger compared to the nickel data presented in Section 5.3. The error bars are also larger and show more deviations for different roughness parameters measured in the case of mild steel compared to nickel as presented in Section 5.6.

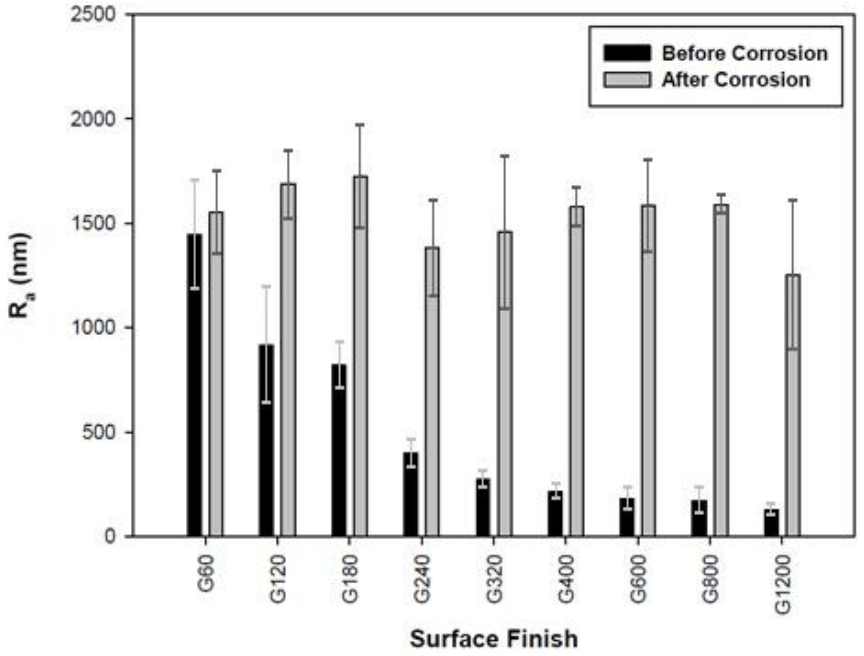

Figure 6-32 R_a values for mild steel before and after corrosion testing.

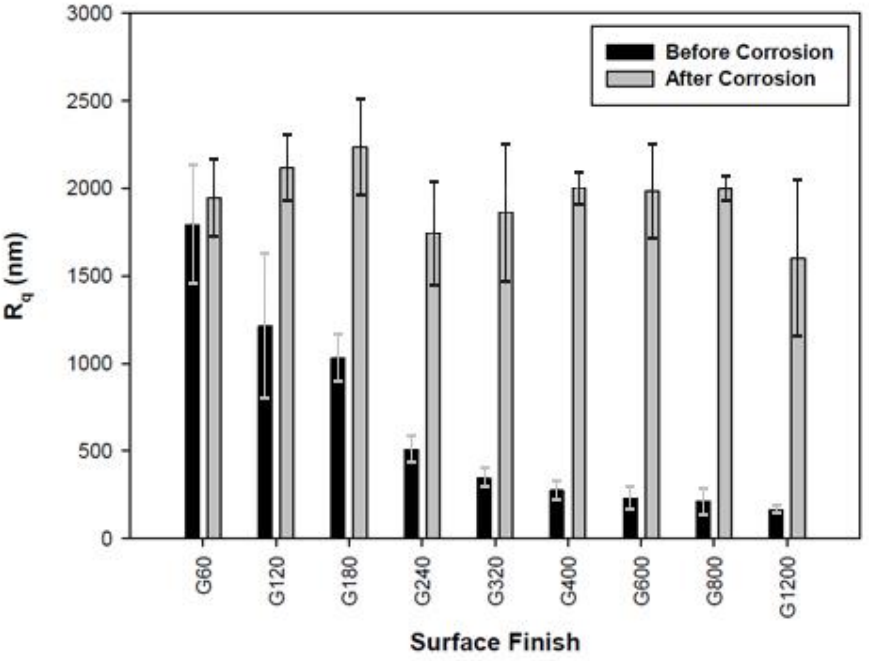

Figure 6-33 R_q values for mild steel before and after corrosion testing.

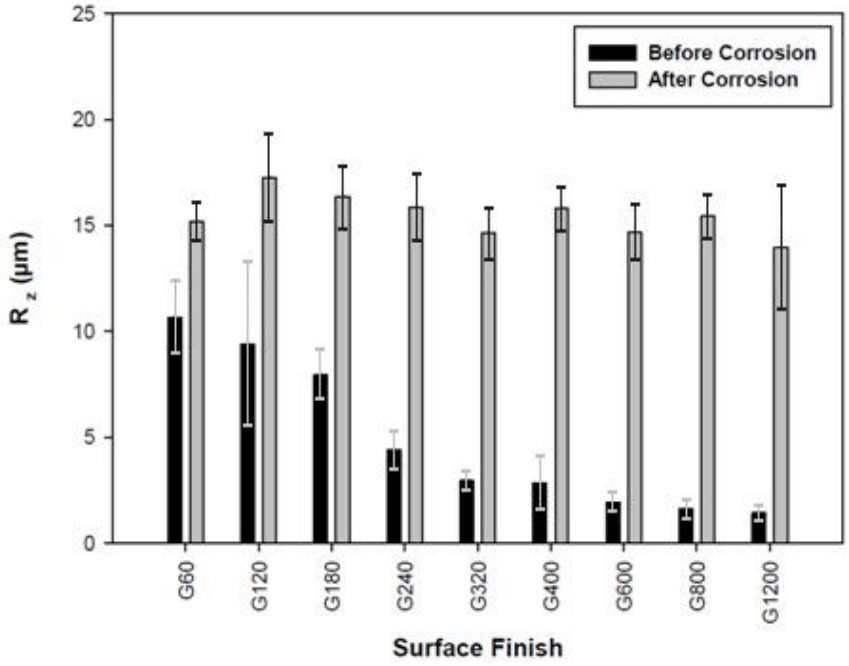

Figure 6-34 R_z values for mild steel before and after corrosion testing.

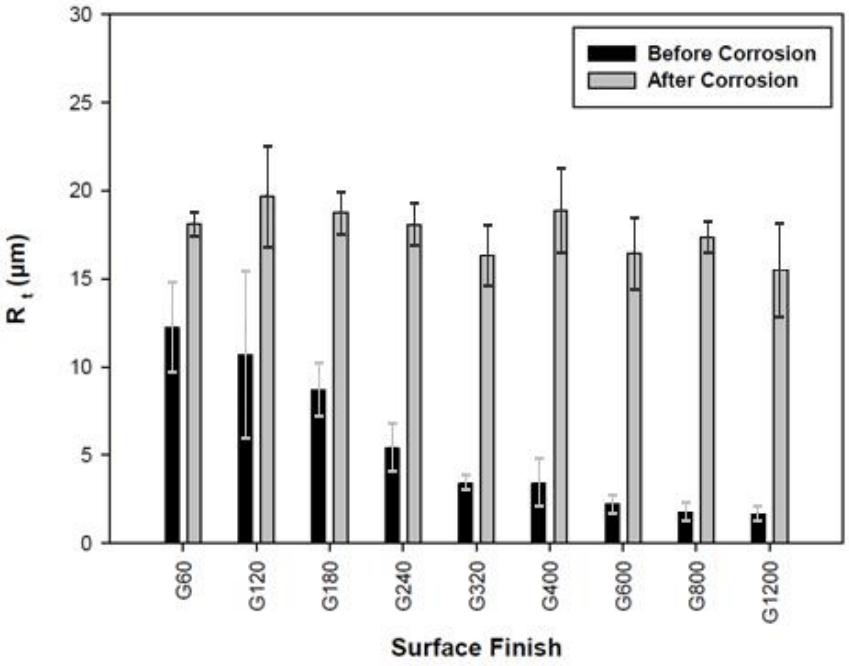

Figure 6-35 R_t values for mild steel before and after corrosion testing.

6.8 Relationship between corrosion rate and different roughness parameters

Figures 6-36 to 6-39 show the change in corrosion rate as determined by potentiodynamic polarization tests versus various surface roughness parameters (R_a in Figure 6-36, R_q in Figure 6-37 R_t in Figure 6-38, and R_z in Figure 6-39). As it is seen, all plots show the same general trends and in all cases by increasing the surface roughness, the corrosion rate decreased. These results are in agreement with previous results which investigated the appearance, oxygen and sulphur concentration and roughness parameters in SEM, EDS and profilometry tests respectively. As noted in the literature survey in Chapter 2, there is a trend (increase of corrosion rate by decreasing roughness) seen for corrosion of metals with no ability to form a passive layer [49, 73]. This trend is in opposite direction compared to metals with ability to form a protective passive film [79, 188].

Looking at the general shape of the plots in Figures 6-36 to 6-39, we can see that after a limit, decreasing the surface roughness dramatically increases the corrosion rate. The rate of change of corrosion rate with roughness decreases before this limit and, for the highest roughnesses, the corrosion rate appears to reach a plateau. In the case of nickel, however, as discussed in Chapter 5, Section 5.7, by increasing the roughness corrosion rate increased to a limit and after that limit the corrosion rate reached a plateau. The interesting point is that in both cases the dependence of corrosion rate on roughness is more until the average roughness of about 200 nm. After this limit the corrosion rate of

nickel increased and the corrosion rate of mild steel decreased and both reached a plateau.

A reverse trend compared to mild steel was also reported by Li and Li [80] for Cu in a 3.5% NaCl solution which was expected (similar to stainless steel, titanium, aluminium and nickel) because in those cases unlike mild steel the metal could form a protective surface layer. In the case of mild steel however, formation of corrosion products in rougher surfaces protected the surface to some extent and resulted in less corrosion. But on smoother surfaces, there is a continuous direct contact between the solution and the substrate and there is no formation and trapping of corrosion products inside the grooves to partially protect the surface. Therefore, more corrosion happens on smoother surfaces.

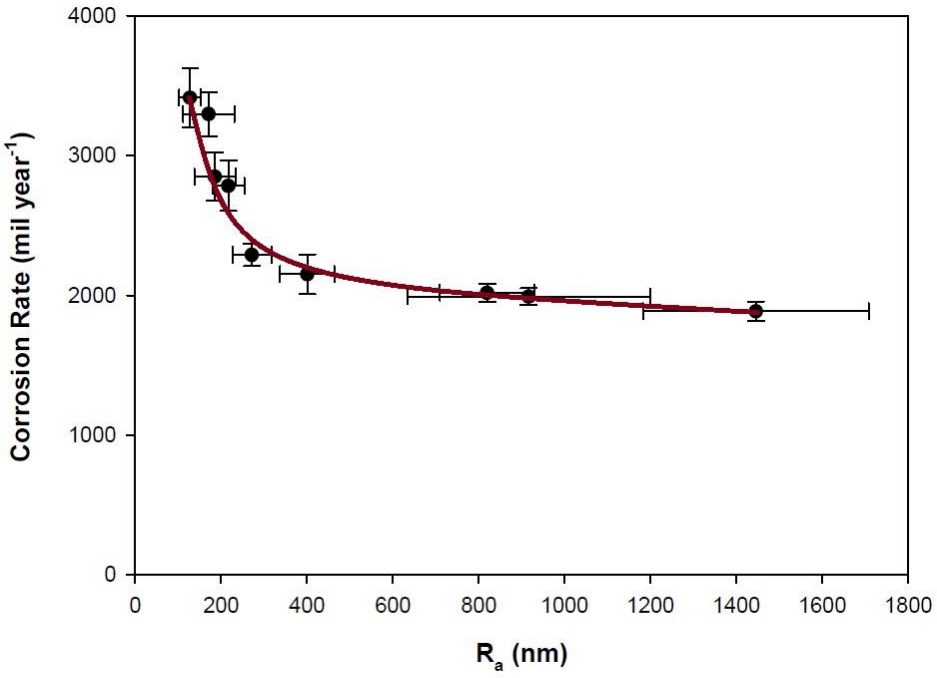

Figure 6-36 Dependence of corrosion rate of mild steel on R_a

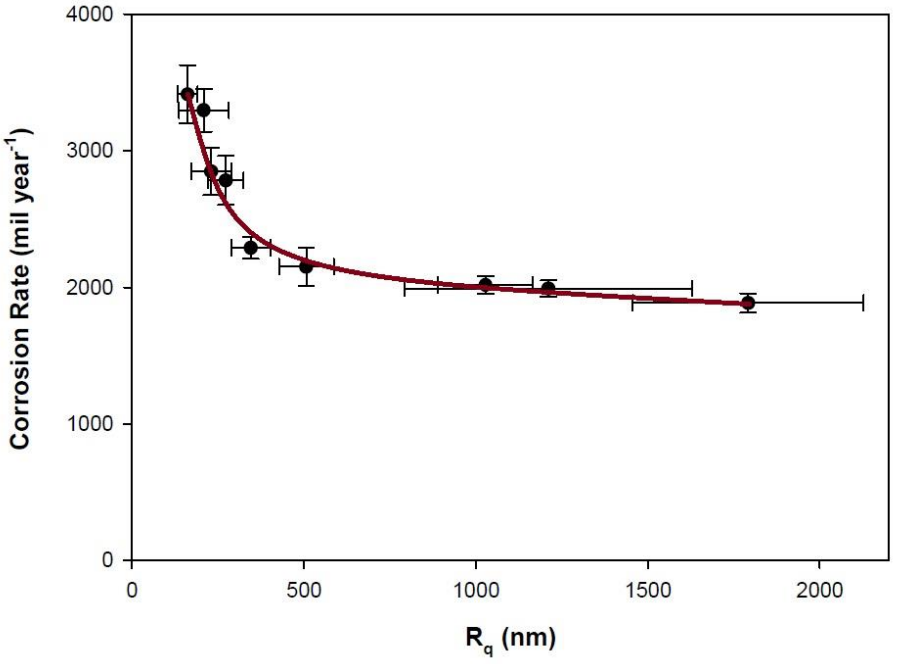

Figure 6-37 Dependence of corrosion rate of mild steel on R_q

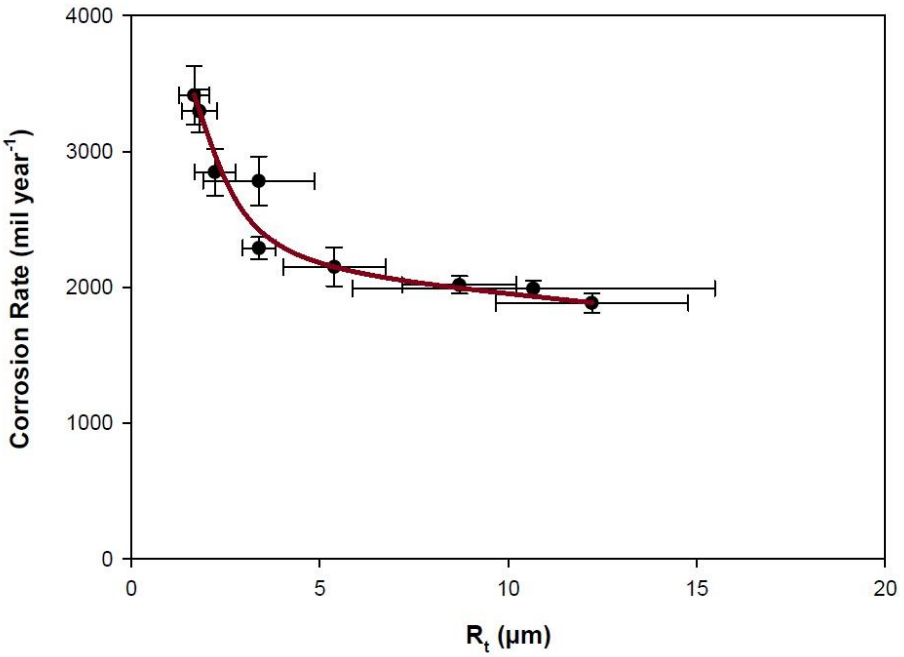

Figure 6-38 Dependence of corrosion rate of mild steel on R_t

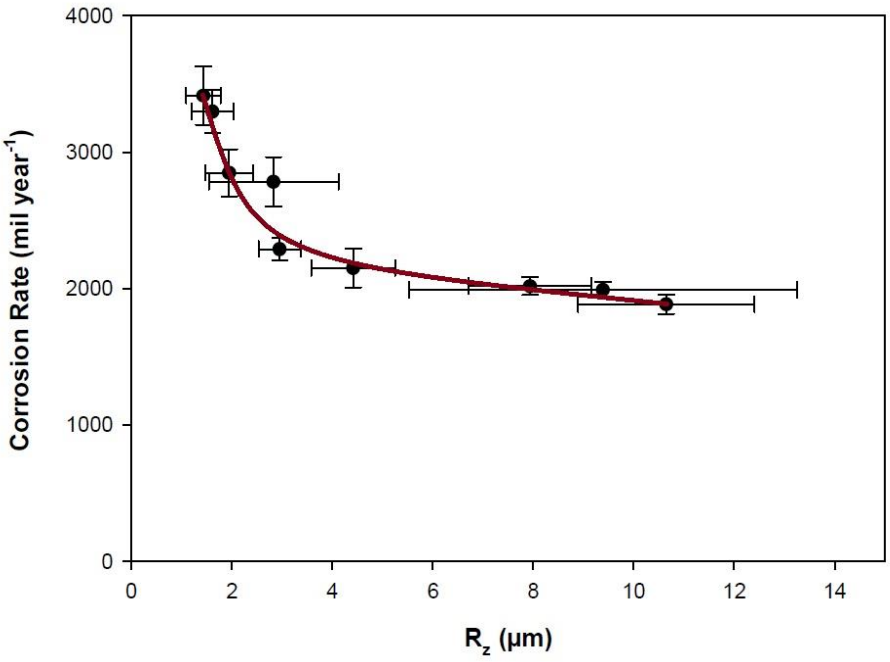

Figure 6-39 Dependence of corrosion rate of mild steel on R_z

To further illustrate the relationship between roughness and corrosion, Figure 6-40 is a plot of R_{ct}, the charge transfer resistance, from EIS and R_p, the polarization resistance obtained from the potentiodynamic polarization tests vs. R_a, the average surface roughness. Both R_{ct} and R_p increase i.e. decreasing corrosion rate, with increasing roughness. A reverse trend in R_p vs roughness has been reported for nickel in 0.5M H_2SO_4 in Chapter 5, Section 5.7 and also by Lee et al. [84] for 21 Cr ferritic stainless steel in a 1M NaCl solution which have the ability to form a stable passive layer. These studies were also for a unidirectional type of roughness. Thus, as can be seen, the results obtained from Tafel polarization showed good agreement with the results obtained from EIS.

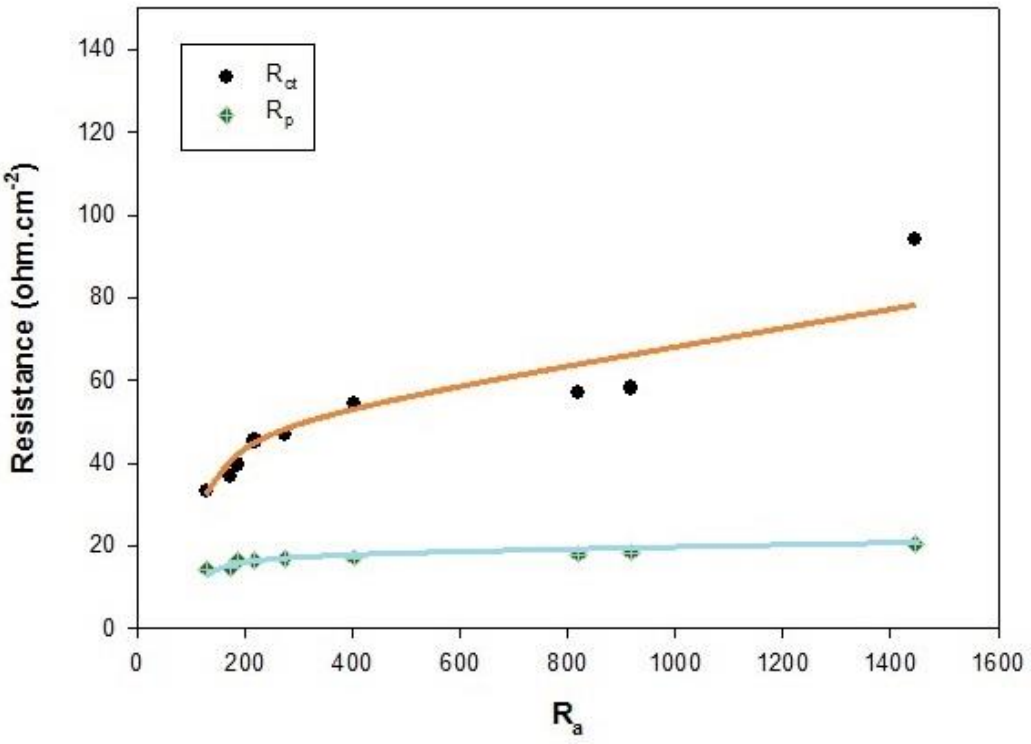

Figure 6-40 The effect of surface roughness of mild steel on R_p and R_{ct}.

Therefore, in the case of mild steel, it is important to notice that this metal has no ability to form a passive layer but both aluminum and stainless steel (as reported by Suter [79] and Burstein [71]) quickly passivate, or develop stable oxide films, when exposed to the atmosphere or water so, a passivated surface, whether it is aluminum or stainless steel, has a higher corrosion potential when compared to an unpassivated, or active, surface. But even if we consider that a protective passive film does not form on mild steel, it cannot be the only reason that why the smoothest surface of mild steel has higher corrosion rates. Existence of active sites is another reason that corrosion occurs on alloys. Examples of these sites are the alloy grains. On metals with the ability to form a

passive layer, these active sites are more available on a rougher surface, because the protective oxide film did not form on the rougher surfaces [79]. On mild steel or magnesium [49], since there is no stable protective passive film on both smooth and rough surfaces, the active sites would be equally available on both surfaces. But there are some grooves which are left from polishing process that act like active sites. These grooves exist more on the surfaces with higher roughnesses. Corrosion products and corrosive ions are trapped in such grooves which results in more corrosion on rough surfaces. In addition, the rough surfaces possess some of the corrosion products which cover the surface and partially protect the substrate. Similar phenomenon could be observed in mild steel. Therefore, the possibility of corrosion will be decreased on rougher surfaces of mild steel because of the corrosion products that exist on the surface. But despite of having fewer places for corrosion nucleation there would be more corrosion on smoother surfaces because there is no passive layer (as in the cse of nickel) or corrosion products (as in the case of rougher surfaces of mild steel) on the polished surface since the places for corrosion to occur would be more in contact with corrosive solution.

Furthermore, at the same conditions, a rough surface has no protective passive layer in mild steel but the smooth surface has not only the passive layer, but also the corrosion products, so the corrosive ions could attack the smoother surface more easily which will result in more corrosion on this surface.

Concept of diffusion is another reason for lower corrosion rate of rough surfaces of mild steel compared to smoother surfaces. It is believed that a rougher surface would prevent the diffusion of the corrosive ions out of the grooves and forming corroded areas by trapping the ions [79], but simultaneously a rougher surface on mild steel surface also could prevent the diffusion of the corrosive ions into the grooves [49]. Thus, the limited diffusion of the aggressive ions into the grooves would reduce the corrosion on the rougher surface. But on smooth mild steel surface which has no protective film or the accumulation of corrosion products, corrosion is dependent on the diffusion of the corrosive ions onto the surface because there would be nothing to prevent the corrosion [79]. In the case of metals with no ability to form a passive layer, no repassivation of the smooth surface will occur, unlike stainless steel, nickel or aluminum, but instead more corrosive ions will be in contact with the smoother surface and help the occurrence of corrosion.

Regarding the corrosion nucleation rate and total area fraction of localized corrosion areas, a similar study was performed on AE44 magnesium alloy which showed the same behaviour as mild steel [49]. The study showed that a general theory could be used for both smooth and rough surfaces as follows. While previous research [70, 75, 79, 86] suggested that more corrosion happened because more sites were available on the rougher surfaces, it is suggested that corrosion is dependent on both surface roughness and the ability of the material to form a protective passive film. If the material has the ability to form a passive film quickly, such as aluminium, nickel or stainless steel, less corrosion is

observed on smooth surfaces because the smooth surface has fewer places for corrosion nucleation and can quickly form a passive film preventing corrosion nucleation. However, in the case of mild steel where the material has no ability to form a passive film, the smoother surface is corroded more quickly because the smoother surface has nothing to prevent corrosion including the corrosion products remained and also a rougher topography that can prevent the corrosive ions from diffusing close to the surface.

The SEM observations in Section 6.2 were in contrast with the results related to metals with ability to form a passive layer which was expected. Lee et al.'s [84] found that stainless steel samples with deep grooves i.e. those with higher reduced valley depth (R_{vk}) values, show poorer corrosion resistance and Suter et al.'s [79] observed that these deeper grooves on aluminum trap the corrosive ions and corrosion products leading to more pitting. In the case of mild steel which has no ability to form a passive layer a reverse trend was observed Section 6.2.2. SEM and profilometry results in this chapter also showed less corrosion for rougher samples. In both tests, the unidirectional roughnesses were still visible on rougher surfaces in a larger scale indicating partially protection of the surface by corrosion products.

In the case of metals such as aluminum and nickel, the higher oxygen content after corrosion and lower corrosion rate were related to the formation of a stable passive film on smoother surfaces as suggested by Suter et al. [79] and also in Chapter 5 but in the case of mild steel no stable passive film is formed

and rougher surfaces showed less corrosion and lower oxygen content after corrosion compared to smoother samples. In the case of mild steel, more oxygen and sulphur after corrosion is related to corrosion products formed on the surface which partially protects the rougher surfaces.

The corrosion measurement results for mild steel are the opposite of those reported for aluminum or stainless steel [74, 79]. The mild steel specimens with smoother surfaces had the highest corrosion rate. The same result was reported by Abosrra et.al [73] for corrosion of mild steel in sodium chloride solution.

It is said that in electrolytes with corrosive ions, mild steel shows some unstable protection behaviour resulted from corrosion products on the surface at the beginning and, due to the existence of these ions on the surface, the protection is easily removed by diffusion of corrosive ions [73]. Thus, by changing the roughness, some changes in corrosion rate are observed which are as a result of a weak formed layer (corrosion products) and the breakdown of the layer with aggressive ions. The result obtained in this work was that mild steel with smoothest polished surfaces (G1200) showed the highest corrosion rate compared to surfaces with higher roughnesses. This is reported to be attributed to the high rate of corrosion propagation after initiation [73]. Localized corrosion is controlled by the diffusion process and in this case once the corrosion started, it propagated at a fast rate due to the continuous diffusion process and the formation of acid media underneath the formed layer of corrosion products [73].

The results are also in agreement with the observations of Alvarez on AE44 magnesium alloy as well [49].

As previously mentioned, these trends were opposite of the trends seen in the literature for aluminum and stainless steel, which include the rough surfaces limiting diffusion out of the forming pits and deep grooves, more available active sites on the rough surfaces, and fast formation of a stable oxide film on the smoother surfaces [70, 79]. EIS results also confirmed more charge transfer resistance of rougher samples indicating more corrosion resistance of these surfaces.

Chapter 7 GENERAL DISCUSSION AND CONCLUSIONS

7.1 Discussion on surface patterning through laser ablation

In this chapter all the mechanisms and justifications regarding the results obtained from different experiments in Chapters 4-6 about patterned surfaces of nickel, nickel surface with unidirectional surfaces, and mild steel with unidirectional surfaces are discussed.

Although the existence of heterogeneous wetting has not been explicitly observed in this study for patterned samples, the conclusion for the existence of a heterogeneous interface and it being the main reason for the observed increase in corrosion resistance is drawn based on the results of three inter-related experimental studies, namely SEM, EDS and potentiodynamic polarization tests. The arguments in support of the existence of the heterogeneous wetting can be summarized as follows:

The potentiodynamic polarization test clearly showed a reduction in the corrosion rate in a number of patterned samples, e.g. D20L40 and D30L60 (Table 4-1). This reduction could be attributed to one or a combination of the following three factors: a) change in the chemical composition of the surface (passivation); b) change of the microstructure of the metallic surface; c) reduction of the overall solid/electrolyte contact surface. The surface analysis (SEM and EDS) clearly showed that there are no detectable changes in the microstructure of the samples before and after patterning. In addition, the EDS analysis showed

that the surface chemical composition has not been altered by the process of surface patterning. These results led to the conclusion that the likely explanation of the observed corrosion rate reduction is the decrease of the overall electrolyte/metal surface contact area.

An additional proof of this hypothesis is the observed difference in the oxygen concentration inside and outside the holes in the samples with significantly reduced corrosion such as D30L60 and D20L40 (Table 4-2). It is clear that the electrolyte/metal surface interaction is different in the holes of samples with decreased corrosion – D30L60 (Table 4-2) and the samples where the corrosion rate was not significantly altered D5L20 (Table 4-2). In areas such as inter-hole spacing, where there is clear electrolyte/metal surface contact, the oxygen concentration has only slightly changed (11–18%, Table 4-2) before and after corrosion tests. This indicates dissolution of any passivation (oxide) layer formed during the corrosion tests. However, the oxygen concentration at the bottom of the holes in the samples with much lower corrosion rates – D30L60 is ~50% higher than the oxygen concentration at the surface where the electrolyte is in contact with the metal surface (Table 4-2). This proves that any passivation (oxide) layer formed during the corrosion tests has not been dissolved by the electrolyte. This leads to the conclusion that the liquid electrolyte is not in contact with at least part of the surface of the hole and therefore the regime of wetting is heterogeneous.

Figure 7-1(a-c) illustrates a schematic of the patterned surface in different conditions including a complete protection before corrosion, a surface with heterogeneous interface and another surface with partially dissolved passive film on the surface and inside the holes in 0.5 M H_2SO_4 solution. In Figure 7-1 (a), the whole surface including inside and outside the holes is covered with a naturally-formed passive layer before corrosion testing. However, in samples with lower corrosion rate, the existence of air/vapour pockets prevented dissolution of the passive layer inside the holes which decreased the contact area between the corrosive solution and the substrate (Figure 7-1 (b)). Examples of these surfaces with more corrosion resistance are samples D20L40 and D30L60. In these samples the reported oxygen content from EDS analysis was also higher inside the holes.

In Figure 7-1 (c) however, a surface is shown where the corrosive solution has been able to reach the surface and also the bottom of the hole. As a result of this process, the solution has dissolved the passive layer both inside and outside the holes and resulted in more corrosion of the sample. Examples of such surfaces are samples D5L5 and D10L10. The SEM and profilometry analysis detailed in Chapter 4 confirmed the corrosion testing results for these samples.

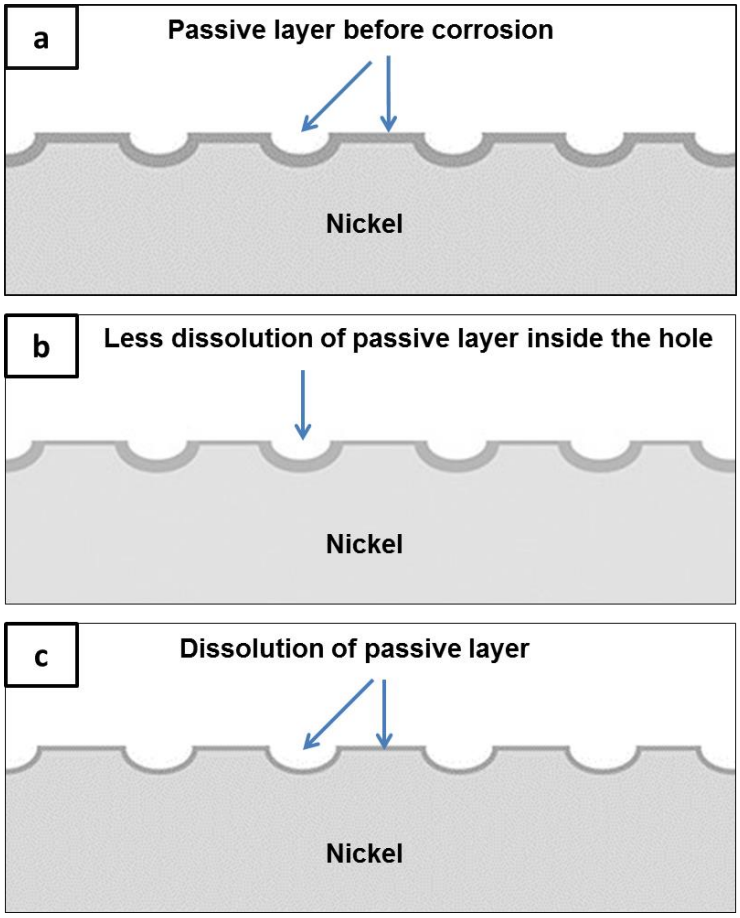

Figure 7-1 Schematics of the patterned surface on nickel a) complete protection before corrosion b) heterogeneous interface c) non-heterogeneous interface.

7.2 Discussion for nickel surface with unidirectional roughness

The relationship between the corrosion rate as determined by potentiodynamic polarization tests and the roughness parameters including R_a, R_q, R_t and R_z showed the same general trend, namely, an increase in roughness leads to an increase in corrosion rate. As noted in the introduction, this is a general trend seen for corrosion of metals that form a protective passive film, such as aluminium, nickel and stainless steel [79, 84]. The rough surfaces limit

diffusion of corrosive ions out of the grooves or corroded areas. There are also more active sites available on the rough surfaces and the formation of a stable oxide film on the smoother surfaces is faster. Thus, the rougher surface has higher corrosion rate.

Looking at the general trends, we can see that any deviation from a perfectly flat surface dramatically increases the corrosion rate. The rate of change of corrosion rate with roughness then decreases and, for the highest roughnesses, the corrosion rate appears to reach a plateau. A similar behaviour was reported by Li and Li [80], who measured the electron work function (EWF) of Cu in a 3.5% NaCl solution and found that the EWF decreased with increasing roughness. The other point of interest is that the patterned samples of nickel show much lower corrosion rates than unidirectional roughness samples with equivalent, or much greater, roughness. This strongly suggests a different corrosion protection mechanism for the patterned samples, which was discussed in Section 7.1.

As well as potentiodynamic polarization results, EIS results are also presented. One measure of corrosion resistance in the EIS studies is R_{ct}, the charge transfer resistance. The EIS results show the same trend, namely decreasing R_{ct}, i.e. increasing corrosion rate, with increasing roughness. A similar trend in R_p (the polarization resistance obtained from the potentiodynamic polarization tests) vs roughness has been reported by Lee et al. [84] for 21 Cr

ferritic stainless steel in a 1M NaCl solution. This study was also for a unidirectional type of roughness.

In the rougher samples, there is more contact area between the corrosive medium and the metal (Ni). There is also trapping of the corrosive ions in the deep grooves, leading to an autocatalytic process such as pitting [176].

Another important observation related to mechanisms is the EDS results for oxygen content on the surface after corrosion. The results for G600 to G1200 suggest the formation of a stable passive film. Such a passive film would provide better corrosion protection, as evidenced by these samples showing the lowest corrosion rates for the unidirectional roughness samples. In the patterned samples, as discussed in Chapter 4, there is a different mechanism and heterogeneous wetting decreases the surface area exposed to the sulphuric acid solution, thus reducing the corrosion rate.

A schematic of the difference between a nickel surface before corrosion, a smooth and a rough surface of nickel in 0.5 M H_2SO_4 solution is presented in Figure 7-2 (a-c). In Figure 7-2 (a), a nickel surface with unidirectional roughnesses is displayed before corrosion testing. In the case of the rougher surface, the passive layer is corroded and more corrosion was observed along the grooves (Figure 7-2 (b)). Corrosion products were also more abundant compared to a smooth surface because the autocatalytic corrosion process happened in the grooves. On a smooth surface (Figure 7-2 (c)) however, as was discussed in Chapter 5, the formation of a passive layer is faster and less

corrosion was observed along the grooves. The passive layer in this case is more uniform and stable which was confirmed by SEM and profilometry in Chapter 5.

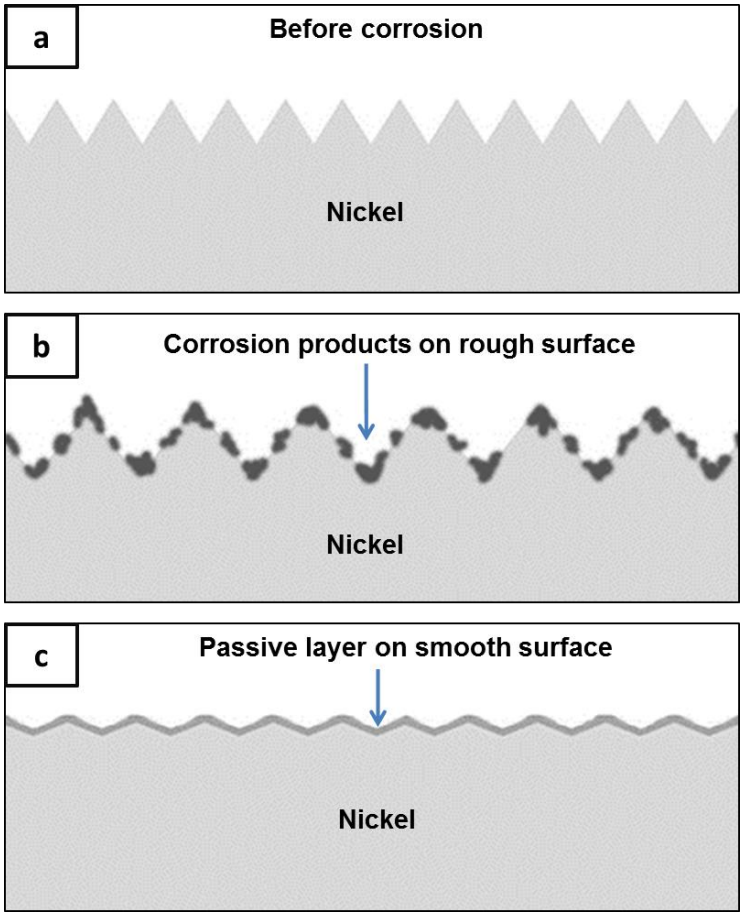

Figure 7-2 Schematics of the unidirectional nickel surface a) before corrosion, b)rough surface after corrosion and c)smooth surface after corrosion.

7.3 Discussion for mild steel surface with unidirectional roughness

The mechanisms behind the different behaviour of mild steel compared to nickel are discussed as follows:

It is said that in electrolytes with corrosive ions such as chloride or sulphate, mild steel shows some unstable corrosion product layer at the beginning and, due to the existence of these ions on the surface, the protection is easily removed [73]. It means that the surface layer is destroyed due to the existence of corrosive ions such as SO_4^{2-} . Thus, by changing the roughness, some variations in corrosion rate are observed, which are as a result of an unstable corrosion product layer and the early breakdown of the layer with aggressive ions. The result obtained in this work was that mild steel with smoothest polished surfaces (G1200) showed the highest corrosion rate compared to surfaces with higher roughnesses. This can be attributed to the high rate of corrosion propagation after initiation [73]. It is said that localized corrosion is controlled by the diffusion process and in this case once the corrosion started, it propagated at a fast rate due to the continuous diffusion process and the formation of acid media at the bottom of the grooves [73].

The results are in a good agreement with the observations of Alvarez on AE44 magnesium alloy which has similar characteristics as mild steel (no ability to form a stable passive film) [49].

Even if consider that a protective film does not form on mild steel, it cannot be the only reason why the smoothest surface of mild steel has higher corrosion rates. Existence of active sites is another reason why corrosion occurs on alloys. Examples of these sites are the alloy grains. On metals with the ability to form a passive layer, these active sites are more available on a rougher surface, because the protective oxide film did not form on the rougher surfaces [79]. On mild steel [49], since there is no stable protective passive film on both smooth and rough surfaces, the active sites would be equally available on both surfaces. But there are some grooves which are left from polishing process that act like active sites. These grooves exist more on the surfaces with higher roughnesses. Corrosion products and corrosive ions are trapped in such grooves which will result in more corrosion on rough surfaces. But this is not the whole story, because the rough surface might still possess some of the corrosion products, which are said to be less reactive than the bulk of metals. The same thing could also occur on mild steel. Therefore, the possibility of corrosion will be decreased on rougher surfaces of mild steel because of the corrosion products that exist on the surface and partially protect the rougher surfaces. But despite having fewer places for corrosion nucleation there would be more corrosion on smoother surfaces because there is no protection on the polished surface since the places for corrosion to occur would be more in contact with corrosive solution.

The concept of diffusion is another reason for the lower corrosion rate of rough surfaces in mild steel. It is said that a rougher surface would prevent the diffusion of the corrosive ions out of the grooves and form pits by trapping the ions [79], but simultaneously a rougher surface on mild steel surfaces also could prevent the diffusion of the corrosive ions into the grooves [49]. Thus, the limited diffusion of the aggressive ions into the grooves would reduce the corrosion on the rougher surface. But on smooth mild steel surfaces, which have no corrosion product or a passive film, corrosion is dependent on the diffusion of the corrosive ions onto the surface because there would be nothing to prevent the corrosion [79]. In the case of metals with no ability to form a passive layer, no repassivation of the smooth surface will occur, unlike stainless steel, nickel or aluminum; instead more corrosive ions will be in contact with the surface and help the occurrence of corrosion.

Therefore, it is suggested that corrosion is dependent on both surface roughness and the ability of the material to form a protective passive film. If the material has the ability to form a passive film quickly, such as aluminium, nickel or stainless steel, less pitting is observed on smooth surfaces because the smooth surface has fewer places for pit nucleation and can quickly form a passive film preventing pit nucleation. However, in the case of mild steel when the material has no ability to form a protective passive film, the smoother surface is corroded more quickly because the smoother surface has nothing to prevent corrosion, including the corrosion products remaining, and also a rougher

topography, which can prevent the corrosive ions from diffusing close to the surface.

As profilometry results also confirmed, in all of the mild steel samples containing unidirectional roughnesses, corrosion has produced a peaks-and-valleys structure on the surface, and it caused an increase in the roughness for all substrates. In the case of smoother surfaces however, increasing roughness is related to the events explained in the previous paragraph, i.e., less corrosion products and diffusion phenomenon. In the case of rougher surfaces, the change in roughness is less because at the beginning of the corrosion process, the corrosion is more severe at some localizes places, which will result in some inordinately high peaks or valleys, and then the surface is coated with the corrosion product layer. Thus, the surface texture becomes hidden, and as SEM showed, some grooves are visible but in a larger scale [175]. The results are in good agreement with EIS and profilometry results, which show less corrosion for a rougher mild steel surface.

Figure 7-3 (a-c) shows a schematic of mild steel surface before corrosion and different corrosion behaviours of smooth and rough surfaces of mild steel in contact with a 0.5 M H_2SO_4 solution. In Figure 7-3 (a), a mild steel surface with unidirectional roughnesses is presented before corrosion testing. As was discussed in Chapter 6, on the smooth surface (Figure 7-3 (b)), there is no protective layer, and also there are no deep grooves to trap corrosion products and partially decrease the corrosion rate. Examples of such surfaces are

samples G1200 and G800. In the case of smooth surfaces, there is always a direct contact between the electrolyte and the mild steel surface which will result in more corrosion compared to rougher surfaces. In the case of the rougher surface, however, the corrosion products are formed on the surface including inside the grooves and partially protect the substrate against the corrosive solution (Figure 7-3 (c)) (exaggerated). SEM confirmed less corrosion and EDS also showed more oxygen and sulphur, which come from the corrosion product on rougher surfaces. Examples of surfaces with the mechanism shown in Figure 7-3 (c) are samples G60, G120 and G180.

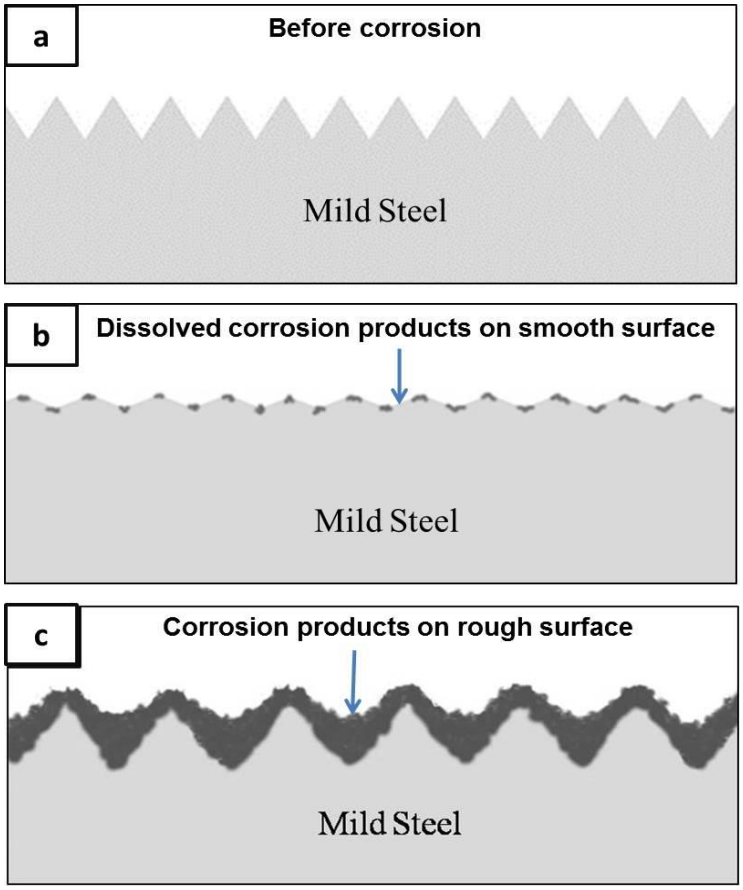

Figure 7-3 Schematic of the unidirectional mild steel surface a) before corrosion, b) smooth surface after corrosion and c) rough surface after corrosion.

7.4 Conclusions

7.4.1 **Surface Patterning**

Surface patterns consisting of holes of different diameters (D) and inter-hole spacings (L) were successfully created on Ni by a laser ablation process. The patterns had a significant effect on corrosion resistance. A specific group of patterns, namely those with pattern densities (D/L) of 0.5 and hole diameters (D) ≥20μm, led to a significant (up to two orders of magnitude) decrease in the corrosion current density and corresponding corrosion rate. This decrease in corrosion rate is attributed to heterogeneous wetting with the formation of air/vapor pockets inside the holes, thereby reducing the surface area of the nickel that is exposed to the electrolyte. Support for this hypothesis was obtained through EDS analysis of the oxygen content at the bottom of the holes and at the surface outside the holes. The use of such surface patterning techniques for improving the corrosion resistance of nickel and its alloys is attractive in engineering applications where the use of coatings or inhibitors is not practical or desirable, e g. in certain fuel cell applications.

7.4.2 **Unidirectional Roughness**

Unidirectional surface roughness of varying magnitudes were created on both nickel and mild steel by grinding on SiC papers with grit sizes from G60 (roughest) to G1200 (smoothest) and the corrosion resistance in 0.5M H_2SO_4 solution was determined using both potentiodynamic polarization and EIS. A different trend of corrosion rate versus roughness was seen for the active-passive metal (nickel) and non-active-passive metal (mild steel). For nickel there

was an increase in corrosion rate with increasing roughness, whereas for mild steel the corrosion rate decreased with increasing surface roughness. Through a detailed examination of the surface before and after corrosion using techniques including profilometry, SEM, EDS, and XRD, it was established that different corrosion mechanisms were operative for nickel and mild steel. For both metals, the smaller grit sizes produced a rougher surface with wider and deeper grooves. In the case of nickel, the higher roughness provided a greater contact area between the corrosive medium and metal and there was trapping of the corrosive ions in the deep grooves. Both of these factors would lead to an increase in corrosion rate. Also, for the smoother nickel surfaces, it is easier to form a stable passive film. For mild steel, which does not form a passive film, corrosion rates are generally much higher than for nickel. For the rougher surfaces with the deeper grooves, the corrosion product, $FeSO_4$, can fill the grooves thereby acting as a barrier to further ingress of the corrosive ions to the un-corroded metal.

7.5 Recommendations for Future Research

According to this research, surface texturing is highly recommended to fabricate surfaces with improved corrosion resistance. Surface texturing could also be performed for other metals. This study compared metals with different passivation behaviours. More studies can be performed on metals with different alloying elements or compositions, and also in different corrosive solutions. The effect of changing the solution pH and also solutions with no corrosive ions could be another future project. Cl^- can be added to the solution to see if pitting affects the process. Different velocities can be utilized to see if corrosive ions are removed or corrosion proceeds.

Different shape patterns also could be created using laser, lithography or other methods to investigate the effect of various textures on corrosion properties of the surface. In such studies, investigation of the effect of surface patterning on other metals with no ability to form a passive layer is useful. Also a study of a metals such as Ti, with no trans-passive region, could be interesting and beneficial.

The effect of surface texturing can be also investigated in lower length scales, i.e. the nano scale, and the effect on the corrosion can be explored.

APPENDICES

Appendix $A_{1\text{-before}}$: 2D images, 3D textures, for nickel samples with different roughnesses before corrosion

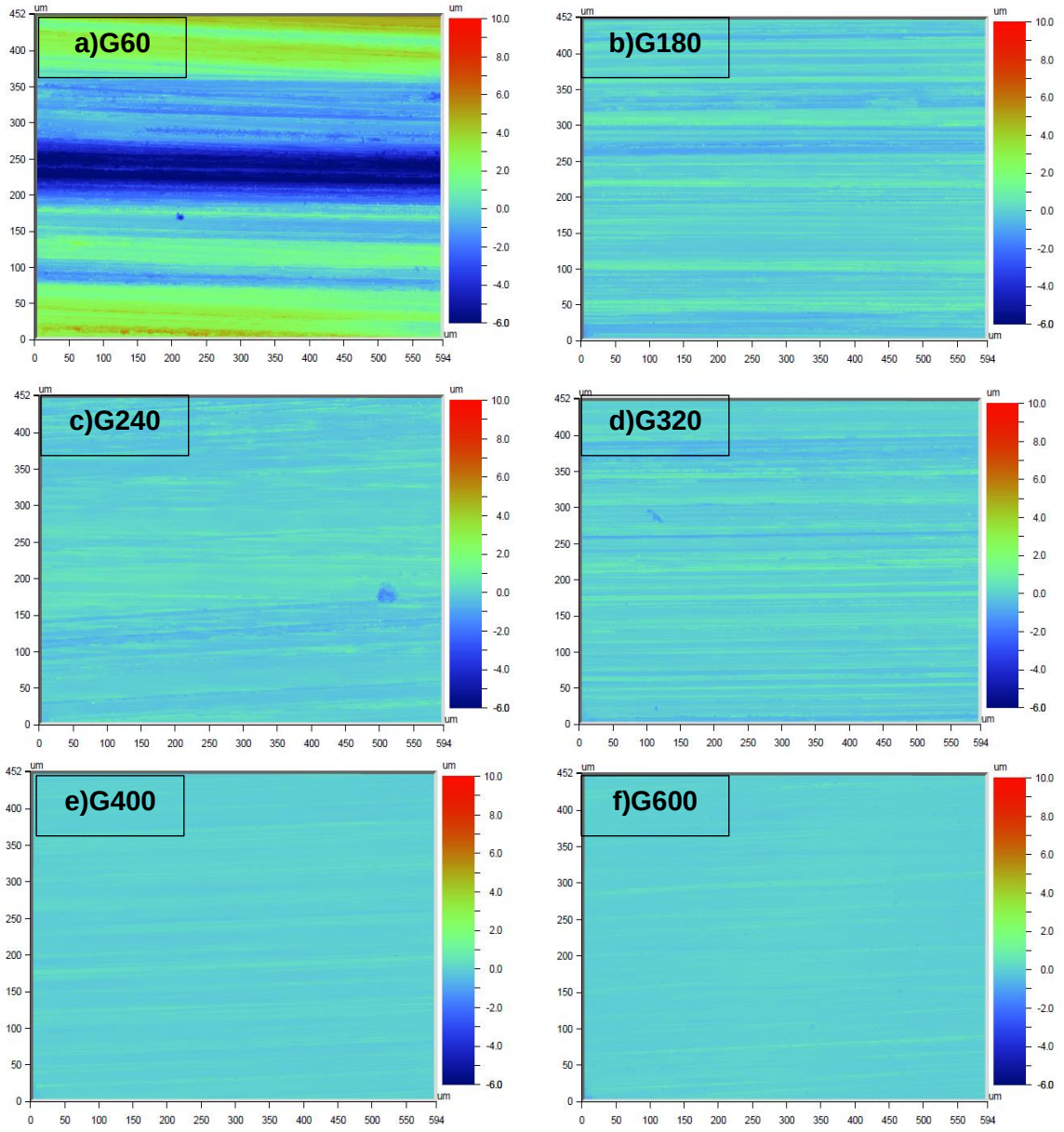

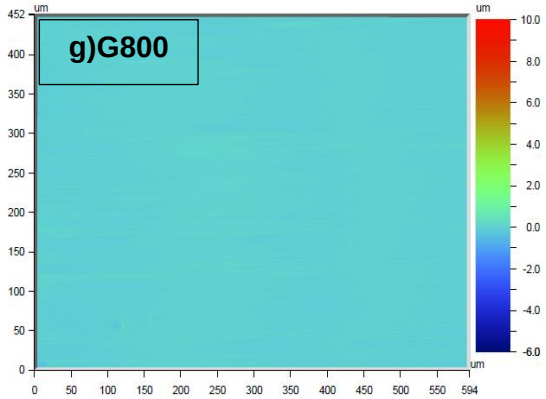

Figure A-1 2D images for nickel samples a)G60, b)G180, c)G240, d)G320, e)G400, f)G600 and g)G800 before corrosion

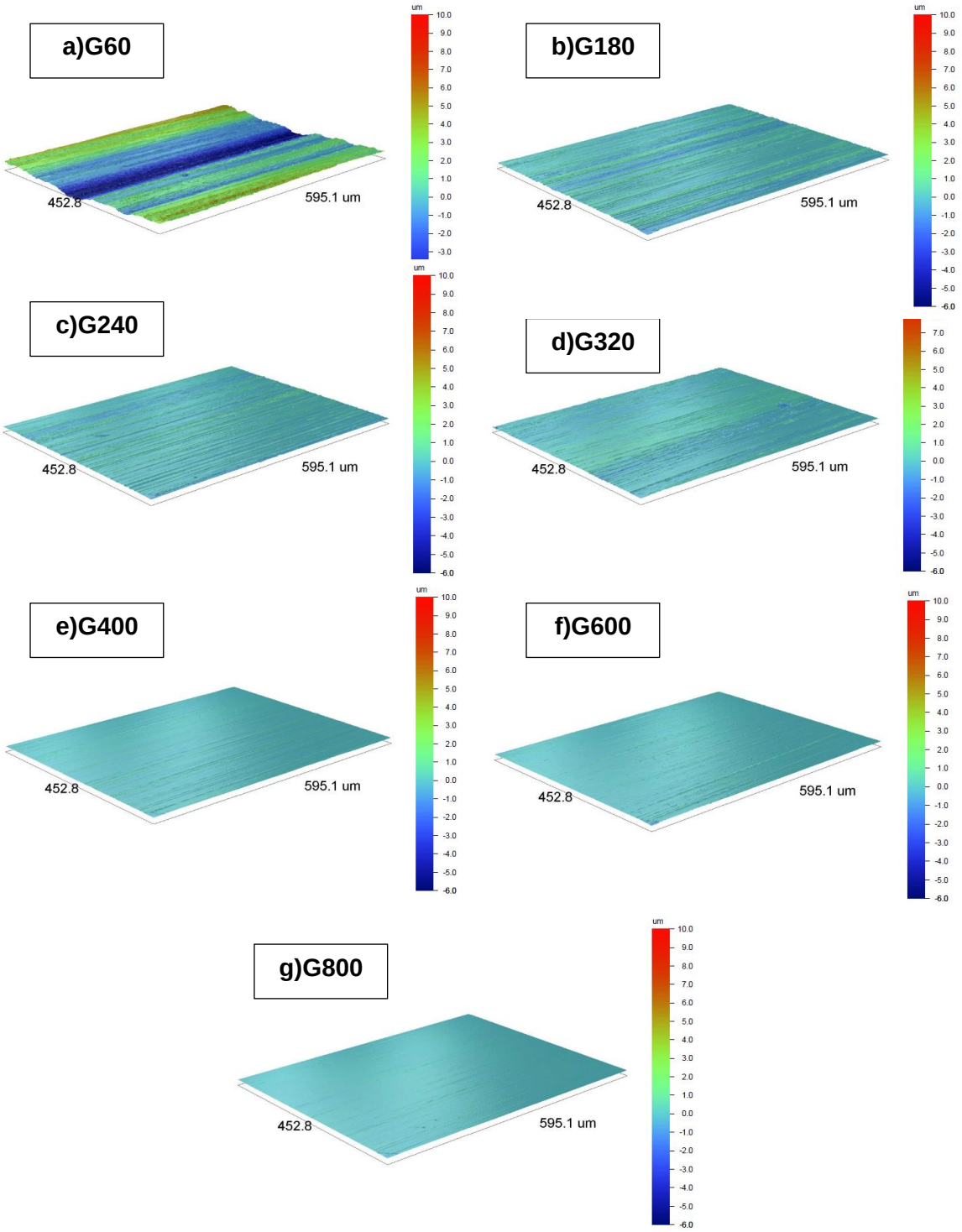

Figure A-2 3D surface textures for nickel samples a)G60, b)G180, c)G240, d)G320, e)G400, f)G600 and g)G800 before corrosion

Appendix $A_{1\text{-after}}$: 2D images, 3D textures, for nickel samples with different roughnesses after corrosion

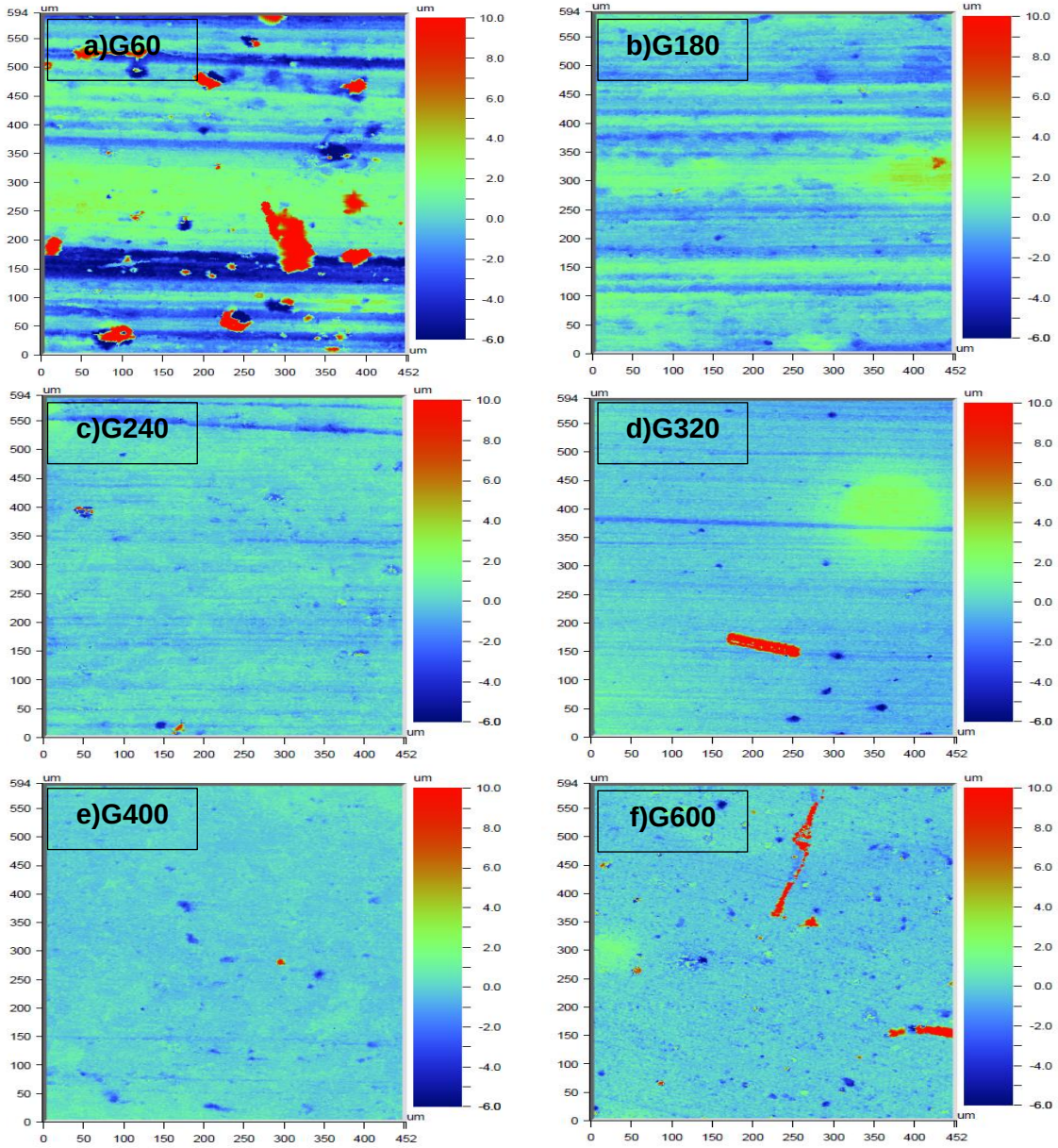

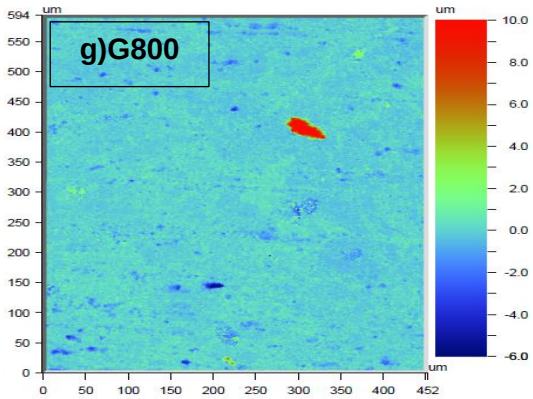

Figure A-3 2D images for nickel samples a)G60, b)G180, c)G240, d)G320, e)G400, f)G600 and g)G800 after corrosion

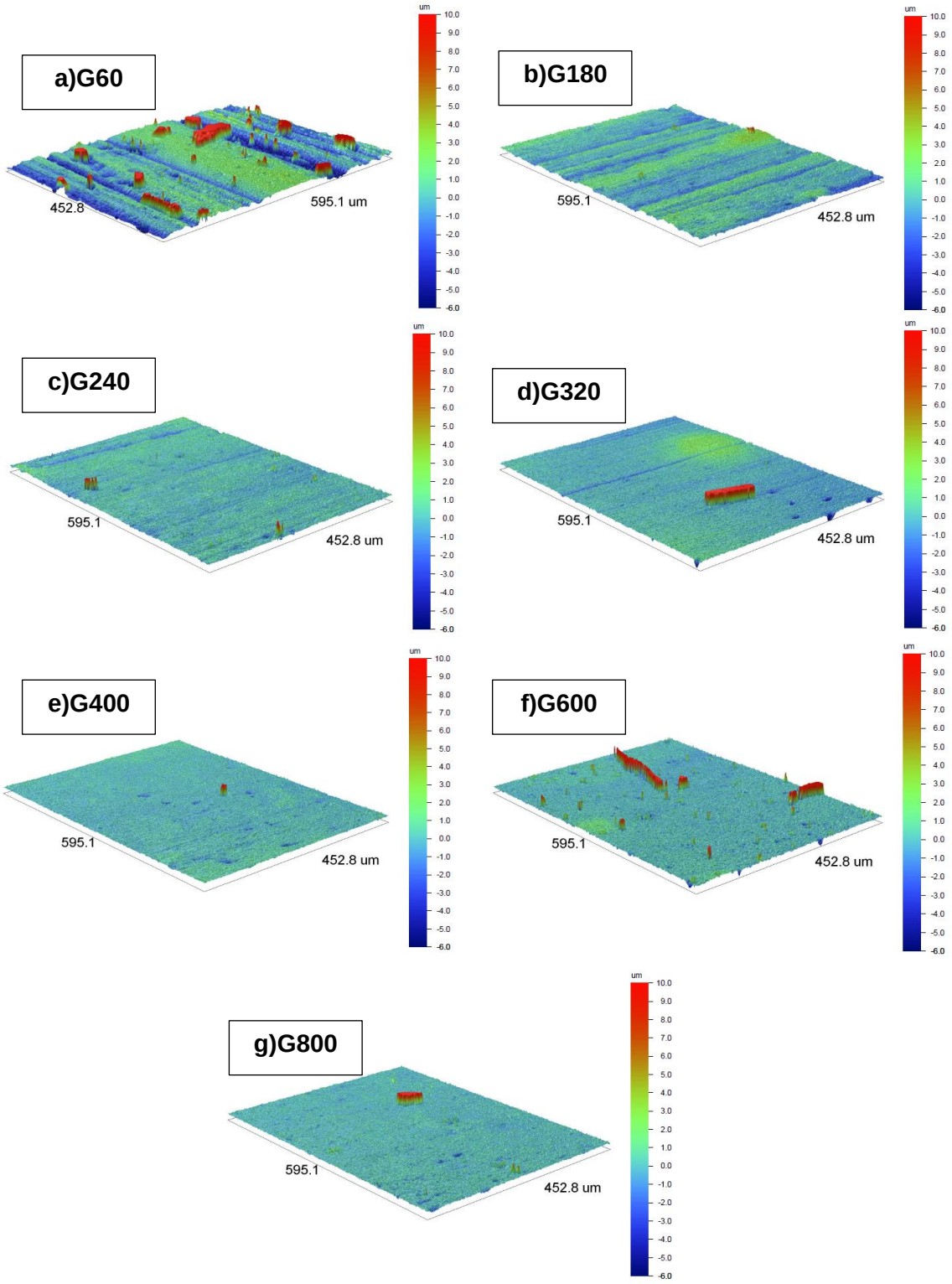

Figure A-4 3D surface textures for nickel samples a)G60, b)G180, c)G240, d)G320, e)G400, f)G600 and g)G800 after corrosion

Appendix $A_{2\text{-before}}$: X and Y profiles for nickel samples with different roughnesses before corrosion

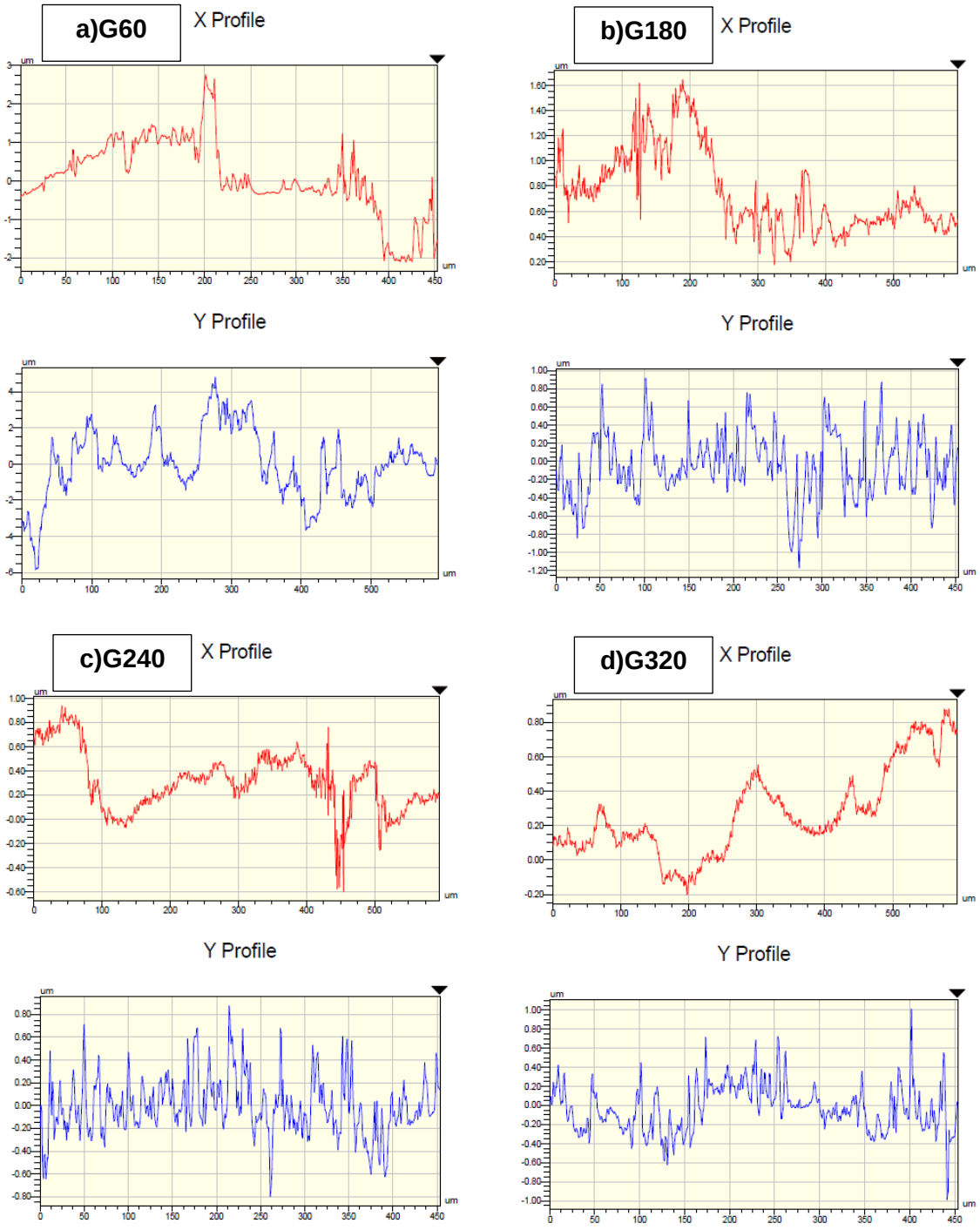

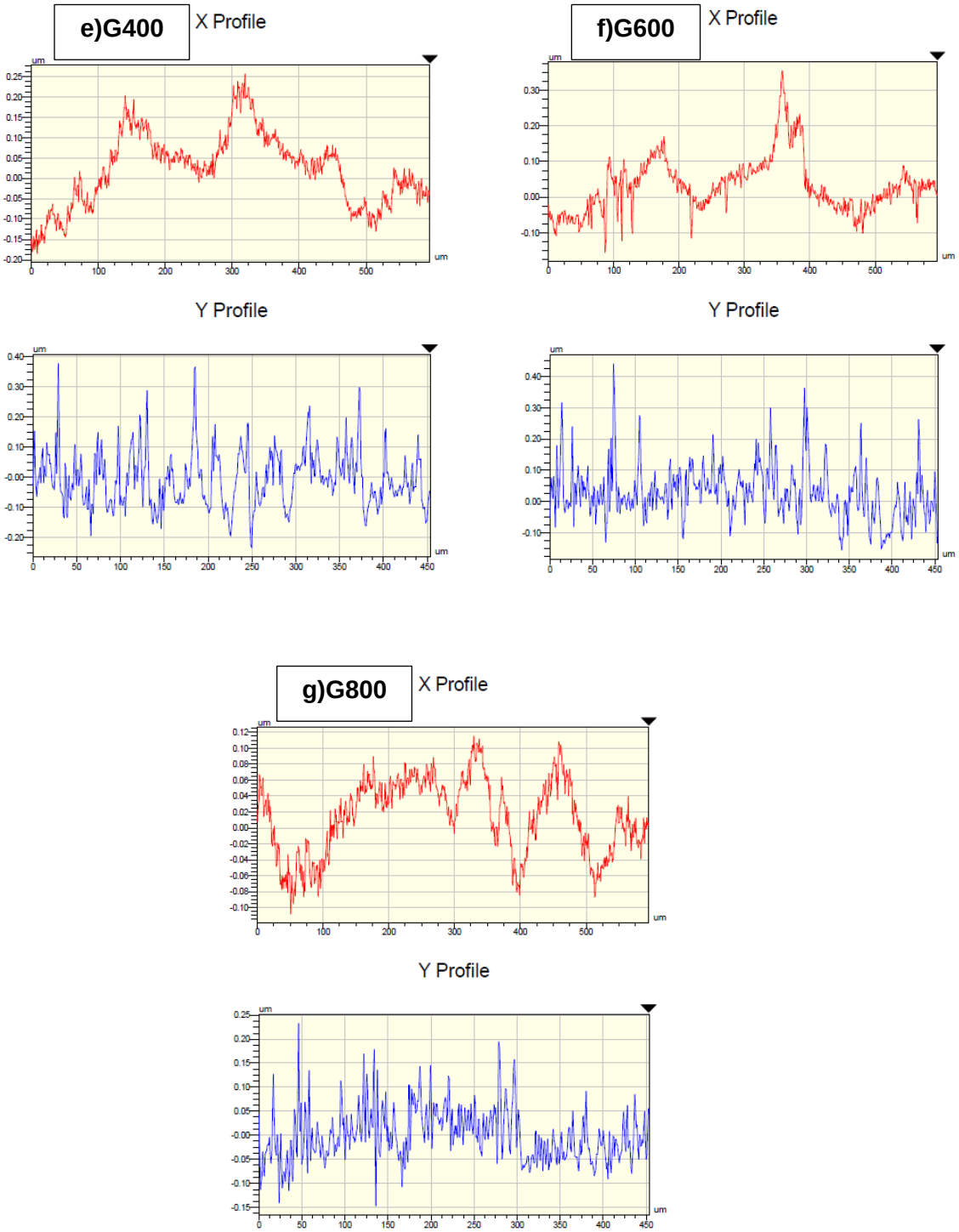

Figure A-5 X and Y profiles for nickel samples a)G60, b)G180, c)G240, d)G320, e)G400, f)G600 and g)G800 before corrosion

Appendix $A_{2\text{-after}}$: X and Y profiles for nickel samples with different roughnesses after corrosion

a)G60 X Profile

Y Profile

b)G180 X Profile

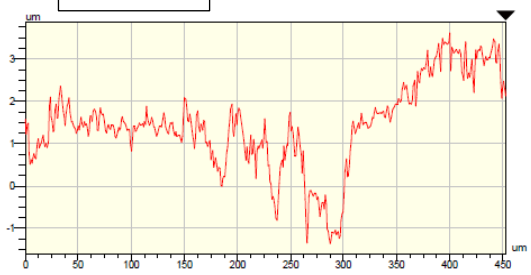

Y Profile

c)G240 X Profile

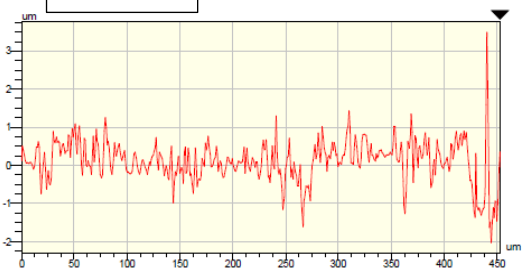

Y Profile

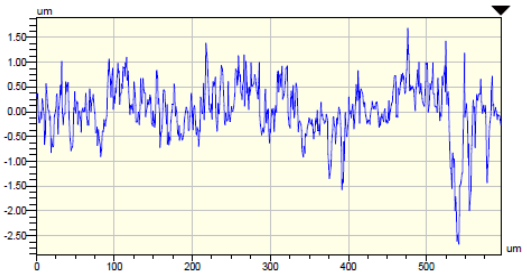

d)G320 X Profile

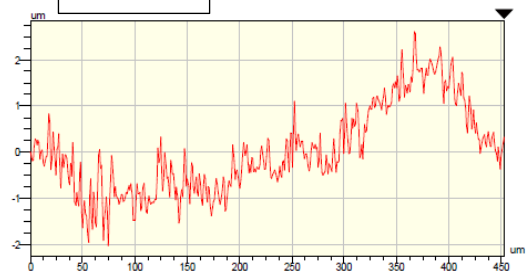

Y Profile

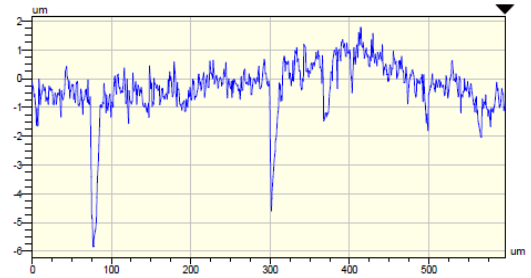

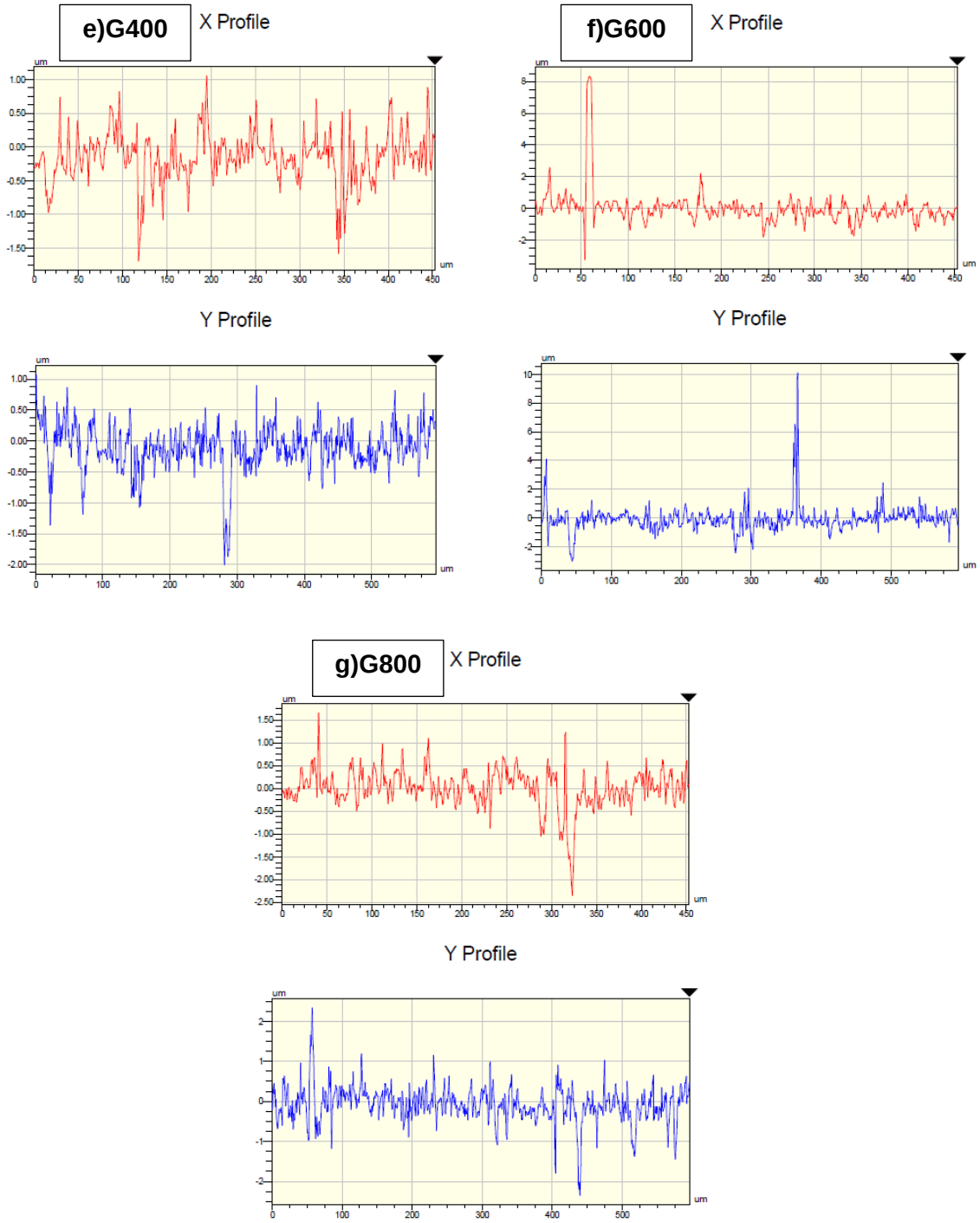

Figure A-6 X and Y profiles for nickel samples a)G60, b)G180, c)G240, d)G320, e)G400, f)G600 and g)G800 after corrosion

Appendix $A_{3\text{-before}}$: Histograms for nickel samples with different roughnesses before corrosion

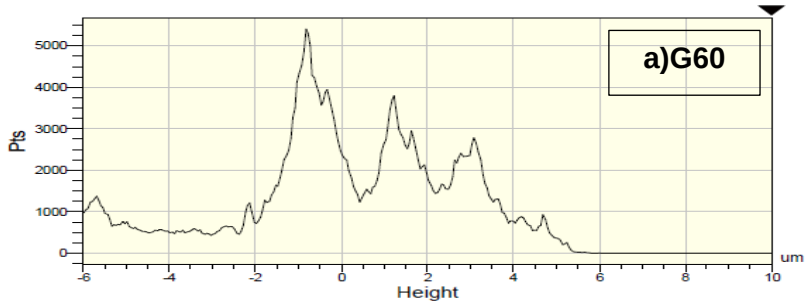

95% of data is between -3080.00 and 5120.00 nm (pv:8200.00)
90% of data is between -2680.00 and 4760.00 nm (pv:7440.00)
85% of data is between -320.00 and 5760.00 nm (pv:6080.00)
80% of data is between 80.00 and 5120.00 nm (pv:5040.00)

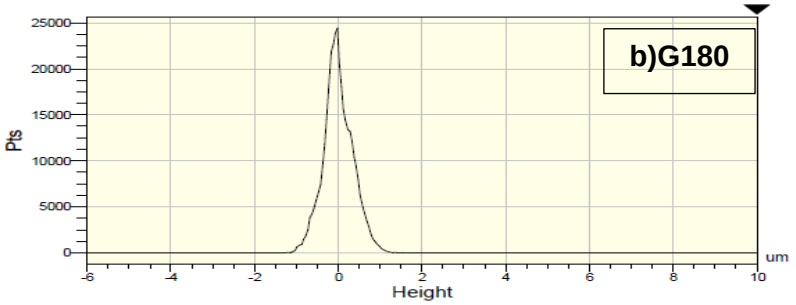

95% of data is between 1400.00 and 2520.00 nm (pv:1120.00)
90% of data is between 1440.00 and 2400.00 nm (pv:960.00)
85% of data is between 1560.00 and 2360.00 nm (pv:800.00)
80% of data is between 1560.00 and 2280.00 nm (pv:720.00)

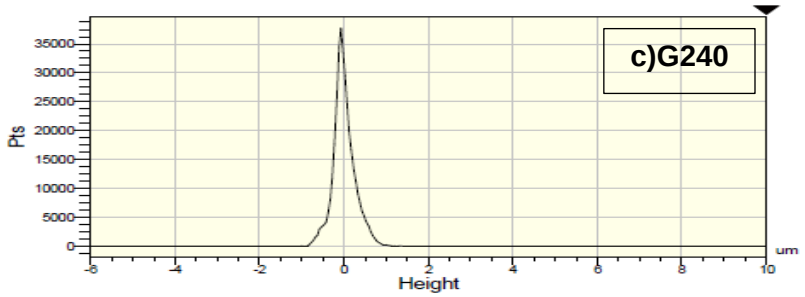

95% of data is between 1520.00 and 2400.00 nm (pv:880.00)
90% of data is between 1600.00 and 2320.00 nm (pv:720.00)
85% of data is between 1640.00 and 2240.00 nm (pv:600.00)
80% of data is between 1720.00 and 2200.00 nm (pv:480.00)

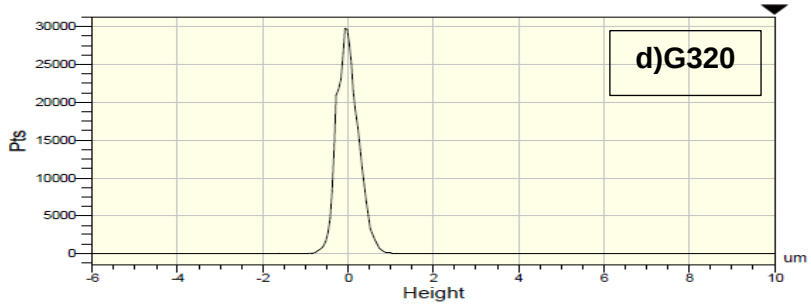

95% of data is between 1600.00 and 2360.00 nm (pv:760.00)
90% of data is between 1680.00 and 2280.00 nm (pv:600.00)
85% of data is between 1720.00 and 2240.00 nm (pv:520.00)
80% of data is between 1680.00 and 2160.00 nm (pv:480.00)

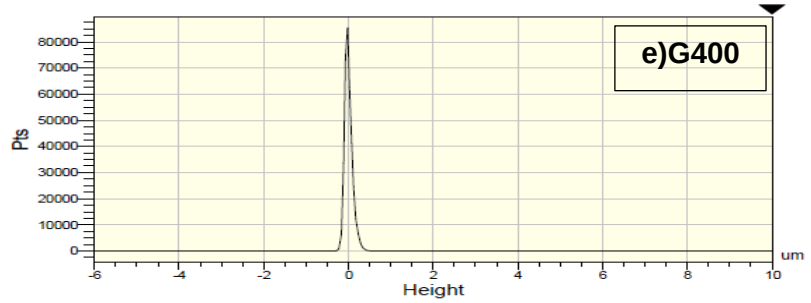

95% of data is between 1840.00 and 2120.00 nm (pv:280.00)
90% of data is between 1880.00 and 2080.00 nm (pv:200.00)
85% of data is between 1840.00 and 2040.00 nm (pv:200.00)
80% of data is between 1880.00 and 2040.00 nm (pv:160.00)

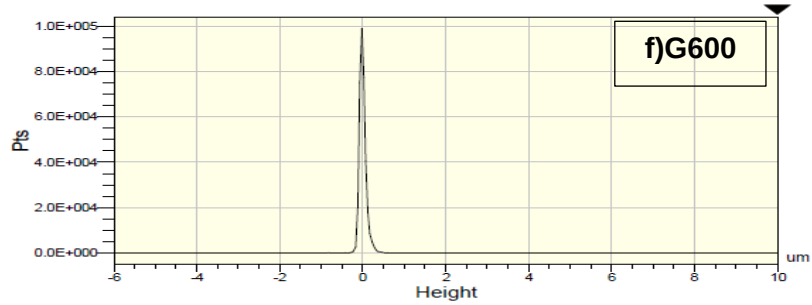

95% of data is between 1880.00 and 2120.00 nm (pv:240.00)
90% of data is between 1880.00 and 2080.00 nm (pv:200.00)
85% of data is between 1880.00 and 2040.00 nm (pv:160.00)
80% of data is between 1920.00 and 2040.00 nm (pv:120.00)

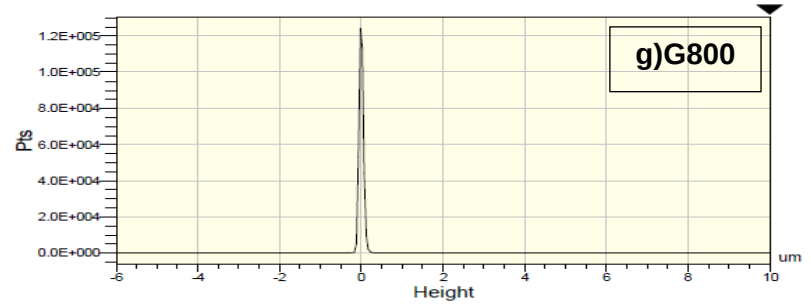

95% of data is between 1880.00 and 2040.00 nm (pv:160.00)
90% of data is between 1920.00 and 2040.00 nm (pv:120.00)
85% of data is between 1920.00 and 2040.00 nm (pv:120.00)
80% of data is between 1920.00 and 2000.00 nm (pv:80.00)

Figure A-7 Histograms for nickel samples a)G60, b)G180, c)G240, d)G320, e)G400, f)G600 and g)G800 before corrosion

Appendix $A_{3\text{-after}}$: Histograms for nickel samples with different roughnesses after corrosion

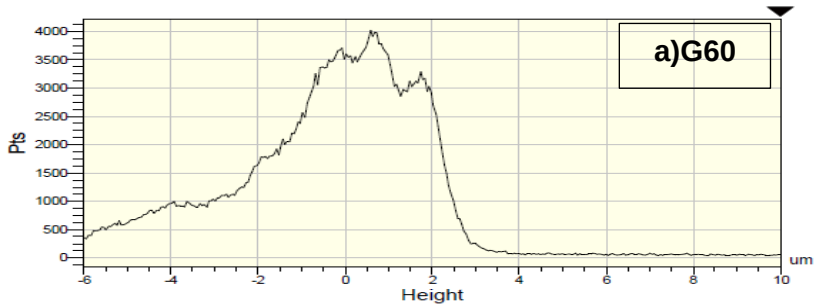

95% of data is between -2640.00 and 4080.00 nm (pv:6720.00)
90% of data is between -1640.00 and 3960.00 nm (pv:5600.00)
85% of data is between -960.00 and 3880.00 nm (pv:4840.00)
80% of data is between -360.00 and 3800.00 nm (pv:4160.00)

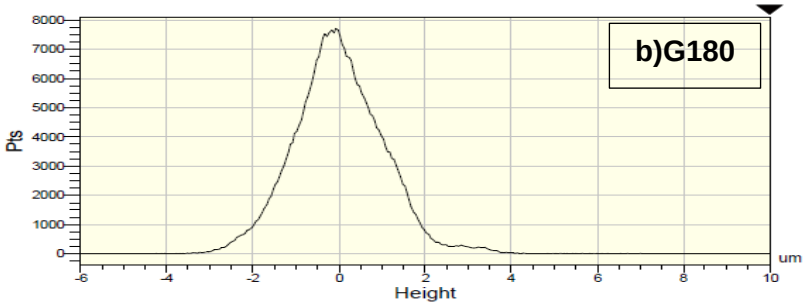

95% of data is between 280.00 and 3520.00 nm (pv:3240.00)
90% of data is between 640.00 and 3280.00 nm (pv:2640.00)
85% of data is between 720.00 and 3040.00 nm (pv:2320.00)
80% of data is between 920.00 and 2960.00 nm (pv:2040.00)

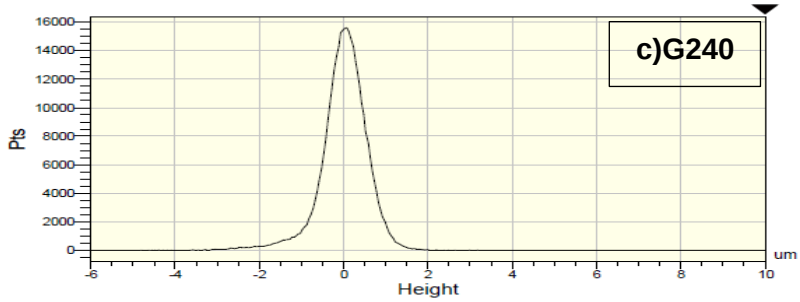

95% of data is between 920.00 and 2800.00 nm (pv:1880.00)
90% of data is between 1320.00 and 2680.00 nm (pv:1360.00)
85% of data is between 1480.00 and 2600.00 nm (pv:1120.00)
80% of data is between 1560.00 and 2520.00 nm (pv:960.00)

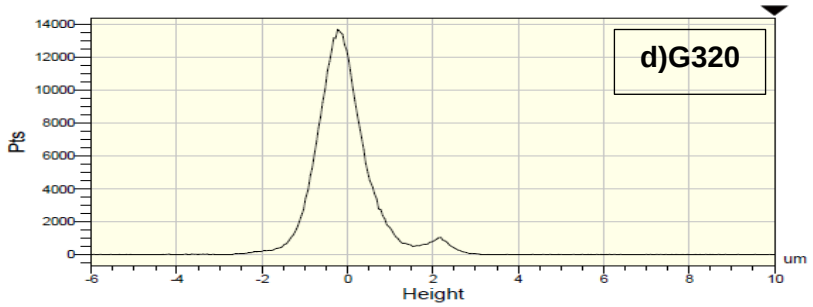

95% of data is between 800.00 and 3520.00 nm (pv:2720.00)
90% of data is between 960.00 and 2760.00 nm (pv:1800.00)
85% of data is between 1080.00 and 2520.00 nm (pv:1440.00)
80% of data is between 1240.00 and 2440.00 nm (pv:1200.00)

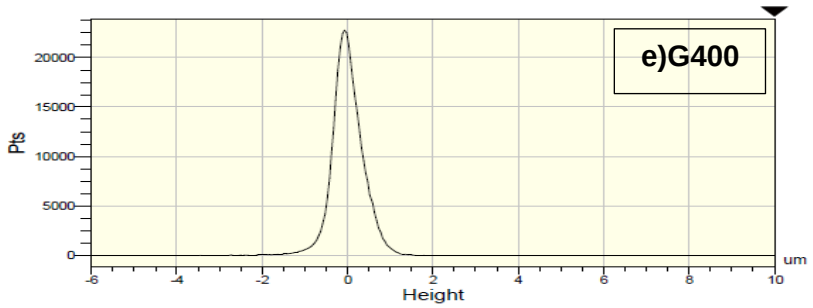

95% of data is between 1440.00 and 2640.00 nm (pv:1200.00)
90% of data is between 1480.00 and 2440.00 nm (pv:960.00)
85% of data is between 1560.00 and 2360.00 nm (pv:800.00)
80% of data is between 1640.00 and 2320.00 nm (pv:680.00)

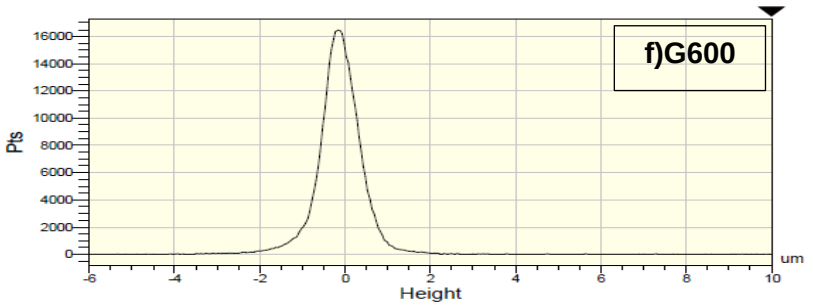

95% of data is between 760.00 and 2720.00 nm (pv:1960.00)
90% of data is between 1200.00 and 2560.00 nm (pv:1360.00)
85% of data is between 1280.00 and 2400.00 nm (pv:1120.00)
80% of data is between 1360.00 and 2320.00 nm (pv:960.00)

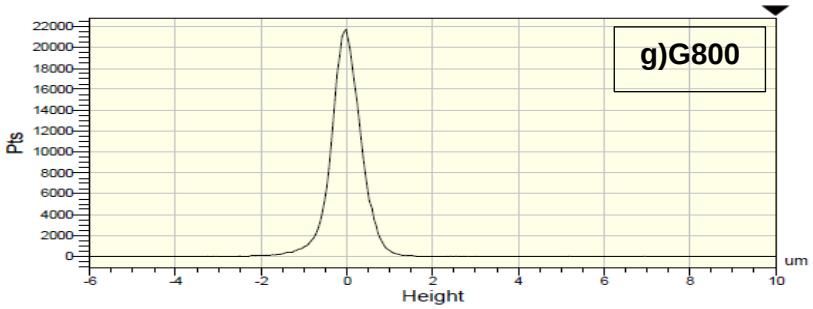

95% of data is between 1280.00 and 2600.00 nm (pv:1320.00)
90% of data is between 1440.00 and 2440.00 nm (pv:1000.00)
85% of data is between 1520.00 and 2360.00 nm (pv:840.00)
80% of data is between 1560.00 and 2280.00 nm (pv:720.00)

Figure A-8 Histograms for nickel samples a)G60, b)G180, c)G240, d)G320, e)G400, f)G600 and g)G800 after corrosion

Appendix B_1: EDS results for nickel samples before corrosion

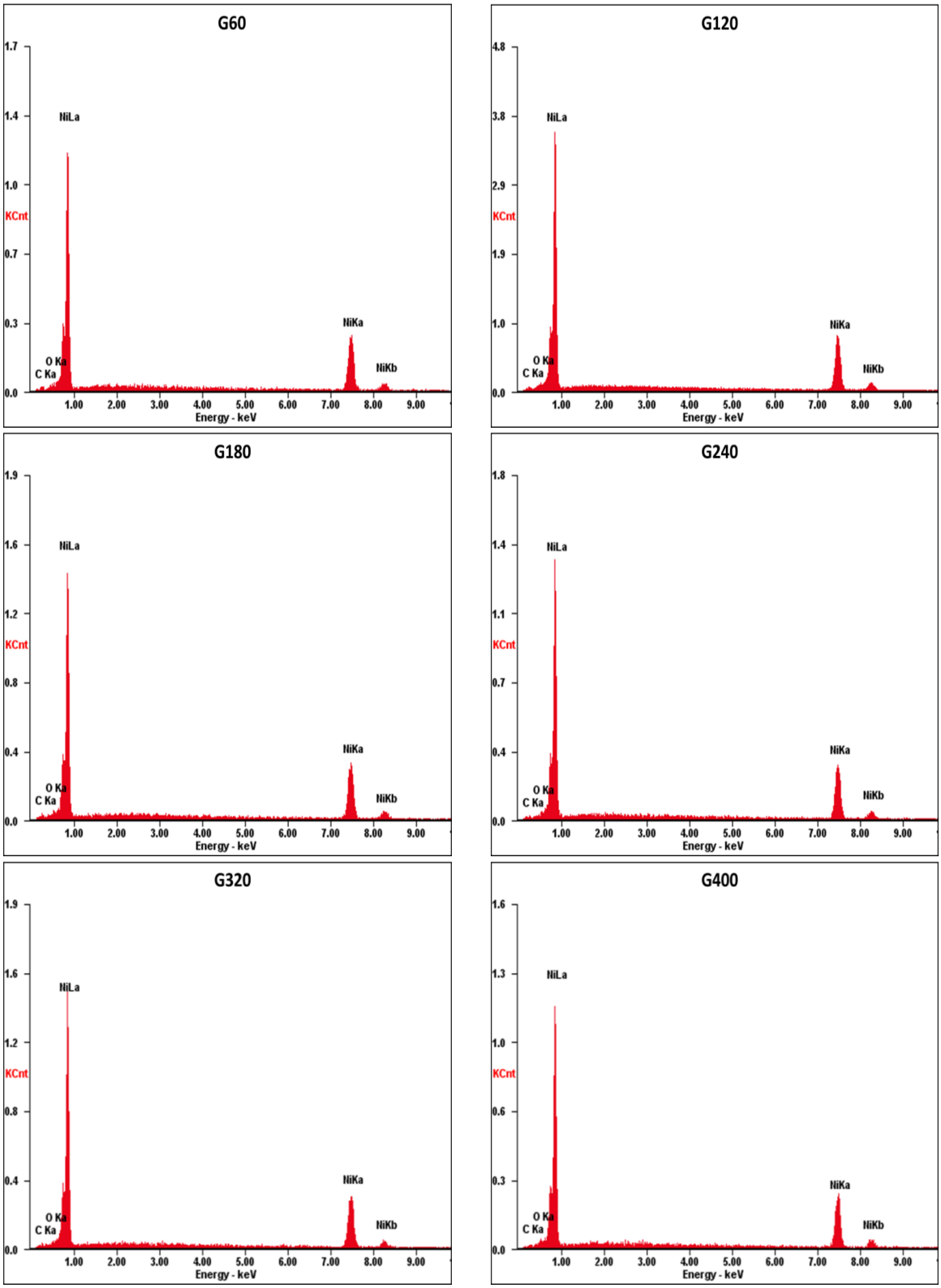

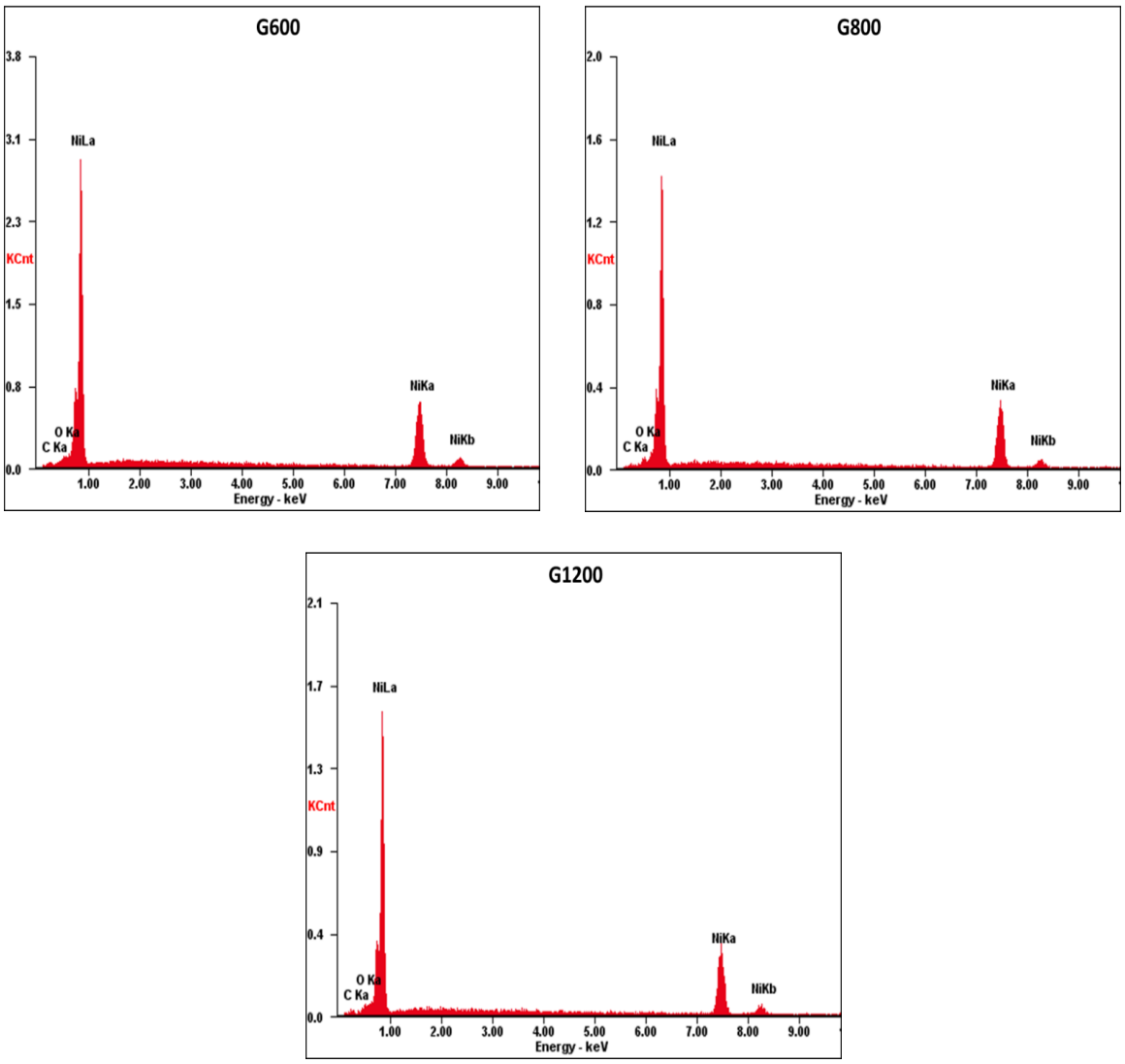

Figure B-1 EDS analysis for nickel samples before corrosion

Appendix B_2: EDS results for nickel samples after corrosion

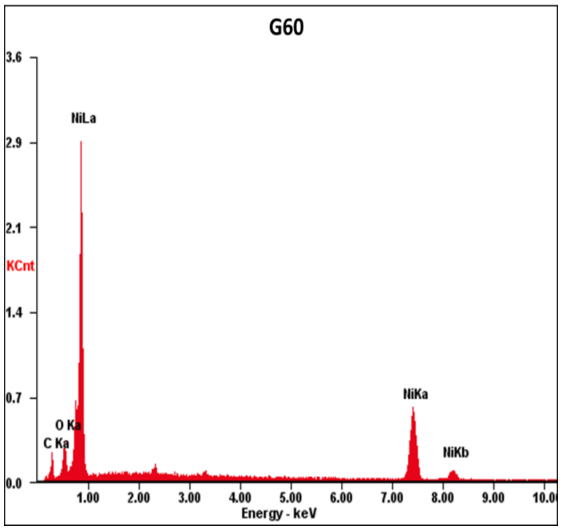

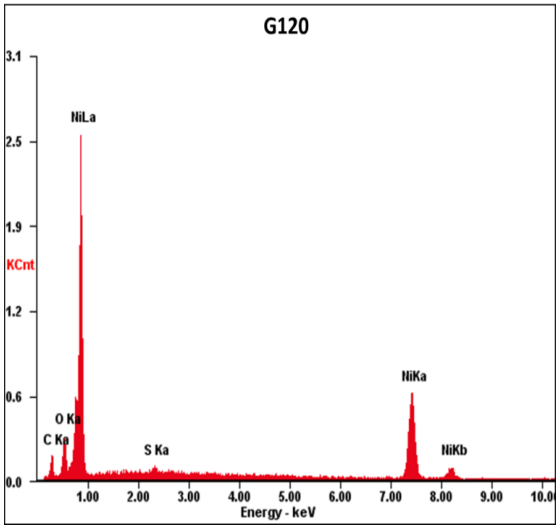

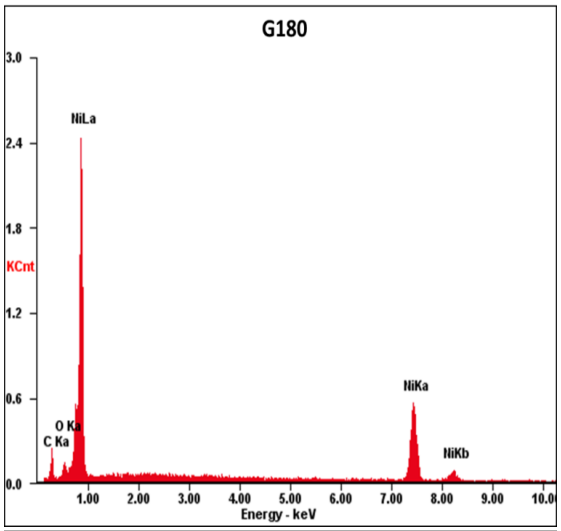

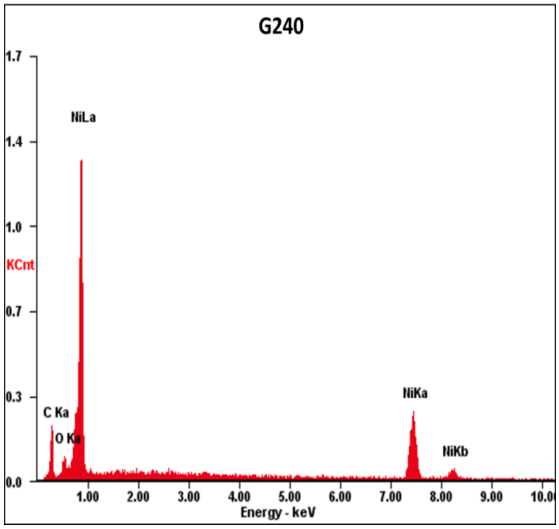

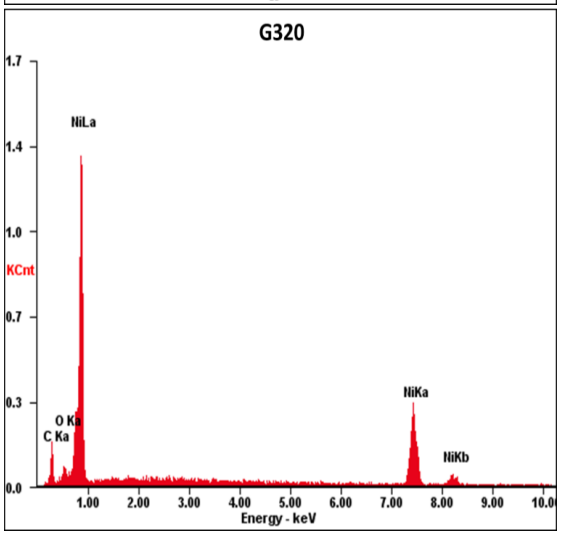

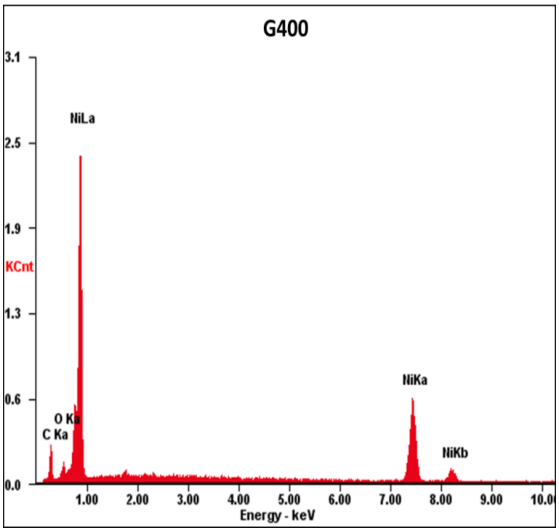

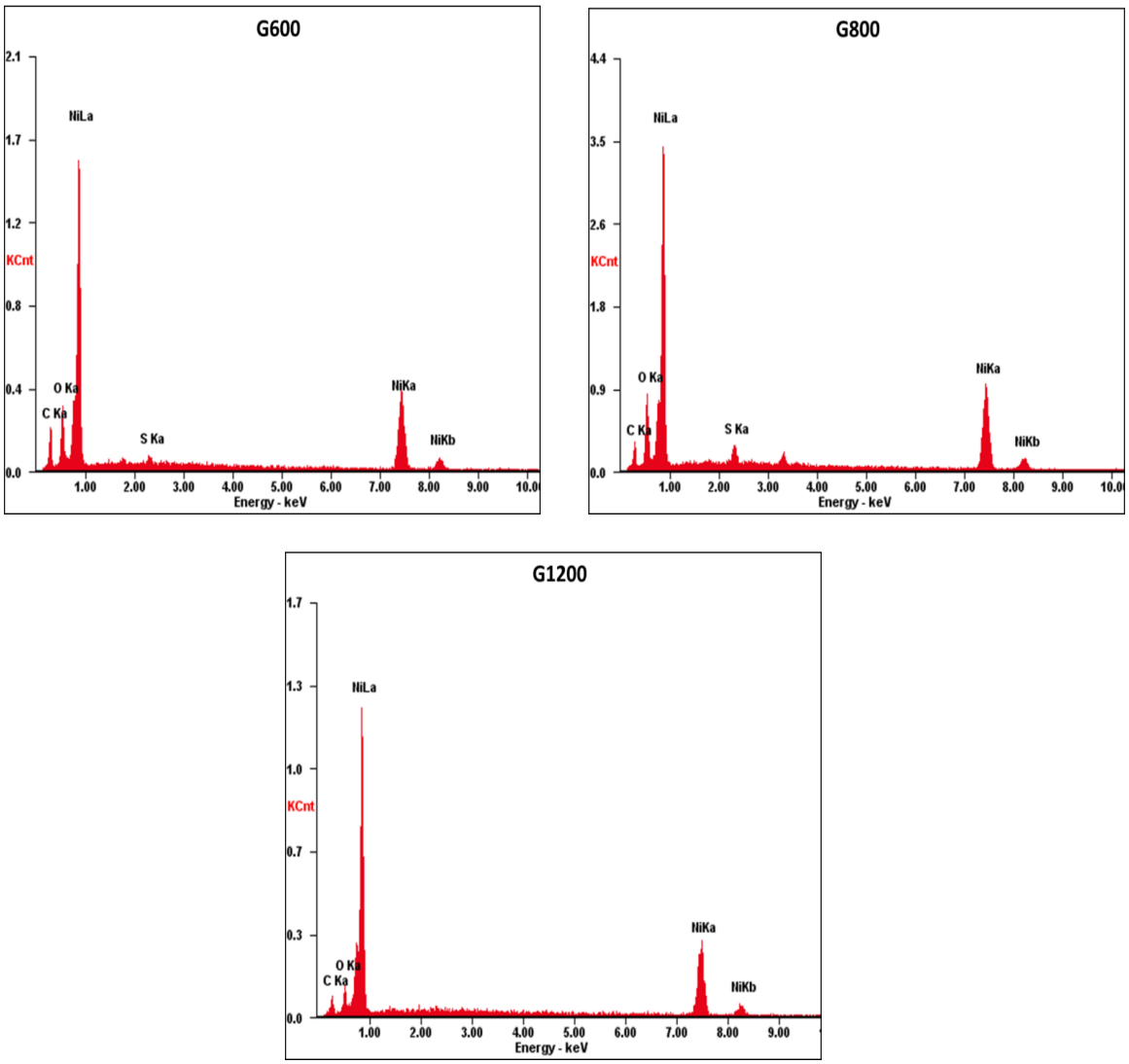

Figure B-2 EDS analysis for nickel samples after corrosion

Appendix $C_{1\text{-before}}$: 2D images, 3D textures, for mild steel samples with different roughnesses before corrosion

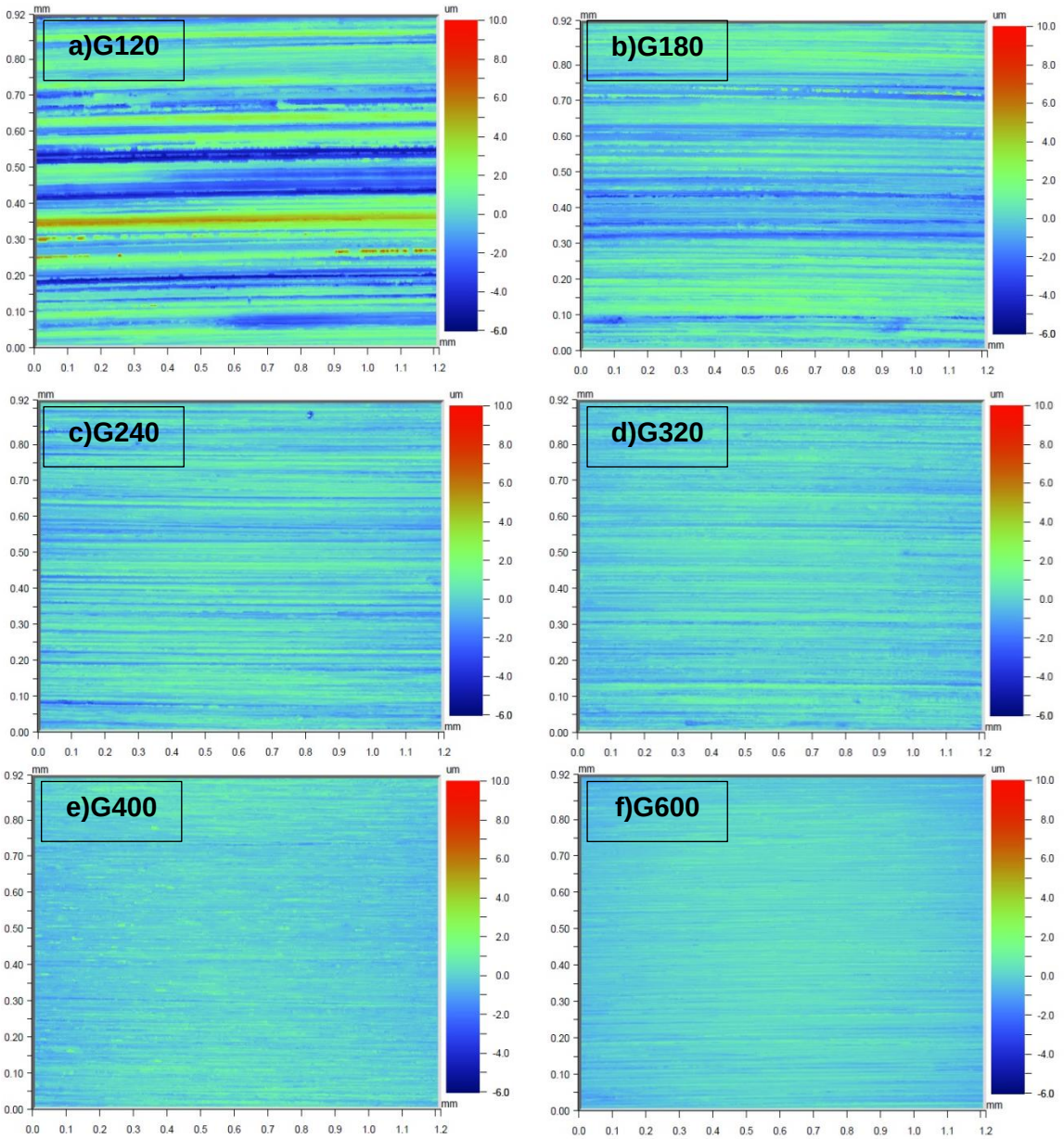

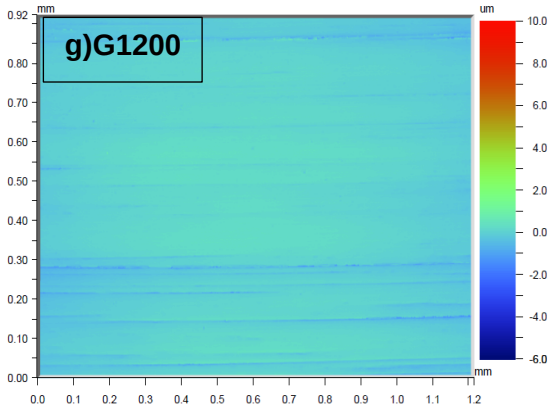

Figure C-1 2D images for mild steel samples a)G120, b)G180, c)G240, d)G320, e)G400, f)G600 and g)G1200 before corrosion

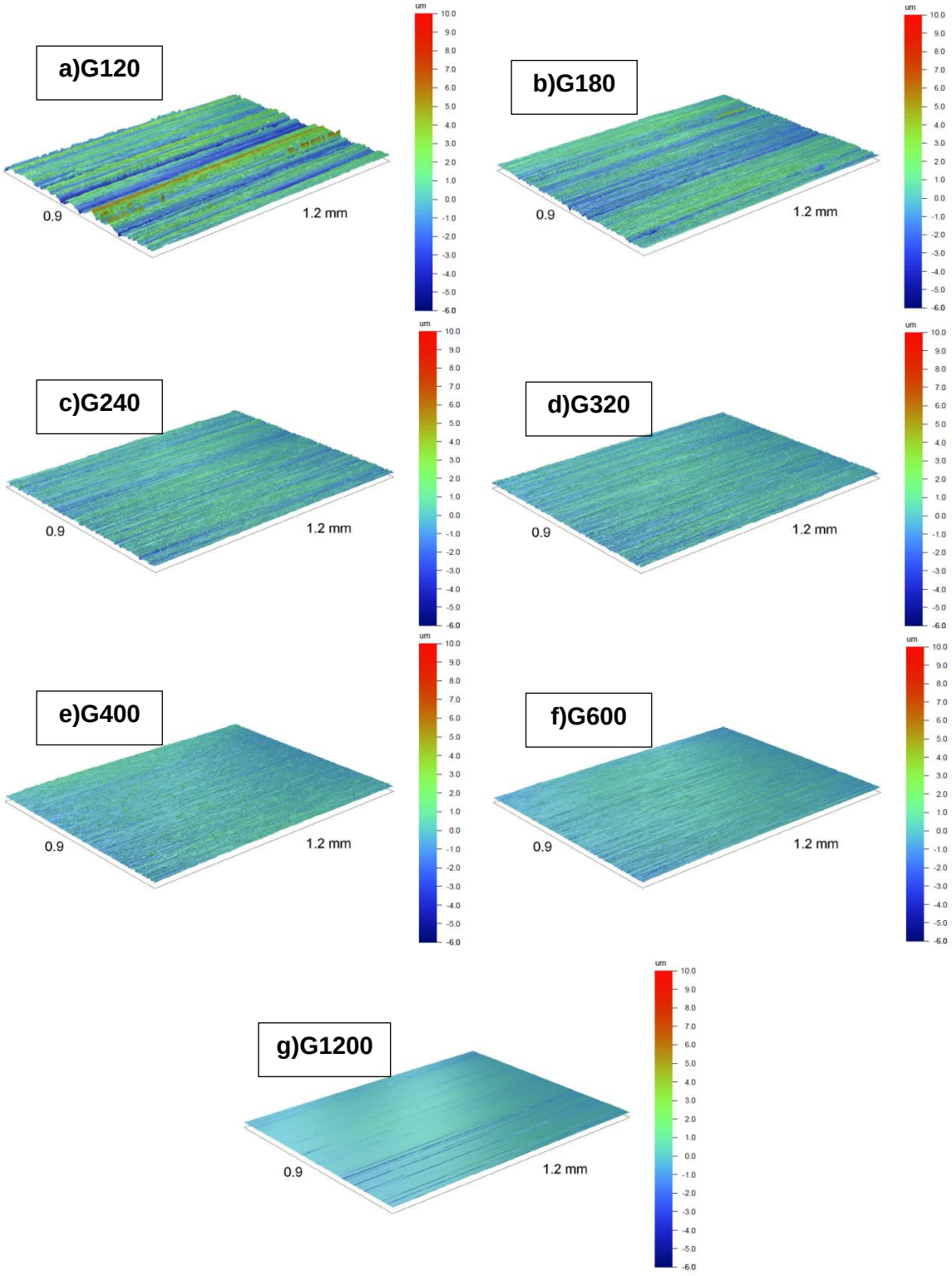

Figure C-2 3D images for mild steel samples a)G120, b)G180, c)G240, d)G320, e)G400, f)G600 and g)G1200 before corrosion

Appendix $C_{1\text{-after}}$: 2D images, 3D textures, for mild steel samples with different roughnesses after corrosion

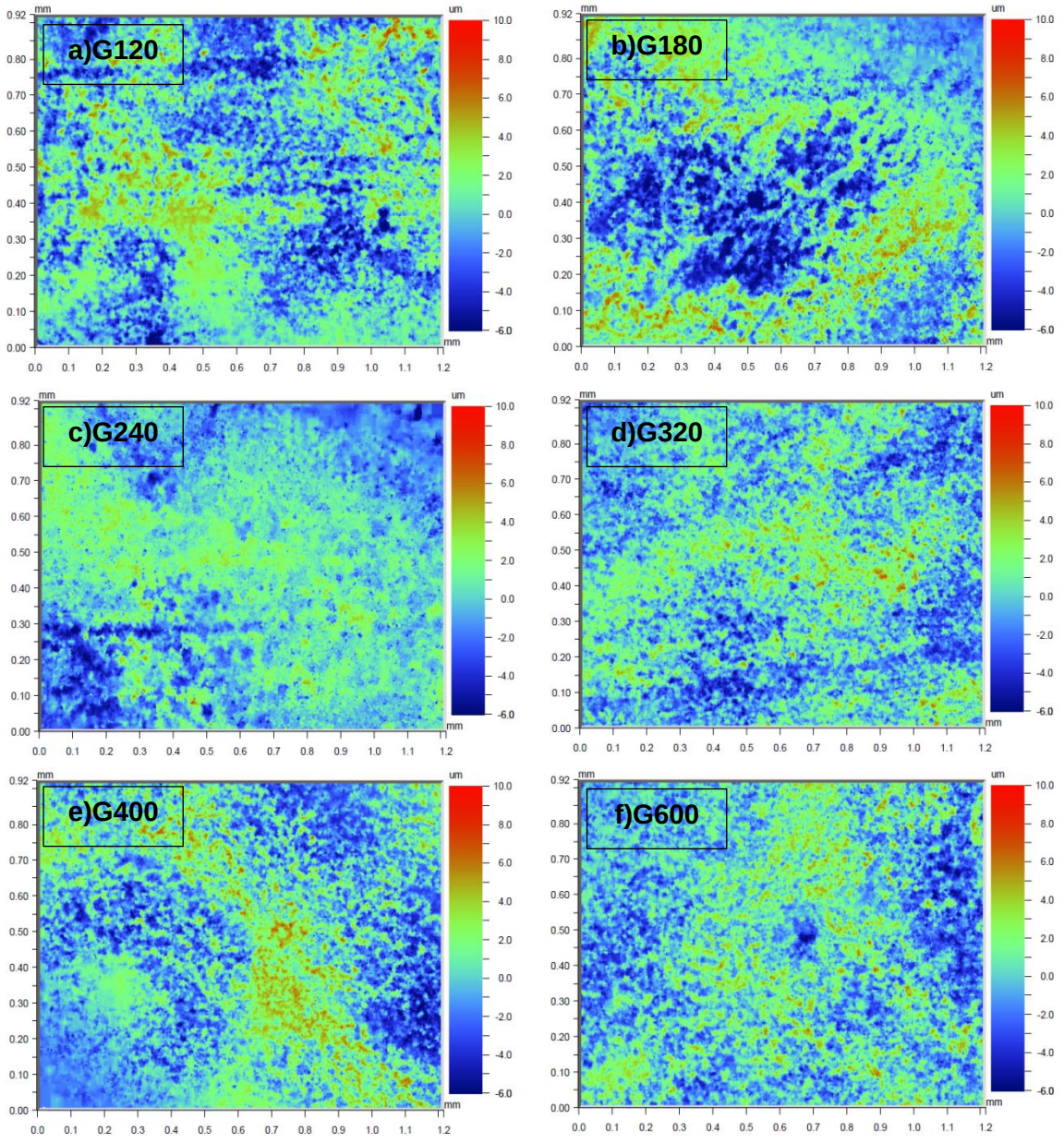

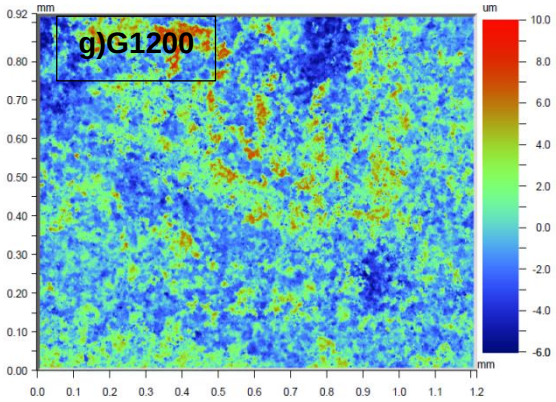

Figure C-3 2D images for mild steel samples a)G120, b)G180, c)G240, d)G320, e)G400, f)G600 and g)G1200 after corrosion

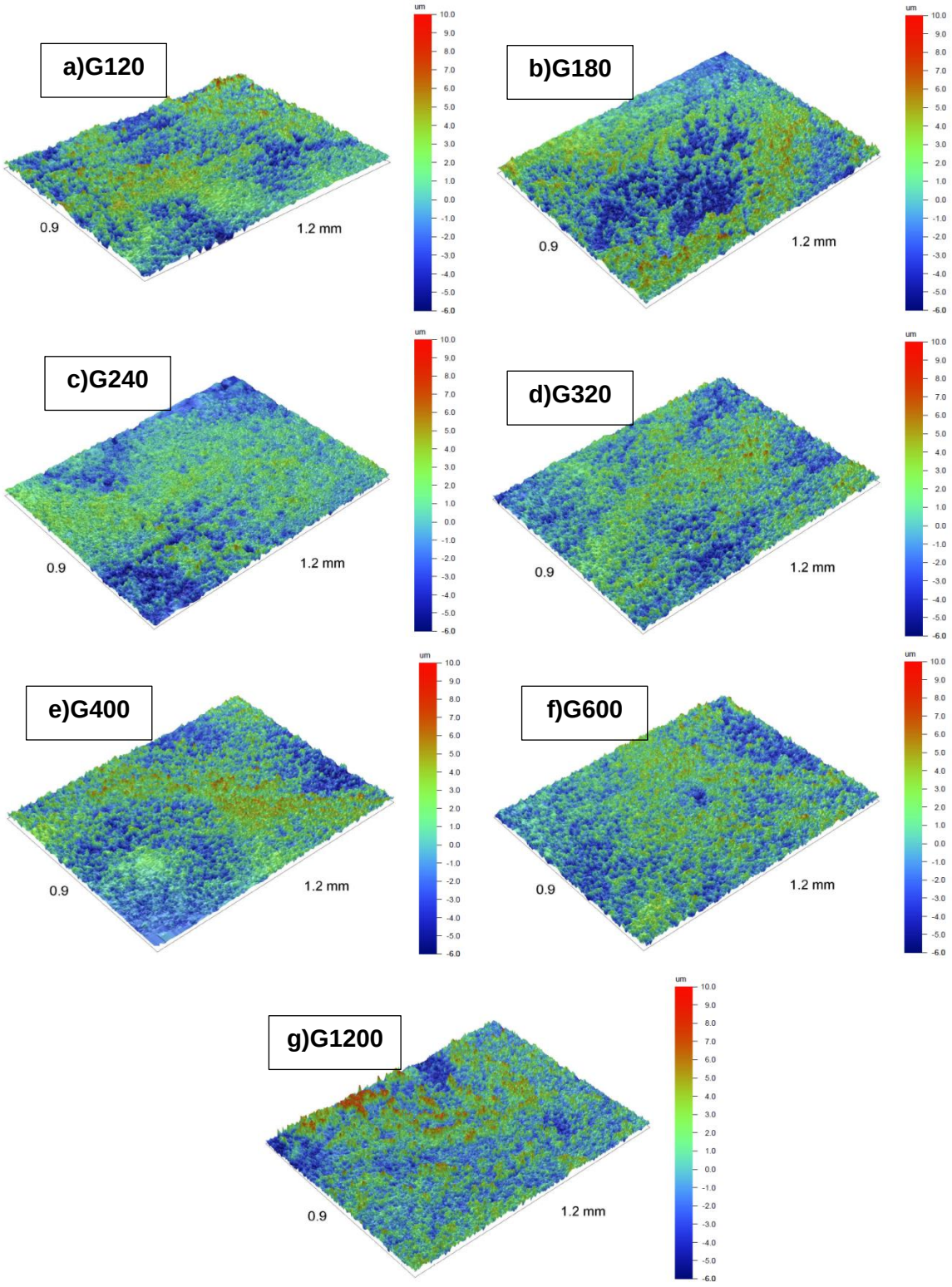

Figure C-4 3D images for mild steel samples a)G120, b)G180, c)G240, d)G320, e)G400, f)G600 and g)G1200 after corrosion

Appendix $C_{2\text{-before}}$: X and Y profiles for mild steel samples with different roughnesses before corrosion

a)G120 X Profile

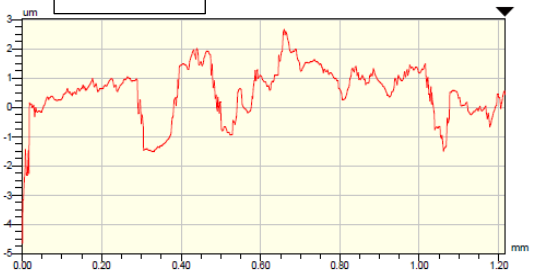

Y Profile

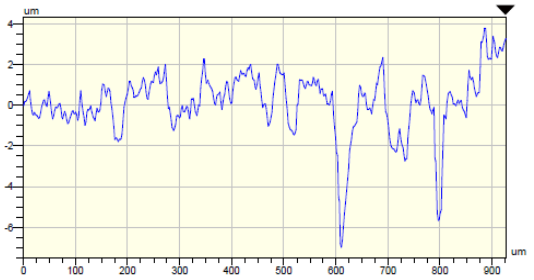

b)G180 X Profile

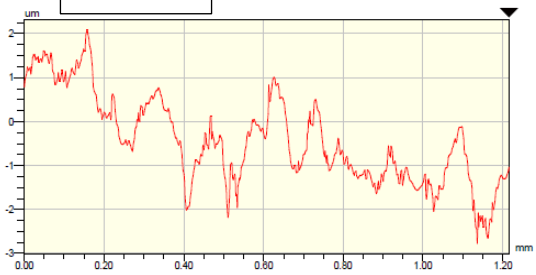

Y Profile

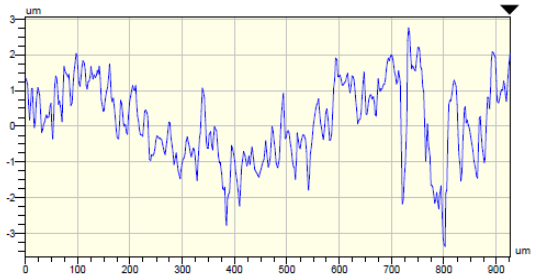

c)G240 X Profile

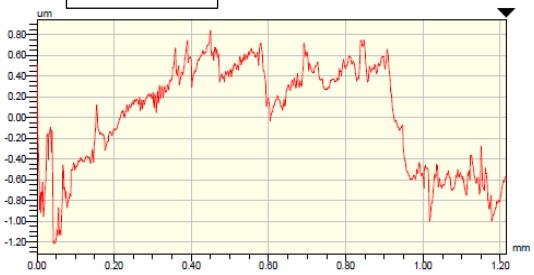

Y Profile

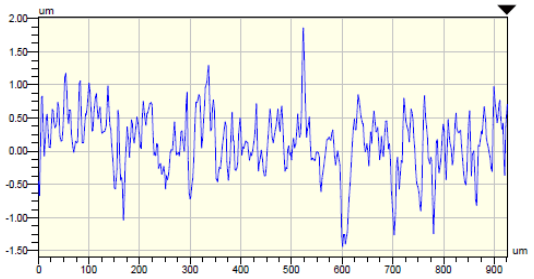

d)G320 X Profile

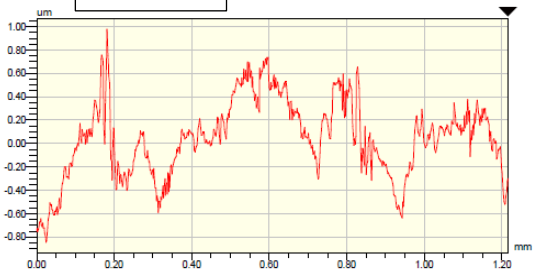

Y Profile

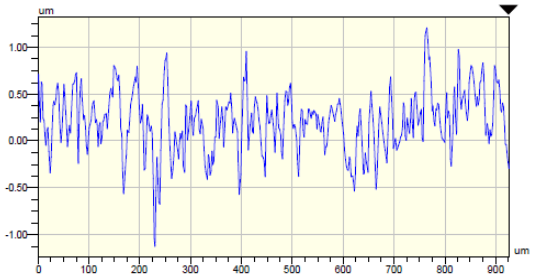

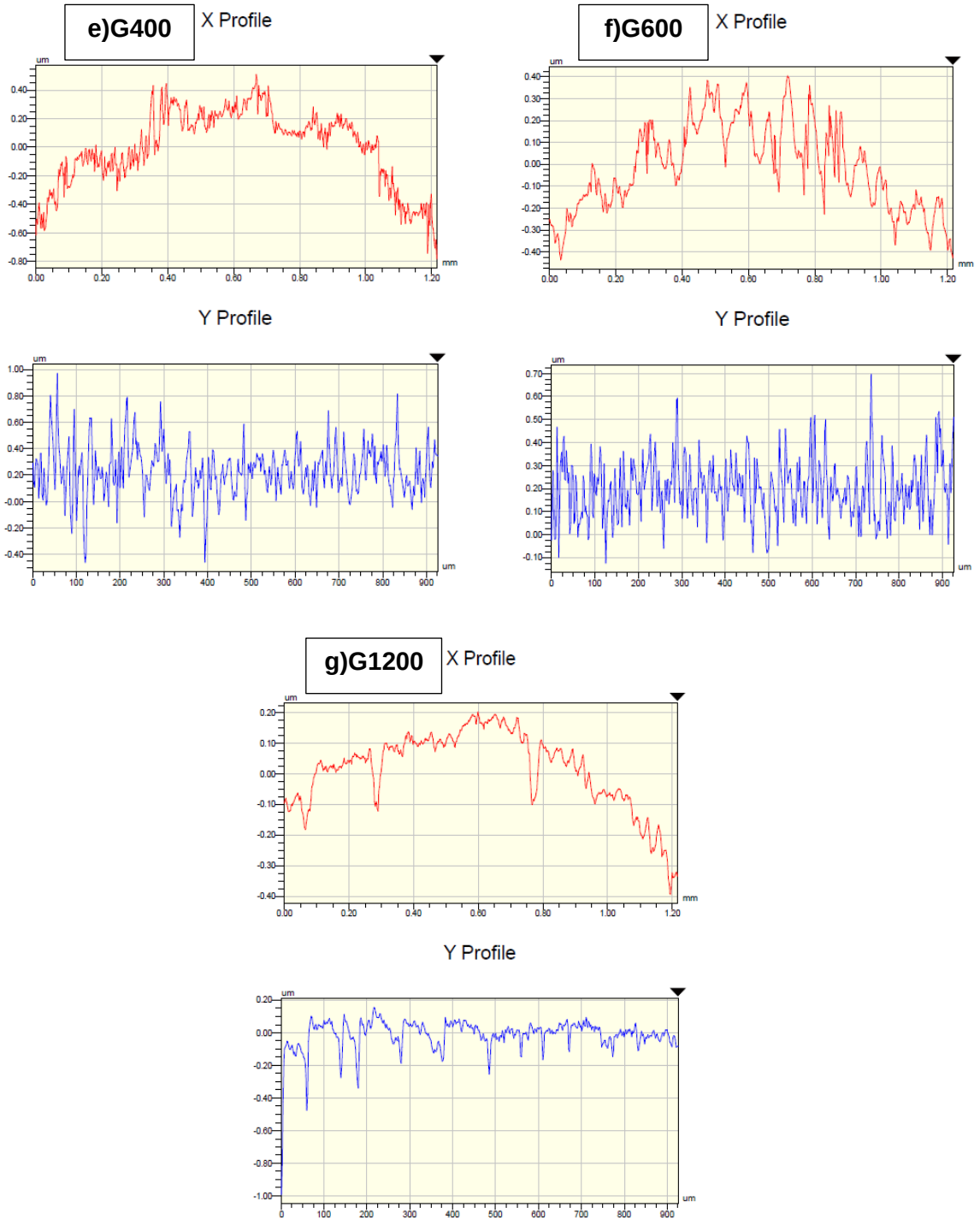

Figure C-5 X and Y profiles for mild steel samples a)G120, b)G180, c)G240, d)G320, e)G400, f)G600 and g)G1200 before corrosion

Appendix $C_{2\text{-after}}$: X and Y profiles for mild steel samples with different roughnesses after corrosion

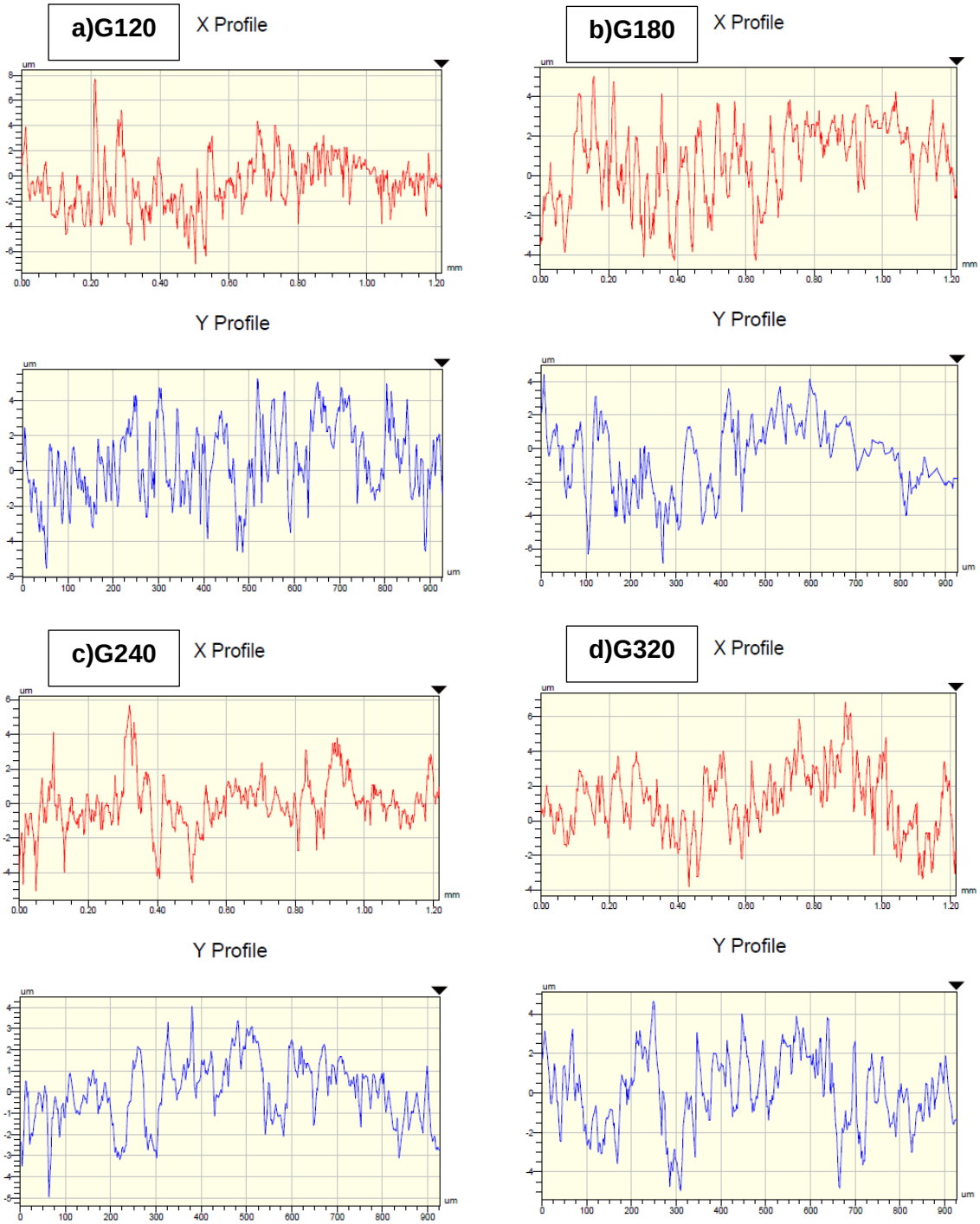

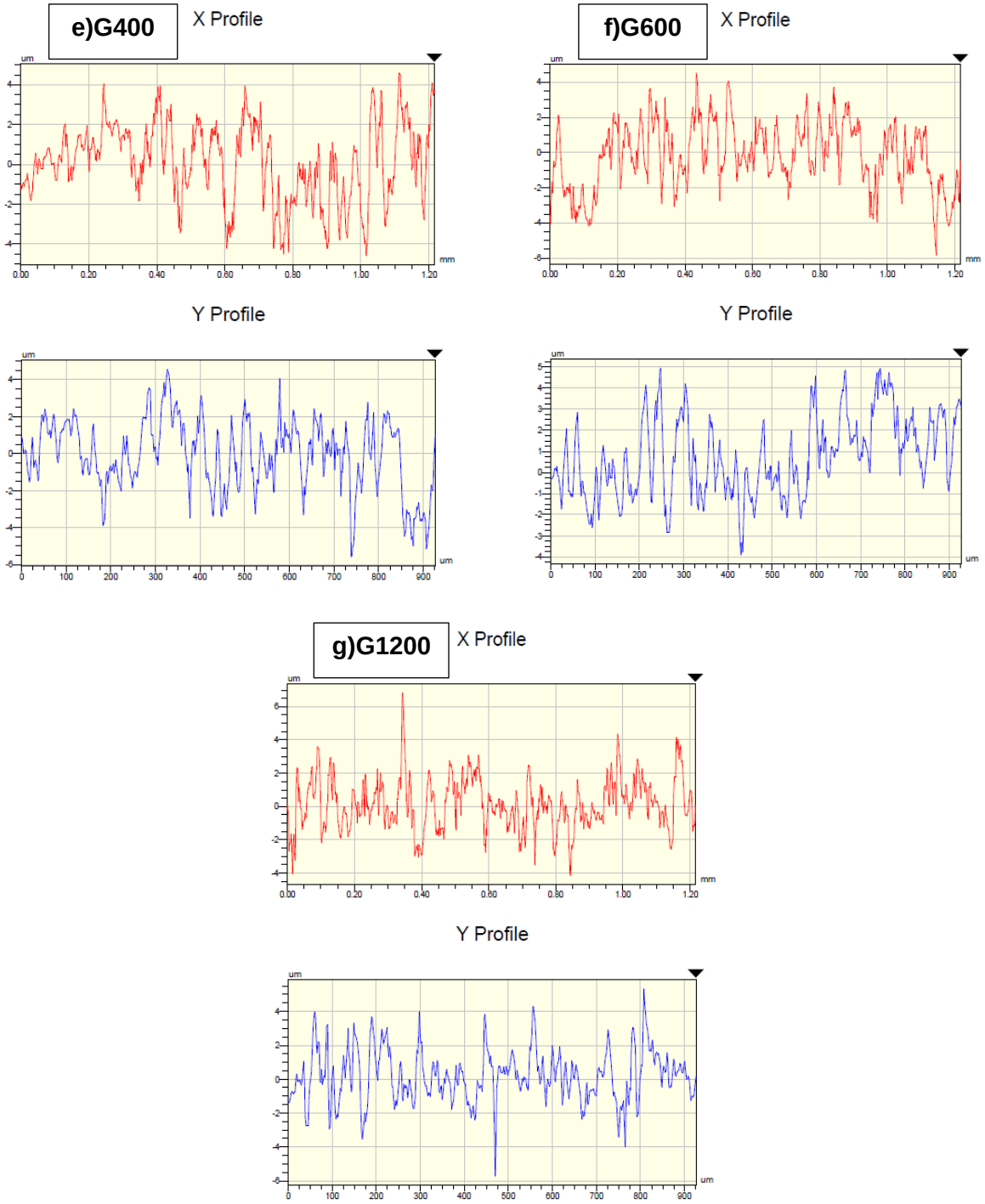

Figure C-6 X and Y profiles for mild steel samples a)G120, b)G180, c)G240, d)G320, e)G400, f)G600 and g)G1200 after corrosion

Appendix $C_{3\text{-before}}$: Histograms for mild steel samples with different roughnesses before corrosion

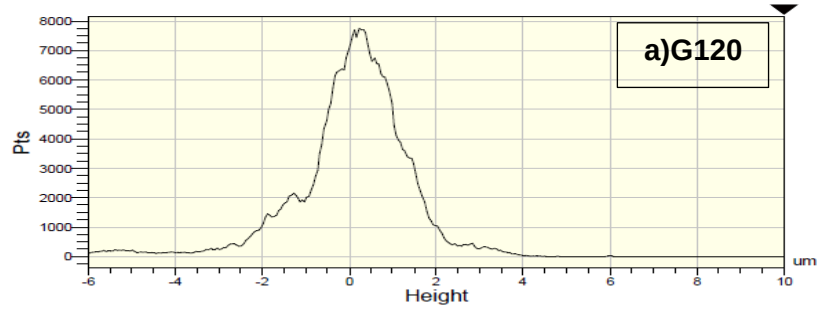

95% of data is between -400.00 and 4240.00 nm (pv:4640.00)
90% of data is between 240.00 and 3480.00 nm (pv:3240.00)
85% of data is between 640.00 and 3320.00 nm (pv:2680.00)
80% of data is between 840.00 and 3160.00 nm (pv:2320.00)

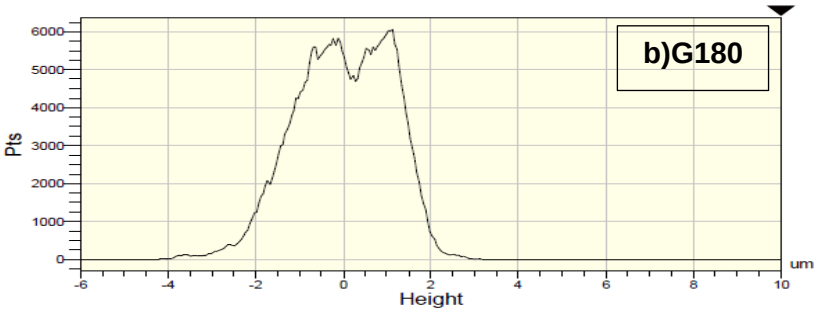

95% of data is between 320.00 and 3400.00 nm (pv:3080.00)
90% of data is between 560.00 and 3240.00 nm (pv:2680.00)
85% of data is between 720.00 and 3120.00 nm (pv:2400.00)
80% of data is between 920.00 and 3080.00 nm (pv:2160.00)

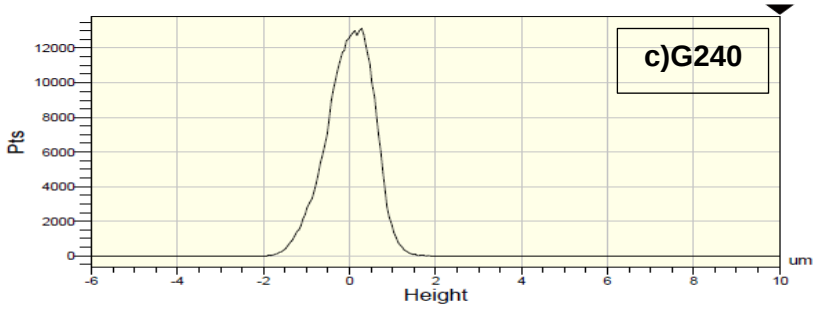

95% of data is between 1080.00 and 2680.00 nm (pv:1600.00)
90% of data is between 1200.00 and 2560.00 nm (pv:1360.00)
85% of data is between 1400.00 and 2560.00 nm (pv:1160.00)
80% of data is between 1440.00 and 2480.00 nm (pv:1040.00)

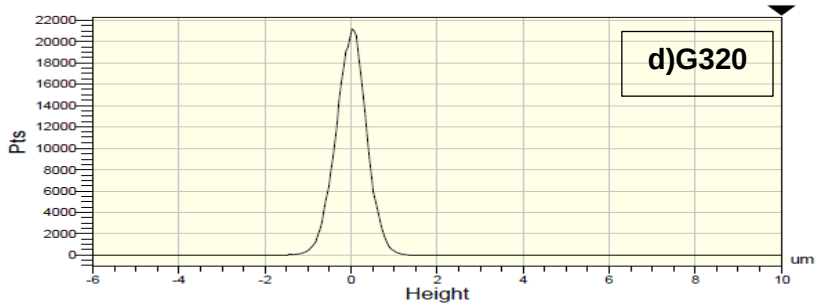

95% of data is between 1400.00 and 2480.00 nm (pv:1080.00)
90% of data is between 1520.00 and 2400.00 nm (pv:880.00)
85% of data is between 1600.00 and 2360.00 nm (pv:760.00)
80% of data is between 1600.00 and 2280.00 nm (pv:680.00)

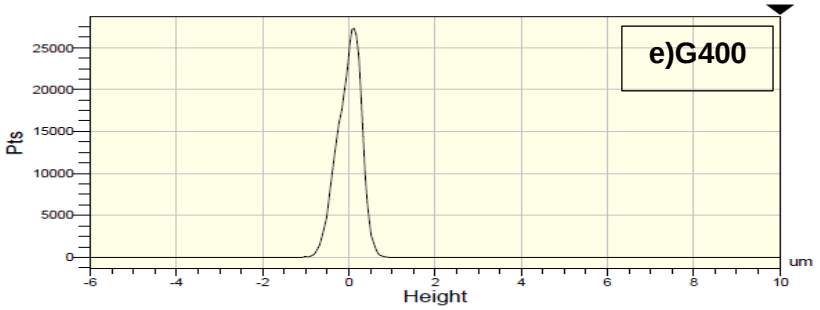

95% of data is between 1520.00 and 2320.00 nm (pv:800.00)
90% of data is between 1600.00 and 2280.00 nm (pv:680.00)
85% of data is between 1640.00 and 2240.00 nm (pv:600.00)
80% of data is between 1680.00 and 2200.00 nm (pv:520.00)

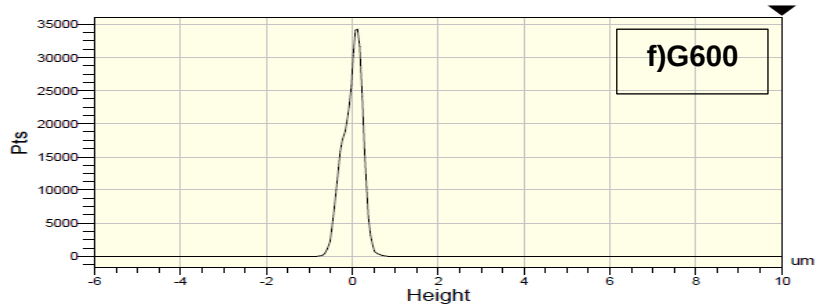

95% of data is between 1600.00 and 2240.00 nm (pv:640.00)
90% of data is between 1640.00 and 2200.00 nm (pv:560.00)
85% of data is between 1720.00 and 2200.00 nm (pv:480.00)
80% of data is between 1720.00 and 2160.00 nm (pv:440.00)

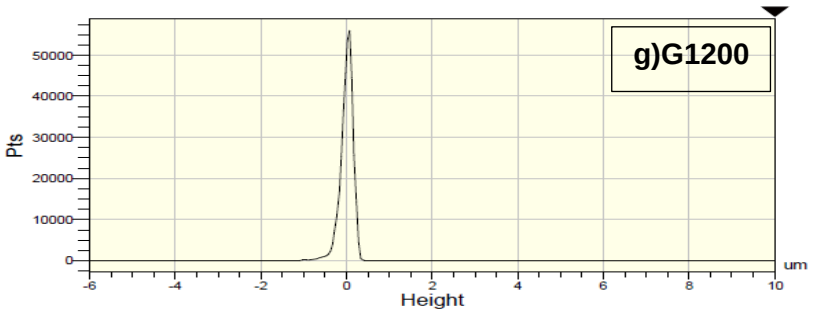

95% of data is between 1720.00 and 2160.00 nm (pv:440.00)
90% of data is between 1760.00 and 2120.00 nm (pv:360.00)
85% of data is between 1840.00 and 2120.00 nm (pv:280.00)
80% of data is between 1880.00 and 2120.00 nm (pv:240.00)

Figure C-7 Histograms for mild steel samples a)G120, b)G180, c)G240, d)G320, e)G400, f)G600 and g)G1200 before corrosion

Appendix $C_{3\text{-after}}$: Histograms for mild steel samples with different roughnesses after corrosion

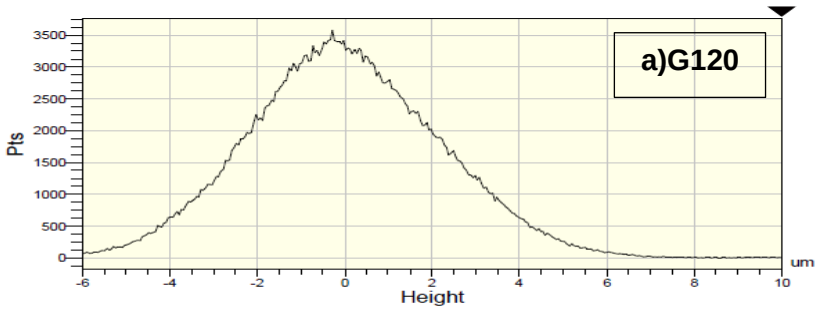

95% of data is between -1520.00 and 5280.00 nm (pv:6800.00)
90% of data is between -960.00 and 4760.00 nm (pv:5720.00)
85% of data is between -640.00 and 4360.00 nm (pv:5000.00)
80% of data is between -400.00 and 4040.00 nm (pv:4440.00)

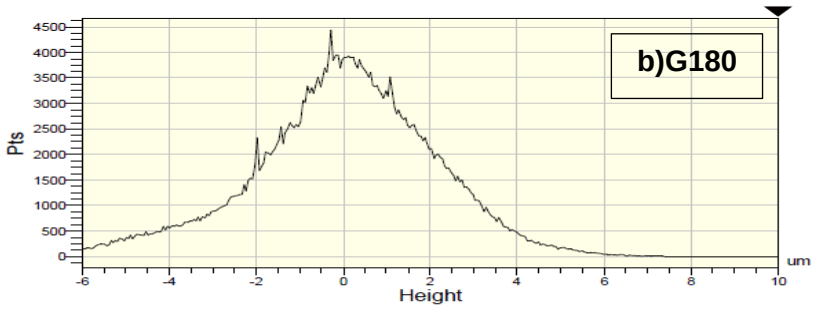

95% of data is between -1800.00 and 5080.00 nm (pv:6880.00)
90% of data is between -840.00 and 4760.00 nm (pv:5600.00)
85% of data is between -360.00 and 4400.00 nm (pv:4760.00)
80% of data is between -80.00 and 4080.00 nm (pv:4160.00)

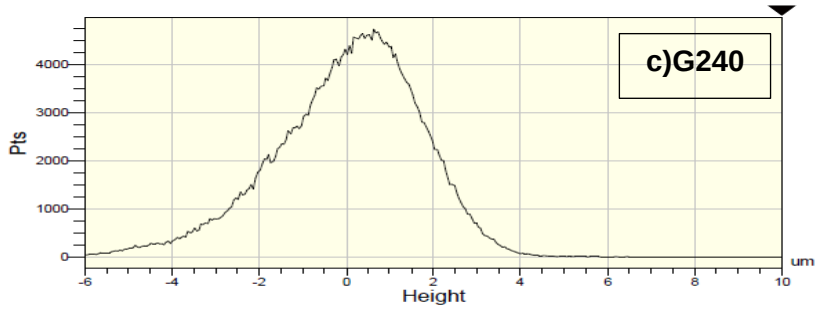

95% of data is between -880.00 and 4320.00 nm (pv:5200.00)
90% of data is between -240.00 and 4040.00 nm (pv:4280.00)
85% of data is between 80.00 and 3800.00 nm (pv:3720.00)
80% of data is between 360.00 and 3640.00 nm (pv:3280.00)

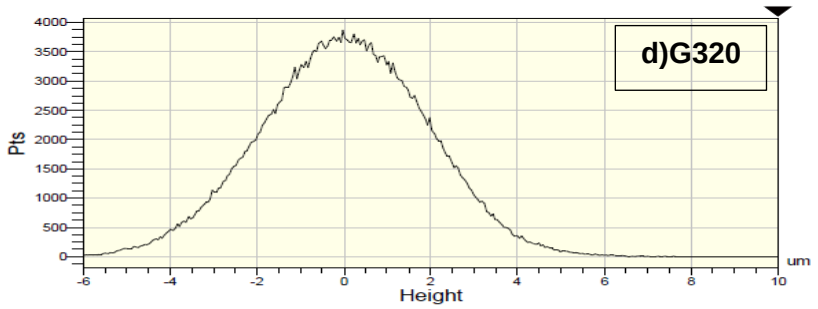

95% of data is between -1080.00 and 4760.00 nm (pv:5840.00)
90% of data is between -640.00 and 4280.00 nm (pv:4920.00)
85% of data is between -320.00 and 4000.00 nm (pv:4320.00)
80% of data is between -80.00 and 3760.00 nm (pv:3840.00)

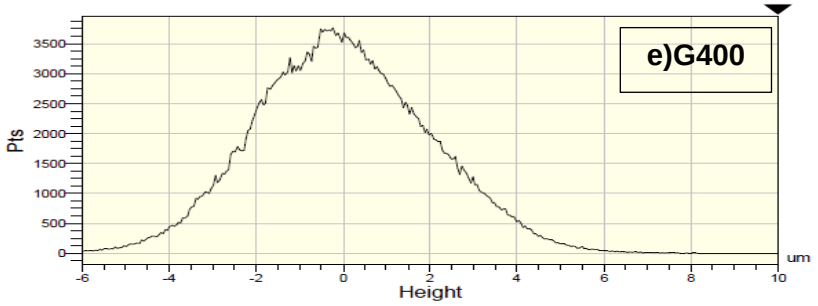

95% of data is between -1080.00 and 5080.00 nm (pv:6160.00)
90% of data is between -680.00 and 4520.00 nm (pv:5200.00)
85% of data is between -400.00 and 4160.00 nm (pv:4560.00)
80% of data is between -280.00 and 3800.00 nm (pv:4080.00)

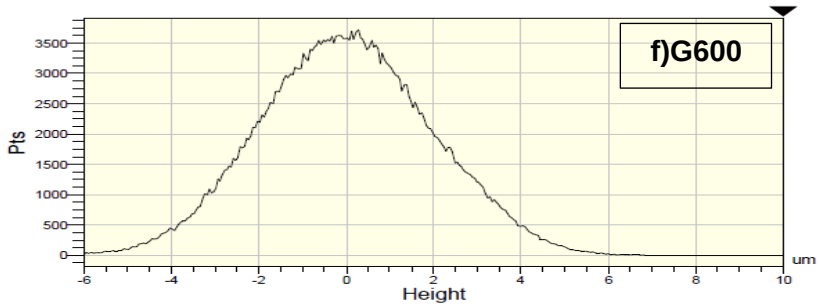

95% of data is between -1000.00 and 5000.00 nm (pv:6000.00)
90% of data is between -600.00 and 4480.00 nm (pv:5080.00)
85% of data is between -360.00 and 4120.00 nm (pv:4480.00)
80% of data is between -160.00 and 3840.00 nm (pv:4000.00)

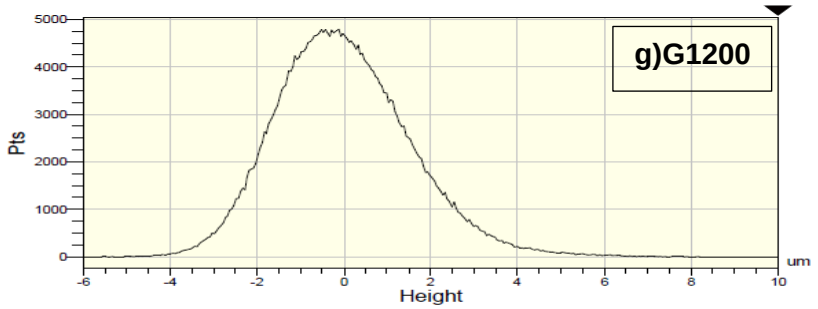

95% of data is between -320.00 and 4400.00 nm (pv:4720.00)
90% of data is between -120.00 and 3800.00 nm (pv:3920.00)
85% of data is between 120.00 and 3520.00 nm (pv:3400.00)
80% of data is between 320.00 and 3320.00 nm (pv:3000.00)

Figure C-8 Histograms for mild steel samples a)G120, b)G180, c)G240, d)G320, e)G400, f)G600 and g)G1200 after corrosion

Appendix D_1: EDS results for mild steel samples before corrosion

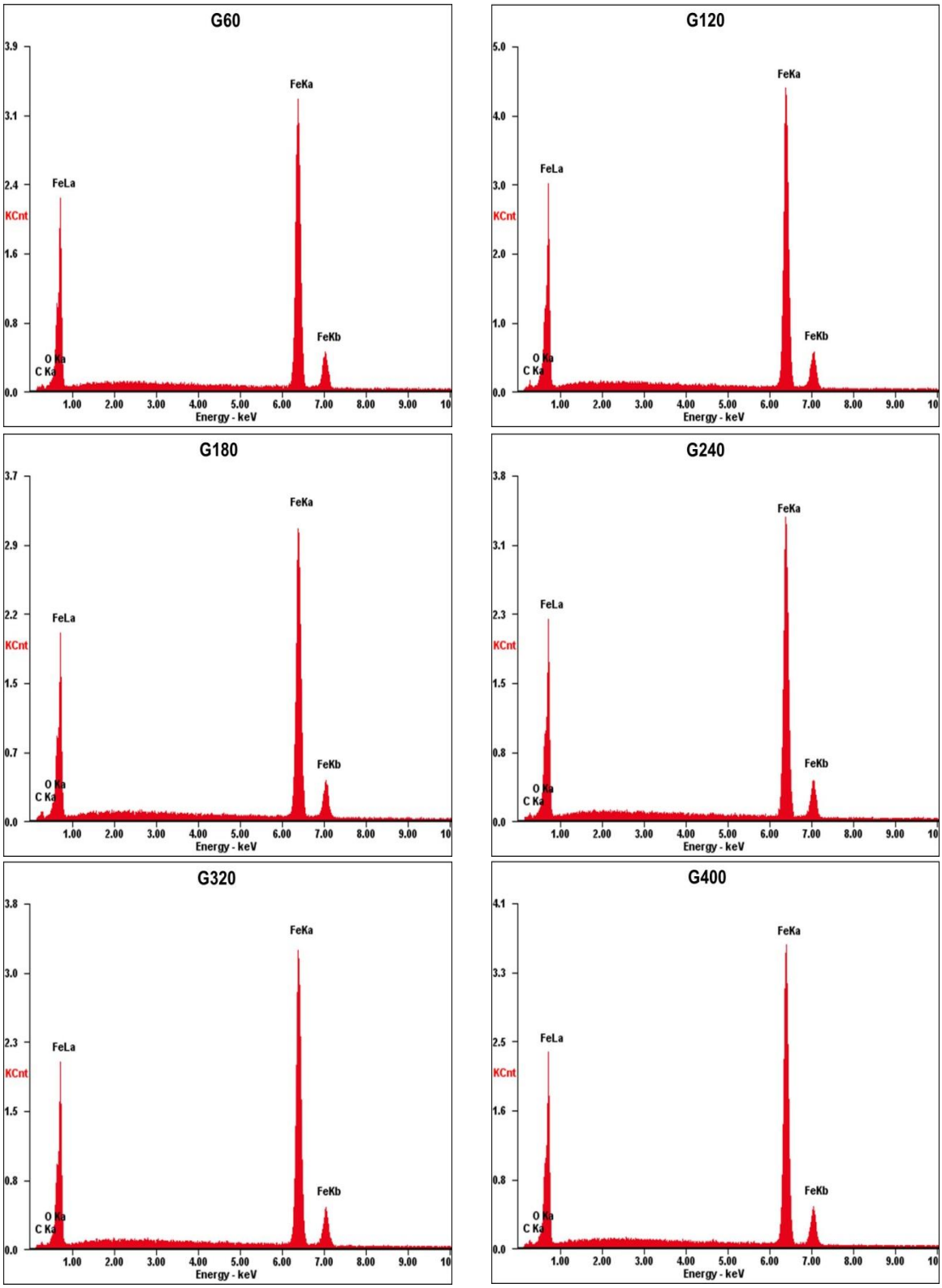

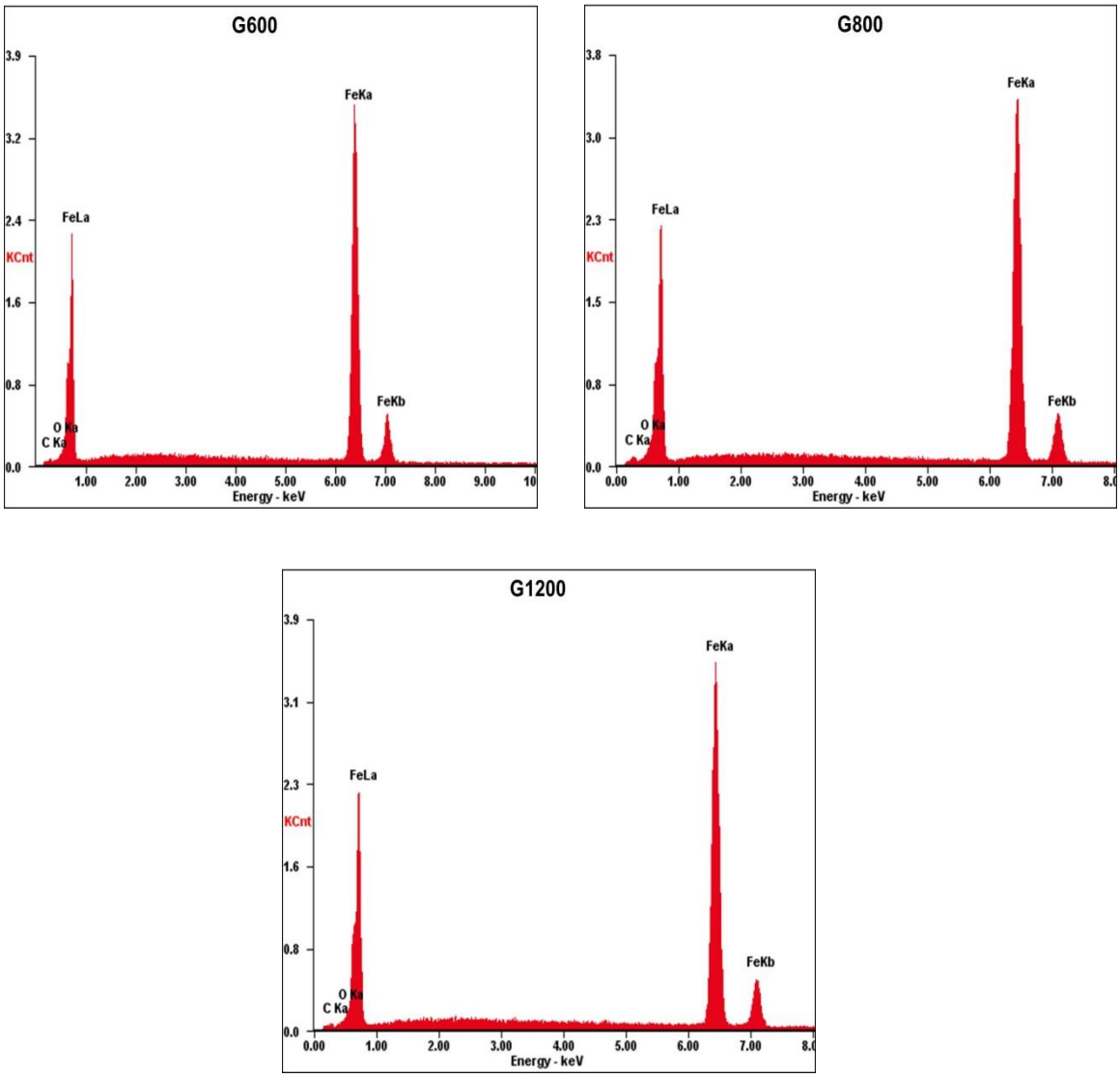

Figure D-1 EDS analysis for mild steel samples before corrosion

Appendix D_2: EDS results for mild steel samples after corrosion

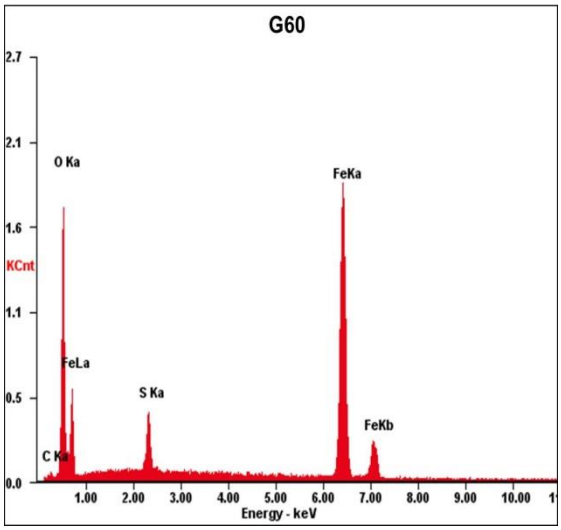

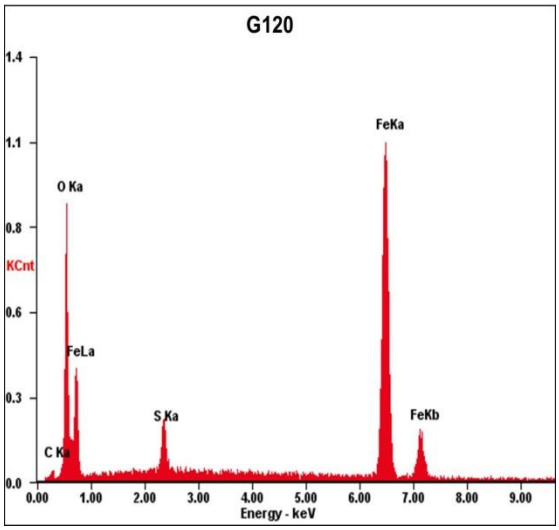

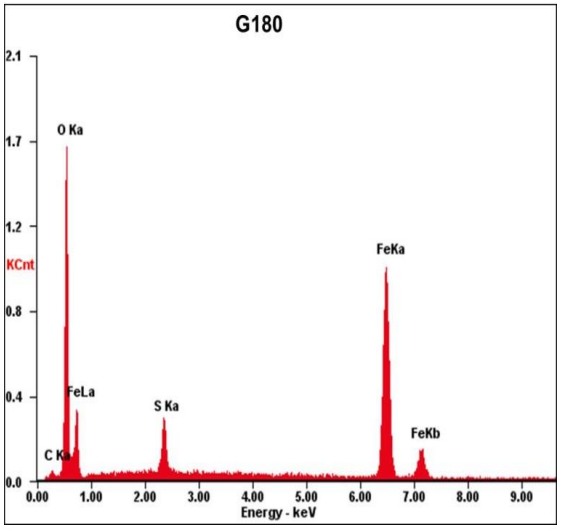

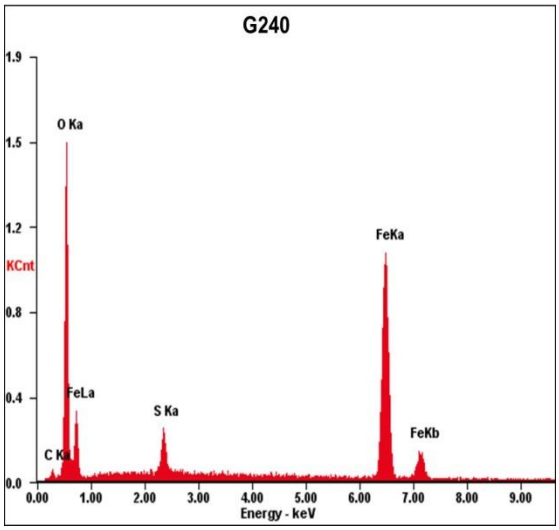

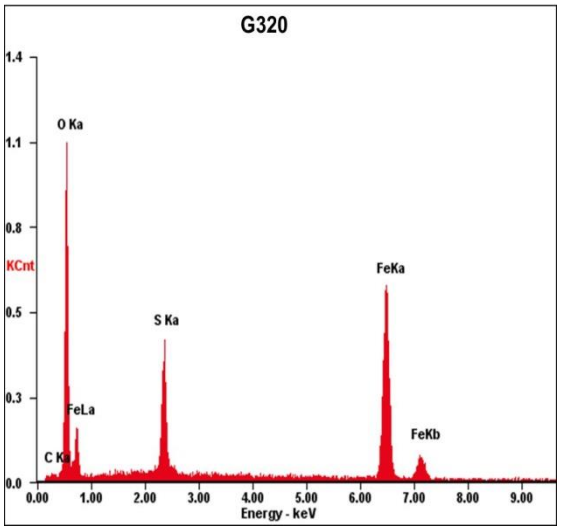

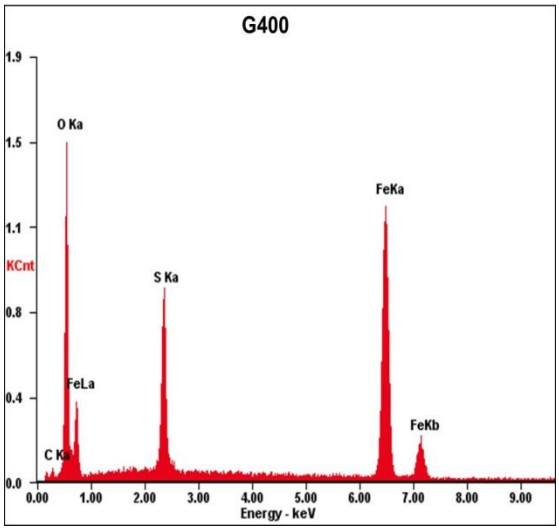

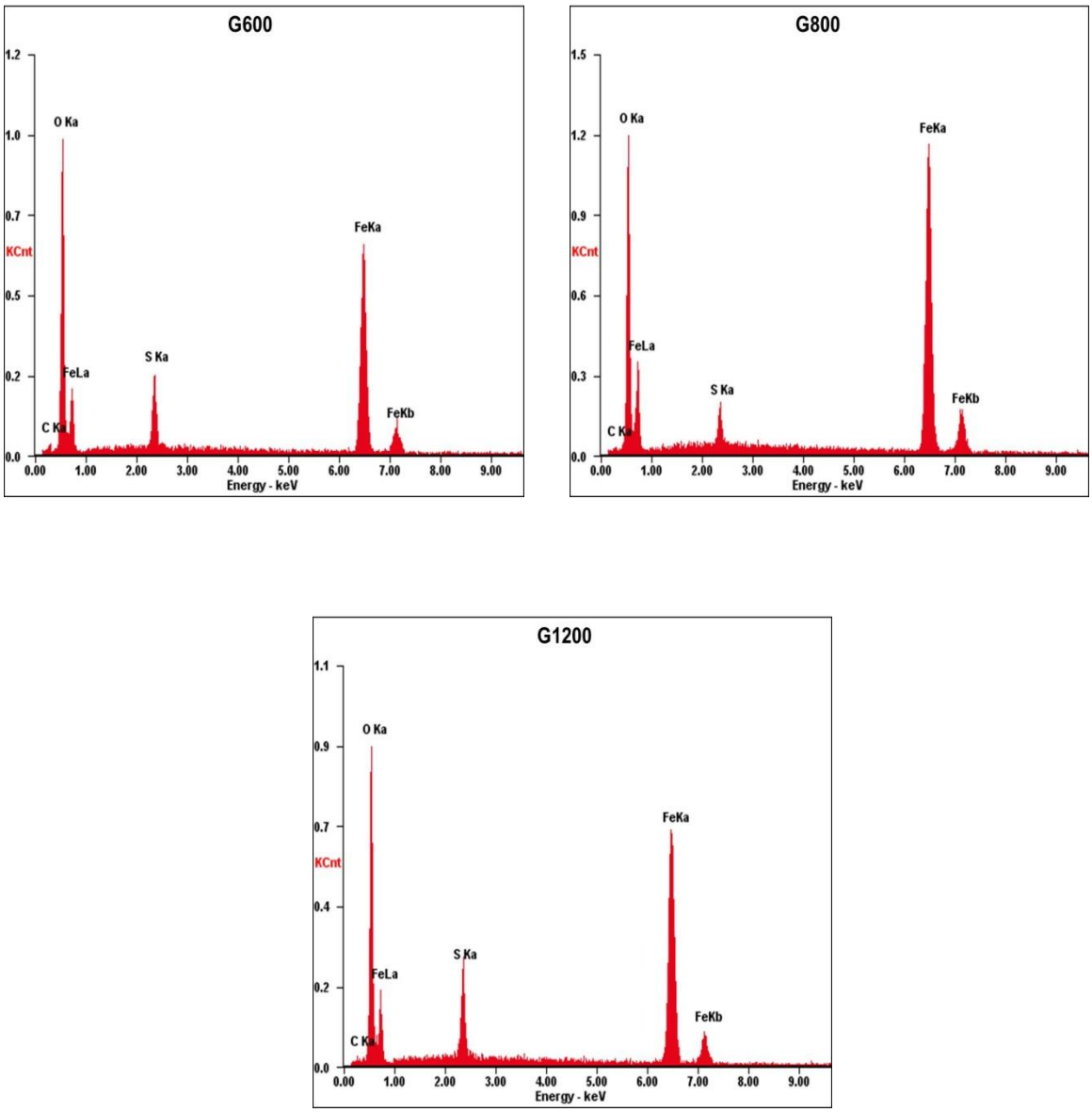

Figure D-2 EDS analysis for mild steel samples after corrosion

PUBLICATIONS

a. Refereed Journal Papers

1. **Toloei, A. S,** Stoilov, V, and Northwood, D. O. "*A new approach to combating corrosion of metallic materials "*, Applied Surface Science, 284 (2013) p 242-247.
2. **Toloei, A. S**., Stoilov, V., and Northwood, D. O. "*The Effect of Different Surface Topographies on the Corrosion Behaviour of Nickel*," WIT Transactions on Engineering Science, 77(2013) p 193-204.
3. **Toloei, A. S**, Stoilov, V, and Northwood, D. O. " *An electrochemical impedance spectroscopy and potentiodynamic polarization study of the effect of unidirectional roughness on the corrosion of nickel* ", International Journal of Computational Methods and Experimental Measurements, Accepted for publication, April 30, 2014.

b. Refereed Conference Proceedings and Conference Presentations

1. **Toloei, A. S**, Stoilov, V, and Northwood, D. O, *The effect of creating different size surface patterns on corrosion properties of Nickel*. Proceedings of ASME 2012 International Mechanical Engineering Congress & Exposition**,** IMECE2012-89407, Houston, Texas, Nov 9-15, 2012, p 1297-1303.

2. **Toloei, A. S**, Stoilov, V, and Northwood, D. O, *The relationship between surface roughness and corrosion*. Proceedings of ASME 2013 International Mechanical Engineering Congress & Exposition**,** IMECE2013-65498, San Diego, California, Nov 18-22, 2013.

c. Conference Presentations

1. **Toloei, A. S**, Stoilov, V, and Northwood, D. O, *Surface Patterning and Corrosion Properties of Nickel.* 24th Canadian Materials Science Conference 2012, London, ON, June 5 -8, 2012 (Poster).

REFERENCES

[1] Shreir, L. L., Jarman, R. A., and Burstein, G. T., 1994, Corrosion (Metal/environment reaction) Butterworth-Heinemann, London.
[2] Geim, A. K., Dubonos, S. V., Grigorieva, I. V., Novoselov, K. S., Zhukov, A. A., and Shapoval, S. Y., 2003, "Microfabricated adhesive mimicking gecko foot-hair," Nature Materials, 2, pp. 461-463.
[3] Dumitru, G., Romano, V., Weber, H. P., Haefke, H., Gerbig, Y., and Pfluger, E., 2000, "Laser microstructuring of steel surfaces for tribological applications. ," Applied Physics A (Materials Science Processing) A70(4), pp. 485-487.
[4] Li, W., Cui, X. S., and Fang, G. P., 2010, "Optimal geometrical design for superhydrophobic surfaces: effects of a trapezoid microtexture" Langmuir, 26(5), pp. 3194–3202.
[5] Wang, Y., Wang, W., Zhong, L., Wang, J., Jiang, Q., and Guo, X., 2010, "Super-hydrophobic surface on pure magnesium substrate by wet chemical method" Applied Surface Science, 256, pp. 3837–3840.
[6] Ou, J., Liu, M., Li, W., Wang, F., Xue, M., and Li, C., 2012, "Corrosion behavior of superhydrophobic surfaces of Ti alloys in NaCl solutions " Applied Surface Science, 258, pp. 4724–4728.
[7] Chen, L. J., Chen, M., Zhou, H. D., and Chen, J. M., 2008, "Preparation of super-hydrophobic surface on stainless steel," Applied Surface Science, 255(5 PART 2), pp. 3459-3462.
[8] Xi, W., Qiao, Z., Zhu, C., Jia, A., and Li, M., 2009, "The preparation of lotus-like super-hydrophobic copper surfaces by electroplating," Applied Surface Science, 255(9), pp. 4836-4839.
[9] Shirtcliffe, N. J., McHale, G., Newton, M. I., and Perry, C. C., 2005, "Wetting and wetting transitions on copper-based super-hydrophobic surfaces," Langmuir, 21(3), pp. 937-943.
[10] Wu, W., Chen, M., Liang, S., Wang, X., Chen, J., and Zhou, F., 2008, "Superhydrophobic surface from Cu-Zn alloy by one step O2 concentration dependent etching," Journal of Colloid and Interface Science, 326(2), pp. 478-482.
[11] Fu, X., and He, X., 2008, "Fabrication of super-hydrophobic surfaces on aluminum alloy substrates," Applied Surface Science, 255(5 PART 1), pp. 1776-1781.
[12] Zhang, Y., Wang, H., Yan, B., Zhang, Y., Yin, P., Shen, G., and Yu, R., 2008, "A rapid and efficient strategy for creating super-hydrophobic coatings on

various material substrates," Journal of Materials Chemistry, 18(37), pp. 4442-4449.
[13] Schweitzer, P. A., 2007, Fundamentals of Metallic Corrosion, Taylor and Francis group, New York.
[14] 1987, ASM Handbook, Volume 13, Corrosion, ASM International, USA.
[15] Fontana, M. G., and Greene, N. D., 1967, Corrosion Engineering, McGraw Hill, New York.
[16] Uhlig, H. H., and Revie, R. W., 2008, Corrosion and Corrosion Control, J. Wiley & Sons, New Jersey.
[17] Paul, A., "Summary of some nickel alloys used in chemical production involving hydrochloric and surfuric acid," Proc. Corrosion conference and expo 2012, NACE, pp. 3520-3532.
[18] Kowsari, E., Payami, M., Amini, R., Ramezanzadeh, B., and Javanbakht, M., 2014, "Task-specific ionic liquid as a new green inhibitor of mild steel corrosion," Applied Surface Science, 289, pp. 478-486.
[19] Gunavathy, N., and Murugavel, S. C., 2013, "Study on the effect of Musa acuminata flower extract on the corrosion inhibition of mild steel in 1 NH2SO4," International Journal of Chemical Sciences, 11(1), pp. 475-486.
[20] Slepski, P., Gerengi, H., Jazdzewska, A., Orlikowski, J., and Darowicki, K., 2014, "Simultaneous impedance and volumetric studies and additionally potentiodynamic polarization measurements of molasses as a carbon steel corrosion inhibitor in 1M hydrochloric acid solution," Construction and Building Materials, 52(0), pp. 482-487.
[21] John, S., and Joseph, A., 2012, "Electroanalytical studies of the corrosion-protection properties of 4-amino-4H-1,2,4-triazole-3,5-dimethanol (ATD) on mild steel in 0.5 N sulfuric acid," Research on Chemical Intermediates, 38(7), pp. 1359-1373.
[22] Mourya, P., Banerjee, S., Rastogi, R. B., and Singh, M. M., 2013, "Inhibition of mild steel corrosion in hydrochloric and sulfuric acid media using a thiosemicarbazone derivative," Industrial and Engineering Chemistry Research, 52(36), pp. 12733-12747.
[23] Marcus, P., and Oudar, J., 1995, Corrosion Mechanisms in Theory and Practice, Marcel Dekker, New York.
[24] Gilli, G., Borea, P., Zucchi, F., and Trabanelli, G., 1969, "Passivation of Ni caused by layers of salts in concentrated H2SO4," Corrosion Science, 9(9), pp. 673-681.
[25] De Gromoboy, T. S., and Shreir, L. L., 1966, "The formation of nickel oxides during the passivation of nickel in relation to the potential/pH diagram," Electrochimica Acta, 11(7), pp. 895-904.

[26] Beverskog, B., and Puigdomenech, I., 1997, "Revised Pourbaix diagrams for nickel at 25–300 °C," Corrosion Science, 39(5), pp. 969-980.
[27] Arvia, A. J., and Posadads, D., 1975, Encyclopedia of electrochemistry of the elements, Marcel Dekker, New York.
[28] Reddy, A. K. N., Rao, M. G. B., and Bockris, J. O. M., 1965, "Ellipsometric determination of the film thickness and conductivity during the passivation process on nickel," The Journal of Chemical Physics, 42(6), pp. 2246-2248.
[29] Armstrong, R. D., and Henderson, M., 1972, "Impedance plane display of a reaction with an adsorbed intermediate," Journal of Electroanalytical Chemistry, 39(1), pp. 81-90.
[30] Sato, N., and Okamoto, G., 1963, "Passivity of nickel," Journal of electrochemical society, 110, pp. 605-614.
[31] Ammar, I. A., and Darwish, S., 1968, "Effect of halogens on passivity of nickel-I. Chloride ions," Electrochimica Acta, 13(4), pp. 781-796.
[32] Cid, M., Jouanneau, A., Nganga, D., and Petit, M. C., 1978, "Comparison between the dissolution and passivity of nickel in sulphuric and hydrofluoric acids," Electrochimica Acta, 23(9), pp. 945-951.
[33] Li, P., Tan, T. C., and Lee, J. Y., 1996, "Impedance spectra of the anodic dissolution of mild steel in sulfuric acid," Corrosion Science, 38(11), pp. 1935-1955.
[34] Fekry, A. M., and Mohamed, R. R., 2010, "Acetyl thiourea chitosan as an eco-friendly inhibitor for mild steel in sulphuric acid medium," Electrochimica Acta, 55(6), pp. 1933-1939.
[35] Khaled, K. F., and Amin, M. A., 2009, "Corrosion monitoring of mild steel in sulphuric acid solutions in presence of some thiazole derivatives - Molecular dynamics, chemical and electrochemical studies," Corrosion Science, 51(9), pp. 1964-1975.
[36] Singh, A. K., Shukla, S. K., and Quraishi, M. A., 2011, "Corrosion behaviour of mild steel in sulphuric acid solution in presence of ceftazidime," International Journal of Electrochemical Science, 6(11), pp. 5802-5814.
[37] Noor, E. A., 2011, "The impact of some factors on the inhibitory action of Radish seeds aqueous extract for mild steel corrosion in 1M H 2SO 4 solution," Materials Chemistry and Physics, 131(1-2), pp. 160-169.
[38] Turner, M., Thompson, G. E., and Brook, P. A., 1973, "The anodic behaviour of nickel in sulphuric acid solutions," Corrosion Science, 13(12), pp. 985-990,IN913,991.
[39] Darowicki, K., Krakowiak, S., and Ślepski, P., 2006, "Selection of measurement frequency in Mott–Schottky analysis of passive layer on nickel," Electrochimica Acta, 51(11), pp. 2204-2208.

[40] Gregori, J., García-Jareño, J. J., Giménez-Romero, D., and Vicente, F., 2005, "Kinetic Calculations of the Ni Anodic Dissolution from EIS," Journal of Solid State Electrochemistry, 9(2), pp. 83-90.
[41] Gonçalves, R. S., Azambuja, D. S., and Serpa Lucho, A. M., 2002, "Electrochemical studies of propargyl alcohol as corrosion inhibitor for nickel, copper, and copper/nickel (55/45) alloy," Corrosion Science, 44(3), pp. 467-479.
[42] Amin, M. A., Shokry, H., and Mabrouk, E. m., 2012, "Nickel corrosion inhibition in sulfuric acid- Electrochemical studies, morphologies, and theoretical approach," Corrosion, 68(8), pp. 699-712.
[43] Hamed, E., Abd El-Rehim, S. S., El-Shahat, M. F., and Shaltot, A. M., 2012, "Corrosion inhibition of nickel in H2SO4 solution by alanine," Materials Science and Engineering: B, 177(5), pp. 441-448.
[44] Abd-El-Nabey, B. A., Abdel-Gaber, A. M., Said Ali, M. E., Khamis, E., and El-Housseiny, S., 2012, "Cannabis Plant Extract as Inhibitor for the Corrosion of Nickel in 0.5 M H_2SO_4," International Journal of Electrochemical Science, 7, pp. 11811 - 11826.
[45] Morad, M. S., 2000, "An electrochemical study on the inhibiting action of some organic phosphonium compounds on the corrosion of mild steel in aerated acid solutions," Corrosion Science, 42(8), pp. 1307-1326.
[46] Rammelt, U., and Reinhard, G., 1990, "On the applicability of a constant phase element (CPE) to the estimation of roughness of solid metal electrodes," Electrochimica Acta, 35(6), pp. 1045-1049.
[47] Aramaki, K., Hagiwara, M., and Nishihara, H., 1987, "The Synergistic Effect of Anion and the Ammonium Cation on the Inhibition of Iron Corrosion in Acid Solution," Corrosion Science, 27(5), pp. 487-497.
[48] Schweinsberg, D., and Flitt, H. J., 2005, "Some Practical Considerations Relevant to the Recording of Corrosion Data," Corrosion and Prevention, 45, pp. 541-553.
[49] Alvarez, R. B., Martin, H. J., Horstemeyer, M. F., Chandler, M. Q., Williams, N., Wang, P. T., and Ruiz, A., 2010, "Corrosion relationships as a function of time and surface roughness on a structural AE44 magnesium alloy," Corrosion Science, 52(5), pp. 1635-1648.
[50] Hilbert, L., Bagge-Ravn, D., Kold, J., and Gram, L., 2003, "Influence of surface roughness of stainless steel on microbial adhesion and corrosion resistance," International Biodeterioration & Biodegradation, 52, pp. 175-185.
[51] Bardal, E., 2004, Corrosion and Protection, Springer-Verlag, London.
[52] Dearnaley, G., 1984, Fundamental Aspects of Corrosion Protection by Surface Modification, The Electrochemical Society, Pennington.
[53] Lee, C. Y., Zhang, B. J., Park, J., and Kim, K. J., 2012, "Water droplet evaporation on Cu-based hydrophobic surfaces with nano- and micro-structures

55," International Journal of Heat Mass Transfer, 55, pp. 2151–2159.
[54] Khan, A., Wang, Z., Sheikh, M. A., Whitehead, D. J., and Li, L., 2011, "Laser micro/nano patterning of hydrophobic surface by contact particle lens array," Applied Surface Science, 258, pp. 774–779.
[55] Wenzel, R. N., 1949, "Surface roughness and contact angle," Journal of Physical & Colloid Chemistry, 53(9), pp. 1466-1467.
[56] Cassie, A. B. D., and Baxter, S., 1944, "Wettability of porous surfaces," Transactions of the Faraday Society, 40, pp. 546-551.
[57] Wenzel, R. N., 1936, "Resistance of solid surfaces to wetting by water," Industrial and Engineering Chemistry, 28, pp. 988-994.
[58] Wang, J., Li , D., Liua, Q., Yin, X., Zhang, Y., Jing, X., and Zhang, M., 2010, "Fabrication of hydrophobic surface with hierarchical structure on Mg alloy and its corrosion resistance, ," Electrochimica Acta, 55, pp. 6897–6906.
[59] He, T., Wang, Y., Zhang, Y., lv, Q., Xu, T., and Liu, T., 2009, "Super-hydrophobic surface treatment as corrosion protection for aluminum in seawater, ," Corrosion Science, 51, pp. 1757–1761.
[60] Etsion, I., 2005, "State of the art in laser surface texturing," Journal of Tribology, 127(1), pp. 248-253.
[61] Kovalchenko, A., Ajayi, O., Erdemir, A., Fenske, G., and Etsion, I., 2005, "The effect of laser surface texturing on transitions in lubrication regimes during unidirectional sliding contact," Tribology International, 38(3), pp. 219–225.
[62] Ryk, G., Kligerman, Y., and Etsion, I., 2002, "Experimental investigation of laser surface texturing for reciprocating automotive components. ," Tribology Transactions, 45(4), pp. 444-449.
[63] Suh, N. P., Mosleh, M., and Howard, P. S., 1994, "Control of friction," Wear, 175(1-2), pp. 151-158.
[64] Varenberg, M., Halperin, G., and Etsion, I., 2002, "Different aspects of the role of wear debris in fretting wear," Wear, 252(11-12), pp. 902-910.
[65] Bushnell, D. M., and Moore, K. J., 1991, "Drag reduction in nature," Ann. Rev. Fluid Mech, 23, p. 65−79.
[66] Genzer, J., and Marmur, A., 2008, "Biological and synthetic self-cleaning surfaces," Mater. Res. Soc. Bull, 33, pp. 742–746.
[67] Scherge, M., and Gorb, S., 2001, Biological Micro- and Nano-tribology, Springer, Berlin.
[68] Autumn, K., Liang, Y. A., Hsieh, S., Zesch, W., Chan, W. P., Kenny, T. W., Fearing, R., and Full, R. J., 2000, "Adhesive force of a single gecko foot-hair.," Nature, 405 pp. 681-685.
[69] Rashwan, O., Stoilov, V., and Guerrero, A., "Effect of surface patterning on the adhesive friction" Proc. ASME 2012 International Mechanical Engineering Congress & Exposition IMECE2012, ASME.

[70] Zuo, Y., Wang, H., and Xiong, J., 2002, "The aspect ratio of surface grooves and metastable pitting of stainless steel," Corrosion Science, 44(1), pp. 25-35.
[71] Burstein, G., and Pistorius, P., 1995, "Surface Roughness and the Metastable Pitting of Stainless Steel in Chloride Solutions," Corrosion, 15(5), pp. 380-385.
[72] Asma, R. N., Yuli, P., and Mokhtar, C., 2011, "Study on the effect of surface finish on corrosion of carbon steel in CO_2 environment," Journal of Applied Sciences 11(11), pp. 2053-2057.
[73] Abosrra, L., Ashour, A. F., Mitchell, S. C., and Youseffi, M., "Corrosion of Mild Steel and 316L Austenitic Stainless Steel with Different Surface Roughness in Sodium Chloride Saline Solutions," WIT Transactions on Engineering Sciences, pp. 161-172.
[74] Sasaki, K., and Burstein, G. T., 1996, "The generation of surface roughness during slurry erosion-corrosion and its effect on the pitting potential," Corrosion Science, 38(12), pp. 2111-2120.
[75] Burstein, G., and Vines, S., 2001, "Repetitive nucleation of corrosion pits on stainless steel and the effects of surface roughness," Journal of The Electrochemical Society, 148(12), pp. B504-B516.
[76] Laycock, N. J., Noh, J. S., White, S. P., and Krouse, D. P., 2005, "Computer simulation of pitting potential measurements," Corrosion Science, 47, pp. 3140–3177.
[77] Shahryari, A., Kamal, W., and Omanovic, S., 2008, "The effect of surface roughness on the efficiency of the cyclic potentiodynamic passivation (CPP) method in the improvement of general and pitting corrosion resistance of 316LVM stainless steel," Materials Letters, 62, pp. 3906–3909.
[78] Cabrini, M., Cigada, A., Rondell, G., and Vicentini, B., 1997, "Effect of different surface finishing and of hydroxyapatite coatings on passive and corrosion current of Ti6Al4V alloy in simulated physiological solution," Biomaterials, 18(11), pp. 783-787.
[79] Suter, T., Müller, Y., Schmutz, P., and von Trzebiatowski, O., 2005, "Microelectrochemical Studies of Pit Initiation on High Purity and Ultra High Purity Aluminum," Advanced Engineering Materials, 7(5), pp. 339–348.
[80] Li, W., and Li, D. Y., 2006, "Influence of surface morphology on corrosion and electronic behavior," Acta Materialia, 54(2), pp. 445-452.
[81] Walter, R., and Kannan, M. B., 2011, "Influence of surface roughness on the corrosion behaviour of magnesium alloy," Materials & Design, 32(4), pp. 2350-2354.
[82] Qiao, Y. X., Zheng, Y. G., Okafor, P. C., and Ke, W., 2009, "Electrochemical behaviour of high nitrogen bearing stainless steel in acidic chloride solution:

Effects of oxygen, acid concentration and surface roughness," Electrochimica Acta, 54, pp. 2298–2304.
[83] Sharland, S. M., 1987, "A review of the theoretical modelling of crevice and pitting corrosion," Corrosion Science, 27(3), pp. 289-323.
[84] Lee, S. M., Lee, W. G., Kim, Y. H., and Jang, H., 2012, "Surface roughness and the corrosion resistance of 21Cr ferritic stainless steel," Corrosion Science, 63(0), pp. 404-409.
[85] Çelik, E., Demirkiran, A. Ş., and Avci, E., 1999, "Effect of grit blasting of substrate on the corrosion behaviour of plasma-sprayed Al_2O_3 coatings," Surface and Coatings Technology, 116-119, pp. 1061–1064
[86] Hong, T., and Nagumo, M., 1997, "Effect of surface roughness on early stages of pitting corrosion of Type 301 stainless steel," Corrosion Science, 39(9), pp. 1665-1672.
[87] Moayed, M. H., Laycock, N. J., and Newman, R. C., 2003, "Dependence of the critical pitting temperature on surface roughness," Corrosion Science, 45, pp. 1203–1216.
[88] Flanders, D., 1980, "Replicationof 175-A˚ lines andspacesinpolymethylmethacrylateusing x-ray lithography," Applied Physics Letters, 36, pp. 93–96.
[89] Smolyaninov, I. I., Mazzoni, D. L., and Davis, C. C., 1995, "Near-field direct-write ultraviolet lithography and shear force microscopic studies of the lithographic process," Applied Physics Letters, 67(26), pp. 3859–3861.
[90] Wendt, J. R., Vawter, G. A., Smith, R. E., and Warren, M. E., 1995, "Nanofabrication of subwavelength, binary, high-efficiency diffractive optical elements in GaAs," Journal of Vaccume Science Technology, B 13, pp. 2705–2708.
[91] Pettersson, U., and S, J., 2003, Influence of surface texture on boundary lubricated sliding contacts, Elsevier Ltd, Stockholm, Sweden.
[92] Schneider, Y. G., 1984, "Formation of surfaces with uniform micropatterns on precision machine and instrument parts " Precision Engineering, 6(4), pp. 219-225.
[93] Xiaolei, W., Adachi, K., Otsuka, K., and Kato, K., 2006, "Optimization of the surface texture for silicon carbide sliding in water," Applied Surface Science, 253(3), pp. 1282-1286.
[94] Wakuda, M., Yamauchi, Y., Kanzaki, S., and Yasuda, Y., 2003, "Effect of surface texturing on friction reduction between ceramic and steel materials under lubricated sliding contact," Wear, 254(3-4), pp. 356-363.
[95] Greco, A., Raphaelson, S., Ehmann, K., Wang, Q. J., and Lin, C., 2009, "Surface texturing of tribological interfaces using the vibromechanical texturing

method," Journal of Manufacturing Science and Engineering, Transactions of the ASME, 131(6), pp. 0610051-0610058.
[96] Koide, S., and Kambe, S., 2002, "Formation of Bi2Sr2Ca1-xYxCu2Oy thin film grown by excimer laser ablation technique," Physica C, 378-381, pp. 1260-1264.
[97] Kononenko, T. V., Garnov, S. V., Pimenov, S. M., Konov, V. I., Romano, V., Borsos, B., and Weber, H. P., 2000, "Laser ablation and micropatterning of thin TiN coatings," Applied Physics A (Materials Science Processing), A71(6), pp. 627-631.
[98] Chen, M. F., Chen, Y. P., Hsiao, W. T., and Gu, Z. P., 2007, " Laser direct write patterning technique of indium tin oxide film," Thin Solid Films, 515, pp. 8515-8518.
[99] Zhou, M., Yang, H. F., Li, B. J., Dai, J., Di, J. K., Zhao, E. L., and Cai, L., 2009, "Forming mechanisms and wettability of double-scale structures fabricated by femtosecond laser," Applied Physics A, 94, pp. 571–576.
[100] Luo, B. H., Shum, P. W., Zhou, Z. F., and Li, K. Y., 2010, "Preparation of hydrophobic surface on steel by patterning using laser ablation process," Surface & Coatings Technology 204, pp. 1180–1185.
[101] Sugihara, T., and Enomoto, T., 2012, "Improving anti-adhesion in aluminum alloy cutting by micro stripe texture," Precision Engineering, 36(2), pp. 229-237.
[102] Hamilton, D. B., Walowit, J. A., and Allen, C. M., 1966, "Theory of Lubrication by Microirregularities," Journal of Basic Engineering, 88(1), pp. 177-185.
[103] Wang, X., Kato, K., Adachi, K., and Aizawa, K., 2003, "Loads carrying capacity map for the surface texture design of SiC thrust bearing sliding in water," Tribology International, 36(3), pp. 189-197.
[104] Etsion, I., Kligerman, Y., and Halperin, G., 1999, "Analytical and experimental investigation of laser-textured mechanical seal faces," Tribology Transactions, 42(3), pp. 511-516.
[105] Tung, S. C., and McMillan, M. L., 2004, "Automotive tribology overview of current advances and challenges for the future," Tribology International, 37(7), pp. 517-536.
[106] Baumgart, P., Krajnovich, D. J., Nguyen, T. A., and A.G, T., 1995, "A new laser texturing technique for high performance magnetic disk drives," IEEE Transactions on Magentics, 31(6), pp. 2946-2951.
[107] Tayebi, N., and Polycarpou, A. A., 2006, "Adhesion and contact modeling and experiments in microelectromechanical systems including roughness effects," Microsystem Technologies, 12(9), pp. 854-869.
[108] Rivin, E., 1999, Stiffness and Damping in Mechanical Design, Taylor & Francis Group, Florence.

[109] Wiklund, D., Rosen, B. G., and Gunnarsson, L., 2008, "Frictional mechanisms in mixed lubricated regime in steel sheet metal forming," Wear, 264(5-6), pp. 474-479.
[110] Geiger, M., Popp, U., and Engel, U., 2002, "Excimer laser micro texturing of cold forging tool surfaces - Influence on tool life," Manufacturing Technology, 15(1), pp. 231-234.
[111] Geiger, M., Roth, S., and Becker, W., 1998, "Influence of laser-produced microstructures on the tribological behaviour of ceramics " Surface and Coatings Technology, 100-101(1-3), pp. 17-22.
[112] Ahuja, A., Taylor, J. A., Lifton, V., Sidorenko, A. A., Salamon, T. R., Lobaton, E. J., Kolodner, P., and Krupenkin, T. N., 2008, "Nanonails: A Simple Geometrical Approach to Electrically Tunable Superlyophobic Surfaces," Langmuir 24(1), pp. 9-14.
[113] Nosonovsky, M., and Bhushan, B., 2005, "Roughness optimization for biomimetic superhydrophobic surfaces," Microsystem Technologies, 11, pp. 535-549.
[114] Que´re´, D., 2005, "Non-sticking drops," Reports on Progress in Physics, 68(11), pp. 2495-2532.
[115] Kota, A. K., Choi, W., and Tuteja, A., 2013, "Superomniphobic surfaces: Design and durability," MRS Bulletin, 38(5), pp. 383-390.
[116] Adamson, A. W., 1990, Physical Chemistry of Surfaces, Wiley, New York
[117] Hiemenz, P., and Rajagopalan, R., 1997, Principles of Colloid and Surface Chemistry, Dekker, New York.
[118] Marmur, A., 2003, "Wetting on hydrophobic rough surfaces: To be heterogeneous or not to be?," Langmuir, 19(20), pp. 8343-8348.
[119] Johnson, R. E., and Dettre, R. H., 1964, "In Contact Angle, Wettability and Adhesion," Advances in Chemistry Series, 43, pp. 112-135.
[120] Patankar, N. A., 2003, "On the modeling of hydrophobic contact angles on rough surfaces," Langmuir 19, pp. 1249-1253.
[121] Lafuma, A., and Que´re´, D., 2003, "Superhydrophobic states," Nature Materials, 2, pp. 457-460.
[122] Tuteja, A., Choi, W., McKinley, G. H., Cohen, R. E., and Rubner, M. F., 2008, "Design parameters for superhydrophobicity and superoleophobicity," Materials Research Bulletin, 33, pp. 752-758.
[123] Singh, R. A., Yoon, E.-S., Kim, H. J., Kim, J., Jeong, H. E., and Suh, K. Y., 2007, "Replication of surfaces of natural leaves for enhanced micro-scale tribological property," Materials Science and Engineering C, 27(4), pp. 875-879.
[124] Burton, Z., and Bhushan, B., 2005, "Hydrophobicity, adhesion, and friction properties of nanopatterned polymers and scale dependence for micro- and nanoelectromechanical systems," Nano Letters, 5(8), pp. 1607-1613.

[125] Cassie, A. B. D., 1948, "Contact angles," Discussions of the Faraday Society, 3, pp. 11-16.
[126] Bico, J., Thiele, U., and Quéré, D., 2002, "Wetting of textured surfaces," Colloids and Surfaces A: Physicochemical and Engineering Aspects, 206(1-3), pp. 41-46.
[127] Feng, X., Zhai, J., and Jiang, L., 2005, "The fabrication and switchable superhydrophobicity of TiO2 nanorod films," Angewandte Chemie - International Edition, 44(32), pp. 5115-5118.
[128] Patankar, N. A., 2004, "Transition between superhydrophobic states on rough surfaces," Langmuir, 20(17), pp. 7097-7102.
[129] Ishino, C., Okumura, K., and Quéré, D., 2004, "Wetting transitions on rough surfaces," Europhysics Letters, 68(3), pp. 419-425.
[130] Tuteja, A., Choi, W., Ma, M., Mabry, J. M., Mazzella, S. A., Rutledge, G. C., McKinley, G. H., and Cohen, R. E., 2007, "Designing superoleophobic surfaces," Science, 318(5856), pp. 1618-1622.
[131] Shastry, A., Case, M. J., and Böhringer, K. F., 2006, "Directing droplets using microstructured surfaces," Langmuir, 22(14), pp. 6161-6167.
[132] Nosonovsky, M., and Bhushan, B., 2008, "Patterned Nonadhesive surfaces: Superhydrophobicity and wetting regime transitions," Langmuir, 24(4), pp. 1525-1533.
[133] Nakajima, A., Hashimoto, K., Watanabe, T., Takai, K., Yamauchi, G., and Fujishima, A., 2000, "Transparent superhydrophobic thin films with self-cleaning properties," Langmuir, 16(17), pp. 7044-7047.
[134] Nakajima, A., Fujishima, A., Hashimoto, K., and Watanabe, T., 1999, "Preparation of transparent superhydrophobic boehmite and silica films by sublimation of aluminum acetylacetonate," Advanced Materials, 11(16), pp. 1365-1368.
[135] Barbieri, L., Wagner, E., and Hoffmann, P., 2007, "Water wetting transition parameters of perfluorinated substrates with periodically distributed flat-top microscale obstacles," Langmuir, 23(4), pp. 1723-1734.
[136] Genzer, J., and Efimenko, K., 2006, "Recent developments in superhydrophobic surfaces and their relevance to marine fouling: A review," Biofouling, 22(5), pp. 339-360.
[137] Sun, T., Feng, L., Gao, X., and Jiang, L., 2005, "Bioinspired surfaces with special wettability," Accounts of Chemical Research, 38(8), pp. 644-652.
[138] Bush, J. W. M., and Hu, D. L., 2006, "Walking on water: Biolocomotion at the interface," pp. 339-369.
[139] Gao, X., and Jiang, L., 2004, "Water-repellent legs of water striders," Nature, 432(7013), p. 36.

[140] Bahadur, V., and Garimella, S. V., 2009, "Preventing the cassie-wenzel transition using surfaces with noneommunicating roughness elements," Langmuir, 25(8), pp. 4815-4820.
[141] Bhushan, B., Israelachvili, J. N., and Landman, U., 1995, "Nanotribology: Friction, wear and lubrication at the atomic scale," Nature, 374(6523), pp. 607-616.
[142] Huikko, K., Östman, P., Grigoras, K., Tuomikoski, S., Tiainen, V. M., Soininen, A., Puolanne, K., Manz, A., Franssila, S., Kostiainen, R., and Kotiaho, T., 2003, "Poly(dimethylsiloxane) electrospray devices fabricated with diamond-like carbon-poly(dimethylsiloxane) coated SU-8 masters," Lab on a Chip - Miniaturisation for Chemistry and Biology, 3(2), pp. 67-72.
[143] Lee, S. J., Huang, C. H., Lai, J. J., and Chen, Y. P., 2004, "Corrosion-resistant component for PEM fuel cells," Journal of Power Sources, 131(1-2), pp. 162-168.
[144] Neinhuis, C., and Barthlott, W., 1997, "Characterization and distribution of water-repellent, self-cleaning plant surfaces," Annals of Botany, 79(6), pp. 667-677.
[145] Scherge, M., and Gorb, S. N., 2000, "Microtribology of biological materials," Tribology Letters, 8(1), pp. 1-7.
[146] Hazel, J., Stone, M., Grace, M. S., and Tsukruk, V. V., 1999, "Nanoscale design of snake skin for reptation locomotions via friction anisotropy," Journal of Biomechanics, 32(5), pp. 477-484.
[147] Cheng, Y. T., Rodak, D. E., Wong, C. A., and Hayden, C. A., 2006, "Effects of micro- and nano-structures on the self-cleaning behaviour of lotus leaves," Nanotechnology, 17(5), pp. 1359-1362.
[148] Blossey, R., 2003, "Self-cleaning surfaces - Virtual realities," Nature Materials, 2(5), pp. 301-306.
[149] Joseph, P., Cottin-Bizonne, C., Benoît, J. M., Ybert, C., Journet, C., Tabeling, P., and Bocquet, L., 2006, "Slippage of water past superhydrophobic carbon nanotube forests in microchannels," Physical Review Letters, 97(15).
[150] Li, X. M., Reinhoudt, D., and Crego-Calama, M., 2007, "What do we need for a superhydrophobic surface? A review on the recent progress in the preparation of superhydrophobic surfaces," Chemical Society Reviews, 36(8), pp. 1350-1368.
[151] Yao, X., Xu, L., and Jiang, L., 2010, "Fabrication and characterization of superhydrophobic surfaces with dynamic stability," Advanced Functional Materials, 20(19), pp. 3343-3349.
[152] Zhang, X., Shi, F., Yu, X., Liu, H., Fu, Y., Wang, Z., Jiang, L., and Li, X., 2004, "Polyelectrolyte Multilayer as Matrix for Electrochemical Deposition of Gold

Clusters: Toward Super-Hydrophobic Surface," Journal of the American Chemical Society, 126(10), pp. 3064-3065.
[153] Shirtcliffe, N. J., McHale, G., Newton, M. I., and Perry, C. C., 2003, "Intrinsically superhydrophobic organosilica sol-gel foams," Langmuir, 19(14), pp. 5626-5631.
[154] Teshima, K., Sugimura, H., Inoue, Y., Takai, O., and Takano, A., 2005, "Transparent ultra water-repellent poly(ethylene terephthalate) substrates fabricated by oxygen plasma treatment and subsequent hydrophobic coating," Applied Surface Science, 244(1-4), pp. 619-622.
[155] Decher, G., Hong, J. D., and Schmitt, J., 1992, "Buildup of ultrathin multilayer films by a self-assembly process: III. Consecutively alternating adsorption of anionic and cationic polyelectrolytes on charged surfaces," Thin Solid Films, 210-211(PART 2), pp. 831-835.
[156] Lau, K. K. S., Bico, J., Teo, K. B. K., Chhowalla, M., Amaratunga, G. A. J., Milne, W. I., McKinley, G. H., and Gleason, K. K., 2003, "Superhydrophobic Carbon Nanotube Forests," Nano Letters, 3(12), pp. 1701-1705.
[157] Ma, M., Hill, R. M., Lowery, J. L., Fridrikh, S. V., and Rutledge, G. C., 2005, "Electrospun poly(styrene-block-dimethylsiloxane) block copolymer fibers exhibiting superhydrophobicity," Langmuir, 21(12), pp. 5549-5554.
[158] Wang, P., Zhang, D., and Qiu, R., 2012, "Liquid/solid contact mode of super-hydrophobic film in aqueous solution and its effect on corrosion resistance," Corrosion Science, 54(1), pp. 77-84.
[159] Liu, T., Yin, Y., Chen, S., Chang, X., and Cheng, S., 2007, "Super-hydrophobic surfaces improve corrosion resistance of copper in seawater," Electrochimica Acta, 52(11), pp. 3709-3713.
[160] Marmur, A., 2008, "From hygrophilic to superhygrophobic: Theoretical conditions for making high-contact-angle surfaces from low-contact-angle materials," Langmuir, 24(14), pp. 7573-7579.
[161] Vaikuntanathan, V., Kannan, R., and Sivakumar, D., 2010, "Impact of water drops onto the junction of a hydrophobic texture and a hydrophilic smooth surface," Colloids and Surfaces A: Physicochemical and Engineering Aspects, 369(1-3), pp. 65-74.
[162] Larmour, I. A., Saunders, G. C., and Bell, S. E. J., 2008, "Assessment of roughness and chemical modification in determining the hydrophobic properties of metals," New Journal of Chemistry, 32(7), pp. 1215-1220.
[163] Li, W., Cui, X. S., and Fang, G. P., 2010, "Optimal geometrical design for superhydrophobic surfaces: Effects of a trapezoid microtexture," Langmuir, 26(5), pp. 3194-3202.

[164] Guo, Z., Zhou, F., Hao, J., and Liu, W., 2005, "Stable biomimetic super-hydrophobic engineering materials," Journal of the American Chemical Society, 127(45), pp. 15670-15671.
[165] Qu, M., Zhang, B., Song, S., Chen, L., Zhang, J., and Cao, X., 2007, "Fabrication of superhydrophobic surfaces on engineering materials by a solution-immersion process," Advanced Functional Materials, 17(4), pp. 593-596.
[166] Roberge, P., 2008, Corrosion Engineering Principles and Practice, McGraw-Hill, New York.
[167] Ponthiaux, P., Wenger, F., Drees, D., and Celis, J. P., 2004, "Electrochemical techniques for studying tribocorrosion processes," Wear, 256(5), pp. 459-468.
[168] Said, F., Souissi, N., Dermaj, A., Hajjaji, N., Triki, E., and Srhiri, A., 2005, "Effect of (R+, X–) Salts Addition on Nickel Corrosion in 1M Sulfuric Acid Medium," Materials and Corrosion, 56(9), pp. 619–623.
[169] Rehim, S. S. A., Hazzazi, O. A., Amin, M. A., and Khaled, K. F., 2008, "On the corrosion inhibition of low carbon steel in concentrated sulphuric acid solutions. Part I: Chemical and electrochemical (AC and DC) studies," Corrosion Science, 50(8), pp. 2258-2271.
[170] Hermas, A. A., and Morad, M. S., 2008, "A comparative study on the corrosion behaviour of 304 austenitic stainless steel in sulfamic and sulfuric acid solutions," Corrosion Science, 50(9), pp. 2710-2717.
[171] Bentiss, F., Lagrenee, M., Traisnel, M., and Hornez, J. C., 1999, "The corrosion inhibition of mild steel in acidic media by a new triazole derivative," Corrosion Science, 41(4), pp. 789-803.
[172] Popova, A., Raicheva, S., Sokolova, E., and Christov, M., 1996, "Frequency Dispersion of the Interfacial Impedance at Mild Steel Corrosion in Acid Media in Presence of Benzimidazole Derivatives," Langmuir, 12(8), pp. 2083-2089.
[173] Rammelt, U., and Reinhard, G., 1987, "The influence of surface roughness on the impedance data for iron electrodes in acid solutions," Corrosion Science, 27(4), pp. 373-382.
[174] Nocedal, J., and Wright, S. J., 1999, Numerical Optimization, Springer, USA.
[175] Surnam, B. Y. R., and Oleti, C. V., 2012, "Using three-dimensional surface roughness parameters in analysis of atmospheric corrosion degradation of carbon steel," Corrosion Engineering Science and Technology, 47(2), pp. 96-106.
[176] Punckt, C., Bolscher, M., Rotermund, H. H., Mikhailov, A. S., Organ, L., Budiansky, N., Scully, J. R., and J.L, H., 2004, "Sudden onset of pitting corrosion on stainless steel as a critical phenomenon," Science, 305, pp. 1133-1136.

[177] Walter, R., Kannan, M. B., He, Y., and Sandham, A., 2013, "Effect of surface roughness on the in vitro degradation behaviour of a biodegradable magnesium-based alloy," Applied Surface Science, 279, pp. 343-348.
[178] Kubisztal, J., Budniok, A., and Lasia, A., 2007, "Study of the hydrogen evolution reaction on nickel-based composite coatings containing molybdenum powder," International Journal of Hydrogen Energy, 32(9), pp. 1211-1218.
[179] Bard, A. J., Inzelt, G., and Scholz, F., 2008, Electrochemical dictionary, Springer, Berlin.
[180] Shervedani, R. K., and Madram, A. R., 2007, "Kinetics of hydrogen evolution reaction on nanocrystalline electrodeposited Ni62Fe35C3 cathode in alkaline solution by electrochemical impedance spectroscopy," Electrochimica Acta, 53(2), pp. 426-433.
[181] Momoh-Yahaya, H., Eddy, N. O., and Oguzie, E. E., 2014, "Inhibitive, adsorptive and thermodynamic study of hypoxanthine against the corrosion of aluminium and mild steel in sulphuric acid," Journal of Materials and Environmental Science, 5(1), pp. 237-244.
[182] Heydari, M., Ravari, F. B., and Dadgarinezhad, A., 2011, "Corrosion Inhibition Propargyl Alcohol on Low Alloy Cr Steel in 0.5 M H2SO4 in the Absence and Presence of Potassium Iodide," Gazi University Journal of Science, 24(3), pp. 507-515.
[183] Bard, A., and Faulkner, L., 2001, Electrochemical methods-fundamentals and applications, John Wiley & Sons, New York.
[184] Khaled, K. F., 2011, "Molecular modeling and electrochemical investigations of the corrosion inhibition of nickel using some thiosemicarbazone derivatives," Journal of Applied Electrochemistry, 41(4), pp. 423-433.
[185] Krstajić, N., Popović, M., Grgur, B., Vojnović, M., and Šepa, D., 2001, "On the kinetics of the hydrogen evolution reaction on nickel in alkaline solution: Part I. The mechanism," Journal of Electroanalytical Chemistry, 512(1–2), pp. 16-26.
[186] Kaninski, M., Nikolic, V., Tasic, G., and ZL, R., 2009, "Electrocatalytic activation of Ni electrode for hydrogen production by electrodeposition of Co and V species," Int J Hydrogen Energy 34, pp. 703–709.
[187] Jin, S., Amira, S., and Ghali, E., 2007, "Electrochemical impedance spectroscopy evaluation of the corrosion behavior of die cast and thixocast AXJ530 magnesium alloy in chloride solution," Advanced Engineering Materials, 9(1-2), pp. 75-83.
[188] Toloei, A. S., Stoilov, V., and Northwood, D. O., 2013, "The Effect of Different Surface Topographies on the Corrosion Behaviour of Nickel," WIT Transactions on Engineering Science, 77, pp. 193-204.

VITA AUCTORIS

Name: Alisina Toloei

Place of Birth: Iran

Year of birth 1985

Education:

- Najafabad University, B. Sc., Materials Science and Engineering (Metallurgical Engineering), Isfahan, Iran, 2007.
- University of Shiraz, M. A. Sc., Materials Science and Engineering (Corrosion Engineering), Shiraz, Iran, 2010.
- University of Windsor, Ph.D., Mechanical, Automotive and Materials Engineering (Corrosion Engineering), Windsor, Ontario, Canada, September 2010 - April 2014.